Fall 2013

Characterization of Fractures Subjected to Normal and Shear Stress

Min-Kwang Choi
Purdue University

Graduate School ETD Form 9
(Revised 12/07)

PURDUE UNIVERSITY
GRADUATE SCHOOL
Thesis/Dissertation Acceptance

This is to certify that the thesis/dissertation prepared

By Min-Kwang Choi

Entitled
CHARACTERIZATION OF FRACTURES SUBJECTED TO NORMAL AND SHEAR STRESS

For the degree of Doctor of Philosophy

Is approved by the final examining committee:

Antonio Bobet
Chair

Laura J. Pyrak-Nolte

Maria C. Santagata

Pablo D. Zavattieri

To the best of my knowledge and as understood by the student in the *Research Integrity and Copyright Disclaimer (Graduate School Form 20)*, this thesis/dissertation adheres to the provisions of Purdue University's "Policy on Integrity in Research" and the use of copyrighted material.

Approved by Major Professor(s): Antonio Bobet

Laura J. Pyrak-Nolte

Approved by: Michael Kreger 09/12/2013
Head of the Graduate Program Date

CHARACTERIZATION OF FRACTURES SUBJECTED TO NORMAL AND SHEAR STRESS

A Dissertation

Submitted to the Faculty

of

Purdue University

by

Min-Kwang Choi

In Partial Fulfillment of the

Requirements for the Degree

of

Doctor of Philosophy

December 2013

Purdue University

West Lafayette, Indiana

To My Parents

ACKNOWLEDGEMENTS

I would like to express my sincere and deep thanks to my advisor Professors Bobet and Pyrak-Nolte for their guidance, patience, inspiration, and motivation in research. They gave me a chance to study at Purdue, guided me into the rock engineering and geophysics area with insightful advice, and shared with me their innovative and brilliant idea.

I deeply appreciate Prof. Santagata and Prof. Zavattieri for kind suggestions and helpful advice for this study.

Thanks to my good friend Ahmad who gave me a lot of helps in my experimental works. I hope only great things are on his way for future. Thanks to great professors and friends in Purdue Geotechnical Area who made my life at Purdue colorful.

I would like to thank all guys in Purdue Korean Civil Engineering and Korean Christian Community Siloam for giving me unforgettable memories.

Finally, thanks to my parents and sister, for their deep love. Without your support, I would not be able to complete this work.

TABLE OF CONTENTS

Page

Page

Page

LIST OF TABLES

Table Page

LIST OF FIGURES

Figure Page

Figure Page

Figure Page

Figure Page

Figure Page

Figure Page

Figure Page

Figure Page

Figure Page

ABSTRACT

Choi, Min-Kwang, Ph.D., Purdue University, December 2013. Characterization of Fractures Subjected to Normal and Shear Stress. Major Professors: Antonio Bobet and Laura J. Pyrak-Nolte.

Results from a series of laboratory experiments to determine fracture specific stiffness, for a fracture subjected to shear and normal stress, are presented and analyzed. The experimental work focuses on the determination of relations between normal and shear fracture specific stiffness and between spatial distribution of fracture specific stiffness and fluid flow through the fracture

The ratio of shear to normal fracture specific stiffness is experimentally investigated on a fracture subjected to shear as well as normal stress. Synthetic fractures made of gypsum and lucite were prepared with different fracture surface conditions: either well-mated or non-mated. For well-mated fracture surfaces, asperities were created by casting gypsum against sandpaper. A block of gypsum was cast against the sandpaper and then a second block was cast against the first block such that the two contact surfaces were well-mated. The surface roughness was controlled by using the sandpapers with different average grit size. Non-mated fracture surfaces were fabricated with two lucite blocks that were polished (lucite PL) or sand-blasted (lucite SB) along their contact surface. In the experiments, each specimen was subjected to normal and shear loading while the fracture

was probed with transmitted and reflected compressional and shear waves. Shear and normal fracture specific stiffnesses were calculated using the displacement discontinuity theory. For non-mated fractures, the stiffness ratio was not sensitive to the application of shear stress and, as normal stress increased, approached a theoretical ratio which was determined assuming that the transmission of compressional and shear waves was equal. The stiffness ratio obtained from well-mated fractures ranged from 0.5 to 1.4, which deviated from the conventional assumption that shear and normal fracture specific stiffness are equal. The stiffness ratio increased with increasing surface roughness and with increasing shear stress. For well-mated surfaces under normal compression and no shear, the theoretical ratio gave a good approximation to experiment measurements. During shear, at constant load, and for well-mated fractures with large surface roughness, the stiffness ratio strongly depended on the shear fracture specific stiffness and increased with shear up to a maximum prior to failure.

The spatial variability of fracture specific stiffness along a fracture was investigated seismically on granite specimens with a single fracture. Seismic measurements on intact and fractured granite specimens were obtained as a function of stress. The granite matrix exhibited stress-sensitivity due to the existence of micro-cracks and was weakly anisotropic, with a ratio of about 0.9 for shear wave velocities in two orthogonal directions. For fractured granite specimens, transmission of P- and S- waves across a fracture significantly increased as the fracture compressed. The increase of transmission was interpreted as the increase of fracture specific stiffness. Spectral analysis on the transmitted waves showed that the transmission of high frequency components of the signals increased and the dominant frequency approached the value of the intact

specimen. The heterogeneity of the granite material resulted in a ±8~12% variation in stiffness, which depended on the selection of an intact standard. Fracture specific stiffness was estimated at the dominant frequency of 0.3 MHz for normal specific stiffness and 0.5 MHz for shear. Fracture specific stiffness was non-uniformly distributed along the fracture plane and changed locally as a function of stress. The spatial variability of stiffness exceeded the variation of stiffness caused by the heterogeneity of granite matrix. It was found that local fracture geometry, e.g. local surface roughness distribution or local micro slope angles, influenced the magnitude of local shear fracture specific stiffness. The more uniform the asperity heights, the stiffer the fracture. Also, high micro-slope angles increased the shear fracture specific stiffness.

The seismic response of the rock matrix (granite) and fracture with and without flow was utilized to correlate fluid flow with fracture specific stiffness. Experiments of fluid invasion into a rock matrix and along a fracture showed an increase in wave velocity and a decrease in wave amplitude when the rock became wet. Invasion velocity was determined seismically by tracking the fluid front in the rock matrix. The velocity through the granite matrix was (5.9 - 16.3) x 10^{-7} m/sec. The fluid invasion velocity into the fracture was found to occur much faster than into the granite matrix, and so propagation of the fluid in a granite fracture is seismically detectable during the early stages of fluid invasion. The fluid-air front was tracked by the increase in wave velocity and the decrease in wave amplitude. The fluid front advanced non-uniformly throughout the fracture plane. The fluid first invaded portions of the fracture that had a relatively low fracture specific stiffness and then spread to regions with high stiffness. The non-uniform propagation of the fluid front correlated well with the spatial distribution of the fracture

specific stiffness. Along with the fluid invasion tests, fluid flow in two orthogonal directions in a fracture was measured as a function of stress. With stress, the fluid flow decreased from 10^{-9} to 10^{-11} m^2/sec as the fracture specific stiffness increased from 10^3 to 10^4 MPa/mm. Flow in the fractures was approximately isotropic and more sensitive to changes in shear specific stiffness than in normal specific stiffness. The fluid flow-fracture specific stiffness observed in this study was compared to the data in the literature, and resulted in that the fracture was weakly spatially correlated and the fluid flow-fracture stiffness relation was in the percolation regime.

CHAPTER 1. INTRODUCTION

1.1 Introduction

The behavior of fractures and fracture systems affects various scientific and engineering applications, e.g., fault zone studies, rock stability investigations, non-destructive testing, oil production from subsurface reservoir, monitoring subsurface, nuclear waste repositories, the control and manipulation of groundwater, and CO_2 sequestration (Möllhoff and Bean (2009)). One of the most relevant methods for the characterization and prediction of fractures is the use of seismic waves (Queen and Rizer (1990)). Attenuation and velocity of seismic waves have been used to estimate some physical properties of fractures such as fluid flow through a fracture, and mechanical properties of rock mass (Fischer et al. (2008) and Li et al. (1998)). Therefore, seismic methods have the potential to characterize the mechanical and hydraulic properties of fracture systems. The main aim of this research is to characterize fracture specific stiffness of a single fracture subjected to normal and shear stress using active monitoring compressional (P-) and shear (S-) wave propagation to determine the ratio of shear to normal fracture specific stiffness, and the spatial distribution of fluid flow through a fracture.

The ratio of shear to normal stiffness is important to numerical modeling of seismic wave propagation through fractured media (Schonberg, (1980), Liu et al. (2000), Sayers and Kachonov (1995), Hsu and Schonberg (1993), and Schonberg and Sayers (1995)). In the

modeling, it is necessary to assign normal and shear specific stiffness values to a fracture and, for an inclined fracture, a specific relationship between shear and normal fracture specific stiffness is required (Pyrak-Nolte (1996)). A fracture can be modeled as a displacement discontinuity at the boundary between two elastic half-spaces (Schonberg (1980), and Pyrak-Nolte (1990)). This approach is used to estimate fracture specific stiffness because of the lack of laboratory and/or field data (Schonberg, (1980), Liu et al. (2000), Sayers and Kachonov (1995), Hsu and Schonberg (1993), Schonberg and Sayers (1995), Far (2011), and Verdon and Wüstefeld (2013)). Conventionally, the shear and normal fracture specific stiffness are assumed to be equal for modeling (Liu et al. (2000), Sayers and Kachonov (1995), and Johnson (1985)). However, recent experimental work does not support such conventional assumption, suggesting that the ratio of shear to normal fracture stiffness is not unique and is sensitive to the filling material in a fracture (Pyrak-Nolte et al. (1990), Sayers (1999), Sayers and Han (2002), Far (2011), and Lubbe et al. (2008)), the orientation of micro-cracks (Liu et al. (2000), Sayers and Kachonov (1995), and Pervukhina (2011)), thermal damage to the rock matrix (MacBecth and Schuett (2007)), and mineralization of the fracture surface (Sayers et al. (2009)). Within the availability of the experiment data, the stiffness ratio ranged from 0 to 3.0 for dry fractures and from 0 to 1.6 for saturated fractures. This research challenges the conventional assumption of a unique ratio of shear to normal stiffness. This study first presents the experimental work performed to determine the ratio of shear (κ_x) to normal fracture specific stiffness (κ_z) for a single fracture subjected to normal and shear stress for well-mated versus non-mated fracture surfaces. Here, a well-mated fracture has a perfectly matched fracture surface; this is typical of natural fractures. In contrast, a non-

mated fracture surface is imperfectly matched; this is the case for an artificial fracture created by polishing, grinding or sand-blasting.

As mentioned, the seismic response of a fracture can be modeled theoretically as a non-welded contact where stress is continuous but the displacement is discontinuous, which is often referred to as displacement discontinuity theory (Schoenberg (1980), and Pyrak-Nolte et al. (1988)). In the theory, the discontinuity in displacement is assumed to be inversely proportional to the fracture specific stiffness. The fracture behaves as a low pass filter that attenuates the high frequency components of the signal (Pyrak-Nolte et al. (1990)). The displacement discontinuity theory has been successfully applied to estimate fracture stiffness based on transmitted waves across a fracture in laboratory experiments (Pyrak-Nolte et al. (1990), Hsu and Schoenberg (1993), and Lubbe et al., (2008)). However, the estimated fracture stiffness at the laboratory scale only probes a portion of the fracture (local stiffness) and the spatial variability of fracture stiffness in the fracture has not been investigated well. Acosta-Colon et al. (2009) used an acoustic lens method to map the spatial variability of fracture stiffness and to determine the effect of the size of the illumination regime on interpreting fracture specific stiffness. They determined that the transmission of a compressional wave across the fracture was not spatially uniform. An additional goal of this study is to determine the effect of mixed mode loading (i.e. normal and shear stress) on the spatial distribution of fracture specific stiffness. Previous studies focused only on the effect of normal loading.

It has been hypothesized that fracture specific stiffness and fluid flow are implicitly related through aperture distribution (Petrovitch et al. (2013), Pyrak-Nolte and Morris (2000) and Pyrak-Nolte (1996)). The link between fracture specific stiffness and fluid

flow is important in interpreting the hydraulic characteristics of the fracture from the seismic response of the fracture because measurements of seismic velocity and attenuation can be used to estimate, remotely, the specific stiffness of a fracture in a rock mass. Currently, there is no analytical solution to link flow and fracture specific stiffness and the link is interpreted to be most likely statistical in nature (Jaeger et al. (2007)). Recently, Petrovitch et al. (2013) performed a Monte Carlo study of fluid flow through a fracture and fracture deformation as a function of scale for spatially uncorrelated fracture aperture distributions. They found that a scaling relationship exists between fluid flow and fracture specific stiffness because stiffness acts as a surrogate for void area in a fracture and captures the deformed topology of the void space in a fracture. Many examinations of the relationship between fluid flow and fracture specific stiffness had been made numerically and experimentally (Pyrak-Notle et al. (1988), Nolte et al. (1991), Pyrak-Nolte et al. (1997), Sisavath et al. (2003), Meyer (2000), Pyrak-Nolte and Morris (2000), and Petrovitch et al. (2013)). These investigations proved the dependency of fluid flow through a fracture on fracture geometry, including spatial correlation of aperture distribution and magnitude of mean aperture, and provided evidence to support a quantitative interrelationship between fracture specific stiffness and fluid flow through a fracture, i.e., a stiff fracture carries less fluid flow than a compliant fracture. In this study, the spatial distribution of fracture specific stiffness in a fracture is correlated to the fluid flow path determined seismically, i.e., the change in transmitted P- and S- waves induced by fluid flow is used to interpret the location of the invading fluid front.

1.2 Objectives and Scope

The overall goal of this research is to characterize the specific stiffness of fractures subjected to normal and shear stresses. A series of experiments were conducted to: (1) determine the relationship between normal and shear fracture specific stiffness under normal and shear loading; (2) characterize the spatial variability of specific stiffness of a single fracture in a rock specimen; and (3) determine if fluid flow-fracture specific stiffness relationship holds for fractures subjected to both normal and shear loading.

The experimental investigation consists of three major tasks:

(1) Investigation of the relationship between normal and shear fracture specific stiffness. The conventional assumption is that normal and shear fracture stiffnesses are equal, and yet there is no experimental evidence to support such an assumption. The goal of this task was to determine the validity of this assumption. An extensive literature review was performed to collect data on both normal and shear fracture stiffnesses. The data was compared to theoretical estimates based on the displacement discontinuity theory. A series of experiments under normal only and normal and shear loading was done to establish a relationship between normal and shear stiffness. The fracture surfaces were controlled to be either well-mated or not-mated.

(2) Investigation of spatial variability of stiffness of a single fracture. In this task, the transmitted P- and S- waves across a fracture were measured using seismic imaging, and then interpreted using the displacement discontinuity theory. The spatial variability of fracture specific stiffness was determined as a function of the applied normal and shear stress.

(3) Determination of a relation between fluid flow and fracture stiffness. Fluid invasion tests were performed on granite samples containing a single fracture. The spatial distribution of the fracture specific stiffness was interpreted and correlated with fluid invasion observations to investigate the relationship between fluid flow and fracture specific stiffness.

1.3 Organization

This dissertation has five chapters in addition to the Introduction Chapter. They are as follows:

Chapter 2 reviews the displacement discontinuity theory and summarizes past work on the relationship between normal and shear fracture specific stiffness and on fracture stiffness - fluid flow relations, as these are the main objectives in this thesis.

Chapter 3 presents a series of experiments to investigate the ratio of shear to normal fracture specific stiffness. The chapter includes deviation of the theoretical ratio of shear to normal fracture specific stiffness, specimen preparation, seismic data acquisition, experimental procedures and stiffness ratio determined from the experiments.

Chapter 4 contains the experiments performed to identify the spatial distribution of fracture specific stiffness. It includes experimental observations on the seismic response of fractures, spatial variability of fracture stiffness and effect of surface roughness and micro-slope angle of asperities on fracture specific stiffness. The spatial variation in fracture specific stiffness is mapped as a function of normal stress.

Chapter 5 describes the experimental work on seismic monitoring of the rock matrix and a fracture when fluid is invaded. An experimental attempt is made to detect the fluid front

seismically and to correlate fluid flow to the fracture specific stiffness. The fluid flow experiments are interpreted and compared with the spatial variability of fracture specific stiffness obtained in Chapter 4.

Finally, Chapter 6 contains a brief summary of the work performed for the thesis, summarizes the main observations and conclusions, and provides recommendations for future studies.

CHAPTER 2. THEORY AND BACKGROUND

2.1 Introduction

In this chapter, an overview on the topics related to the objectives of this study is presented. The fundamental theory of wave propagation across a fracture, i.e., displacement discontinuity theory, is presented first and a literature review of papers associated with the relationship between shear and normal fracture stiffness and on fluid flow in fracture follows.

2.2 Displacement Discontinuity Theory

Elastic wave propagation across a fracture can be mathematically modeled by assuming that the seismic wavelength is much greater than the mean separation between asperities of the fracture and that the seismic wavelength is less than the fracture spacing. The problem assumes an infinite fracture between two elastic half spaces that are non-welded. The fracture (non-welded contact) is represented by a set of boundary conditions that link the two elastic half-spaces. In the theoretical modeling, the effect of fractures on wave propagation depends only on density of background material, elastic properties of the elastic half-spaces, and specific stiffness of the fracture. The specific stiffness is defined as the ratio of the increment in stress applied to the fracture to the increment in displacement that occurs. This mathematical model constitutes the ‘displacement

discontinuity model'. The boundary conditions that represent the fracture assume that the stress across the interface is continuous while the displacement is discontinuous. The magnitude of the displacement discontinuity is inversely proportional to the specific stiffness of the fracture. The general solution for compressional and shear waves propagated at oblique angles of incidence to a displacement discontinuity is given by Schoenberg (1980) and Kitsunezaki (1983). Pyrak-Nolte et al. (1990) showed that the displacement discontinuity model predicts well the effect of a single natural fracture on the spectral amplitude of transmitted compressional and shear waves. If a fracture is filled with fluid, the adhesion or cohesion of the fluid to the fracture is captured by a specific viscosity of the fracture that results in discontinuities in both the displacement and velocity across the fracture (Nihei (1992), Suarez-Rivera (1992), and Pyrak-Nolte et al. (1996)).

In the displacement discontinuity theory, the rheological behavior of a fracture may be modeled by any of the following representations: (i) a spring, (ii) a dashpot, (iii) a spring and dashpot in parallel (Kelvin model), or (iv) a spring and dashpot in series (Maxwell model). The spring and dashpot represent the specific stiffness of a fracture and the specific viscosity of the fracture, respectively. The specific fracture viscosity is defined as the ratio of the increment in stress applied to the fracture to the increment in velocity that it produces, and considers the possible viscous coupling between the two surfaces of the fracture due to the presence of a fluid or the rock type. Pyrak-Nolte (1996) derived the full solution for a fracture represented by a spring and dashpot in parallel (Kelvin) and in series (Maxwell). In this section the theory is re-derived for both normal and shear

loading. The solutions for a spring or dashpot can be obtained only when setting the specific viscosity to zero or the specific fracture stiffness to zero in the Kelvin model.

2.2.1 Kelvin Non-Welded Fracture Model

The Kelvin non-welded fracture model consists of a spring and dashpot in parallel. If the non-welded contact between two elastic half-spaces lies in the *x*-*y* plane, the boundary conditions of the combined discontinuities for displacement and velocity for an incident compressional wave (P-wave) are:

$$\kappa_z(u_{z1}-u_{z2})+\eta_z(\dot{u}_{z1}-\dot{u}_{z2})=\tau_{zz} \tag{2.2.1-1}$$

$$\kappa_x(u_{x1}-u_{x2})+\eta_x(\dot{u}_{x1}-\dot{u}_{x2})=\tau_{zx} \tag{2.2.1-2}$$

$$\tau_{zz1}=\tau_{zz2} \tag{2.2.1-3}$$

$$\text{where } \tau_{zz}=\lambda\frac{\partial u_x}{\partial x}+(\lambda+2\mu)\frac{\partial u_z}{\partial z} \tag{2.2.1-4}$$

$$\tau_{zx1}=\tau_{zx2} \tag{2.2.1-5}$$

$$\text{where } \tau_{zx}=\mu\left(\frac{\partial u_x}{\partial z}+\frac{\partial u_z}{\partial x}\right) \tag{2.2.1-6}$$

where a dot on top of a variable denotes a derivative with respect to time. The schematic diagram of the Kelvin model is shown in Figure 2.2.1-1. The x- and z- directions in the figure are tangential and normal to the fracture plane, respectively.

Equations (2.2.1-1) and (2.2.1-2) are the boundary conditions that describe a fracture with both displacement and velocity discontinuities for the normal (*z*) and the tangential (*x*)

components. In equations (2.2.1-1) and (2.2.1-2), κ represents the specific stiffness of the fracture and η represents the specific viscosity of the fracture; u is the displacement induced by the applied stress; μ and λ are the Lamé's constants. Subscript 1 represents the half-space for z > 0 and subscript 2 represents the half-space for z < 0. The boundary conditions given by equations (2.2.1-1) to (2.2.1-6) are also applicable for an incident Sv-wave, where the shear wave is polarized in the x-direction.

For an incident Sh wave, where the shear wave is polarized in the y- direction (out of plane direction), the boundary conditions are:

$$\kappa_y(u_{y1} - u_{y2}) + \eta_y(\dot{u}_{y1} - \dot{u}_{y2}) = \tau_{zy} \tag{2.2.1-7}$$

$$\tau_{zy1} = \tau_{zy2} \tag{2.2.1-8}$$

$$\text{where } \tau_{zy} = \mu\left(\frac{\partial u_y}{\partial z}\right) \tag{2.2.1-9}$$

By applying the boundary conditions in equations (2.2.1-1) to (2.2.1-9) to the solution of the wave equation for compressional and shear waves, the complete solution for the reflected and transmitted components of P- and Sv- waves, for all angles of incidence when the seismic impedance of the elastic half-spaces differs, is obtained. Equations (2.2.1-10) to (2.2.1-12) provide the solution, where Z is the seismic impedance defined as the product of the density to phase velocity of the elastic half-spaces (Pyrak-Nolte, 1996).

$$A=\begin{bmatrix} -(\kappa_z-i\omega\eta_z)\cos\theta_1 & (\kappa_z-i\omega\eta_z)\sin\phi_1 & -(\kappa_z-i\omega\eta_z)\cos\theta_2+i\omega Z_{P2}\cos 2\phi_2 & (\kappa_z-i\omega\eta_z)\sin\phi_2-i\omega Z_{S2}\sin 2\phi_2 \\ -(\kappa_x-i\omega\eta_x)\sin\theta_1 & -(\kappa_x-i\omega\eta_x)\cos\phi_1 & (\kappa_x-i\omega\eta_x)\sin\theta_2-i\omega\dfrac{Z_{S2}^2}{Z_{P2}}\sin 2\theta_2 & (\kappa_x-i\omega\eta_x)\cos\phi_2-i\omega Z_{S2}\cos 2\phi_2 \\ -Z_{P1}\cos 2\phi_1 & Z_{S1}\sin 2\phi_1 & Z_{P2}\cos 2\phi_2 & -Z_{S2}\sin 2\phi_2 \\ \dfrac{Z_{S1}^2}{Z_{P1}}\sin 2\theta_1 & Z_{S1}\cos 2\phi_1 & \dfrac{Z_{S2}^2}{Z_{P2}}\sin 2\theta_2 & Z_{S2}\cos 2\phi_2 \end{bmatrix} \tag{2.2.1-10}$$

For P- wave,

$$A\cdot\begin{Bmatrix} R_P \\ R_{SV} \\ T_P \\ T_{SV} \end{Bmatrix}=\begin{bmatrix} -(\kappa_z-i\omega\eta_z)\cos\theta_1 \\ (\kappa_x-i\omega\eta_x)\sin\theta_1 \\ Z_{P1}\cos 2\phi_1 \\ \dfrac{Z_{S1}^2}{Z_{P1}}\sin 2\theta_1 \end{bmatrix} \tag{2.2.1-11}$$

For Sv-wave,

$$A\cdot\begin{Bmatrix} R_P \\ R_{SV} \\ T_P \\ T_{SV} \end{Bmatrix}=\begin{bmatrix} (\kappa_z-i\omega\eta_z)\sin\phi_1 \\ (\kappa_x-i\omega\eta_x)\cos\phi_1 \\ -Z_{S1}\sin 2\phi_1 \\ Z_{S1}\cos 2\phi_1 \end{bmatrix} \tag{2.2.1-12}$$

The solution for Sh- wave is (Pyrak-Nolte, 1996),

$$A=\begin{bmatrix} -(\kappa_y-i\omega\eta_y) & (\kappa_y-i\omega\eta_y)-i\omega Z_{S2}\cos\phi_2 \\ Z_{S1}\cos\phi_1 & Z_{S2}\cos\phi_2 \end{bmatrix} \tag{2.2.1-13}$$

$$A\cdot\begin{Bmatrix} R_{Sh} \\ T_{Sh} \end{Bmatrix}=\begin{bmatrix} (\kappa_y-i\omega\eta_y) \\ Z_{S1}\cos\phi_1 \end{bmatrix} \tag{2.2.1-14}$$

In equations (2.2.1-10) to (2.2.1-14), θ is the angle of incidence of the incident, reflected and transmitted P-wave and ϕ is an angle of incidence of incident, reflected and transmitted Sv- or Sh- waves in an elastic half-space, as seen in Figure 2.2.1-2. ω is the angular frequency and $i = \sqrt{-1}$. R and T stand for the reflection and transmission coefficients, respectively. The subscripts P, SV and Sh indicate the type of elastic wave, i.e., compressional for P, shear polarized in the x- direction for SV and in the y-direction for Sh.

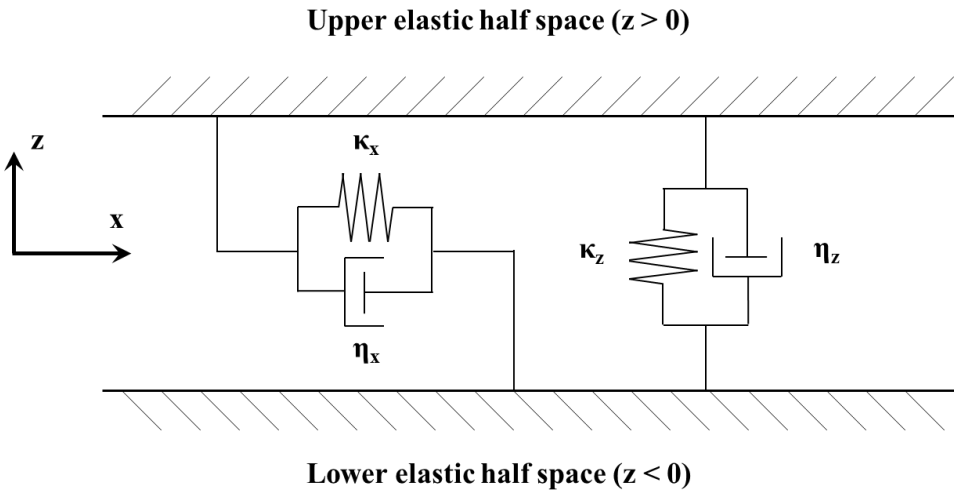

Figure 2.2.1-1. Schematic diagram of Kelvin non-welded fracture model. Springs and dashpots in parallel represent the specific stiffness of the fracture (κ) and the specific viscosity of the fracture (η), respectively, in x- (tangential) and z- (normal) directions.

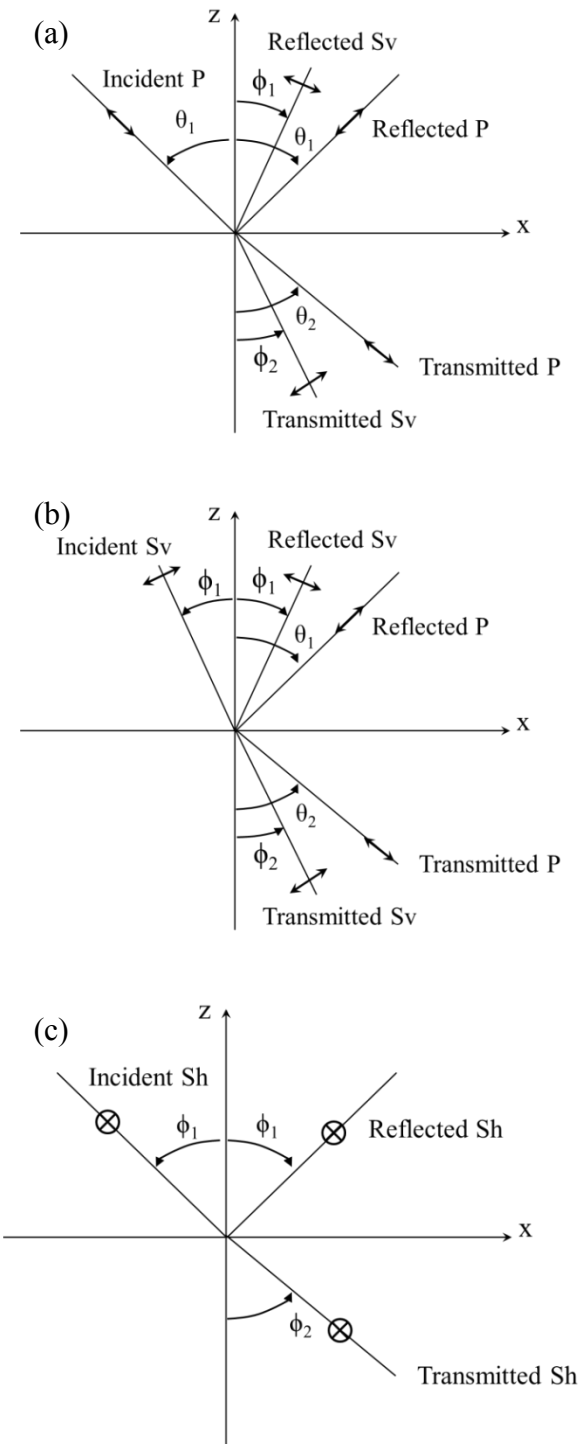

Figure 2.2.1-2. Converted, reflected and transmitted components of: (a) P-wave, (b) Sv-wave, and (c) Sh- waves on a displacement discontinuity (modified after Pyrak-Nolte (1990)).

2.2.2 Maxwell Non-Welded Fracture Model

The Maxwell non-welded fracture model consists of a spring and dashpot in series. Figure 2.2.2-1 presents the schematic diagram of the Maxwell model. The x- and z-directions in the figure are tangential and normal to the fracture plane, respectively. If the discontinuous boundary between two elastic half-spaces lies in the *x-y* plane, the boundary conditions for displacement and velocity for an incident P- or Sv- wave are (Pyrak-Nolte, 1996):

$$(\dot{u}_{1z} - \dot{u}_{2z}) = \frac{\dot{\tau}_{2zz}}{\kappa_z} + \frac{\tau_{2zz}}{\eta_z} \tag{2.2.2-1}$$

$$(\dot{u}_{1x} - \dot{u}_{2x}) = \frac{\dot{\tau}_{2zx}}{\kappa_x} + \frac{\tau_{2zx}}{\eta_x} \tag{2.2.2-2}$$

$$\tau_{1zz} = \tau_{2zz} \tag{2.2.2-3}$$

$$\text{where } \tau_{zz} = \lambda \frac{\partial u_x}{\partial x} + (\lambda + 2\mu) \frac{\partial u_z}{\partial z} \tag{2.2.2-4}$$

$$\tau_{1zx} = \tau_{2zx} \tag{2.2.2-5}$$

$$\text{where } \tau_{zx} = \mu \left(\frac{\partial u_x}{\partial z} + \frac{\partial u_z}{\partial x} \right) \tag{2.2.2-6}$$

For an incident Sh-wave, the boundary conditions are (Pyrak-Nolte, 1996):

$$(\dot{u}_{1y} - \dot{u}_{2y}) = \frac{\dot{\tau}_{2zy}}{\kappa_y} + \frac{\tau_{2zy}}{\eta_y} \tag{2.2.2-7}$$

$$\tau_{zy} = \mu \frac{\partial u_y}{\partial z} \tag{2.2.2-8}$$

The variables in equations of (2.2.2-1) to (2.2.2-8) are defined as before.

In a manner similar to the Kelvin fracture model, the boundary conditions in equations (2.2.2-1) to (2.2.2-8) are applied to the solution of the wave equations for compressional and shear waves. The complete solution for the reflected and transmitted components of P-, Sv- and Sh- waves for all angles of incidence (and for different values of seismic impedance for media 1 and 2) are obtained and are given by equations (2.2.2-9) to (2.2.2-11) (Pyrak-Nolte, 1996). In equation (2.2.2-9), γ is defined as the ratio of specific fracture stiffness κ to specific fracture viscosity η , i.e. γ = η / κ . The symbols used in equations (2.2.2-1) to (2.2.2-13) are the same as those in section 2.2.1.

$$A = \begin{bmatrix} \eta_z \cos\theta_1 & -\eta_z \sin\phi_1 & \eta_z \cos\theta_2 + (1 - i\omega\gamma_z)(Z_{P2} - \frac{2Z_{S2}^2}{Z_{P2}} \sin^2\theta_2) & -\eta_z \sin\phi_2 + (i\omega\gamma_z - 1) Z_{S2} \sin 2\phi_2 \\ \eta_x \sin\theta_1 & \eta_x \cos\phi_1 & \eta_x \sin\theta_2 - (1 - i\omega\gamma_x) \frac{Z_{S2}^2}{Z_{P2}} \sin 2\theta_2 & -\eta_x \cos\phi_2 + (i\omega\gamma_x - 1) Z_{S2} \cos 2\phi_2 \\ -Z_{P1} + \frac{2Z_{S1}^2}{Z_{P1}} \sin^2\theta_1 & Z_{S1} \sin 2\phi_1 & Z_{P2} - \frac{2Z_{S2}^2}{Z_{P2}} \sin^2\theta_2 & -Z_{S2} \sin 2\phi_2 \\ -\frac{Z_{S1}^2}{Z_{P1}} \sin 2\theta_1 & -Z_{S1} \cos 2\phi_1 & -\frac{Z_{S2}^2}{Z_{P2}} \sin 2\theta_2 & -Z_{S2} \cos 2\phi_2 \end{bmatrix} \tag{2.2.2-9}$$

For P-waves,

$$A \cdot \begin{Bmatrix} R_P \\ R_{SV} \\ T_P \\ T_{SV} \end{Bmatrix} = \begin{bmatrix} \eta_z \cos\theta_1 \\ -\eta_x \sin\theta_1 \\ Z_{P1} - \dfrac{2Z_{S1}^2}{Z_{P1}} \sin^2\theta_1 \\ -\dfrac{Z_{S1}^2}{Z_{P1}} \sin 2\theta_1 \end{bmatrix} \tag{2.2.2-10}$$

For Sv-waves,

$$A \cdot \begin{Bmatrix} R_P \\ R_{SV} \\ T_P \\ T_{SV} \end{Bmatrix} = \begin{bmatrix} -\eta_z \sin\phi_1 \\ -\eta_x \cos\phi_1 \\ -Z_{S1} \sin 2\phi_1 \\ -Z_{S1} \cos 2\phi_1 \end{bmatrix} \tag{2.2.2-11}$$

The solution for Sh waves is,

$$A = \begin{bmatrix} -Z_{S1} \cos\phi_1 & -Z_{S2} \cos\phi_2 \\ \eta_y & -\eta_y - (1 - i\omega\gamma_y) Z_{S2} \cos\phi_2 \end{bmatrix} \tag{2.2.2-12}$$

$$A \cdot \begin{Bmatrix} R_{Sh} \\ T_{Sh} \end{Bmatrix} = \begin{bmatrix} -Z_{S1} \cos\phi_1 \\ -\eta_y \end{bmatrix} \tag{2.2.2-13}$$

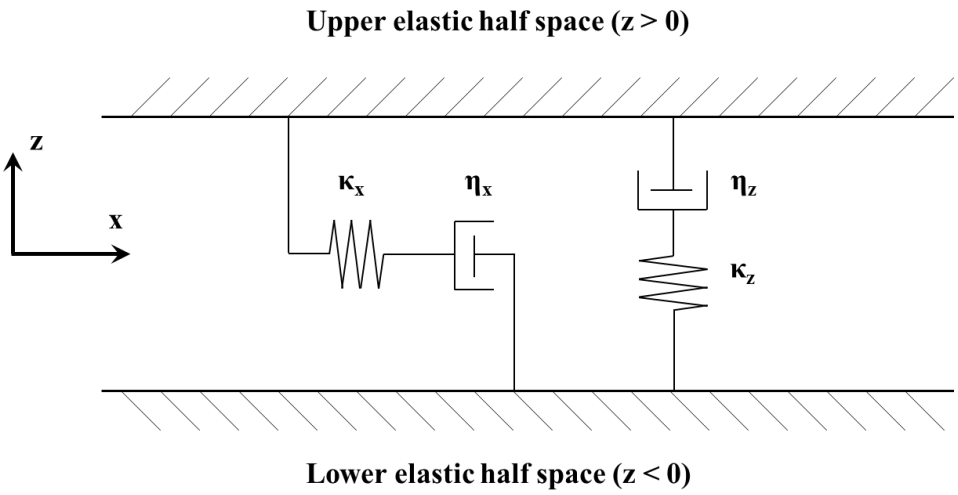

Figure 2.2.2-1. Schematic diagram of Maxwell non-welded fracture model. Springs and dashpots in series represent the specific stiffness of the fracture (κ) and the specific viscosity of the fracture (η), respectively, in x- (tangential) and z- (normal) directions.

2.2.3 Comparison between Kelvin and Maxwell Models

The theoretical behavior of a fracture represented as either a Kelvin or a Maxwell non-welded contact has been investigated. To simplify the comparison between the two models, the following assumptions were made (Pyrak-Nolte (1996)):

i) The incident angle of the wave is 0˚, i.e. the wave is propagating normal to the fracture.

ii) The two elastic half-spaces have the same seismic impedance, $Z=Z_1=Z_2$.

iii) The ratio of specific fracture viscosity to seismic impedance is constant.

With the three assumptions, the coefficients of transmission T_p and reflection R_p of a P-wave can be obtained from equations (2.2.1-10) and (2.2.1-11) for the Kelvin model and from equations (2.2.2-9) and (2.2.2-10) for the Maxwell model.

For the Kelvin non-welded fracture model, the solution is given by:

$$T_p = \frac{2\left(1 - i \cdot c\frac{\omega Z}{\kappa}\right)}{2 - i(1+2c)\frac{\omega Z}{\kappa}} \tag{2.2.3-1}$$

$$R_p = \frac{i \cdot \frac{\omega Z}{\kappa}}{2 - i(1+2c)\frac{\omega Z}{\kappa}}. \tag{2.2.3-2}$$

For the Maxwell non-welded fracture model,

$$T_p = \frac{\left(1+\frac{1}{2c}\right)+i\frac{1}{2}\left(\frac{\omega Z}{\kappa}\right)}{\left(1+\frac{1}{2c}\right)^2+\frac{1}{4}\left(\frac{\omega Z}{\kappa}\right)^2} \tag{2.2.3-3}$$

$$R_p = \frac{-\frac{1}{2c}\left(1+\frac{1}{2c}\right)-\frac{1}{4}\left(\frac{\omega Z}{\kappa}\right)^2+i\frac{1}{2}\left(\frac{\omega Z}{\kappa}\right)}{\left(1+\frac{1}{2c}\right)^2+\frac{1}{4}\left(\frac{\omega Z}{\kappa}\right)^2}. \tag{2.2.3-4}$$

Equations (2.2.3-1) to (2.2.3-4) show that the coefficients of transmission and reflection are a function of the constant $c = \eta / Z$ and normalized frequency $\omega Z / \kappa$.

For the Kelvin model, Figure 2.2.3-1 shows the magnitude of the transmission and reflection coefficients for P-waves as a function of normalized frequency $\omega Z / \kappa$. It is clear that the transmission and reflection coefficients depend on the normalized frequency. The fracture behaves as a low-pass filter by transmitting low-frequency components of the signals and attenuating the high frequencies. When the specific stiffness of a fracture approaches zero, the normalized frequency $\omega Z / \kappa$ goes to infinity, i.e. $\omega Z / \kappa = \infty$, the transmission coefficient decreases to zero and the reflection coefficient increases to one. In this case, the fracture is behaving as a free surface. In contrast, as the fracture specific stiffness approaches infinity, i.e. $\omega Z / \kappa = 0$, the fracture behaves as a welded contact and all the energy is transmitted across the fracture, with no energy partitioned into the reflected signal. The specific viscosity of the fracture reduces the energy transmitted at low frequencies and increases the energy transmitted at high frequencies. Also the transmission coefficient becomes independent of the frequency when the specific viscosity term dominates the solution.

In Figure 2.2.3-2, the transmission and reflection coefficients for the Maxwell model for P- waves depend on frequency, on specific fracture stiffness and specific viscosity. Increasing η / Z increases the transmitted amplitude of a compressional wave propagated across a Maxwell non-welded contact and decreases the reflection coefficient. The detailed investigation for theoretical behavior of a single fracture is well-described in the study of Pyrak-Nolte (1990 and 1996).

In this study, a Matlab code was developed to solve the solution of the Kelvin non-welded fracture model numerically. The code calculates the fracture specific stiffness for P-, Sv- and Sh- incident waves with an arbitrary angle to the fracture as a function of frequency, and is based on experimentally measured transmission coefficients of both transmission and reflection. In the code, the theoretical transmission curve for the frequency range of interest (i.e. from 0 MHz to 2.0 MHz, which is of interest in the experiments) was calculated first by assuming an arbitrary fracture specific stiffness value. The obtained transmission curve was then compared with the experimentally measured transmission curve to determine the fracture specific stiffness. Then, the fracture specific stiffness was increased or decreased until the difference between the two curves was less than 3%.

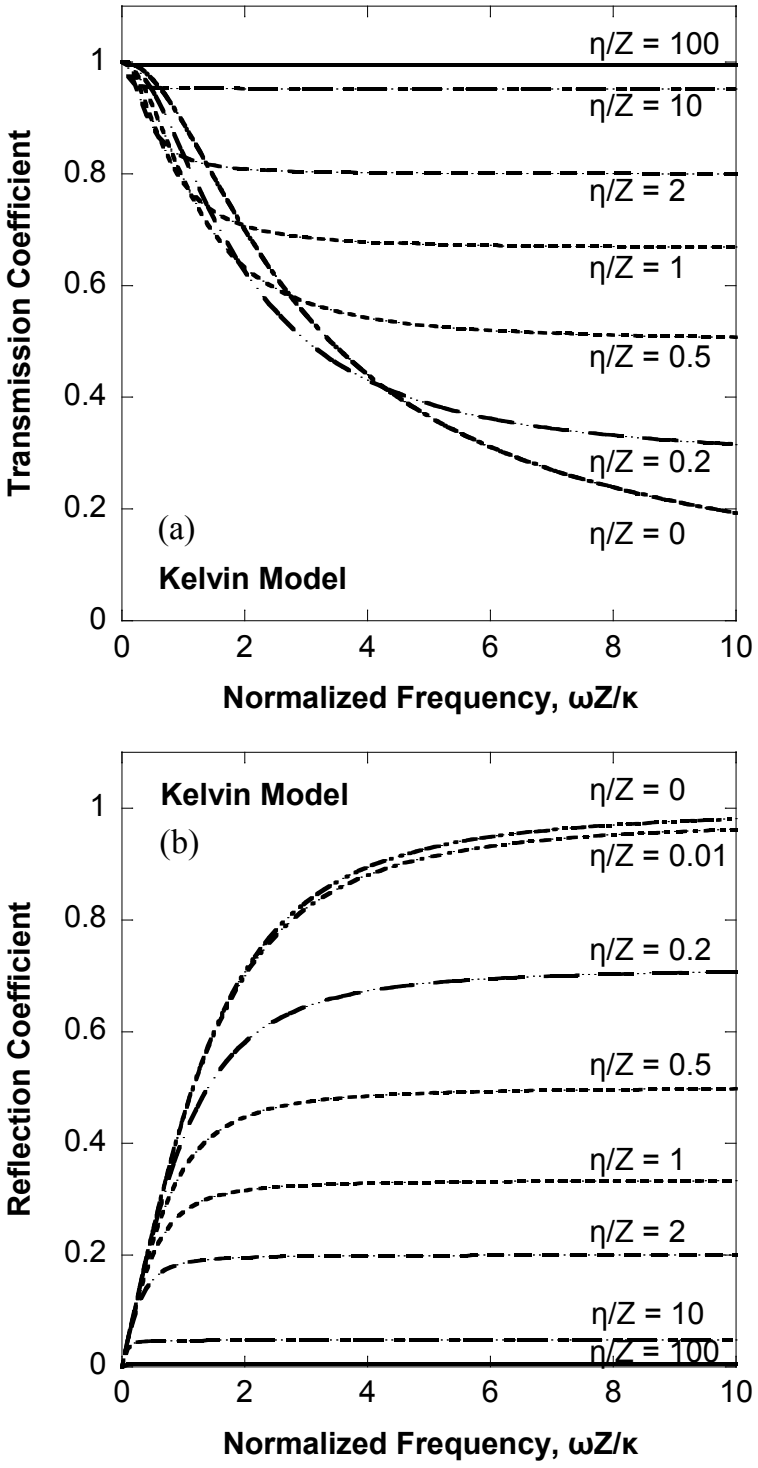

Figure 2.2.3-1. Magnitudes of (a) transmission and (b) reflection coefficients for P-wave normally incident in Kelvin model as a function of normalized frequency, for normalized specific viscosity η / Z =0~100.

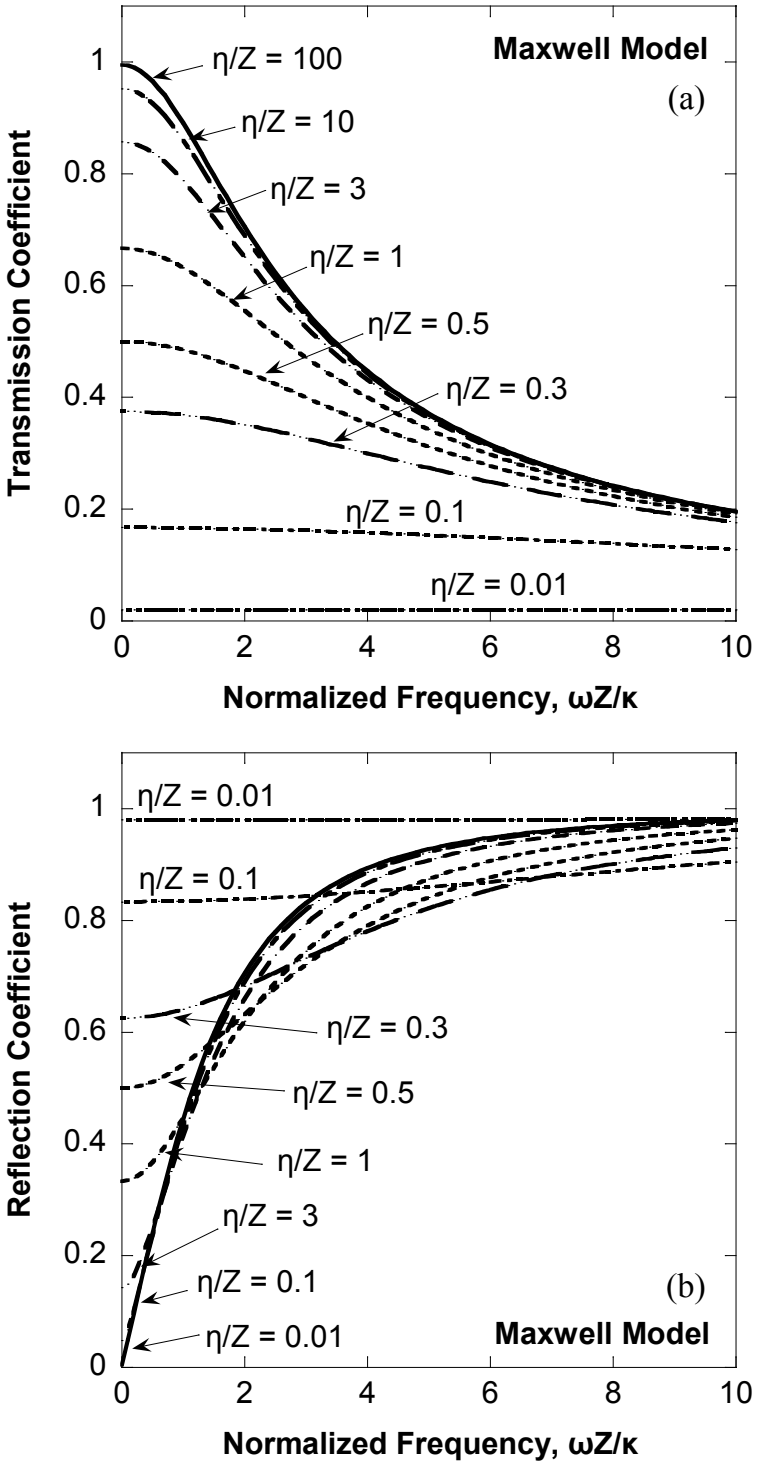

Figure 2.2.3-2. Magnitudes of (a) transmission and (b) reflection coefficients for P-wave normally incident in Maxwell model as a function of normalized frequency, for normalized specific viscosity η / Z =0.01~100.

2.2.4 Fracture Specific Stiffness from Transmission and Reflection

Analyses of the Kelvin and Maxwell non-welded fracture models found that the Kelvin model predicted better the seismic behavior of a fracture. Myer et al (1985) applied the Kelvin fracture model to predict the amplitude of waves propagated across synthetic fractures. Pyrak-Nolte (1990) found that the Kelvin fracture model precisely predicted the group velocity for rock samples containing a single fracture. Hence, the discussions related to the displacement discontinuity theory contained in this section are limited to the Kelvin non-welded fracture model.

For the Kelvin model, equations (2.2.1-10) to (2.2.1-14) can be reduced to equation (2.2.4-1) and (2.2.4-2) for a normal incident wave when the two half-spaces have the same seismic impedance Z (i.e., material properties) and the fracture is dry, i.e. $\eta = 0$. For normal incidence, there is no conversion between P- and S- waves at the fracture.

$$R = \frac{-i\omega}{[-i\omega + 2(\kappa / Z)]} \tag{2.2.4-1}$$

$$T = \frac{2(\kappa / Z)}{[-i\omega + 2(\kappa / Z)]} \tag{2.2.4-2}$$

By taking the ratio of reflection to transmission coefficient, R / T, a simple equation for stiffness estimation was derived, which is shown in equation (2.2.4-3). In the equation, the ratio R / T has a linear relationship with the normalized frequency $\omega Z / \kappa$. Hence, once the ratio of reflection to transmission, R / T, is determined from experimental data,

the fracture specific stiffness κ for a normal incident wave can be directly calculated by equation (2.2.4-3), given the seismic impedance Z and angular frequency ω.

$$\left|\frac{R}{T}\right| = \frac{1}{2}\left|\frac{\omega Z}{\kappa}\right| \tag{2.2.4-3}$$

Figure 2.2.4-1 shows the variation of the transmission and the reflection coefficients as well as the ratio R / T, as a function of the normalized frequency ωZ / κ. As the fracture specific stiffness κ increases, i.e., as the normalized frequency decreases, transmission increases and reflection decreases. It is noted that, when the normalized frequency decreases from 15 to 4, the reflection coefficient only decreases by about 10%, while the transmission coefficient increases significantly from 0.13 to 0.45, a factor of 3.4. It implies that, in the range of the normalized frequency $\omega Z / \kappa \geq 4$, the reflection coefficient is not very sensitive to the change of fracture specific stiffness while the transmission coefficient is sensitive. If the normalized frequency ωZ / κ is less than 4, both the transmission and reflection coefficients are sensitive to the change of fracture specific stiffness. Based on this analysis, the transmission coefficient is more useful for detecting changes in fracture specific stiffness for normalized frequencies within the range 0 - 15.

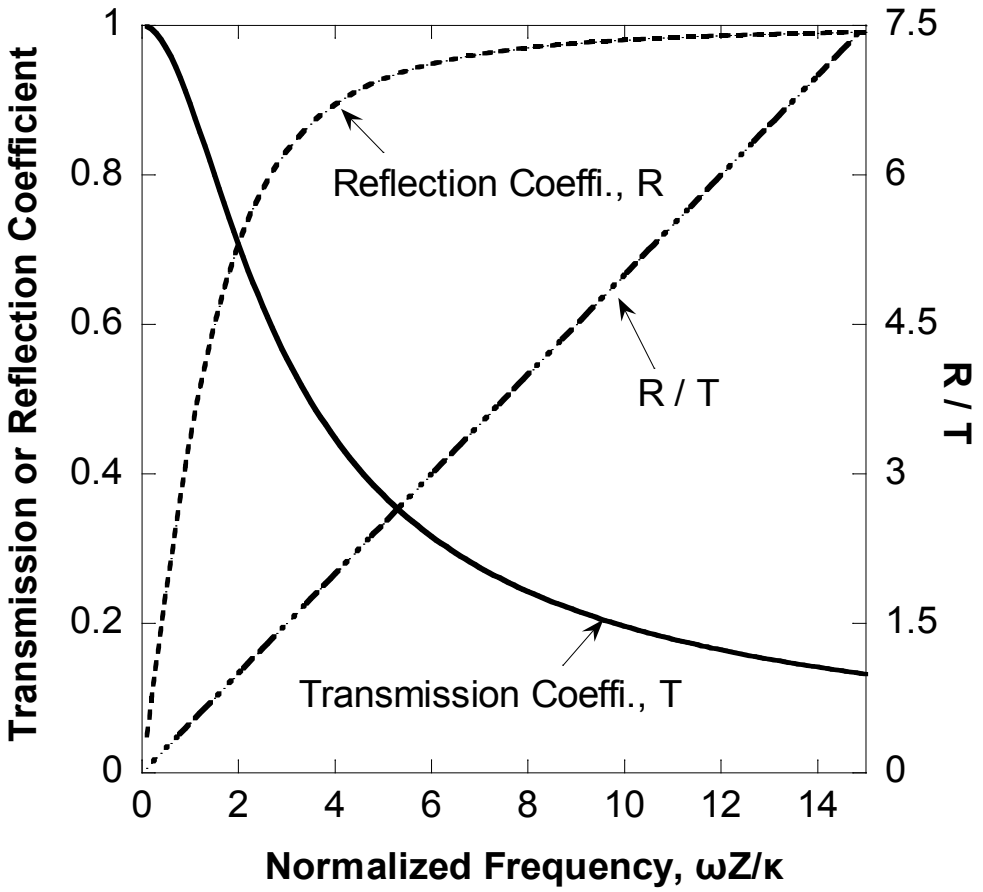

Figure 2.2.4-1. Transmission and reflection coefficients and ratio R / T as a function of normalized frequency ωZ / κ. The frequency ω is normalized by the specific stiffness of the fracture κ and seismic impedance Z.

2.3 Relationship between Normal and Shear Fracture Stiffness

As discussed in the section 2.2, wave propagation across a displacement discontinuity is dominated by the magnitude of the fracture specific stiffness. For waves propagating at oblique angles across a displacement discontinuity it is necessary to specify the relationship between normal fracture specific stiffness κ_z and shear fracture specific stiffness κ_x in equations (2.2.1-10) - (2.2.1-14). Because of the sensitivity of the seismic response to fracture specific stiffness, i.e., normal and shear fracture specific stiffness, an understanding of the ratio of shear to normal fracture specific stiffness is important for characterizing fractures using seismic waves.

2.3.1 Theoretical Approaches to Stiffness Ratio

A number of theoretical studies have assumed that a fracture consists of a planar distribution of small isolated areas of slip (cracks) (Liu et al. (2000), Kachanov et al. (2010), Hsu and M. Schoenberg (1993), Hudson (1981), Sayers and Kachonov (1995), and Pervukhina et al. (2011)), while other studies have modeled a fracture as a planar distribution of imperfect interfacial contacts (Liu et al. (2000), Kachanov et al. (2010), Hudson (1997) and Johnson (1985)). Both models are based on the concept of average stress and strain acting on the fracture plane and assume a linear relationship between displacement discontinuity across the fracture and applied stress that is governed by the fracture compliance, which is equal to the inverse of fracture stiffness (Hill (1963), and Hudson and Knopoff (1989)).

If the cracks within a fracture are represented as open penny-shaped geometries with a radius *a* in an isotropic material with Poisson's ratio ν and Young's modulus E, the normal and shear compliances (B_N and B_T) are given by (Rice (1979)):

$$B_N = 16(1-\nu^2)\frac{a}{3\pi E} \tag{2.3.1-1}$$

$$B_T = 32(1-\nu^2)\frac{a}{3\pi E(2-\nu)} = \frac{B_N}{1-\nu/2} \tag{2.3.1-2}$$

Therefore, the compliance ratio B_N/B_T is

$$\frac{B_N}{B_T} = 1-\frac{\nu}{2} \tag{2.3.1-3}$$

Here, the compliance ratio B_N/B_T is equivalent to the ratio of shear to normal fracture specific stiffness κ_x/κ_z.

Sayers and Kachanov (1995) proposed a fundamental formulation to estimate fracture compliance when a fracture consisted of a planar distribution of small isolated areas of slip (cracks). Assuming that the interaction between cracks is small enough to be taken as negligible, the average vector u_i of the displacement discontinuity (fracture) can be given, in terms of the average traction t_i applied at the crack and the crack compliance tensor B_{ij}, as:

$$[u_i] = B_{ij} t_j = B_{ij} \sigma_{jk} n_k \tag{2.3.1-4}$$

where σ_{jk} is the applied stress and n_k is the *k*th component of unit vector that is normal to the surface of the crack. Here, the crack compliance tensor B_{ij} can be represented as the sum of the normal and shear compliances, B_N and B_T.

$$B_{ij} = B_N n_i n_j + B_T(\delta_{ij} - n_i n_j) \tag{2.3.1-5}$$

where δ_{ij} is the Kronecker delta. Then, the incremental compliance tensor ΔS_{ijkl} due to the existence of cracks is defined as,

$$\Delta S_{ijkl} = \frac{1}{4}(\delta_{ik}\alpha_{jl} + \delta_{il}\alpha_{jk} + \delta_{jk}\alpha_{il} + \delta_{jl}\alpha_{ik}) + \beta_{ijkl} \tag{2.3.1-6}$$

$$\alpha_{ij} = \frac{1}{V}\sum_r B_T^r n_i^r n_j^r A^r \tag{2.3.1-7}$$

$$\beta_{ijkl} = \frac{1}{V}\sum_r (B_N^r - B_T^r) n_i^r n_j^r n_k^r n_l^r A^r \tag{2.3.1-8}$$

Here, r is the number of planar discontinuities with crack area A^r. Note that the values of α_{ij} and β_{ijkl} depend only on the values of the indeces but not on their order, e.g., $\beta_{1122} = \beta_{1212}$ and $\beta_{1133} = \beta_{1313}$, etc. Equations (2.3.1-6) to (2.3.1-8) can consider the distribution of crack orientations by specifying α_{ij} and β_{ijkl}. Sayers and Kachanov (1995) predicted that, if B_N is equal to B_T for all cracks, β_{ijkl} goes to be zero and ΔS_{ijkl} depends only on

the second-rank tensor α_{ij}. This case corresponds to a transversely isotropic material with the axis of orthotropy coinciding with the principal axes of α_{ij}. Kachanov (1980) and Sayers and Kachanov (1991) also showed that the compliance tensor B_{ij} has orthotropic symmetry, i.e., three orthogonal planes of mirror symmetry, if $B_N = B_T$.

Kachanov et al. (2010) extended the theoretical framework of Sayers and Kachanov (1995) by substituting equations (2.3.1-1) and (2.3.1-2) into equations (2.3.1-6) to (2.3.1-8) to obtain ΔS_{ijkl} as follows,

$$\Delta S_{ijkl} = \frac{32(1-\nu^2)a}{3(2-\nu)E}\left[\frac{1}{4}(\delta_{ik}\alpha_{jl} + \delta_{il}\alpha_{jk} + \delta_{jk}\alpha_{il} + \delta_{jl}\alpha_{ik}) - \frac{\nu}{2}\beta_{ijkl}\right] \qquad (2.3.1\text{-}9)$$

The authors showed that the fourth-rank tensor β_{ijkl} plays a secondary role on the incremental compliance tensor ΔS_{ijkl} because of the relatively small multiplier $\nu/2$ in equation (2.3.1-9). Given the assumption of neglecting β_{ijkl}, it was proven that orthorhombic symmetry holds with the axis of orthotropy coinciding with the principal axes of α_{ij}. However, orthotropy may not hold if B_N and B_T are such that neglecting β_{ijkl} is not possible.

Alternatively, a fracture can be assumed as a collection of a planar distribution of imperfect interfacial contacts (Liu et al. (2000), Kachanov et al. (2010), Hudson et al. (1997) and Johnson (1985)). Johnson (1985) derived equations (2.3.1-10) and (2.3.1-11) that calculate total pressures on a unit indentation in the normal (B_N) and tangential (B_T) directions on a circular region of radius a on the surface of an elastic half-space. The equations are:

$$B_N = \frac{-4(\lambda+\mu)}{(\lambda+2\mu)} \tag{2.3.1-10}$$

$$B_T = \frac{-8(\lambda+\mu)}{(3\lambda+4\mu)} \tag{2.3.1-11}$$

where, μ and λ are the Lamé's constants.

Hudson et al. (1997) modeled a fracture as two rough surfaces based on a random distribution of circular contacts and derived the equations for normal and shear specific stiffness. Worthington and Hudson (2000) modified the equations of Hudson et al. (1997) to include the effect of material filling the void spaces of a fracture. Equations (2.3.1-12) and (2.3.1-13) show the normal and shear specific stiffnesses from Worthington and Hudson (2000).

$$\kappa_z = r^w \frac{4\mu}{\pi a}\left(1-\frac{\beta^2}{\alpha^2}\right)\left\{1+\frac{2(r^w)^{1/2}}{\sqrt{\pi}}\right\}+\frac{K'+\frac{4}{3}\mu'}{\Delta} \tag{2.3.1-12}$$

$$\kappa_x = r^w \frac{8\mu}{\pi a}\left(1-\frac{\beta^2}{\alpha^2}\right)\left\{1+\frac{2(r^w)^{1/2}}{\sqrt{\pi}}\right\}\Big/\left(3-\frac{2\beta^2}{\alpha^2}\right)+\frac{\mu'}{\Delta} \tag{2.3.1-13}$$

where α, β are the compressional and shear wave velocities, respectively, and μ is the Lamé's constant. r^w is the proportion of the fracture surface area that is in contact and *a* is the mean radius of the contact areas. μ' and K' are the Lamé's constant and bulk modulus of the fracture fill and Δ is the mean aperture of the fracture. If a fracture is dry, i.e., gas-

filled fracture, the second term in equations (2.3.1-12) and (2.3.1-13), which are related to the fracture filling material, is negligible.

Both Johnson (1985) and Hudson et al. (1997) provided the ratio of shear to normal fracture specific stiffness κ_x / κ_z ($=B_N/B_T$) as:

$$\frac{\kappa_x}{\kappa_z} = \frac{B_N}{B_T} = \frac{1-\nu}{1-\nu/2} \tag{2.3.1-14}$$

Baik and Thomson (1984) modeled a fracture as a planar array of ellipsoidal voids with semi-axes $a = b$ in the fracture plane and $c \leq a$ perpendicular to the fracture plane. They gave the normal compliance B_N as,

$$B_N = \frac{4\pi a^2 cN}{3(1-\nu)}\left[2\nu\frac{\varepsilon_{11}^T}{\sigma_{33}} + (1-\nu)\frac{\varepsilon_{33}^T}{\sigma_{33}}\right] \tag{2.3.1-15}$$

where ν is the Poisson's ratio, N is the number density of the cracks, σ_{33} is the applied stress in the x_3 direction, and $\varepsilon_{11}{}^T$ and $\varepsilon_{33}{}^T$ are the equivalent strains obtained by Baik and Thompson (1984) using the solution of Eshelby (1961). Here, the interactions between the cracks were neglected. The shear compliance B_T was re-derived by Sayers et al. (2009) after correcting several misprints from Nagy (1992) as,

$$B_T = \frac{4\pi a^2 cN}{3\mu\gamma} \tag{2.3.1-16}$$

where

$$\gamma = \frac{1}{4\pi(1-\nu)}\left[(2-\nu)I + \frac{c^2}{a^2-c^2}(4\pi - 3I)\right] \qquad (2.3.1\text{-}17)$$

$$I = \frac{2\pi a^2 c}{(a^2-c^2)^{3/2}}\left[\cos^{-1}\frac{c}{a} - \frac{c}{a}\left(\frac{a^2-c^2}{a^2}\right)^{1/2}\right] \qquad (2.3.1\text{-}18)$$

In summary, for the case of a planar distribution of small isolated areas of slip, the stiffness ratio is equal to (1-ν/2), where ν is the Poisson's ratio. If a fracture is assumed to be a planar distribution of imperfect interfacial contacts, the ratio is given by the expression: (1-ν) / (1-ν/2). In both cases, the value of κ_x / κ_z can be approximated as 1.0 because the Poisson's ratio is typically small. For a fracture approximated as a planar array of ellipsoidal voids with low values of the aspect ratio, i.e. $c/a \leq 0.1$, that are similar to a penny-shaped crack, the value of the stiffness ratio is also close to 1.0, as seen in Figure 2.3.1-1.

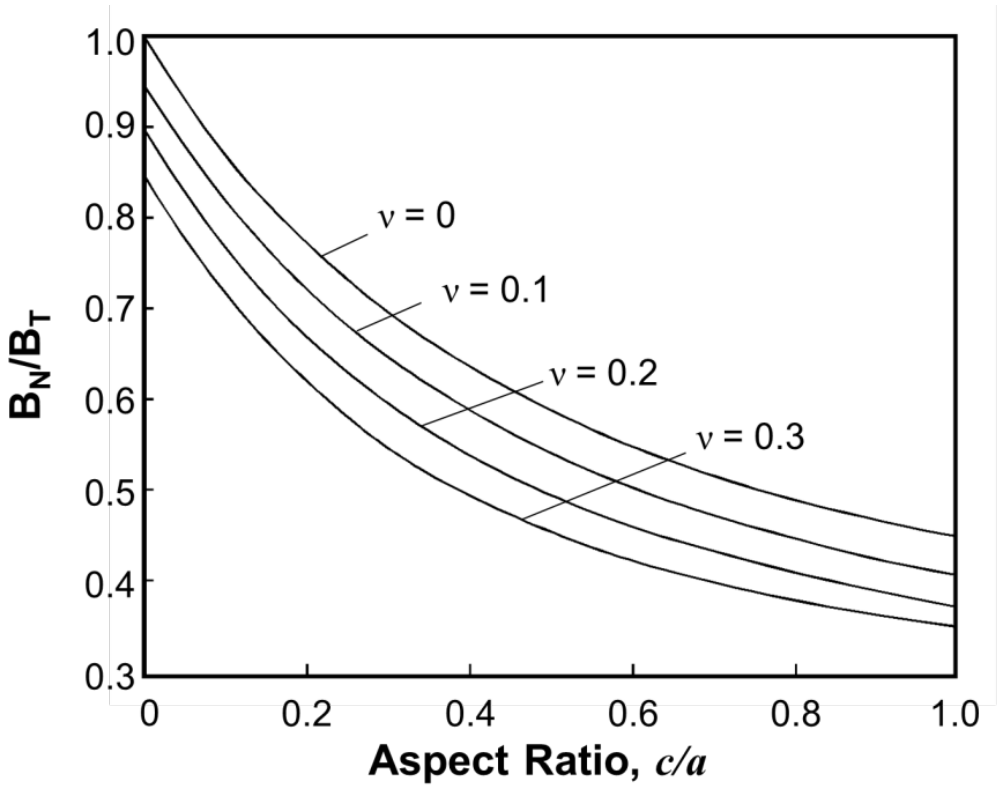

Figure 2.3.1-1 Compliance ratio B_N/B_T as a function of aspect ratio *c/a* for various values of Poisson's ratio (modified after Sayers et al. (2009)).

2.3.2 Values of Stiffness Ratio from Experiments

Fracture stiffness has been measured at a different range of scales: at the grain-scale (micro-cracks) in cored samples (Sayers (1999); Sayers and Han (2002); MacBeth and Schuett (2007); Verdon et al. (2008); Angus et al. (2009); and Pervukhina (2011)), at laboratory scale from synthetic fractures (Hsu and Schoenberg (1993); Rathore et al. (1994); and Far (2011)), from single fractures also at the laboratory scale (Pyrak-Nolte et al. (1990); and Lubbe el al. (2008)), and at the field-scale (Verdon and Wüstefeld (2013); and Hobday and Worthington (2012)). Table 2.3.2-1 provides a compilation of stiffness ratios, at different scales, obtained from the technical literature.

Sayers (1999), Sayers and Han (2002), Verdon et al. (2008), Angus et al. (2009) and Pervukhina et al. (2011) used ultrasonic waves to measure seismic fracture stiffness of micro-cracks in a rock matrix. Sayers and Han (2002) and Sayers (1999) obtained ratios varying from 0.25 to 3.0 for sandstones and shale samples when the samples were dry, while the ratio dropped to 0.05 to 1.1 when the samples were saturated with water. MacBeth and Schuett (2007) investigated the stiffness ratio when the sample was thermally damaged. Ultrasonic measurements were used to estimate the stiffness ratio of the undamaged sample first and then after damage by heating. They found that for the undamaged sample, the ratio ranged from 0 to 0.6 while it changed to 0-1.2 when damaged. They concluded that heating the diagenetic infilling in the pre-existing micro-cracks in the rock induced an increase of the stiffness ratio. Verdon et al. found a ratio of $0.68 < \kappa_x / \kappa_z < 1.06$ for a sample from the Clair oil field tested under dry conditions. Angus et al. (2009) estimated the ratio to be between 0.25 and 1.5. Pervukhina et al. (2011) obtained stiffness ratios of 0.2-1.0 on various types of shale recovered from

depths between 200 m and 3,604 m. In summary, the results of the experiments carried on cracks at the grain scale do not agree with the conventional assumption that $\kappa_x / \kappa_z \approx 1.0$.

Hsu and Schoenberg (1993) created a synthetic fracture made of lucite and determined a ratio of 0.8-1.0 for dry conditions, but found values less than 0.1 when the fracture was saturated with honey. Far (2011) also made a block composed of multiple lucite plates and measured a ratio of 0.11-0.76 for dry conditions. When filling the fracture with rubber pellets, the stiffness ratio increased to 1.6. Rathore et al. (1995) developed a method to create a synthetic fracture with cementing sand. A known distribution of crack-like fractures was created by including metal discs. The metal discs were removed after the sample was solidified leaving behind crack-like voids. Compressional and shear wave velocities were measured across the synthetic fracture. With the data, Verdon (2012) computed a ratio of 0.46.

Lab-scale data on a single fracture is limited. Pyrak-Nolte et al. (1990) measured the normal and shear fracture specific stiffness of natural fractures on three cored samples of quartz monzonite at a normal stress of up to 85 MPa. The estimated ratio of shear to normal specific stiffness ranged from 0.2 to 0.7 when the rock was dry and from 0.04 to 0.5 when saturated. Lubbe et al. (2008) fabricated limestone samples with a single fracture by placing two blocks of limestone in contact and controlled the fracture roughness by coarsely grinding, finely grinding, or polishing the fracture surface. They determined the stiffness ratio from ultrasonic measurements, which was found to be in the range of 0.2-0.55; the ratio dramatically dropped to 0.02-0.05 with honey saturation.

Hobday and Worthington (2012) and Verdon and Wüstefeld (2013) carried out field scale experiments to estimate the stiffness ratio. Hobday and Worthington (2012) obtained the ratio for a saturated outcrop of Upper Caithness Flagstone using hammer seismics. The fracture spacing, in the field, was approximately 0.5 m. The estimated stiffness ratio was less than 0.1. Verdon and Wüstefeld (2012) applied S-wave splitting (SWS) to downhole microseismic data and found a stiffness ratio of 0.7-0.78 for dry conditions and a ratio of 1-2 during proppant injection.

Figure 2.3.2-1 summarizes the ratios of shear to normal fracture stiffness obtained from the previous experimental studies. All data were obtained under normal compression only, i.e., no shear stress was applied to the fracture. It is clear from the figure that many of the results deviate from the theoretical estimate of $\kappa_x / \kappa_z = 1.0$, and it suggests that the common convention of assuming that $\kappa_x / \kappa_z = 1.0$ may be incorrect. There are a number of factors that may change or affect the stiffness ratio such as presence of filling material in the fracture (Pyrak-Nolte et al. (1990), Sayers (1999), Sayers and Han (2002), Far (2011), and Lubbe et al. (2008)), orientation of micro-cracks (Liu et al. (2000), Sayers and Kachonov (1995), and Pervukhina et al. (2011)), thermal damage to rock matrix (MacBecth and Schuett (2007)), and mineralization of material (Sayers et al. (2009)).

Pyrak-Nolte et al. (1996) studied the effect of both normal and shear stresses on the shear fracture specific stiffness. They made measurements of interface waves in three dolomite cores that had a single fracture to determine the change in shear specific stiffness of fractures subjected to both normal and shear stress. Transmitted shear waves were measured as a function of normal stress (0.03 MPa to 11.5 MPa). The effect of shear stress on fracture specific stiffness was examined by orienting the fracture in the direction

of loading. Three orientations were investigated: Sample A had a 30° angle with the normal load, Sample B 7.5°, and Sample C 52.5°; see Figure 2.3.2-2. The figure shows the change in shear fracture specific stiffness with normal stress when only a normal stress is applied (closed symbols) and when both normal and shear stresses are applied (open symbols). As one can see, the shear fracture specific stiffness increases faster with increasing both normal and shear stress than with normal stress alone, implying that the shear fracture specific stiffness is very sensitive to changes in shear stress. It suggests that increasing shear stress may induce the increase of contact area sensitive to shear specific stiffness and that consideration of the loading condition (e.g. uniaxial, bi-axial, mixed mode) is very important.

.

Table 2.3.2-1. Published measurements of κ_x / κ_z from laboratory and field studies (modified after Verdon and Wüstefeld (2013)) (continued).

Reference	Description	κ_x / κ_z
Verdon et al. (2008)	Dry samples. Ultrasonic measurement on grain-scale fabrics. Data from Hall et al. (2008)	0.68-1.06
Angus et al. (2009)	Dry samples. Ultrasonic measurement on grain-scale fabrics. Data collated from a range of literature sources.	0.25 - 1.5
Sayers and Han (2002)	Dry samples. Ultrasonic measurement on grain-scale fabrics. Data from Han et al. (1986) As above. Water saturated	0.25 - 3 0.05 - 1.1
Sayers (1999)	Dry samples. Ultrasonic measurement on shale samples. Data from Johnston and Christensen (1993) and Vernik (1993) As above. Water saturated. Data from Hornby (1994)	0.47 - 0.8 0.26-0.41
MacBeth and Schuett (2007)	Dry samples. Undamaged sample. Ultrasonic measurement on grain-scale fabrics. As above. Sample thermally damaged.	0 - 0.6 0 - 1.2
Pervukhina et al. (2011)	Sealed samples taken at depth of 200m to3,604m Water saturated	0.2-2.0
Hsu and Schoenberg (1993)	Representative medium of compressed perspex plates. Ultrasonic measurements on dry samples. As above, honey saturated.	0.8 - 1 0.1
Far (2011)	Representative medium of compressed perspex plates. Ultrasonic measurements on dry, unfilled samples. As above, but 'cracks' contain rubber pellet inclusions	0.11-0.75 0.16 - 1.6
Rathore et al. (1995)	Synthetic sample containing a population of cracks. Ultrasonic data re-analyzed by Hudson et al. (2001).	0.46
Pyrak-Nolte et al. (1990)	Quartz monzonite samples containing a single fracture. Ultrasonic measurements on dry samples. As above, water saturated.	0.2 - 0.7 0.04 - 0.5

Table 2.3.2-1. Published measurements of κ_x / κ_z from laboratory and field studies (modified after Verdon and Wüstefeld (2013)).

Lubbe et al. (2008)	Limestone samples cut and reassembled to create a single fracture. Ultrasonic measurements on dry samples. As above, honey saturated.	0.2 - 0.55 0.02-0.05
Hobday and Worthington (2012)	Hammer seismic imaging of outcrop of Caithness Flagstone. Water saturated.	≤ 0.1
Verdon and Wüstefeld (2013)	Inversion of S-wave splitting (SWS) data obtained in the laboratory and the field During proppant-injected saturation	0.7-0.78 1-2

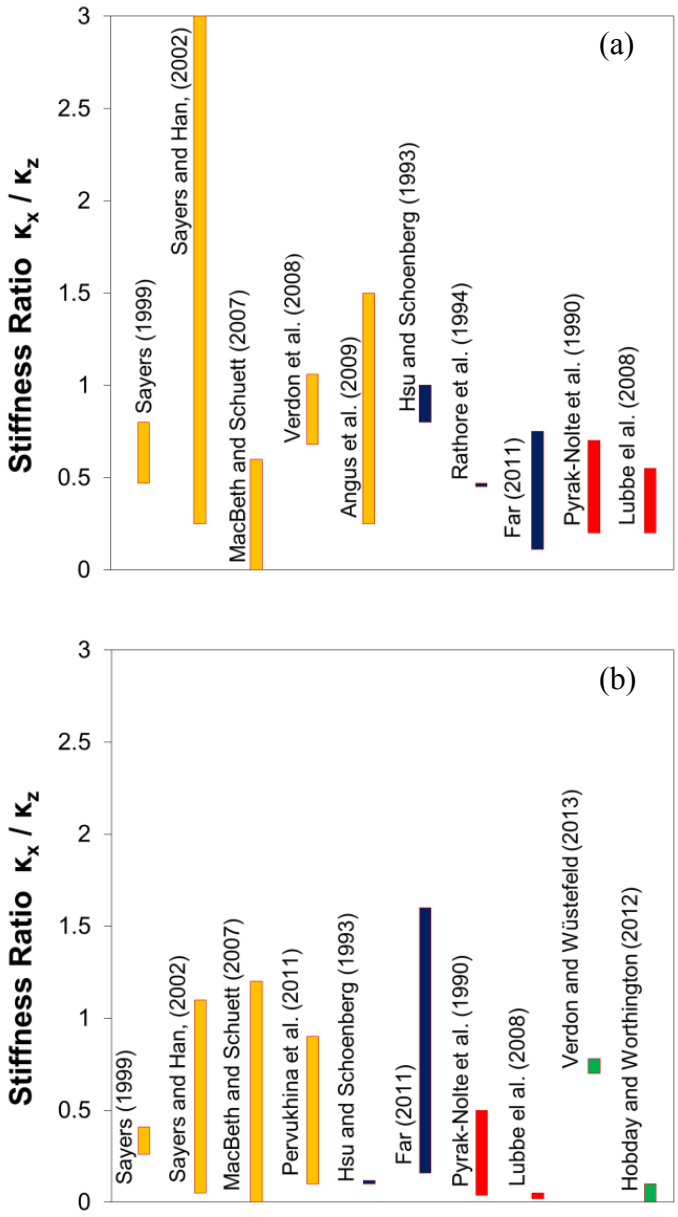

Figure 2.3.2-1. Stiffness ratio of shear to normal fracture specific stiffness (a) when a fracture is dry and (b) when saturated with fluid, filled with rubber or thermally damaged. Yellow bars represent fractures at the grain-scale, blue synthetic fractures at laboratory scale, red a single fracture at the laboratory scale, and green field-scale fractures (modified after Verdon and Wüstefeld (2013)).

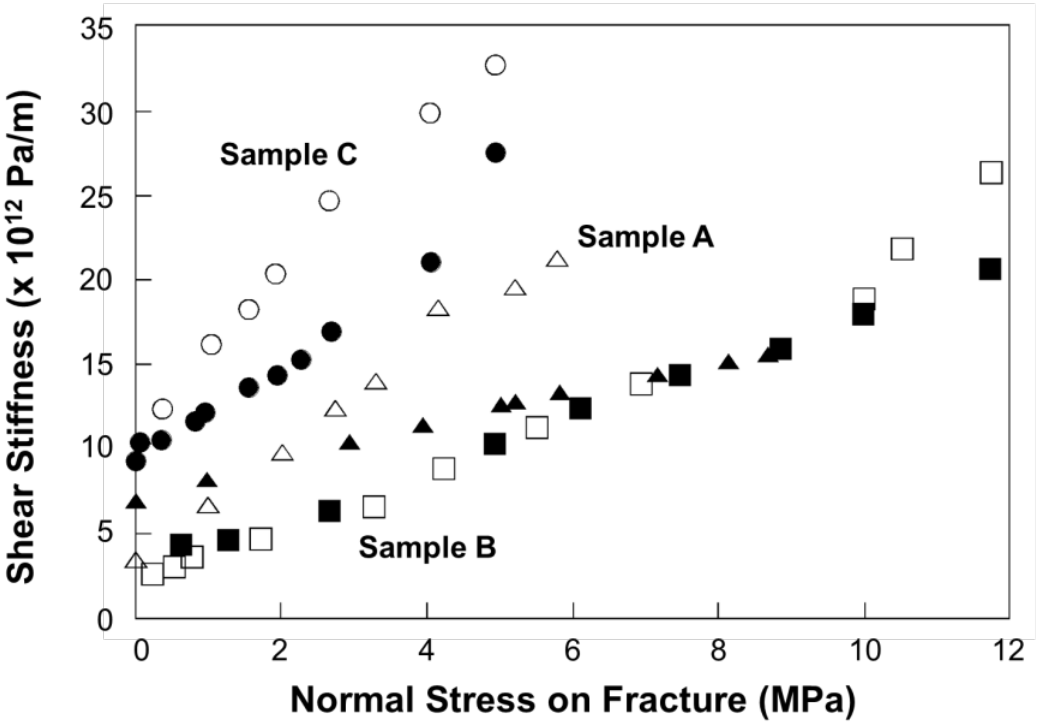

Figure 2.3.2-2. Fracture specific stiffness as a function of normal stress for samples A (triangles), B (squares), and C (circles). Closed symbols refer to normal load only; open symbols to both normal and shear loading.

2.4 Fracture Stiffness and Fluid Flow

Mechanical, hydraulic, and seismic properties of fractures are primarily influenced by the geometry of the asperities in contact and by the spatial distribution of the void spaces within the fracture (Pyrak-Nolte, 1996). When stress is applied to rock containing a fracture, there is deformation of the fracture, which is in excess of that of the intact rock. Fracture deformation affects fluid flow through the fracture by reducing the aperture of the fracture and by increasing contact area, which results in complex fluid flow paths. In addition, seismic wave propagation across a fracture depends on the contact area and on the void space distribution within the fracture (Pyrak-Nolte, 1998). It is well known that seismic wave propagation across a fracture depends on fracture specific stiffness (Pyrak-Nolte et al., 1990, and Hsu and Schoenberg 1993), as described in the section 2.2. Because both fluid flow and fracture specific stiffness depend on contact area and aperture and on their spatial distribution within the fracture, there is an implicit link between fluid flow and fracture specific stiffness. The connection between fluid flow and fracture specific stiffness is an important interrelationship because seismic measurements of fracture specific stiffness can be a useful tool for predicting the hydraulic properties of a fracture.

2.4.1 Fluid Flow in a Fracture

Fluid flow along a fracture depends on the aperture of the fracture (Jaeger et al. (2007)). For smooth and parallel plates, there is a direct relationship, the so-called “cubic law”, between aperture and fluid flow. In the “cubic law”, the flow rate is proportional to the cube of the fracture aperture, under the assumption of steady-state laminar flow of a

viscous incompressible fluid through a fracture that is composed of two smooth and parallel walls:

$$Q / \Delta h = C(2b)^3 \qquad (2.4.1\text{-}1)$$

where Q is the flow rate, Δh is the hydraulic head, C is a constant that depends on flow geometry and fluid properties, and 2b is the fracture aperture.

Many researchers have discussed the validity and applicability of the cubic law for rough-walled fractures (Gale (1975), Gangi (1978), Sharp (1970), Witherspoon et al. (1980), Tsang and Witherspoon (1981), Engelder and Scholz (1981), Cook (1988), Renshaw (1995), Sisavath et al. (2003), Liu (2005), and Klimczak et al. (2010)).

Witherspoon et al. (1980) investigated the validity of the cubic law when the fracture surfaces were in contact and the aperture decreased under stress. Test specimens of granite, basalt, and marble with a single tensile fracture were created and fluid flow though the fracture was either longitudinal to the fracture or radial. Apertures were estimated to range from 250 μm down to 4 μm. The authors introduced a correction factor *f* to the original cubic law to account for the deviation from ideal conditions of the cubic law. The cubic law is recovered when *f* is equal or close to one. The experiment results showed that the cubic law was valid for correction factors f in the range of 1.04 to 1.65, which seemed to indicate that deviations from the ideal parallel plate concept were not serious. However, marked deviations from the ideal cubic law were found when apertures were less than 10μm. Explanation about the deviation was not provided in the literature.

Tsang and Witherspoon (1981) suggested a simple physical model to replace the aperture with an appropriately weighted average aperture $<b^3>$. They assumed a fracture as a collection of voids; closure of the fracture was the result of void deformation. The parameter $<b^3>$ was the statistical average of a variable aperture and was determined from $b = (b_0 - \Delta V - h)$, where b_0 is the maximum possible aperture, h is the height of asperity, and ΔV is the fracture closure induced by a change of normal stress. The modified cubic law is,

$$Q = -\frac{W}{L}\frac{\rho g}{12\mu} < b^3 > \Delta H \qquad (2.4.1\text{-}2)$$

where, Q is the flow rate, W is the width of the fracture, L is the length of fracture, ρ is the density of the fluid, g is the gravitational acceleration, μ is the viscosity of the fluid and ΔH is the pressure head drop. The modified cubic law provided a good agreement with results from experiments with normal stress. Tsang and Witherspoon (1981) also found that the fraction of total asperities in contact was only around 15% at a normal stress of 20 MPa, and that the fracture behaved very much like intact rock in terms of elastic properties. Such finding indicated that a fracture cannot close completely unless the applied normal stress is extremely high. This is consistent with the study of Kranz et al. (1979) who obtained flow rates from a rock with and without a fracture that were close in magnitude when the fracture was subjected to extremely high values of normal stress, of about 200 to 300 MPa.

As discussed, the "cubic law" is valid for a fracture at relatively low stress and with large apertures; however, it does not work well for relatively small apertures, where a clear departure from the cubic law was observed (Witherspoon et al. (1980)); in this case, the fluid flow decreased faster than what was predicted by the cubic law and finally became insensitive to changes in aperture. This observation implies that the curve of specific fluid flow, i.e. flow per unit head gradient, and fracture aperture has a slope larger than 3 in a log-log scale.

Pyrak-Nolte et al. (1987) also found a similar discrepancy between predictions from the cubic law and experiments in natural fractures. They found that specific flow decreased much more rapidly than the aperture to the third power. Fluid flow then approached an irreducible specific flow, which is an aperture-independent limit at the highest stress and thus at the smallest aperture. A linear relation between $(Q_\infty\text{-}Q)$ and $(d_m\text{-}d)$ was derived from a log-log scale of experimental data, where Q_∞ was the irreducible specific flow at high stress, d_m was the maximum aperture at zero stress and d was the aperture closure. The plot of $(Q_\infty\text{-}Q)$ versus $(d_m\text{-}d)$ showed that the slope was 7.6 for the "loosest" fracture and 9.8 for the "tightest" fracture. Both values are much larger than 3. In addition, Cook (1992) indicated that specific flow became more or less independent of further reduction in aperture with increasing stress. He concluded that, for a natural fracture in partial contact, at low stress apertures providing flow paths decrease more rapidly than fracture closure and that the tortuosity of the flow paths becomes virtually independent of stress or aperture closure at high stress.

Sisavath et al. (2003) investigated numerically the change of fluid flow with fracture roughness. To capture the features of a rough wall, they approximated the fracture walls

with a sinusoidal function symmetric with respect to the fracture plane. In the fracture model, the roughness of the fracture (δ) and the wavelength of the fracture roughness (λ) remained constant, while fracture closure was obtained by moving the two opposing walls toward each other. For $H_0 >> \delta$ (H_0 is the mean aperture) and small δ / λ, the roughness of the fracture surface (δ) became negligible such that the relation between the mean aperture (H_0) and the specific flow could be taken as cubic. As the mean aperture (H_0) decreased, the relationship with specific flow did not follow the cubic law because the fracture roughness (δ) was significant. For fractures with $\delta / \lambda = 0.04 - 0.24$, it was found that the log-log exponent between specific flow and aperture was as large as 8.3-9.8, as the mean aperture (H_0) decreased. These values are comparable to the 7.6 to 9.8 values obtained by Pyrak-Nolte et al. (1987). Sisavath et al. concluded that fluid flow through a fracture could be divided into three regimes: (I) at very low aperture, fluid flow became independent of the change of aperture; (II) flow rate decreased faster than the cube of aperture suggesting that roughness became significant as the fracture closed; and (III) the flow changed with the cube of the mean aperture when apertures were substantially larger than the roughness of the fracture.

In summary, the relationship between aperture and fluid flow, the so-called cubic law, is valid when the aperture is significantly larger than the fracture roughness. As the fracture closes, fracture roughness starts to control fluid flow. Under very high normal stress, some portions of the fracture remain open and provide a flow path. The observation of stress-independent fluid flow at high stresses implies that no new asperities come into contact. Under this condition, fluid probably flows along channel-like narrow conduits and these tortuous conduits generate the main resistance to flow (Cook, 1992). Finally

fluid flow through a fracture may be fully explained considering the fracture geometry, such as the fraction of total asperities in contact with load, the ratio of aperture to fracture roughness, spatial distribution of aperture with joint closure and change of flow path with load.

2.4.2 Fracture Geometry and Fluid Flow

Many researchers have conducted experimental and numerical investigations to ascertain the relationship between fracture geometry, including aperture distribution and contact area, and hydraulic behavior. The study of Sisavath et al. (2003), discussed in the previous section, presented the effect of fracture roughness on fluid flow. If the roughness of the fracture is of the same order of magnitude as the mean aperture of the fracture, both the roughness of the fracture and the aperture should be taken into account. Pyrak-Nolte et al. (1988) and Nolte et al. (1991) applied a stratified percolation model to generate spatially correlated synthetic apertures for phenomenological modeling of fluid flow through the fracture. They found that fluid flow was dominated by the critical path (path of largest apertures) and was controlled by the critical neck (the smallest aperture along the path of largest apertures). Pyrak-Nolte and Montemagno (1994) experimentally showed the importance of the critical path using Wood's metal injection porosimetry on a coal core and measuring the flow rate of methane. Filling the critical path with Wood's metal caused a dramatic reduction in flow rates, by 70% to 98%, supporting the dominance of the critical path on fluid flow through a fracture. Pyrak-Nolte et al. (1997) showed that the aperture distributions of natural fracture networks were spatially correlated over 10 mm to 30 mm, which are comparable to the size of the samples in the

laboratory. The observation that the spatial correlations are of the same order of magnitude as the sample length implies that if fractures at the core scale are correlated over a few centimeters or less, the same fracture at the field scale may behave as an uncorrelated fracture.

Pyrak-Nolte and Morris (2000) showed that the relationship between fluid flow and fracture specific stiffness arises directly from the size and spatial distribution of the contact area and void space within a fracture. They presented experimental and numerical evidence to support a quantitative interrelationship between fracture specific stiffness and fluid flow through a fracture, i.e. a stiff fracture will allow less fluid flow than a compliant fracture. Figure 2.4.2-1 shows the relationship between fracture specific stiffness and fluid flow for thirteen fractures. The fracture stiffness-fluid flow relationship exhibits two types of behavior. STR2, S9, S10, S33, Sample 1-3, E30, E32, and E35 show a nine order of magnitude decrease of flow with only a three orders of magnitude increase in fracture specific stiffness. The other type of behavior is illustrated by H1, Sample 5, and Granite where the flow was less sensitive to the change of stiffness. From modeling, they concluded that the difference in fracture specific stiffness-fluid flow relationship was related to the spatial correlation of the aperture distribution in the fracture. For fractures with aperture distributions that were spatially correlated, the flow decreased rapidly with an increase of fracture specific stiffness. In contrast, fractures with aperture distributions that were spatially uncorrelated showed that fluid flow was less sensitive to changes in fracture specific stiffness.

Petrovitch et al. (2013) performed a finite-size scaling analysis to quantify a fundamental scaling relationship between fractures specific stiffness and fluid flow, for single

fractures with uncorrelated aperture distributions. For fractures with different sizes ranging from 0.0625 m to 1.0 m, fluid flow and fracture specific stiffness were correlated as a function of stress. They found a scaling relationship that all of the fluid flow - fracture specific stiffness relationships at all scales fell on a single curve. The curve was clearly divided into two regions with distinct slopes: effective medium regime and percolation regime. In effective regime, the flow field across the fracture plane was homogeneous and approached the cubic law, as the contact area in the fracture reduced to zero. However, for flow in the percolation regime, the flow paths closed and only a few narrow channels survived leaving many regions of the void spaces without flow. They concluded that a scaling relationship existed between fluid flow and fracture specific stiffness because stiffness acted as a surrogate of void area in a fracture and captured the deformed topology of the void space.

These experimental and numerical results have proved the dependency of fluid flow through a fracture on fracture geometry; that is, on the spatial correlation of aperture distribution and on the magnitude of the mean aperture. The interrelationship between fracture specific stiffness and fluid flow through a fracture has been understood based on imaging and on quantification of aperture distribution in fractures. Therefore, measurement of aperture distribution is expected to provide information on the spatial distribution of the fracture specific stiffness and on the distribution of fluid flow through the fracture.

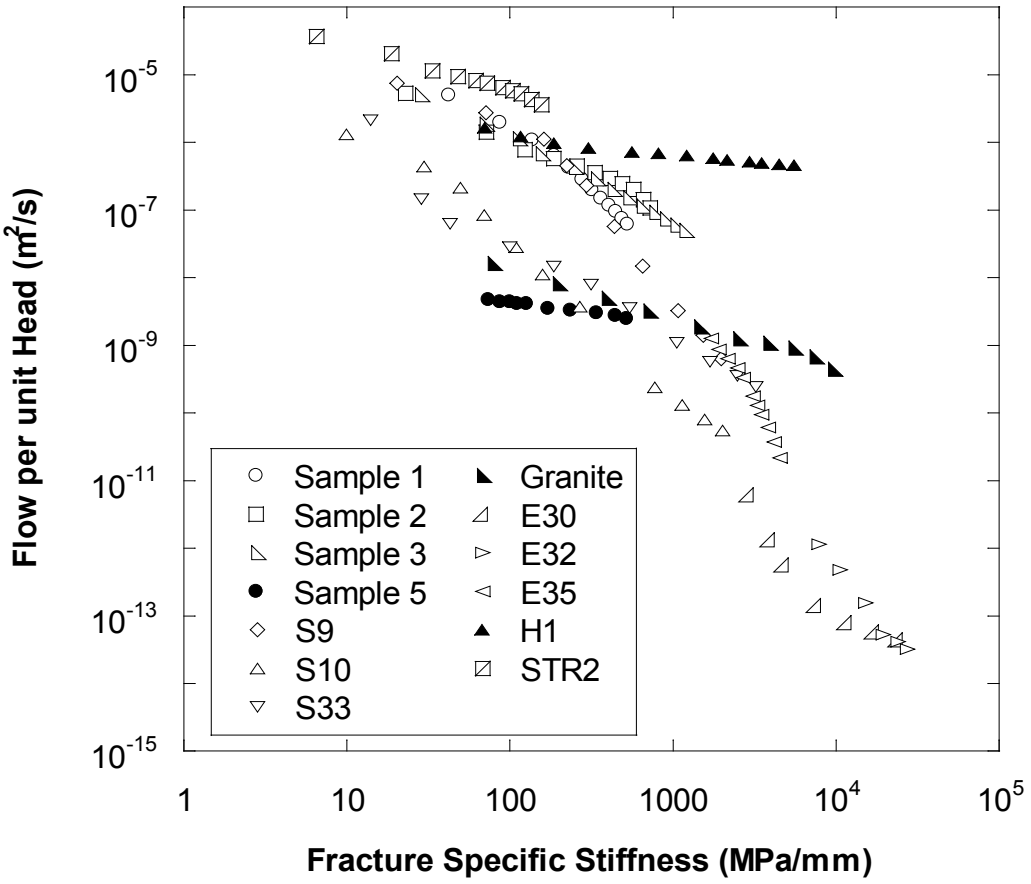

Figure 2.4.2-1. Specific fluid flow as a function of normal fracture specific stiffness for thirteen fractures (taken from Pyrak-Nolte and Morris (2000).

2.4.3 Shear Displacement and Fluid Flow

Shearing is the process that results in relative movement between fracture surfaces and is caused by shifting the upper surface with respect to the lower surface with/without dilation (Lanaro and Stephansson (2003)). Lanaro (2000) and Lanaro and Stephansson (2003) presented a statistical model that predicts the change in mean value of aperture and variance of the aperture after a shear displacement. Equations (2.4.3-1) and (2.4.3-2) show the change of mean aperture and variance of the aperture.

$$\mu_{av} = \mu_a + S_{slope} v \tag{2.4.3-1}$$

$$\sigma_{av}^2 = \sigma_a^2 + \gamma_z(v) - 2\,\mathrm{cov}(\Delta z^v, a) \tag{2.4.3-2}$$

where μ_{av} and μ_a are the mean values of aperture before and after a shear displacement ν with a dilation slope S_{slope} respectively, and σ_{av} and σ_a are the variance of the aperture before and after the shear displacement, respectively. γ_z is the variogram of the asperity height calculated at a distance equal to the magnitude of the shearing displacement ν, Δz^v is the increment of the asperity height between two points at distance ν, and *a* is the aperture. Equation (2.4.3-2) suggests that the change in aperture during shear depends mainly on the variogram of the asperities because the covariance term between aperture and asperity height is smaller than the variogram of the asperity height. It also suggests that the variance of the aperture increases during shearing.

Power and Durham (1997) experimentally observed that the size of the contact spots (the areas in contact) increased during shearing while the number of contact areas decreased.

The growth of the contact spots can result in an increase in the correlation length of aperture, providing less tortuosity and complexity of the fluid flow paths and more fluid flow path in the fracture. Yeo et al. (1998) and Watanabe et al. (2008) also found a similar experimental observation; that is, with increasing shear displacement, mean aperture and variance of the aperture of the fracture increased. At zero shear displacement, the fracture had a similar spatial correlation in all directions. As shear displacement increased, the aperture in the direction perpendicular to the shear displacement became more spatially correlated. The change in spatial correlation made the fracture more permeable in the direction perpendicular to the shear displacement, inducing anisotropic flow in the fracture. Koyama et al. (2006), Nemoto et al. (2009), and Matsuki et al. (2010) investigated anisotropic fluid flow in a single fracture during shearing using numerical modeling. Their results confirmed the experimental work that showed shear-induced anisotropic flow in a fracture, indicating that fracture aperture increased anisotropically during shearing with a pronounced increase in the direction perpendicular to the shear displacement. Less tortuosity in the flow path in the direction perpendicular to shear displacement was the result of the alignment of contacts of asperities in the perpendicular direction.

CHAPTER 3. NORMAL AND SHEAR STIFFNESS

3.1 Introduction

A series of laboratory experiments were performed on synthetic fractures using gypsum and lucite to investigate the relationship between shear and normal fracture specific stiffness in a single fracture subjected to normal and shear stress. Specimens with two types of fracture surfaces were made by placing two blocks in contact with each other: well-mated or non-mated. In the experiments, each specimen was subjected to normal and shear loading while transmitted and reflected P- and S- waves were measured. The fracture was subjected to normal and shear stress simultaneously to observe how the application of normal and shear stress influenced the normal and shear specific stiffness.

3.2 Theoretical Ratio of Shear to Normal Stiffness

3.2.1 Displacement Discontinuity Theory

The full solution for Kelvin fracture model was presented in Chapter 2. In equations (2.2.1-10) to (2.2.1.-14), the fracture specific viscosity η represents the viscous coupling between fracture surface and fluid. If a fracture is filled with no water or fluid, the specific viscosity of the fracture can be neglected and a fracture can be modeled with a spring only, i.e. the stress across the fracture is continuous but the displacements are not.

The displacements are inversely proportional to the fracture specific stiffness κ. Setting the terms with specific viscosity equal to zero, the solution for P- and Sv, and Sh incident waves is given as follows:

For P- and Sv- waves,

$$A=\begin{bmatrix} -\kappa_z\cos\theta_1 & \kappa_z\sin\phi_1 & -\kappa_z\cos\theta_2+i\omega Z_{P2}\cos 2\phi_2 & \kappa_z\sin\phi_2-i\omega Z_{S2}\sin 2\phi_2 \\ -\kappa_x\sin\theta_1 & -\kappa_x\cos\phi_1 & \kappa_x\sin\theta_2-i\omega\dfrac{Z_{S2}^2}{Z_{P2}}\sin 2\theta_2 & \kappa_x\cos\phi_2-i\omega Z_{S2}\cos 2\phi_2 \\ -Z_{P1}\cos 2\phi_1 & Z_{S1}\sin 2\phi_1 & Z_{P2}\cos 2\phi_2 & -Z_{S2}\sin 2\phi_2 \\ \dfrac{Z_{S1}^2}{Z_{P1}}\sin 2\theta_1 & Z_{S1}\cos 2\phi_1 & \dfrac{Z_{S2}^2}{Z_{P2}}\sin 2\theta_2 & Z_{S2}\cos 2\phi_2 \end{bmatrix} \tag{3.2.1-1}$$

For Sh- waves,

$$A=\begin{bmatrix} -\kappa_y & \kappa_y-i\omega Z_{S2}\cos\phi_2 \\ Z_{S1}\cos\phi_1 & Z_{S2}\cos\phi_2 \end{bmatrix} \tag{3.2.1-2}$$

Note that the variables and symbols in equations (3.2.1-1) and (3.2.1-2) are exactly the same as those described in Chapter 2.

3.2.2 Theoretical Stiffness Ratio for Normal Incident Wave

Based on the displacement discontinuity theory, the fracture specific stiffness κ for a normal incident wave can be calculated from measurements of the angular frequency ω, seismic impedance Z, and transmission coefficient T, as shown in equation (2.2.4-2).

Note that measurements from P- waves are used to estimate the normal fracture stiffness κ_z and from S- waves the shear fracture specific stiffness κ_x. From equation (2.2.4-2), the ratio of shear to normal fracture specific specific stiffness is:

$$\frac{\kappa_x}{\kappa_z} = \frac{\dfrac{\omega_S V_S}{\sqrt{\dfrac{1}{T_S^2}-1}}}{\dfrac{\omega_P V_P}{\sqrt{\dfrac{1}{T_P^2}-1}}} = \frac{\omega_S V_S}{\omega_P V_P}\frac{\sqrt{\dfrac{1}{T_P^2}-1}}{\sqrt{\dfrac{1}{T_S^2}-1}} = \frac{\omega_S V_S}{\omega_P V_P} f(T_P, T_S) \qquad (3.2.2\text{-}1)$$

where ω is the angular frequency, V is the wave velocity, and T is the transmission coefficient; subscripts S and P indicate shear and compressional waves, respectively. If the transmission of P- and S- waves across the fracture are close enough or equal, i.e. $T_P \approx T_S$, the function f (T_P, T_S) is close or equal to one, and equation (3.2.2-1) simplifies into:

$$\frac{\kappa_x}{\kappa_z} = \frac{\omega_S}{\omega_P}\frac{V_S}{V_P} = \frac{\omega_S}{\omega_P}\Big/\sqrt{\frac{1-\nu}{1-\nu/2}} \qquad (3.2.2\text{-}2)$$

where ν is the Poisson's ratio. Equation (3.2.2-2) implies that the stiffness ratio is dependent on frequency and on the ratio of the S- to P-wave velocities, which is also a function of the Poisson's ratio. If the same frequencies are selected for S- and P- waves, i.e., $\omega_S = \omega_P$, the stiffness ratio reduces to the ratio of S- wave to P-wave velocity. If the stiffness ratio, based on experimental measurements, deviates from equation (3.2.2-2),

then the function $f(T_P, T_S)$ in equation (3.2.2-1) is not equal to one and so the transmission of either S- or of P- waves is dominant. That is, when the stiffness ratio, from experiments, is less than the value estimated from equation (3.2.2-2), the transmission of P- waves dominates, compared with S- waves. The opposite is true when the stiffness ratio is larger than the value given by the equation.

The usefulness of equation (3.2.2-2) as predictor of the stiffness ratio was first investigated with the data from Lubbe et al. (2008) and Pyrak-Nolte (1988). These experiments were selected because stiffness was measured for a single fracture and the information on velocity and frequency were available in the articles.

Lubbe et al. (2008) measured the normal and shear fracture specific stiffness of artificial fractures when the fractures were normally compressed up to 60 MPa. Mono-frequency compressional and shear wave transducers having a central frequency of 0.9 MHz and 0.75 MHz, respectively, were employed to measure the reflected P- and S- waves. Two types of limestone were used to fabricate a specimen with a single fracture: Portland Pond Freestone (PPF) and Carboniferous limestone. The fracture surface was controlled by grinding/polishing. A PPF specimen was coarsely grounded to a roughness of ±5μm. The Carboniferous limestone specimens had asperities of ±5 μm for coarsely grounded, 2.72±0.2 μm for grounded and 0.62±0.1 μm for polished surfaces. The theoretical stiffness ratios for their samples ranged from 0.44 to 0.48 based on equation (3.2.2-2). Figure 3.2.2-1 (a) plots the stiffness ratio as a function of the applied normal stress compared to the theoretical ratio predicted by equation (3.2.2-2). In the figure, the theoretical ratios for each rock type are represented by dotted lines. It does not seem that there is a clear relationship between the size of fracture asperity and stiffness ratio. It is

possible that the controlled asperity size was not large enough to produce a significant impact on the stiffness ratio since the size of the asperities of the specimens' fracture surfaces ranged from 0.62±0.1 μm to ±5 μm. In the range of the applied normal stress, up to 50 MPa, the stiffness ratio ranged from 0.2 to 0.6 and showed good agreement with the theoretical ratio for normal stresses larger than 30 MPa

Pyrak-Nolte (1988) measured the normal and shear fracture specific stiffness on three granite samples, E30, E32, and E35, each containing a single fracture. The fractures were created using a technique similar to Brazilian testing (Jaegar et al. 2007). Specimen E35 had the most compliant fracture, E32 the stiffest, and E30 had an intermediate stiffness. Even though the asperity size of the specimens was not provided, the fractures probably had well-mated surfaces because the process of creating them, in contrast to the artificial fractures of Lubbe et al. (2008). A stiffness ratio of 0.2 to 0.8 was obtained for normal stresses up to 80 MPa. The theoretical ratio was calculated for a central frequency of 0.6-0.7 MHz and 0.45-0.5 MHz for P- and S- waves, respectively, and ranged from 0.37 to 0.48. Figure 3.2.2-1 (b) shows the stiffness ratios from E35, E30, and E32 tests and the predicted values of 0.37 (minimum) and 0.48 (maximum). The predictions slightly overestimate the stiffness ratio for the most compliant fracture E35, while good agreement is observed for the other samples at medium to high normal stresses. Both the Lubbe et al. (2008) and Pyrak-Nolte (1988) data exhibited a stress-dependent stiffness ratio.

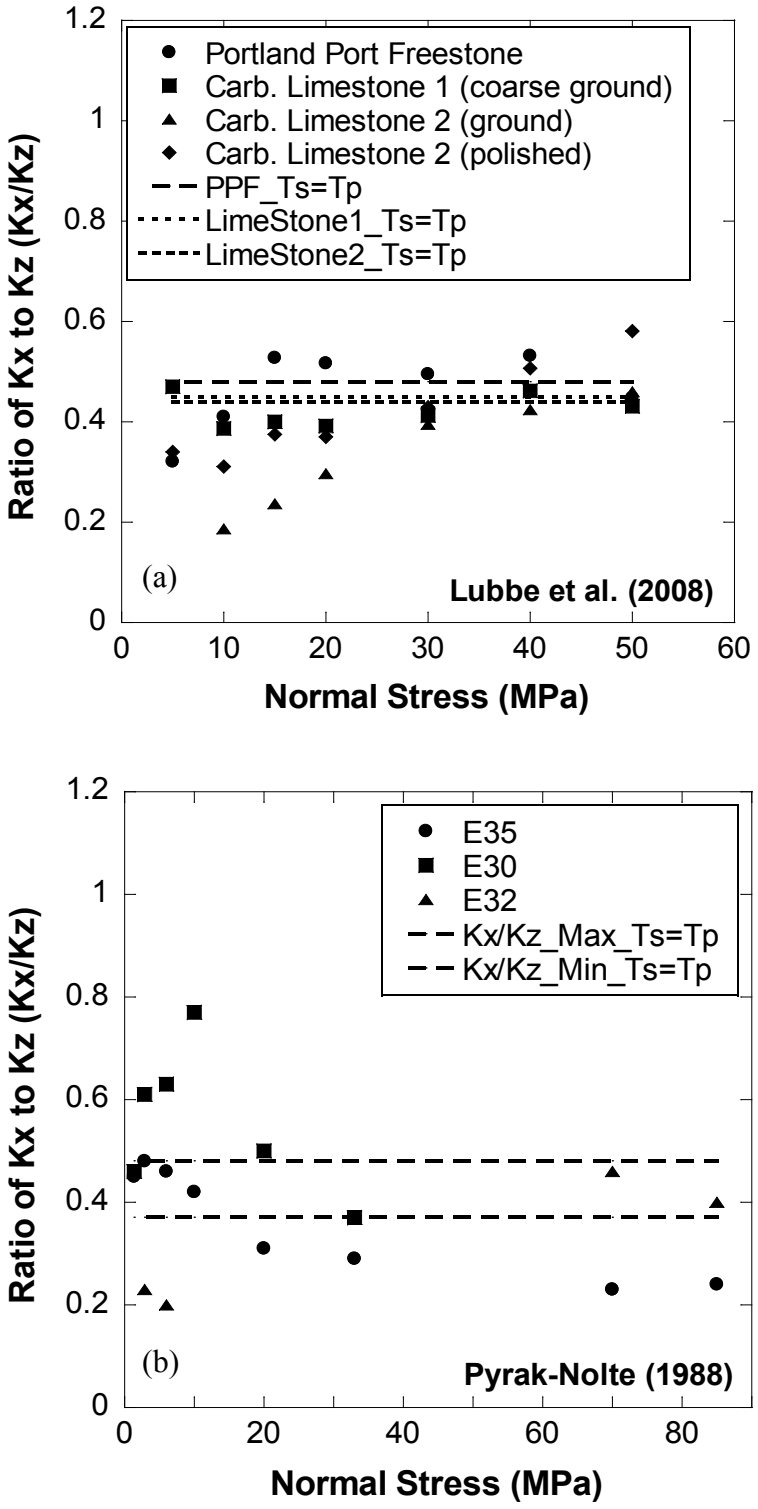

Figure 3.2.2-1. Ratio of shear to normal fracture specific stiffness obtained from: (a) Lubbe et al. (2008) and (b) Pyrak-Nolte (1998). The ratios are compared with equation (3.2.2-2) (dotted lines).

3.3 Experimental Method

To investigate the ratio of shear to normal fracture specific stiffness, prismatic block samples with different fracture surface conditions were prepared: well-mated or non-mated. The specimens were subjected to normal and shear stress while seismic measurements were made.

3.3.1 Sample Preparation

The materials used for the experiments were gypsum and lucite. These materials have been extensively used for experimental simulations of rock with flaws or fractures (Reyes et al. (1991), Takeuchi (1991), Hsu and Schoenberg et al. (1993), Shen et al. (1995), Bobet and Einstein (1998), Wong and Einstein (2006), Ko et al. (2006), Lubbe et al. (2008), and Far (2011)).

To create a specimen with a well-mated fracture, two prismatic blocks of gypsum were made, each with dimensions 152.4 mm (6 inch) length, 127 mm (5 inch) wide, and 25.4 mm (1 inch) thick. The specimens were prepared in the laboratory by mixing gypsum, diatomaceous earth, and water and casting the gypsum paste in a mold. The mass proportions were water/gypsum = 0.6 and water/diatomaceous earth = 35. Diatomaceous earth prevents bleeding of water to the top of the specimen during fabrication. The proportions of water, gypsum, and diatomaceous earth used to create one block are as follows:

Water =	400 cc
Gypsum =	1,000 g
Diatomaceous earth =	11.43 g

To control the size of the asperities on the fracture surface, sandpaper with different average grit sizes was used. Table 3.3.1-1 lists the types of sandpaper employed to control the size of the asperities as well as the names of the test specimens. The average grit size of the sandpaper ranged from 68 μm to 530 μm. The procedure for the fabrication of the specimens was strictly followed to ensure repeatability and consisted of the following steps:

(1) Place the sandpaper/plastic plate at the bottom of the mold

(2) Mix the measured amount of water and diatomaceous earth in a blender for 30 seconds at high speed.

(3) Add gypsum to the blender bowl and mix for 30 seconds at slow speed and then for 4 minutes at high speed.

(4) Pour the gypsum mixture into the mold up to a thickness of about 1 inch.

(5) Vibrate the mold on a vibrating table for 5 minutes to remove any entrapped air in the mixture.

(6) Place the gypsum-filled mold on a horizontal table for 75 minutes to allow hardening of the gypsum paste.

(7) Flip over the first block of gypsum and remove the sandpaper.

(8) Apply a release agent to the contact surface (fracture) to prevent the second block from sticking to the first block.

(9) Cast a second block against the first block, creating a well-mated contact surface (fracture).

(10) 75 minutes after casting the second block, take the specimen out of the mold and let it cure at room temperature for 24 hours.

(11) Place the specimen in an oven at 40 °C for four days for additional curing.

(12) After fabrication and curing, carefully polish the sides of the specimen parallel to the contact surface to obtain flat, smooth, perfectly parallel surfaces. This operation ensures that the loads applied are either normal or parallel to the contact surface.

In addition to specimens fabricated with different sandpaper, two more specimens with a well-mated fracture were prepared: a flat fracture specimen and a replica specimen of a natural fracture. The specimen with the flat fracture surface was made using a plastic plate instead of sandpaper, and the replica specimen (GS01R specimen) was fabricated by casting gypsum against an induced fracture in granite. The GS01R was a replica of the GS01 specimen, which will be discussed in section 4.2.2.1. Figure 3.3.1-1 shows photographs of: (a) the gypsum #36 specimen and (b) the replica specimen GS01R.

Test specimens with non-mated fractures were fabricated using lucite (i.e. acrylic material). Lucite was selected because of its well-known homogeneity and isotropy. Two prismatic lucite blocks were machined from a large solid lucite block to have the same external dimensions as the gypsum blocks. The fracture surface roughness of each block was produced either by polishing (lucite PL) or sand-blasting (lucite SB) with 25 μm grit. Figure 3.3.1-2 contains the photographs of: (a) the lucite PL and (b) lucite SB specimens.

Table 3.3.1-1. Sandpaper used to prepare fracture roughness and specimen name.

# of sandpaper	Average grit size of sandpaper (μm)	Sample name
#36	530	Gypsum #36
#60	265	Gypsum #60
#220	68	Gypsum #220
Flat plastic plate	-	Gypsum Flat

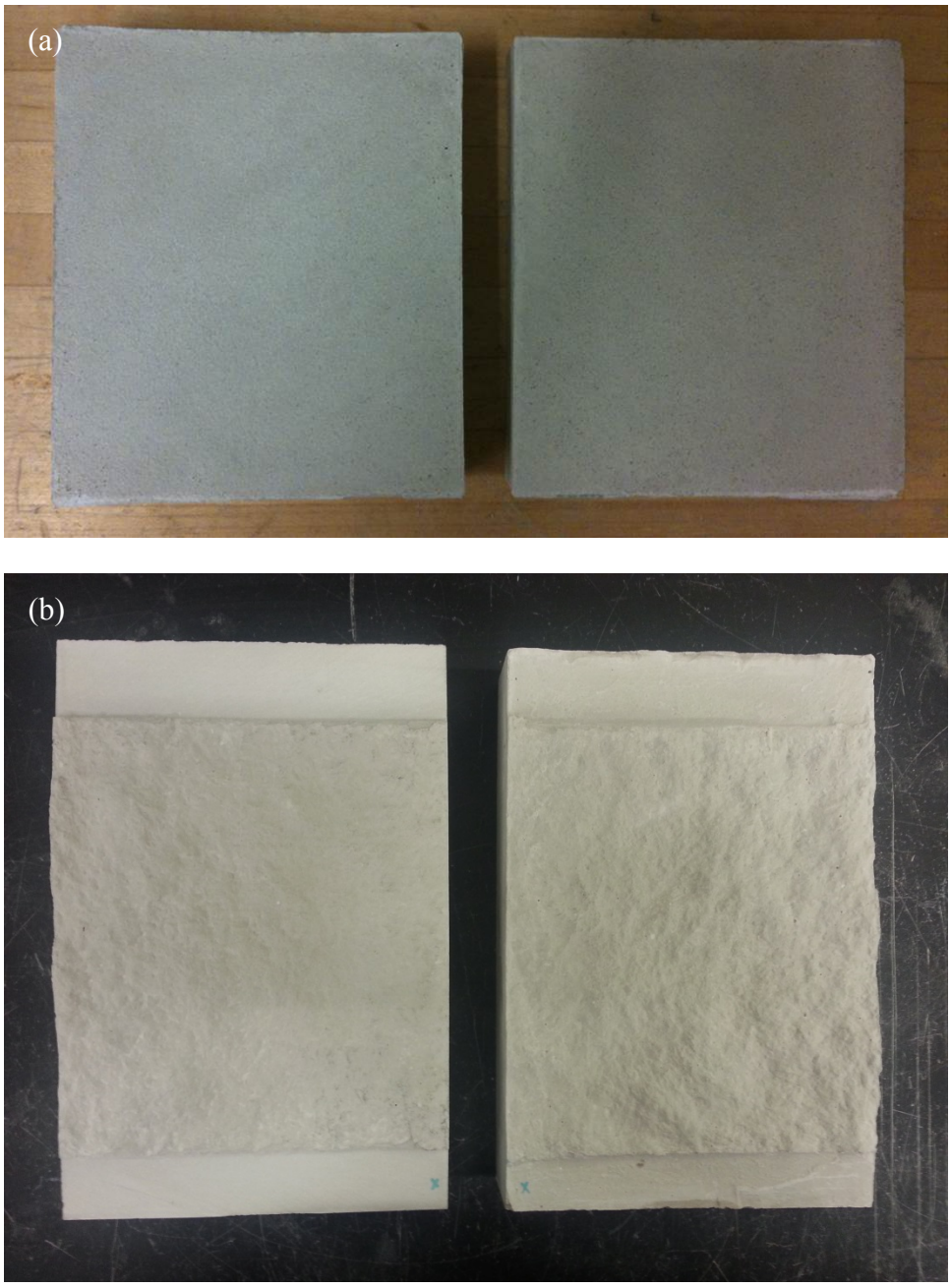

Figure 3.3.1-1. Photographs of: (a) gypsum #36 specimen and (b) replica GS01R specimen with a well-mated fracture.

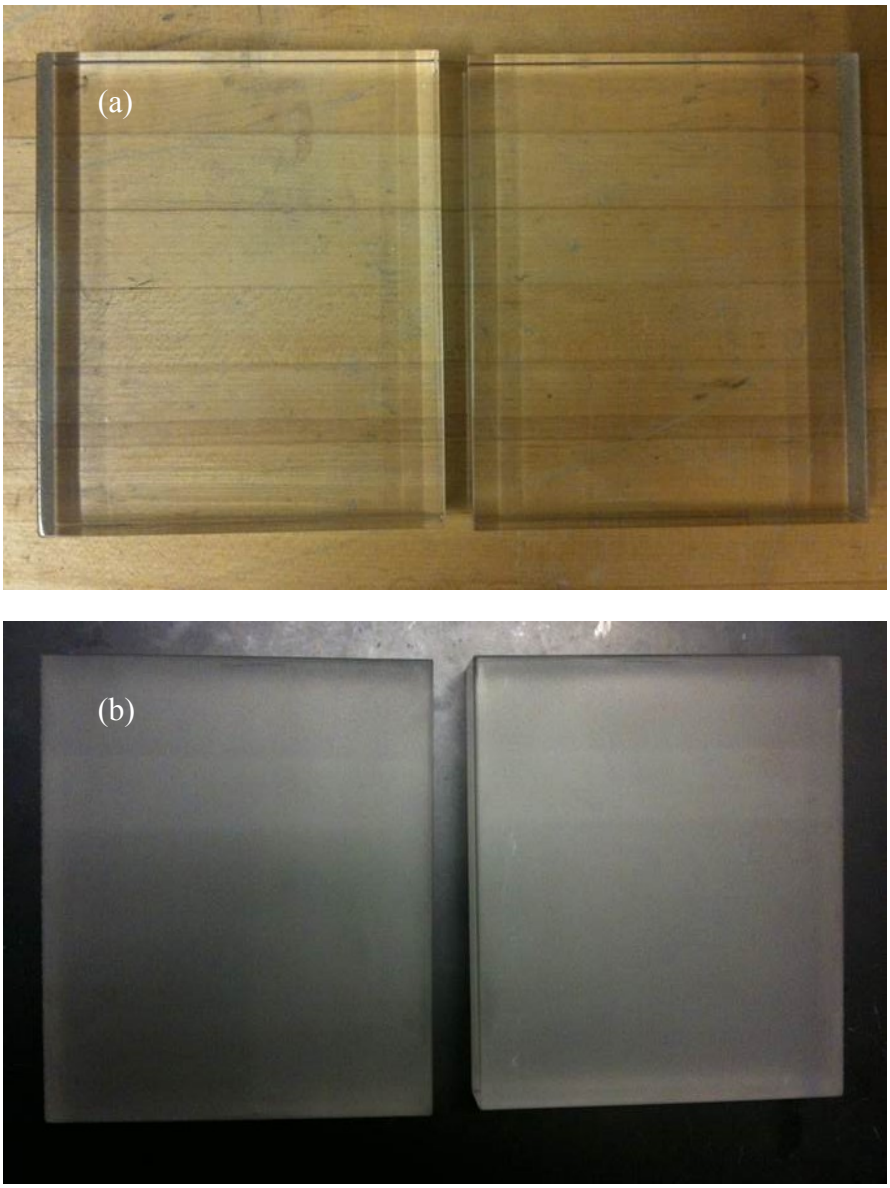

Figure 3.3.1-2. Photographs of: (a) the lucite PL and (b) lucite SB specimens with a non-mated fracture.

3.3.2 Seismic Imaging System

A fast computer-controlled seismic imaging array system was used to acquire transmitted and reflected full-waveforms for post-processing analysis. The equipment consisted of a chassis (PXI-1042) that contained a real-time onboard computer controller (PXI-8106) with two multiplexer matrix switches, a two channel 14 bit 100 MHz digitizer (PXI-5122) for acquiring full waveforms, two 10 channel power multiplexer (PXI-2585), and one multiplexer terminal block (TB-2630) for switching among multiple seismic sources and receivers. Broadband transducers with a central frequency of 1 MHz were housed in specially designed load platens placed on each side of the specimen to measure the transmitted and reflected P- and S- waves.

The platens were machined from two solid steel blocks that housed the source and receiver transducers, while transmitting the load to the specimen. Each transducer was placed on a Belleville washer spring and on a number of shims so that its tip protruded 0.008” (±0.001”) from the loading platen. The washer spring under the transducer kept the transducer always in contact with the specimen.

A pulse generator excited the transducers with a 100V square wave at a repetition rate of 5 kHz. Thirteen source-receiver transducers pairs were employed: three shear wave transducers polarized parallel to the direction of shear, four shear wave transducers perpendicular to the direction of shear, and six compressional wave transducers. Using two different polarizations for the shear wave transducers enabled us to determine if the test specimen exhibited shear wave anisotropy.

Figure 3.3.2-1 shows a photograph of the seismic imaging system and the transducer layout; in the figure, the direction of the elongated box indicates the polarization direction

of shear wave transducers. The capital letters P and S represent compressional and shear wave transducers, respectively. The S- wave transducers were used to obtain the shear fracture specific stiffness, while the P-wave transducers monitored changes in normal fracture specific stiffness.

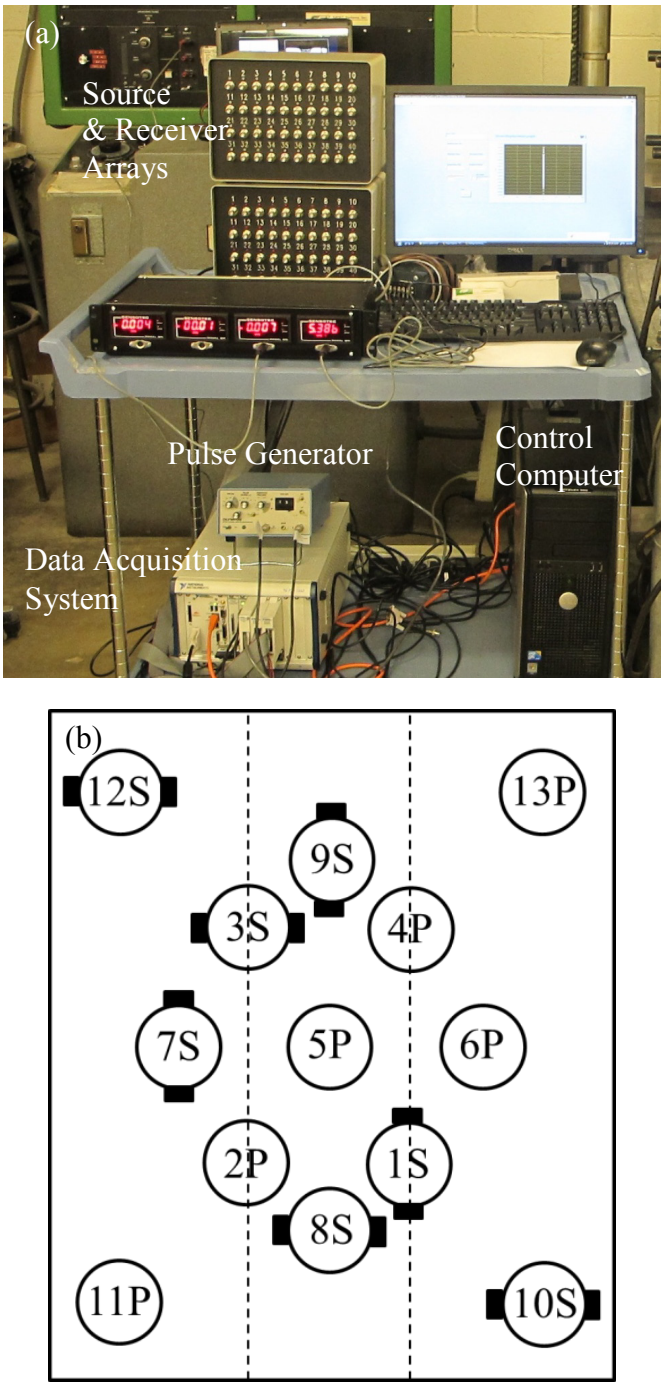

Figure 3.3.2-1. (a) Photograph of seismic imaging system and (b) layout of seismic transducer layouts. Elongated boxes show the polarization direction of shear wave transducers. The dashed lines indicate the location of selected asperity profiles that pass under transducers 3S-2P and 4P-1S.

3.3.3 Experimental Procedures

The procedure for seismic data acquisition was standardized to ensure test repeatability. First, a thin plastic film was placed over the surfaces of the specimen in contact with the transducers. The plastic film was necessary to prevent penetration of the honey into the pores of the specimen. Then the transducers were coupled to the surface with honey. Before application, the honey was dehydrated at 90°C for 75 minutes to dry 8% of its weight. Then a 1 MPa normal stress was applied to the specimen for 3 hours to allow the couplant to equilibrate. This process resulted in stable, repeatable transmitted P- and S-wave signals. After 3 hours, the load was removed and the experiments were performed.

The experiments were performed in two stages: no slip and slip. During the no slip stage, the applied shear stress was set to be less than the shear strength of the fracture, so shear failure would not occur. To investigate systematically the stiffness ratio before shear failure, a stepwise loading path for normal and shear loads was applied. The loading path is shown in Figure 3.3.3-1 (a). The imposed shear stress (τ) was calculated as the applied normal stress (σ) times tan θ, i.e, $\tau=\sigma\cdot\tan\theta$. Figure 3.3.3-1 (b) shows the experimental set-up. A horizontal loading frame applied a normal (confining) stress to the specimen and a conventional loading machine was used to apply the shear load. In the second stage, where slip was induced, the shear stress was applied to the fracture with a constant displacement rate until final slip/failure occurred. During the application of the shear load, the normal stress was held constant. During all tests, the seismic imaging system constantly monitored the fracture by measuring transmitted and reflected waves through the specimen. The seismic measurements were used to estimate the change of stiffness ratio with loading.

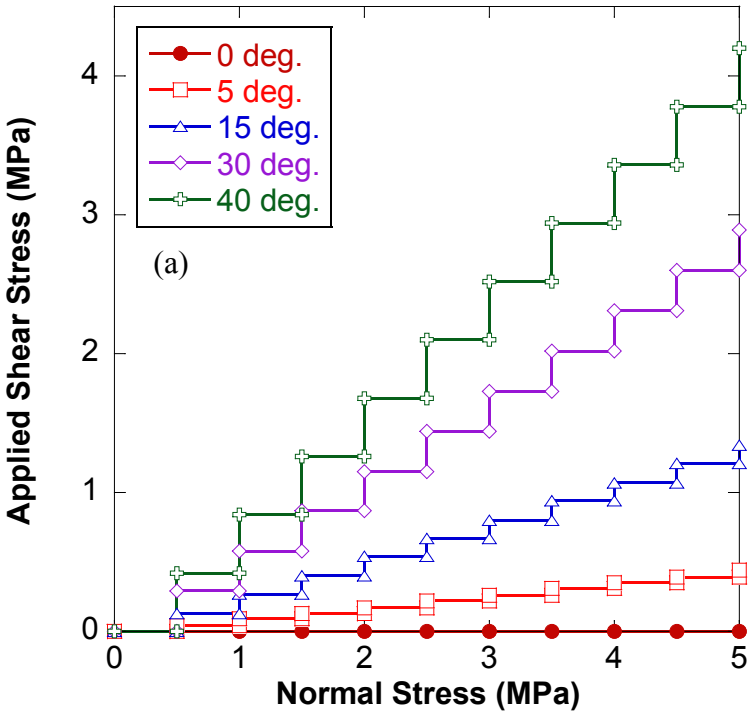

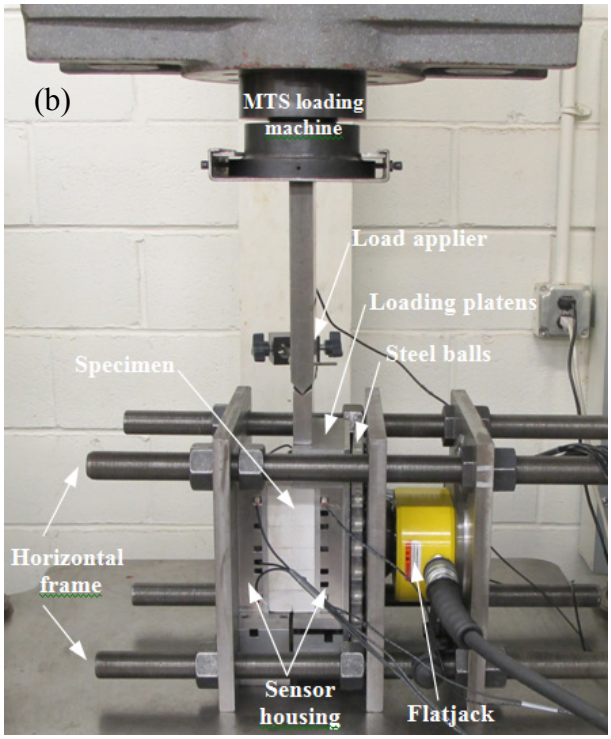

Figure 3.3.3-1. (a) Loading path for normal and shear load and (b) a photo of biaxial apparatus with seismic transducer housing.

3.3.4 Surface Roughness Measurements

A laser profilometer was used to characterize the roughness of the fracture surfaces. The system consisted of: (1) a laser LK-G152, from Keyence Corporation, to measure the height of the surface; (2) a motion controller ESP-300, from Newport Corporation, to control the horizontal and vertical movements of the specimen holder under the laser; and (3) a customized Labview program to record data and control the movement of the laser. Figure 3.3.4-1 shows the laser profilometer. The Labview program controlling the profilometer defines the step size, velocity, and acceleration for the vertical and horizontal displacements of the platform where the specimen is placed. The Labview code enabled us to scan a surface with an area of 127mm x 100mm in 0.25 mm increments, for two orthogonal directions, in 3-4 days. The laser profilometer was calibrated with a micrometer and the maximum and minimum measurable height range of the laser was ±9.969 mm, with an accuracy of 0.5 μm. The shape of the laser spot was circular and had a diameter of 120 μm. Before a specimen was mounted on the biaxial loading frame, the fracture surface roughness was measured in 250 μm increments and in two orthogonal directions using the laser profilometer. The surface roughness measurements were corrected by applying three orthogonal rotations to minimize positioning errors caused by placing the sample in the holder (Sharifzadeh, 2008).

The measurements of surface roughness are summarized in Table 3.3.4-1. The distribution of surface roughness measurements are shown in Figure 3.3.4-2. As seen in the Table, the fracture roughness ranged from around 60 μm to 2,870 μm. The roughness distributions for the lucite SB, gypsum Flat, #220, #60, #36, and GS01R specimens are similar to a normal distribution. The roughness measurements of the lucite PL were not

made because the material was transparent and the laser profilometer was not able to take measurements.

As seen in Table 3.3.4-1, the fracture surface of the gypsum flat specimen had a mean asperity of 59-70 μm with 28 μm standard deviation, which are comparable to those of gypsum #220. For comparison of the measured asperities of the flat specimen to that of #220 specimen, two profiles were selected (see Figure 3.3.2-1), i.e., 3S-2P and 4P-1S. Figure 3.3.4-3 contains the roughness profiles of the gypsum Flat and #220 specimens. For the gypsum Flat specimen, the asperities along the profiles of 3S-2P and 4P-1S (see Figure 3.3.2-1. (b)) varied within about ±0.050 mm and were the result of the waviness of the fracture surface. The gypsum #220 specimen had a more planar surface and had randomly distributed asperities along the profiles. The spatial distribution of asperities along the profiles is the main difference between the gypsum Flat and #220 specimens.

Table 3.3.4-1. Measured mean asperity height and standard deviation.

Fracture Type	Sample name	Mean asperity (μm)	Standard deviation (μm)
Well-Mated	GS01R	2,680 ~ 2,870	878 ~ 887
	Gypsum #36	335 ~ 537	65 ~ 67
	Gypsum #60	265 ~ 267	64 ~ 67
	Gypsum #220	62 ~ 70	22 ~ 23
	Gypsum Flat	59 ~ 70	28
Non-Mated	Lucite SB	62.5 ~ 106	10 ~ 18
	Lucite PL	N/A	N/A

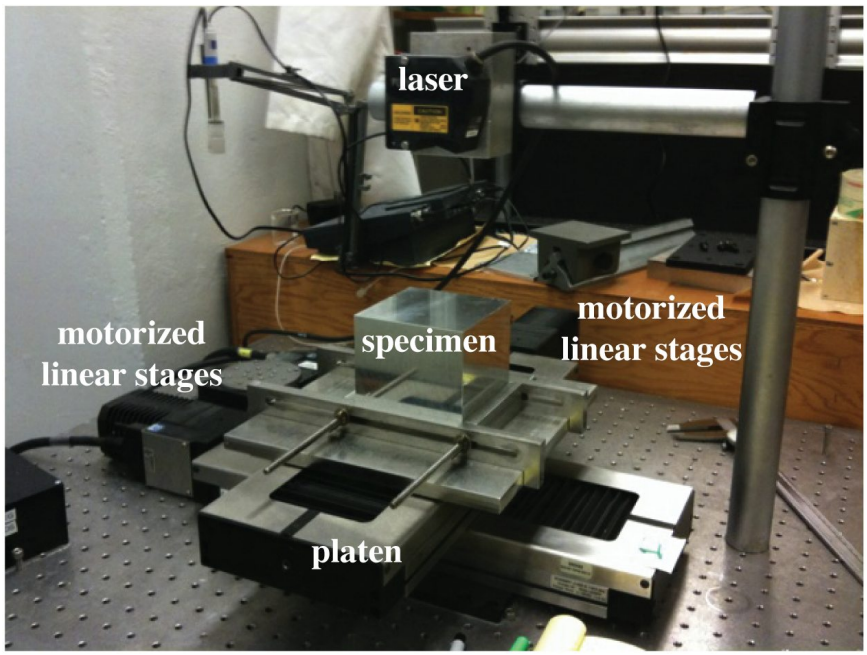

Figure 3.3.4-1. Photograph of laser profilometer.

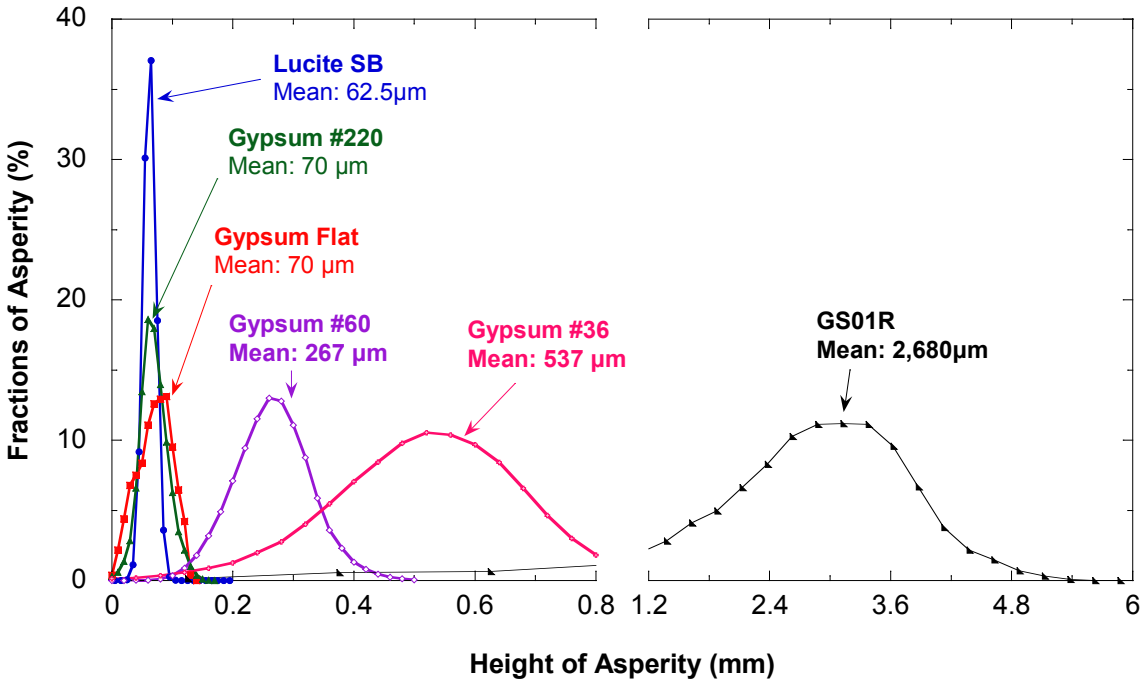

Figure 3.3.4-2. Surface roughness distribution of contact surfaces for lucite sand-blasted (SB), gypsum Flat, #220, #60, #36, and GS01R specimens.

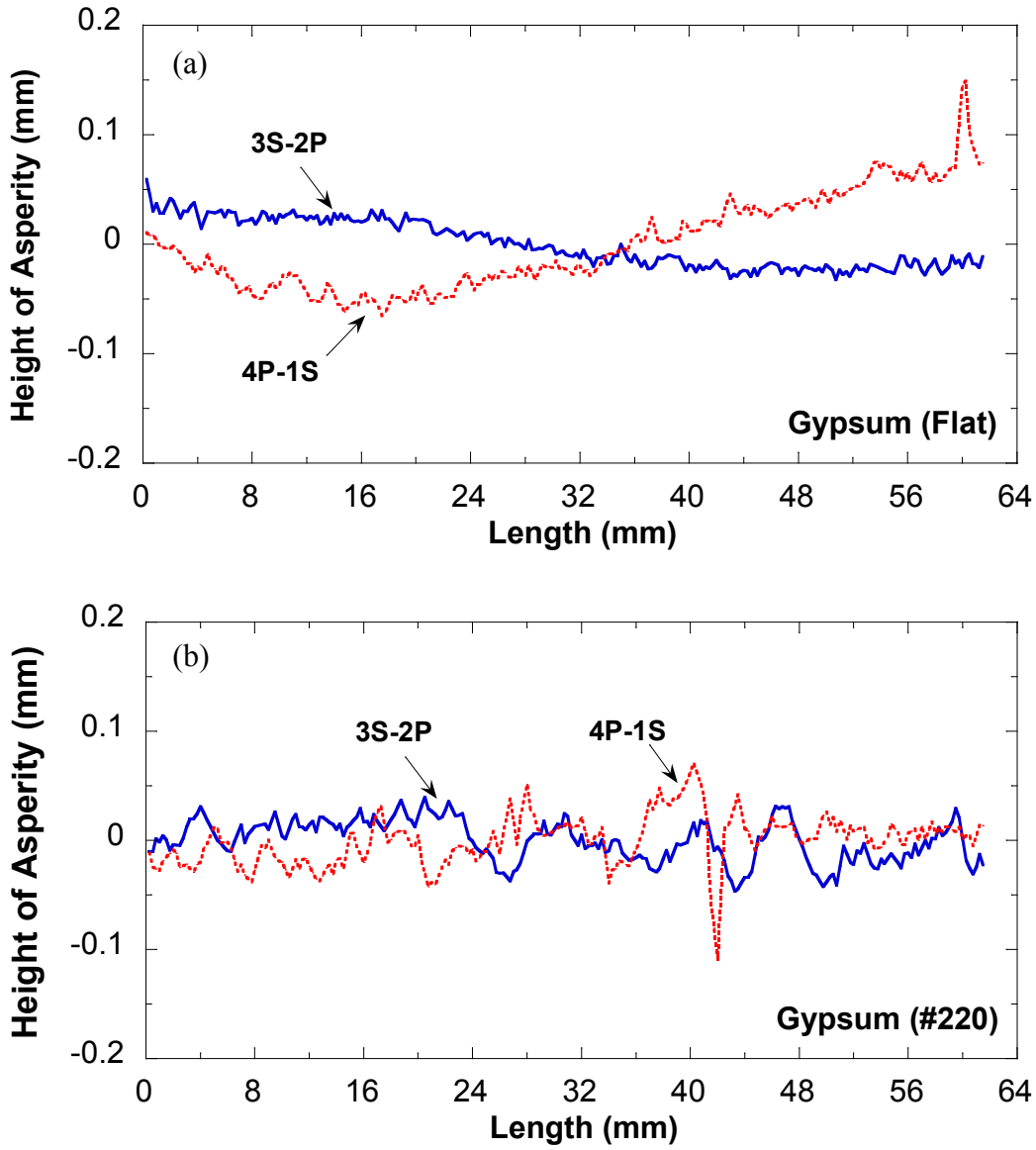

Figure 3.3.4-3. Selected fracture profiles along 3S-2P (solid line) and 4P-1S (dashed line) for: (a) gypsum Flat and (b) gypsum #220. See Figure 3.3.2-1. (b) for profiles location.

3.4 Results and Analysis

The stiffness ratio was investigated for both well-mated and non-mated fracture surfaces. The lucite PL sample, with a non-mated surface, was subjected to 0°, 5°, and 15° loading paths, while the lucite SB sample, also with non-mated surface, to 0°, 15°, and 30°. Angles larger than 30^{o} were not used because slip would be induced. The well-mated fracture specimens listed in Table 3.3.4-1 were tested for 0°, 15°, 30°, and/or 40° loading paths. None of the loading paths induced slip on the fractures.

3.4.1 Seismic Measurements on Intact Specimens

Prior to testing specimens with fractures, seismic measurements on intact specimens (without fractures) were made under the loading shown in Figure 3.3.3-1 (a). The results showed that waves propagated through the solid matrix of lucite and gypsum were insensitive to stress. Figures 3.4.1-1 and 3.4.1-2 contain the wave velocities and peak-to-peak amplitudes of transmitted compressional and shear waves, respectively, on intact lucite and gypsum as a function of loading. The figures show that both wave velocity and amplitude were independent of the applied normal or shear stress, which can be explained by the absence of microcracks in the materials. The compressional and shear wave velocities were employed to calculate the seismic impedance of the material, which is needed to compute the fracture specific stiffness, as discussed in Chapter 2.

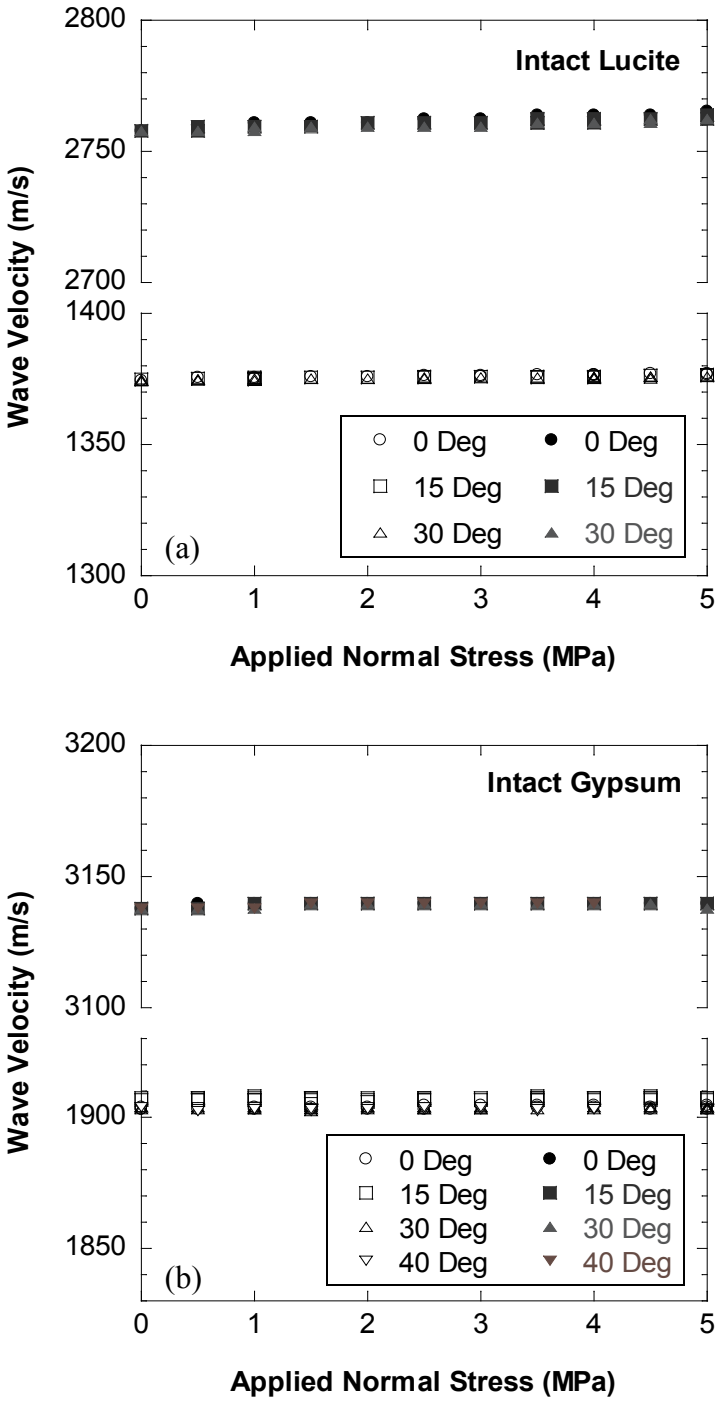

Figure 3.4.1-1. Compressional (closed symbols) and shear (open) wave velocities measured from transducer pairs 2P-2P and 8S-8S for: (a) intact lucite; and (b) intact gypsum specimen, with normal stress.

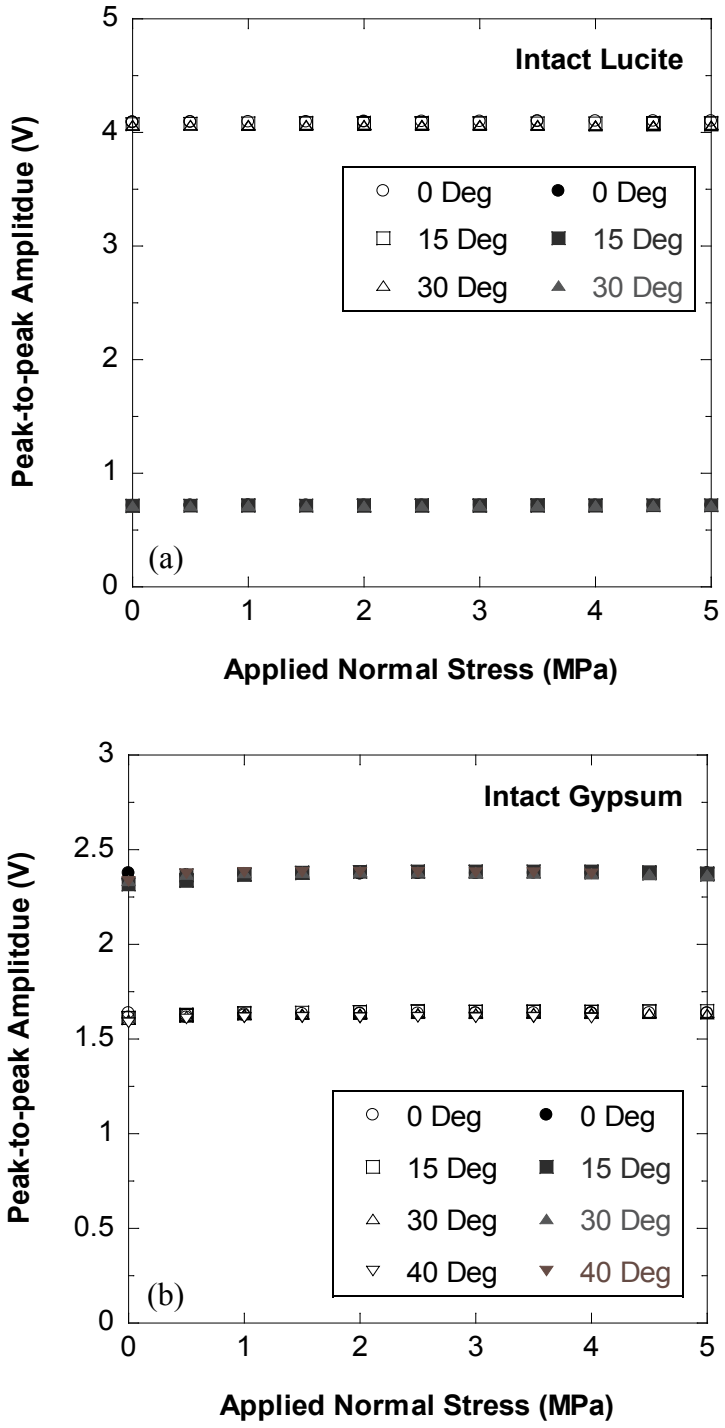

Figure 3.4.1-2. Peak-to-peak amplitude of compressional (closed symbols) and shear (open) waves measured from transducer pairs 2P-2P and 8S-8S for: (a) intact lucite and (b) intact gypsum, as a function of normal stress.

3.4.2 Seismic Measurements on Specimens with a Fracture

3.4.2.1 Non-Mated Fractures

Figures 3.4.2-1 (a) and (b) show representative waveforms of P- and S- waves for the lucite PL specimen. Amplitude and wave velocity were essentially constant once the applied normal stress was larger than 0.5 MPa. This suggests that the fracture was tightly closed and so the specimen behaved as intact for stresses larger than 0.5 MPa.

For the lucite SB specimen, the waveforms of P- wave transducer pairs 2P-2P and S-wave transducer pairs 8S-8S, which can be taken as a representative of P- and S- waves, are shown in Figure 3.4.2-2. The figure shows that amplitude and wave velocity increased gradually with increasing normal load, for the 0° loading. The increase in amplitude of the signals from transducer pair 8S-8S was larger than from 2P-2P. The peak-to-peak amplitude of the shear wave from 8S-8S increased from 1.1 V to 3.0 V, a factor of 2.7, over the range of applied normal stress 0.5 MPa to 4.0 MPa, while the amplitudes of the compressional wave 2P-2P increased only from 0.39 V to 0.52 V, by a factor of 1.3, over the same range of normal stresses. The greater increase of amplitude of shear wave means that the increase of shear fracture specific stiffness is larger than the increase of normal fracture specific stiffness.

Figure 3.4.2-3 compares the variation of peak-to-peak amplitudes from transducer pairs 2P-2P and 8S-8S, when the lucite PL and SB specimens were subjected to the loading paths 0° to 30°. For lucite PL, the peak-to-peak amplitudes of 2P-2P and 8S-8S transducers were independent of stress; that is, they were insensitive to the application of shear stress. The data from the lucite SB specimen showed that both amplitudes of

compressional and shear waves increased significantly with increasing normal stress. At the same normal stress, the amplitudes of compressional and shear waves increased about 10%.

3.4.2.2 Well-Mated Fractures

For the specimens with a well-mated fracture, i.e. gypsum Flat, #220, #60, and #36, measurements of the transmitted and reflected full-waveforms were made during the experiments using the seismic imaging system. It was observed for all well-mated gypsum specimens that the change in amplitude of the transmitted wave signals was greater than for the reflected wave signals. For example, Figure 3.4.2-4 shows the compressional waveforms measured by the P-wave transducer pair 2P-2P for the gypsum #60 specimen. The peak-to-peak amplitude of the transmitted wave increased from 0.15 V to 1.04 V (a factor of 7) over the range of the applied normal stress of 0.5 MPa to 4.0 MPa, while the amplitudes of the reflected waves decreased by 13% for the same range of normal stresses. Similarly, the amplitudes of transmitted shear waves significantly increased while the reflected wave amplitude decreased by 10%, as seen in Figure 3.4.2-5. Based on the displacement discontinuity theory, the increase of amplitude of the transmitted wave and the decrease of the reflected wave can be interpreted as an increase of fracture specific stiffness.

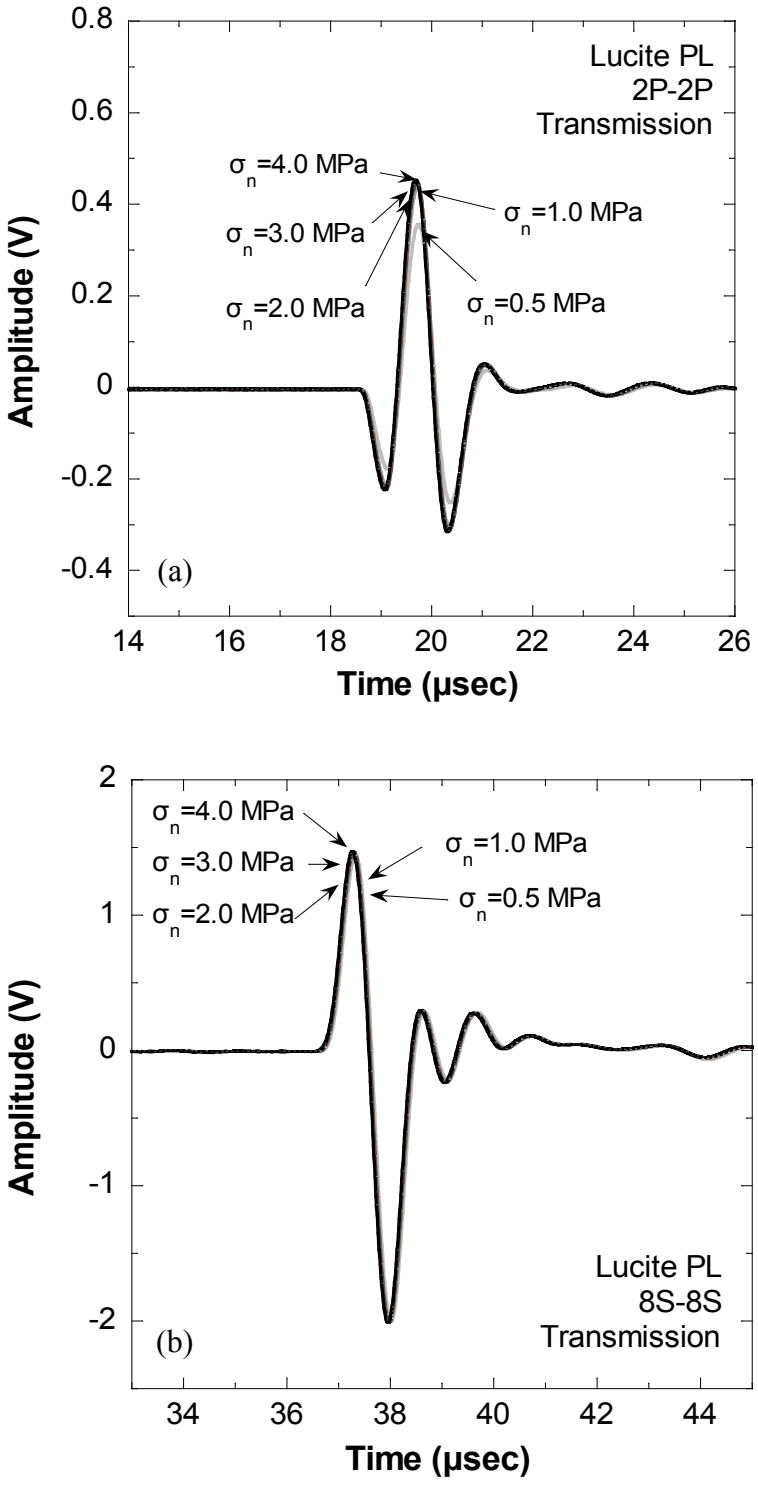

Figure 3.4.2-1. Measured waveforms from lucite PL for: (a) compressional transducer pair 2P-2P; and (b) shear transducer pair 8S-8S, for normal stresses from 0.5 MPa to 4.0 MPa for the 0° loading path.

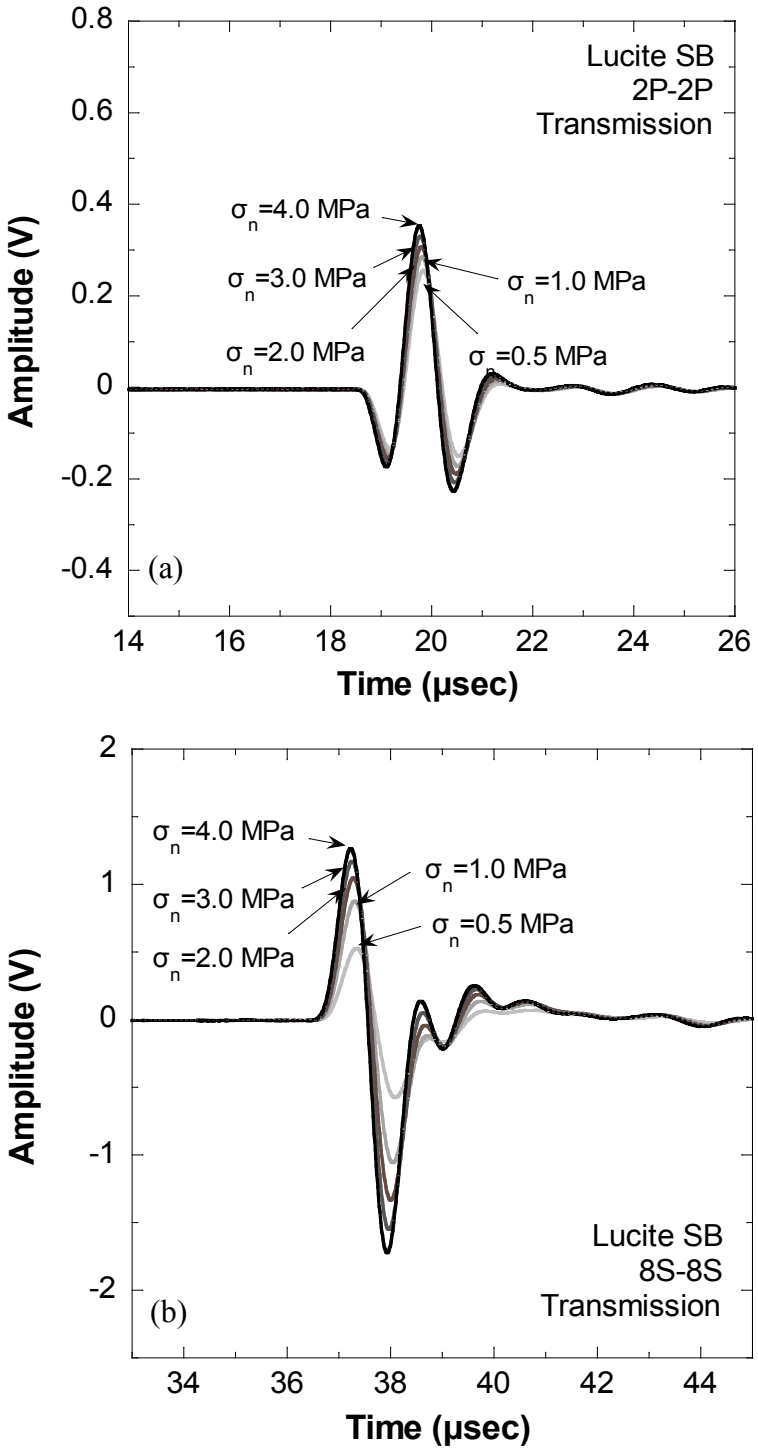

Figure 3.4.2-2 Measured waveforms from lucite SB for: (a) compressional transducer pair 2P-2P; and (b) shear transducer pair 8S-8S, for normal stresses from 0.5 MPa to 4.0 MPa and for loading path 0°.

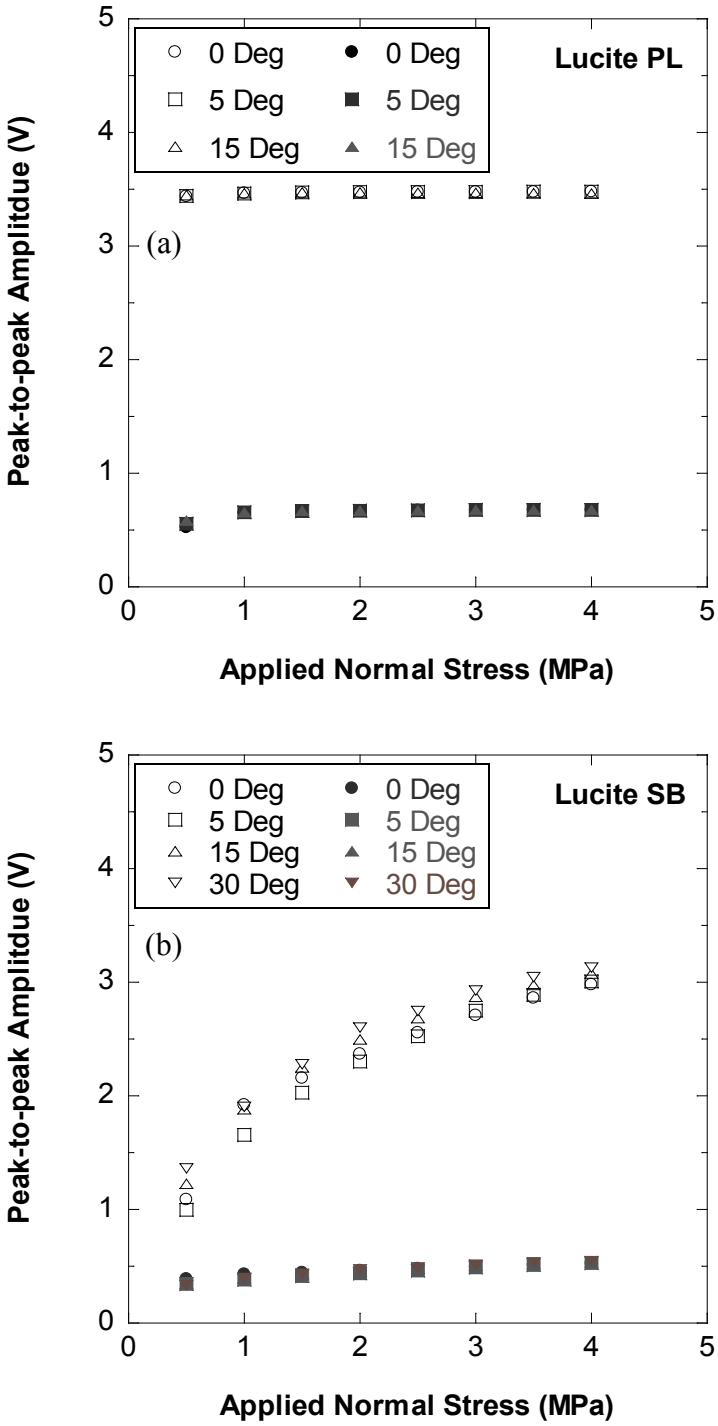

Figure 3.4.2-3. Peak-to-peak amplitude of compressional (closed symbols) and shear (open) waves measured from transducer pairs 2P-2P and 8S-8S for: (a) lucite PL specimen; and (b) lucite SB specimen, for different loading paths, as defined in Figure 3.3.3-1 (a).

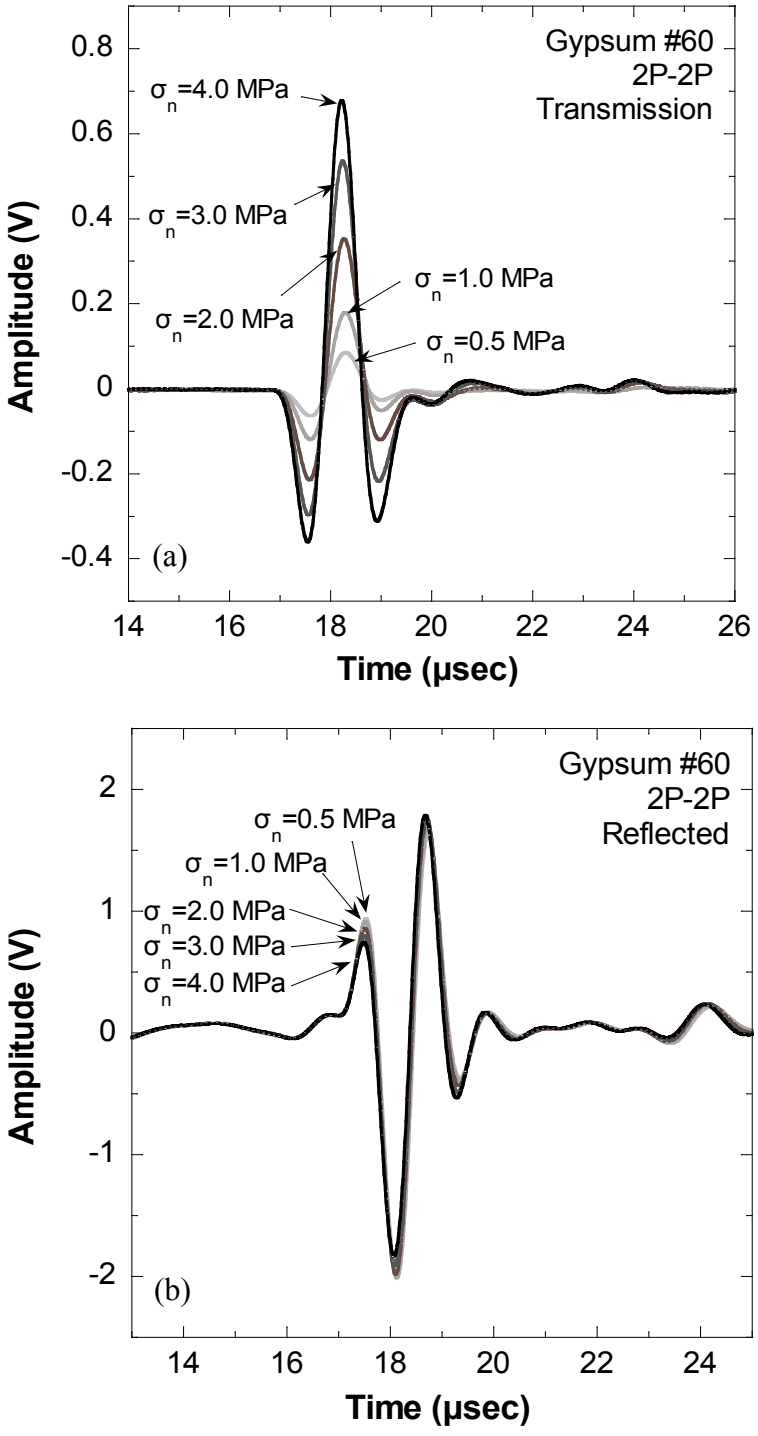

Figure 3.4.2-4. Measured waveforms of: (a) transmitted; and (b) reflected P-waves measured from transducer pair 2P-2P, for gypsum #60 specimen and for normal stresses 0.5 MPa to 4.0 MPa, for the 0° loading path.

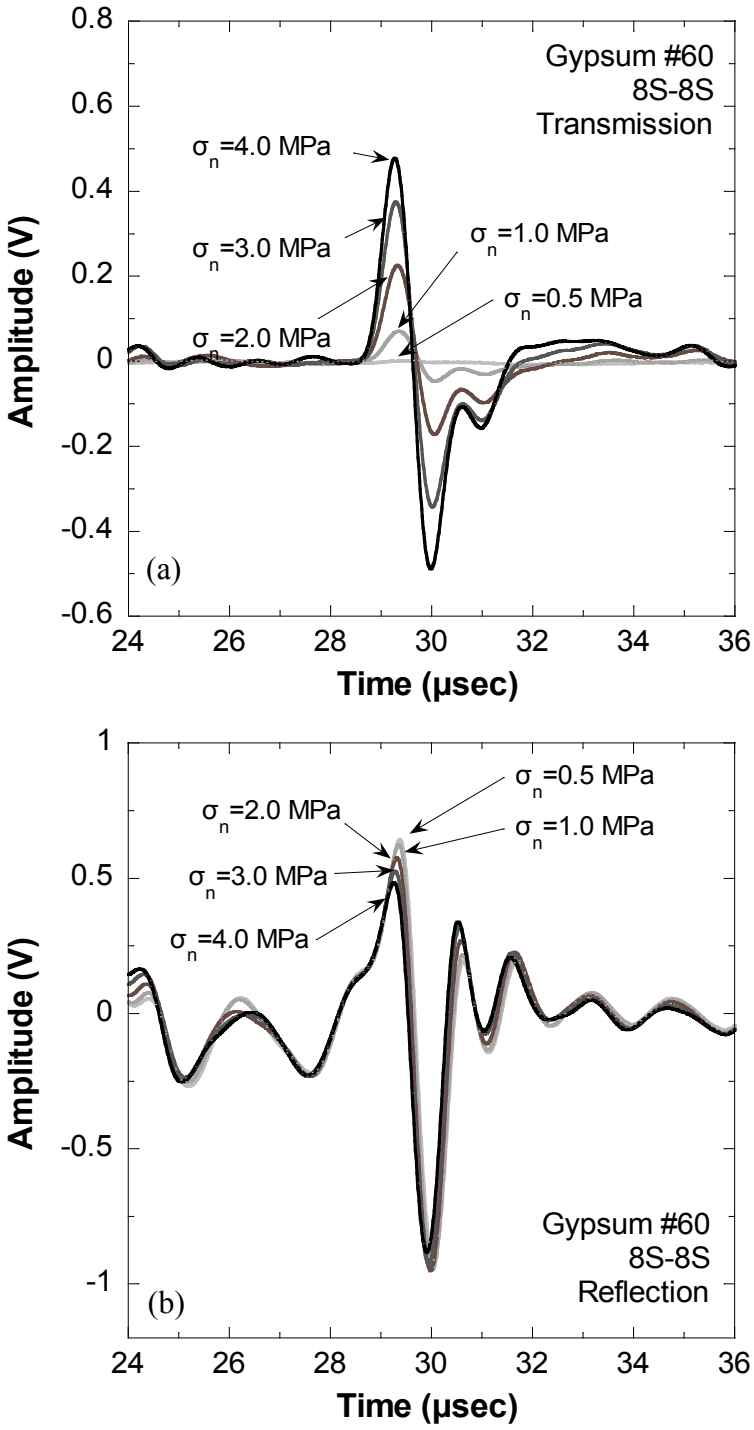

Figure 3.4.2-5. Measured waveforms of: (a) transmitted; and (b) reflected S-waves measured from transducer pair 8S-8S, for gypsum #60 specimen at normal stresses from 0.5 MPa to 4.0 MPa, for the 0° loading path.

3.4.3 Spectral Analysis

3.4.3.1 Tapering

The displacement discontinuity theory (see section 2.2) was used to interpret the fracture specific stiffness from the seismic measurements taken from the tests. The compressional and shear waves were first tapered to extract the first arrival from subsequent reflections. The shape of taper was determined to give the best representation of the spectral energy of the first arrival. The taper combined an open step function of 0.85 μsec duration with one-half closing cosine of 1.71 μsec. The determined taper was applied to the compressional and shear waves. Figure 3.4.3-1 shows an example of the shape of the selected taper along with a waveform measured from experiments. This taper isolated the initial signal from subsequent reflections and preserved the low frequency content of the original signal without significant distortion of the high frequency components. After applying the combined taper to the recorded signal, spectral amplitudes were obtained by performing a Fast Fourier Transform (FFT) on the tapered signals.

3.4.3.2 Fast Fourier Transform

Figure 3.4.3-2 compares the spectral amplitudes of the lucite PL specimen with those of the intact lucite, obtained from transducer pairs 2P-2P and 8S-8S for the 0° loading path. In the Figure, the solid and dotted lines represent the lucite intact and the lucite PL, respectively. For both 2P-2P and 8S-8S transducers, the spectral amplitude for frequency components lower than 0.3 MHz for the transmitted P- and S- waves of the lucite PL specimen were close to those of the intact lucite, supporting the prediction from the

displacement discontinuity theory that a fracture behaves as a low pass filter. Beyond the normal stress of 0.5 MPa, the spectral amplitudes for 2P-2P and 8S-8S transducers remained constant and there was no significant change in the most probable frequency, i.e., dominant frequency, of the lucite PL specimen.

The spectral amplitudes obtained from the lucite SB specimen, for the 0° loading path, and for 2P-2P and 8S-8S transducer pairs, are compared in Figure 3.4.3-3 with those from the intact lucite. In contrast to the lucite PL specimen, the spectral amplitudes of the lucite SB specimen exhibited stress-sensitivity in the range of normal stress from 0.5 to 4.0 MPa. As the applied normal stress increased, both the spectral amplitudes and the dominant frequency increased. For example, the maximum spectral amplitude for the shear wave increased from 0.36 V to 0.90 V while the corresponding dominant frequency shifted from 0.42 MHz to 0.56 MHz. In a similar manner, the maximum spectral amplitude of the compressional wave changed from 0.11 V to 0.15 V with the increase of the dominant frequency from 0.63 MHz to 0.66 MHz. It is necessary to note that the increase of amplitude and dominant frequency is more significant for shear waves than for compressional waves. This implies that the increase in shear fracture specific stiffness is larger than the normal fracture specific stiffness, or that the shear fracture specific stiffness is initially much lower than the normal stiffness.

For the specimens with a well-mated fracture (gypsum Flat, #220, #60, and #36), full waveforms were measured for both transmission and reflection, as discussed in section 3.4.2.2. Fast Fourier Transformation was performed on both the transmitted and reflected waves to obtain spectral amplitudes. Figures 3.4.3-4 to 3.4.3-7 contain the spectral amplitudes from specimens with a well-mated fracture. The figures show the spectral

amplitudes for 2P-2P and 8S-8S transducer pairs for the 0° loading path. For gypsum specimens Flat, #220, #60, and #36, the spectral amplitudes of the reflected wave essentially remained constant with increasing normal stress within the range 0.5 MPa to 4.0 MPa, while the spectral amplitudes of transmitted waves increased, as well as the dominant frequency. Small variations in the spectral amplitudes of the reflected waves, along with relatively large changes of the transmitted waves, are predicted by the displacement discontinuity theory reviewed in section 2.2.4. Figure 2.2.4-1 shows that the reflection coefficient is almost constant, while the transmission coefficient is sensitive to the fracture specific stiffness for normalized frequencies within the range $\omega Z / \kappa \geq 4$.

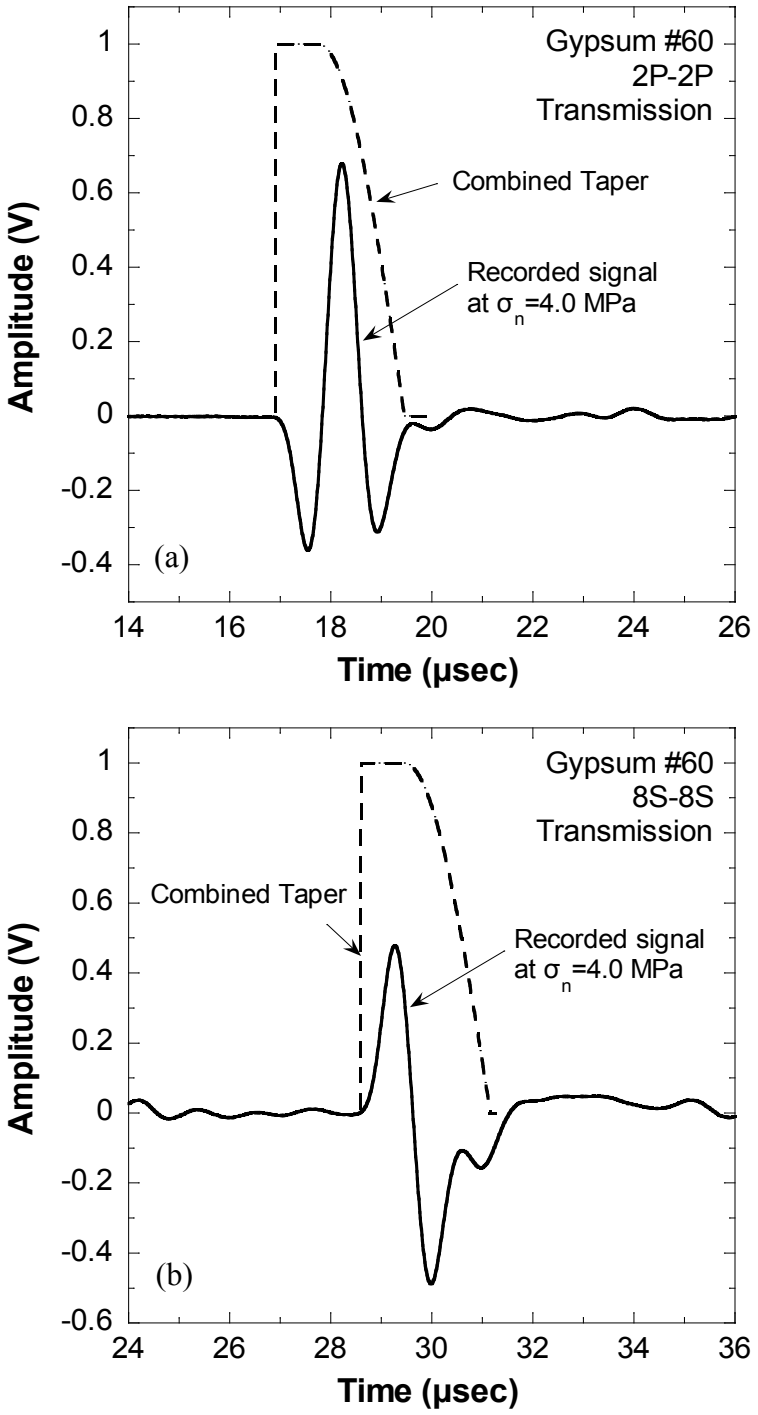

Figure 3.4.3-1. Combined taper with a step opening of 0.85 μsec and one-half closing cosine of 1.71 μsec applied to: (a) the P- ; and (b) S-waves from gypsum #60 specimen at a normal stress of 4.0 MPa.

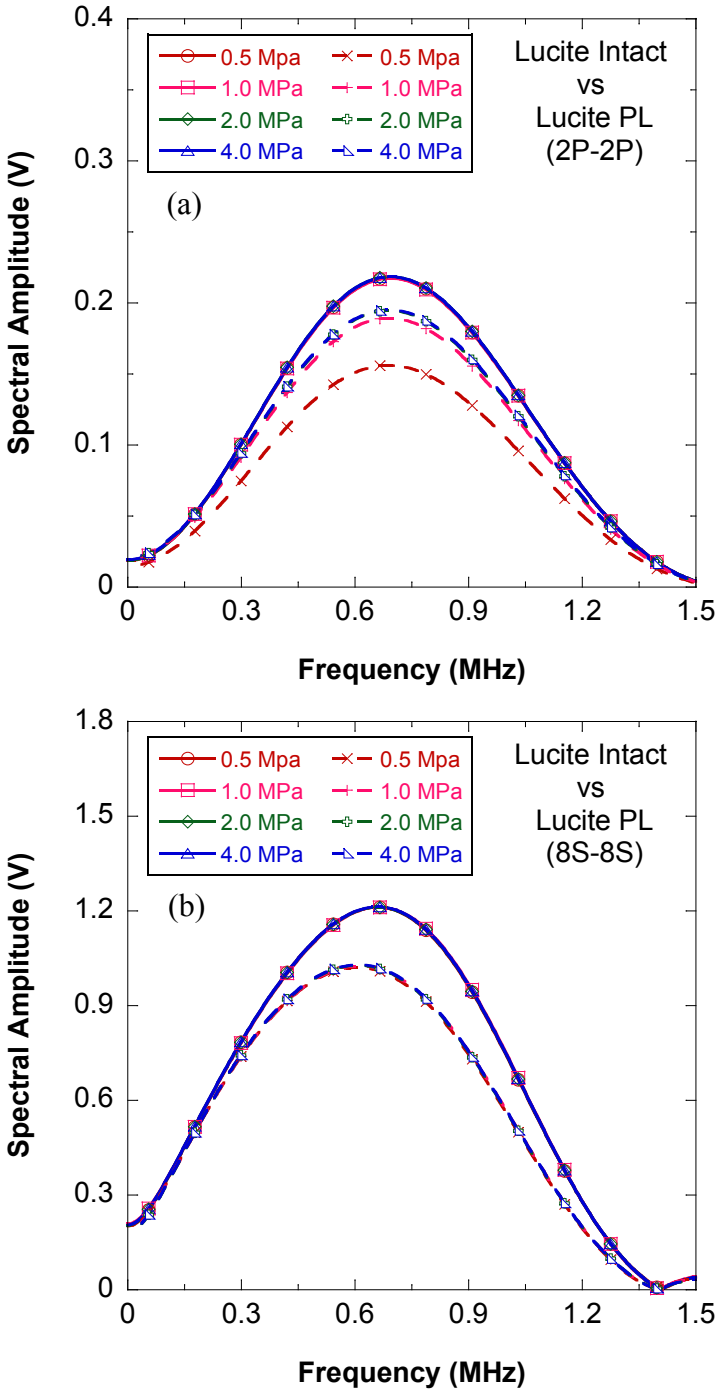

Figure 3.4.3-2. Comparison of spectral amplitudes between the lucite intact (solid lines) and lucite PL (dotted lines) specimens for: (a) transducer pairs 2P-2P; and (b) 8S-8S for 0° loading path.

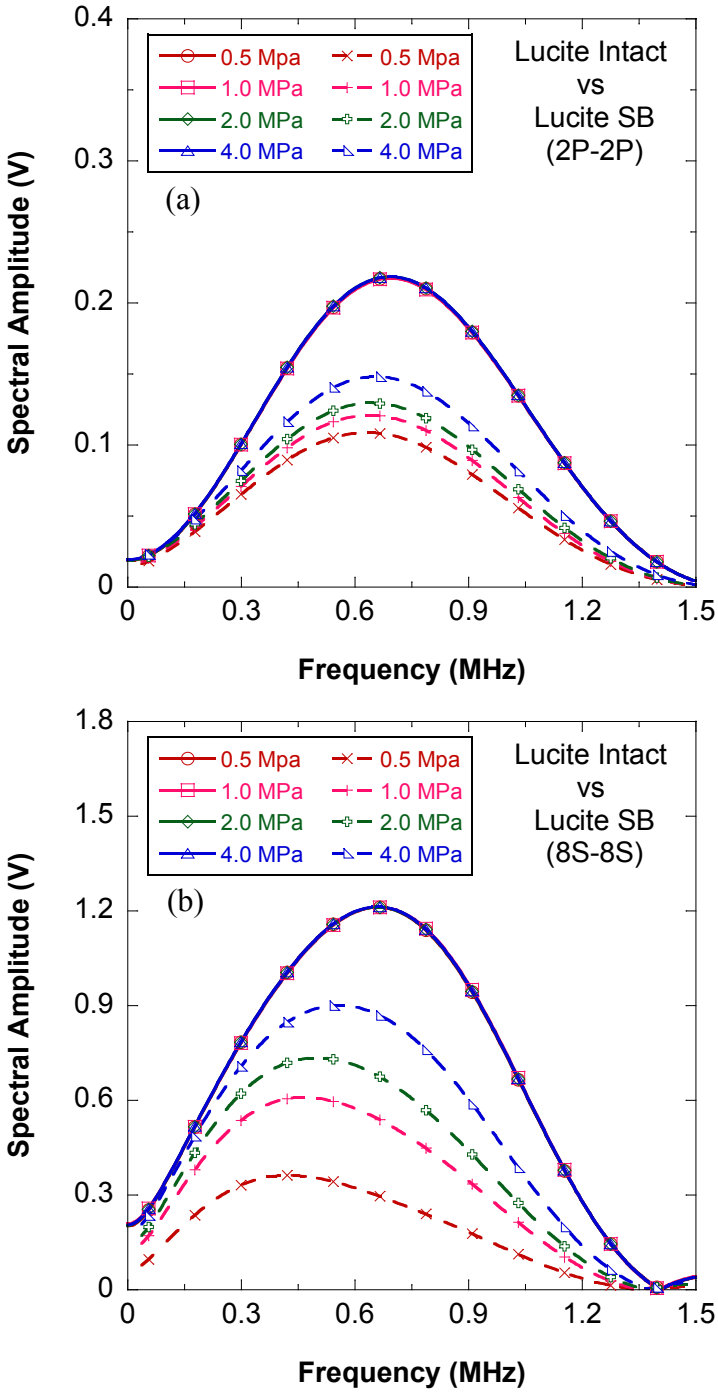

Figure 3.4.3-3. Comparison of spectral amplitudes between the lucite intact (solid lines) and lucite SB (dotted lines) specimens for: (a) transducer pairs 2P-2P; and (b) 8S-8S for 0° loading path.

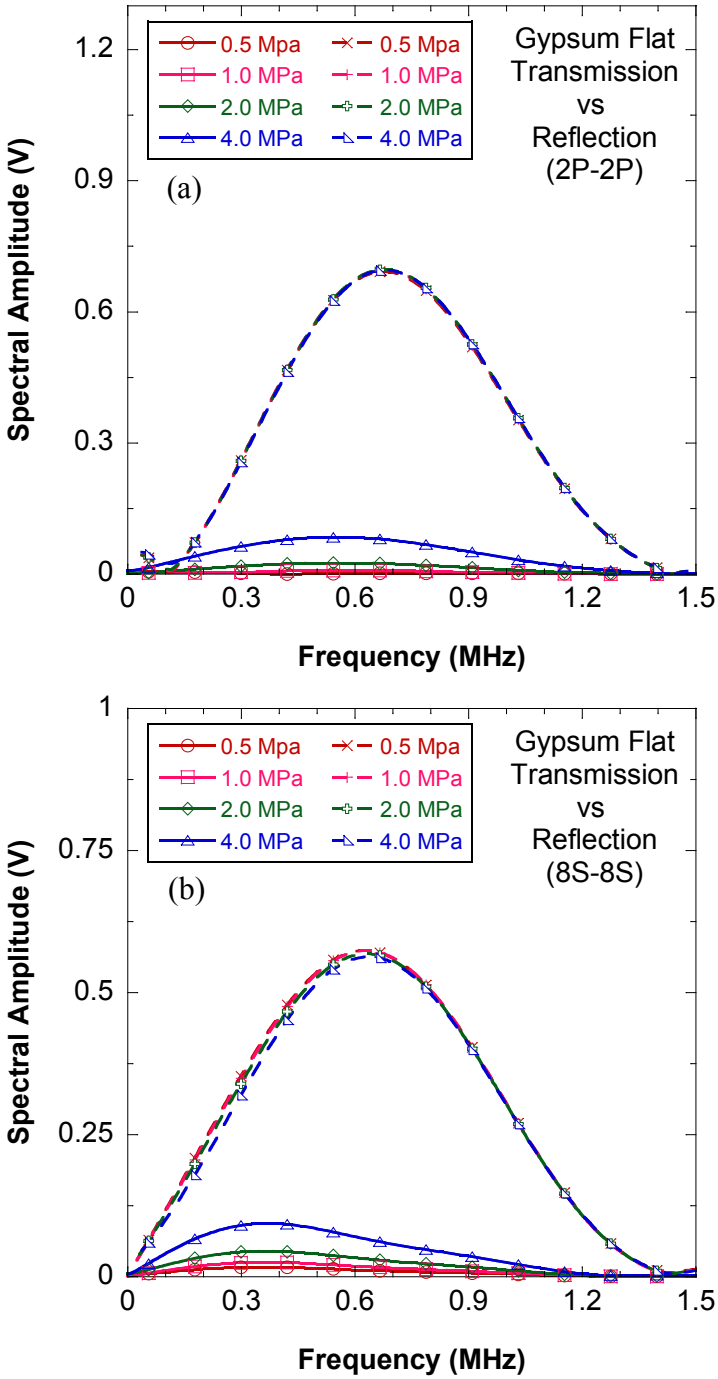

Figure 3.4.3-4. Comparison of spectral amplitudes between the transmitted (solid lines) and reflected (dotted lines) waves for: (a) transducer pairs 2P-2P; and (b) 8S-8S for the gypsum Flat specimen and for the 0° loading path.

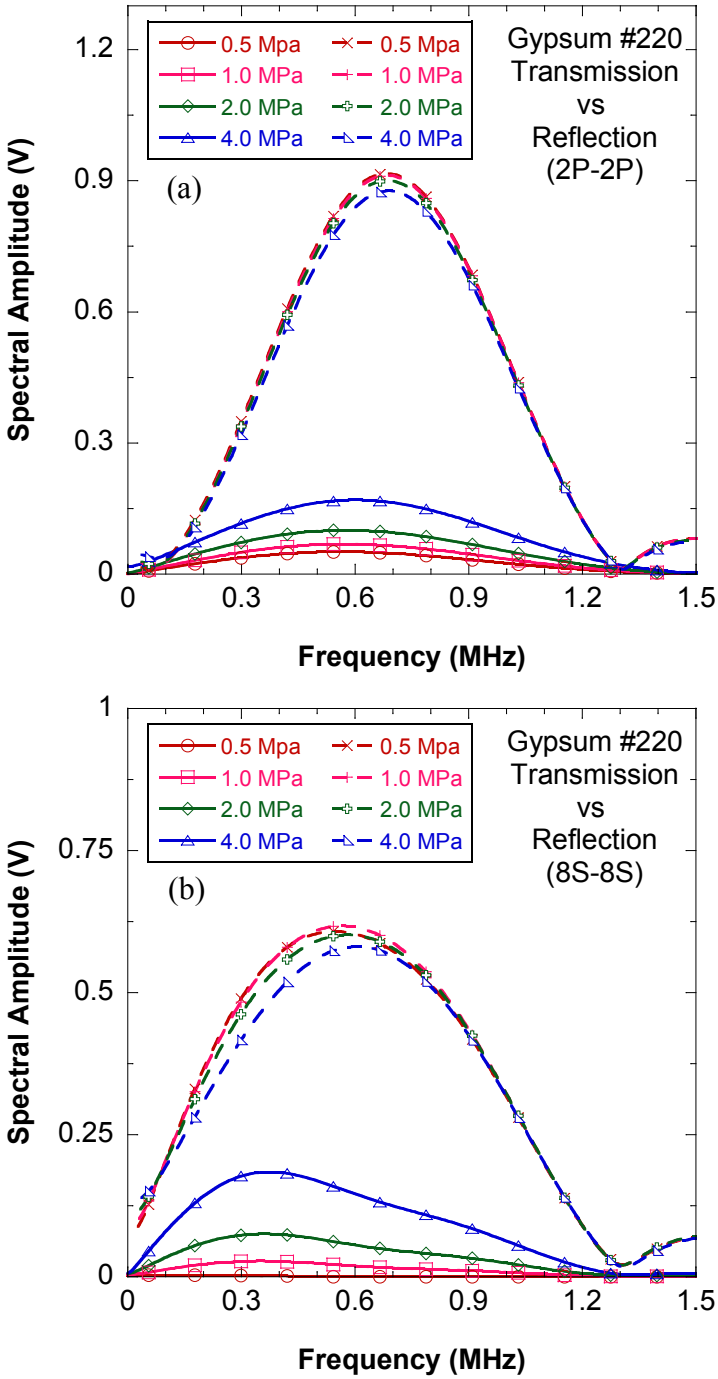

Figure 3.4.3-5. Comparison of spectral amplitudes between the transmitted (solid lines) and reflected (dotted lines) waves for: (a) transducer pairs 2P-2P; and (b) 8S-8S for the gypsum #220 specimen and for the 0° loading path.

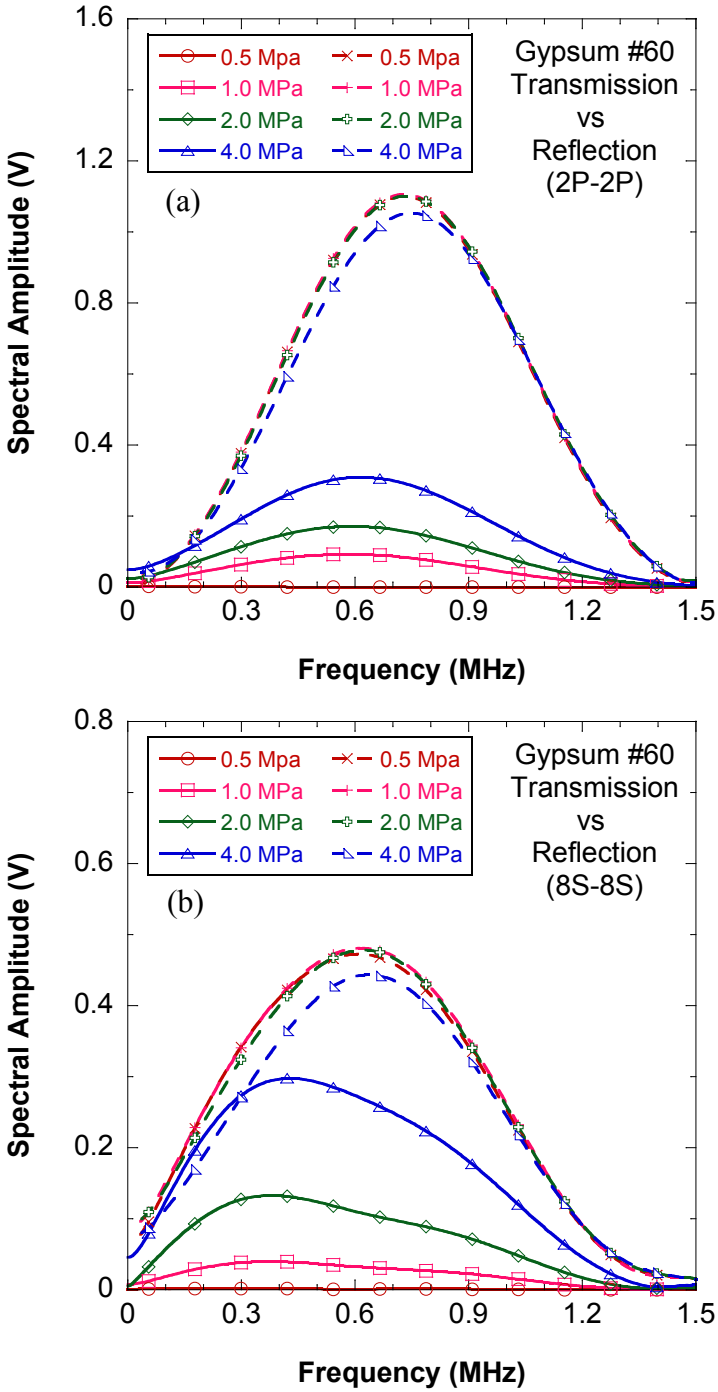

Figure 3.4.3-6. Comparison of spectral amplitudes between the transmitted (solid lines) and reflected (dotted lines) waves for: (a) transducer pairs 2P-2P; and (b) 8S-8S for the gypsum #60 specimen and for the 0° loading path.

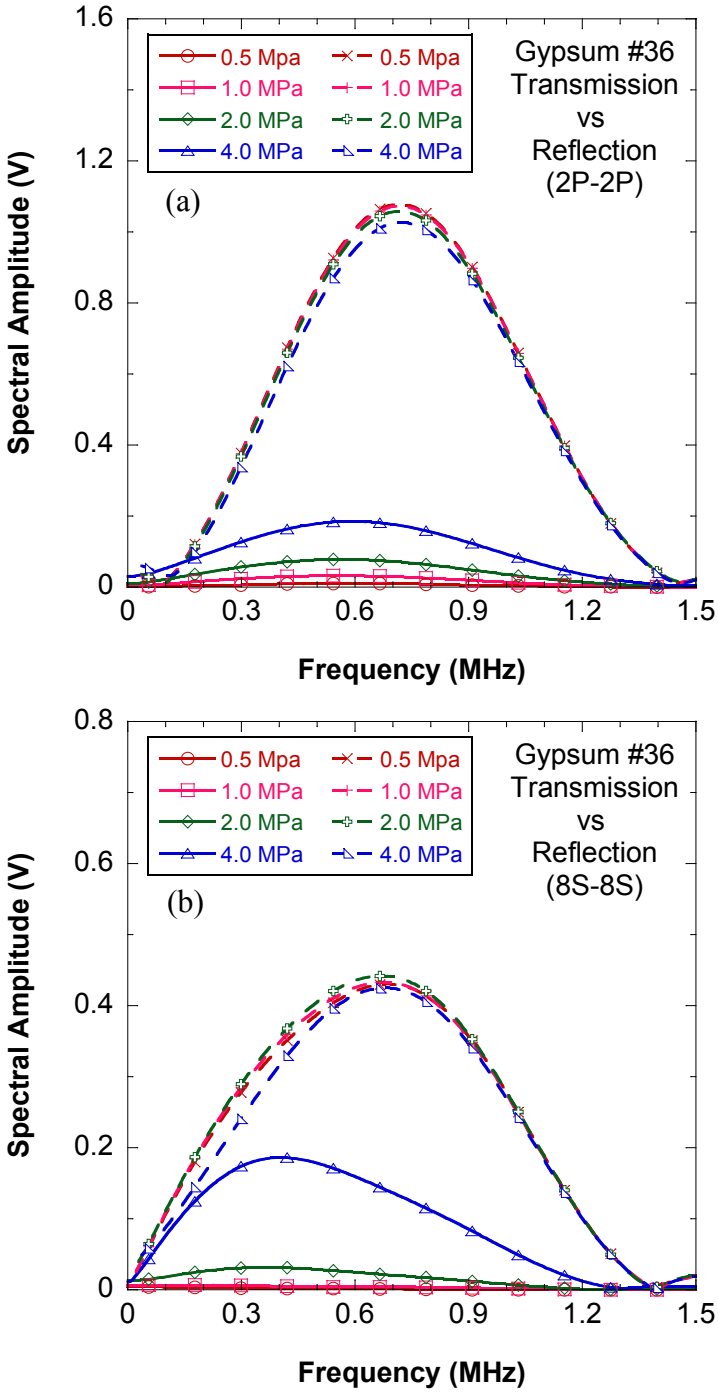

Figure 3.4.3-7. Comparison of spectral amplitudes between the transmitted (solid lines) and reflected (dotted lines) waves for: (a) transducer pairs 2P-2P; and (b) 8S-8S for the gypsum #36 specimen and for the 0° loading path.

3.4.4 Stiffness Ratio

Given the spectral amplitudes obtained from the Fast Fourier Transforms (FFT), equations (2.2.4-2) and/or (2.2.4-3) were used to determine the fracture specific stiffness. Once the shear fracture specific stiffness was estimated from the five shear wave transducers (1S, 3S, 7S, 8S, and 9S) and the normal fracture specific stiffness from the four compressional wave transducers (2P, 4P, 5P and 6P), the fracture specific stiffnesses were averaged to estimate the ratio of shear to normal fracture specific stiffness.

3.4.4.1 Non-Mated Fractures

Figure 3.4.4-1 contains the stiffness ratio of the non-mated fractures as a function of stress, for the lucite PL and SB specimens. The figure shows that the loading paths from 0° to 30° did not change the ratio of shear to normal fracture specific stiffness. The stiffness ratio approached an asymptote close to the theoretical ratio 0.46 estimated from equation (3.2.2-2). The lucite PL specimen approached the theoretical ratio by decreasing from an initial ratio of 1.3 at 0 stress to 0.7 at a normal stress of 0.5 MPa. In contrast, for the lucite SB specimen, the stiffness ratio gradually increased from a value of 0.3 at a normal stress of 0.5 MPa to the theoretical value. The result indicates that, as the normal stress increased, the magnitude of the transmission coefficient of the compressional and the shear waves became equal.

An interesting note is that the stiffness ratios of the two non-mated fractures were different at normal stresses 0-1.0 MPa. Note that the fracture surfaces of the lucite PL and SB had different surface roughness, obtained by polishing and sand-blasting. Based on

the limited number of test results, fracture roughness is an important factor in the determination of the ratio of shear to normal fracture specific stiffness at low normal stresses.

3.4.4.2 Well-Mated Fractures

The stiffness ratio of the well-mated gypsum specimens is shown in Figure 3.4.4-2 as a function of normal stress. Figure 3.4.4-2 (a) includes the data for gypsum Flat and #220, and Figures 3.4.4.-2 (b) for gypsum #60 specimens, 3.4.4.-2 (c) for gypsum #36, and 3.4.4.-2 (d) for gypsum GS01R.

For gypsum Flat and #220 specimens, the stiffness ratio behaved in a manner similar to the non-mated fracture specimens lucite PL and SB. For the gypsum Flat specimen, the stiffness ratio decreased from 0.9-1.5 values to 0.55-0.67, while for the gypsum #220 specimen the stiffness ratio gradually increased with normal stress from around 0.4 to 0.59-0.71. The major difference between the gypsum Flat and gypsum #220 and the lucite PL and SB specimens is that the stiffness ratios from gypsum exhibited shear stress dependency. For example, the stiffness ratio of the gypsum #220 specimen increased from 0.59 to 0.71 over the normal stress range 3-4 MPa.

Figures 3.4.4-2 (b) to (d) contain the change of stiffness ratio for the gypsum #60, #36 and GS01R specimens. The stiffness ratio of gypsum #60 and #36 specimens, with normal compression only (0° loading path), was stress-dependent and increased with increasing normal stress. It is hard to determine if the stiffness ratio for the 0° loading path reached a plateau within the range of applied normal stress, 0-4.0 MPa. However,

the stiffness ratio for GS01R, also for the 0° loading path, was almost stress-independent. The stiffness ratio for the three specimens, and for the 15°-40° loading path, was almost stress-independent when the normal stress was greater than 1.5 MPa (Figure 3.4.4-2 (b), (c), and (d)). The gypsum #60 had stiffness ratios of 0.72±0.02 for the 15° loading path, 0.94±0.01 for the 30°, and 1.03±0.03 for the 40° loading path, for normal stresses larger than 1.5 MPa. Similar observations were found for the gypsum #36 and GS01R specimens for the same range of normal stresses. The stiffness ratios obtained from the gypsum #36 specimen were 0.59±0.13 for the 0° loading path, 0.83±0.03 for the 15°, 1.07±0.05 for the 30°, and 1.24±0.07 for the 40° loading path. The GS01R specimen had stiffness ratios of 1.02±0.08, 1.23±0.03, and 1.37±0.06 for the 15°, 30°, and 40° loading paths.

3.4.4.3 Discussion

The stiffness ratio of the non-mated and the well-mated fractures from lucite SB and gypsum #220 is examined first. These specimens had comparable mean asperity sizes and standard deviation (Figure 3.3.4-2 (a) and Table 3.3.4-2). The overall variation of the stiffness ratio of the non-mated and mated fractures with normal stress was approximately the same in the two tests. However, the stiffness ratio of the mated fractures depended on the applied shear stress, in contrast to the behavior of the non-mated fractures. The stiffness ratio of the gypsum #220 specimen increased from 0.59 to 0.71 for normal stresses greater than 3 MPa with increasing shear stress, while the lucite SB specimen had the same stiffness ratio with shear stress (see Figure 3.4.4-1 and 3.4.4-2

(a)). This comparison indicates that the type of surface, i.e. well-mated or not-mated, has an important effect on the stiffness ratio, even if the asperity size and distribution are the same in both surfaces.

Figure 3.4.4-3 shows shear fracture specific stiffness obtained from gypsum #60. The shear specific stiffness with normal compression only (0° loading path) was stress-dependent and increased with increasing normal stress. Compared to the 0° loading path, shear specific stiffness increased with increasing shear stress (from 15°-40° loading). The dependency of shear specific stiffness on shear stress was observed from all of well-mated fractures. The results for well-mated fractures is consistent with the study of Pyrak-Nolte et al. (1996), which showed that the shear specific stiffness increased with increasing shear stress (see Figure 2.3.2-2 in section 2.3.2).

The sensitivity of well-mated fractures to the applied shear stress is shown in Figure 3.4.4-4. The figure shows the averaged stiffness ratios obtained from gypsum Flat, #220, #60, #36, and GS01R for the loading paths 0°, 15°, 30°, and 40°. The average was obtained from data for normal stresses greater than 1.5 MPa. As one can see in the figure, the stiffness ratio depends on shear stress and the dependency increases as the fracture roughness increases. For example, for the gypsum #36 specimen, the stiffness ratio increased from 0.59±0.13 to 1.24±0.07 with increasing shear stress (from 0°-40° loading path). As the mean asperity size of the fracture increased from 62-70 μm (gypsum Flat) to 2,680-2,870μm (GS01R), the stiffness ratio from the 30° loading path increased from 0.70±0.02 to 1.23±0.03. The sensitivity of the stiffness ratio to the shear stress is an important observation for well-mated fracture specimens, since it suggests that the stiffness ratio depends on the stress path imposed to the fracture.

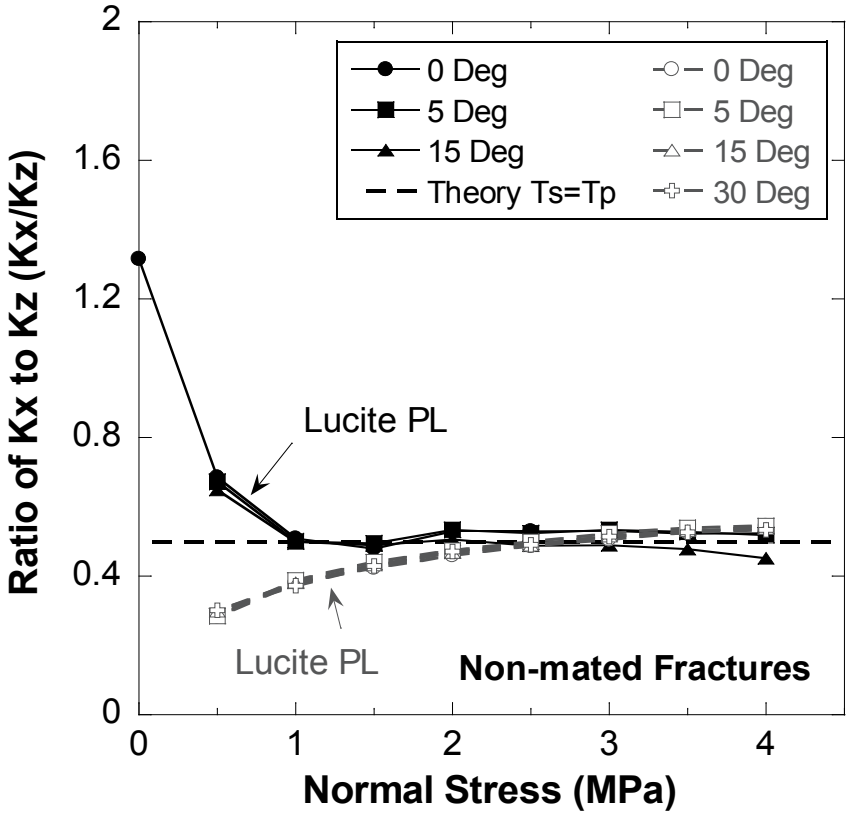

Figure 3.4.4-1. Ratio of shear to normal fracture specific stiffness from lucite PL (solid lines) and lucite SB (dashed lines) specimens. Loading paths are defined in Figure 3.3.3-1 (a).

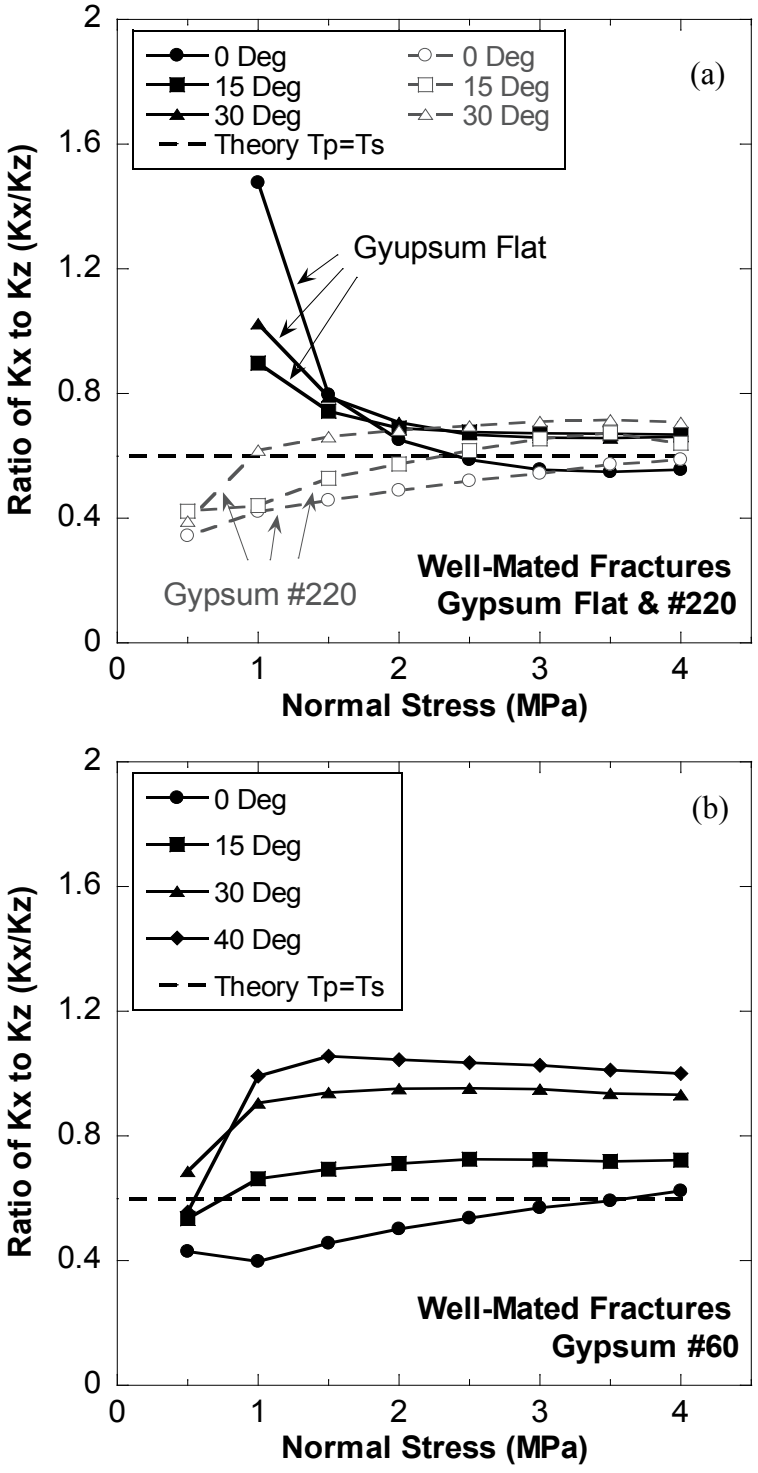

Figure 3.4.4-2. Ratio of shear to normal fracture specific stiffness from: (a) gypsum Flat (solid lines) and #220 specimens (dashed lines); (b) #60 specimen; (c) #36 specimen; and (d) GS01R specimen. Loading paths are defined in Figure 3.3.3-1 (a) (continued).

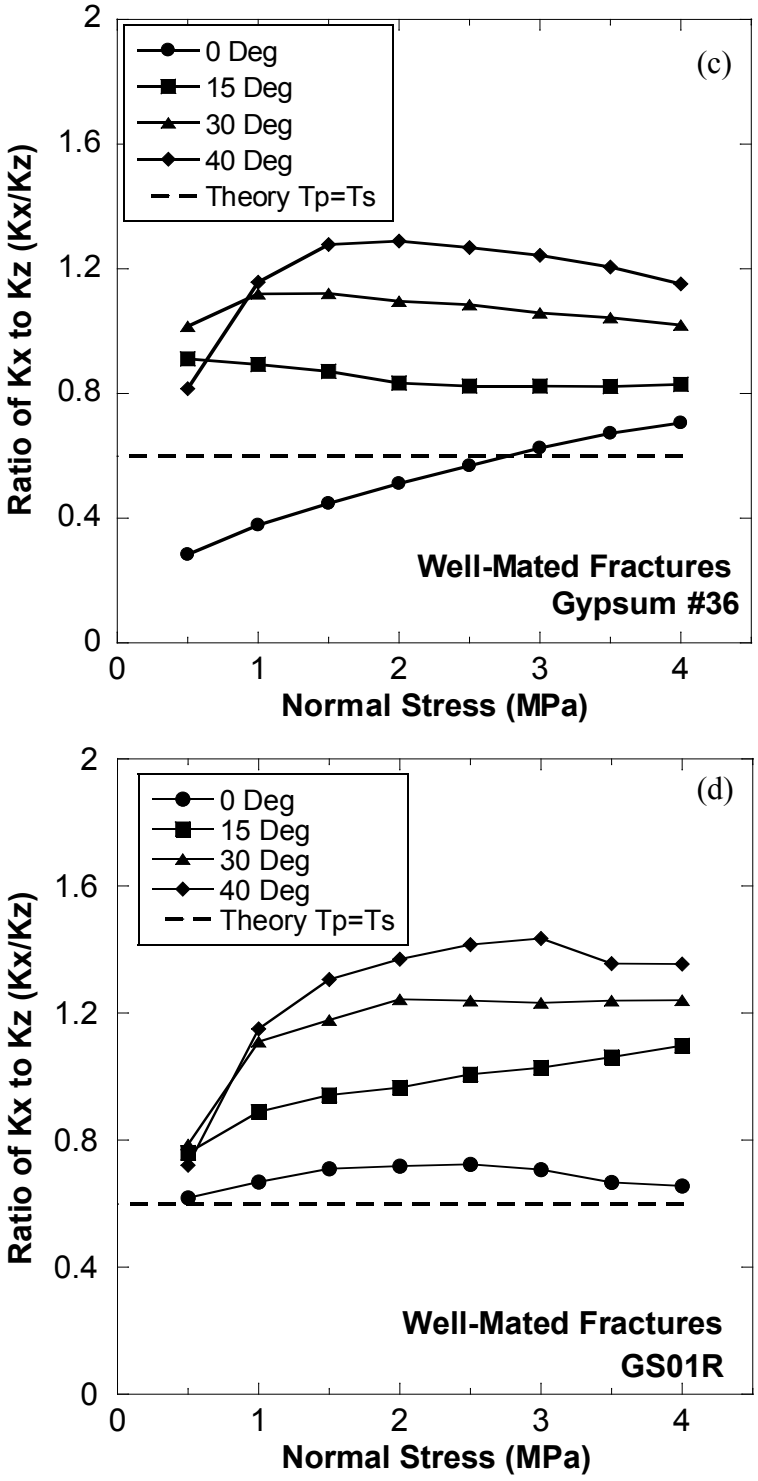

Figure 3.4.4-2 Ratio of shear to normal fracture specific stiffness from: (a) gypsum Flat (solid lines) and #220 specimens (dashed lines); (b) #60 specimen; (c) #36 specimen; and (d) GS01R specimen. Loading paths are defined in Figure 3.3.3-1 (a).

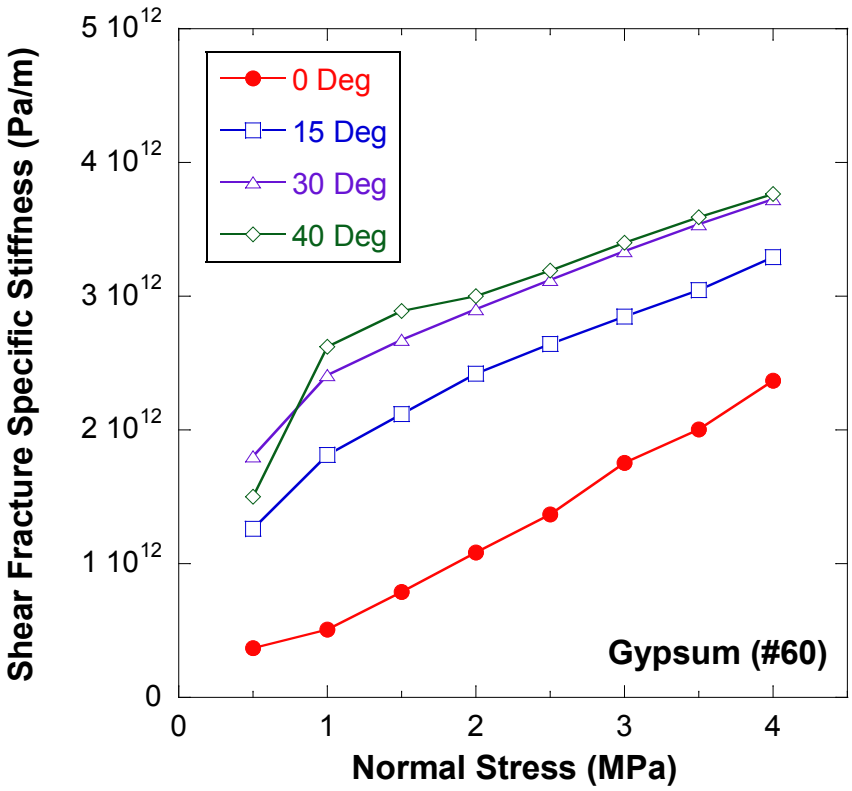

Figure 3.4.4-3. Shear fracture specific stiffness for gypsum #60 specimen as a function of loading path, as defined in Figure 3.3.3-1 (a).

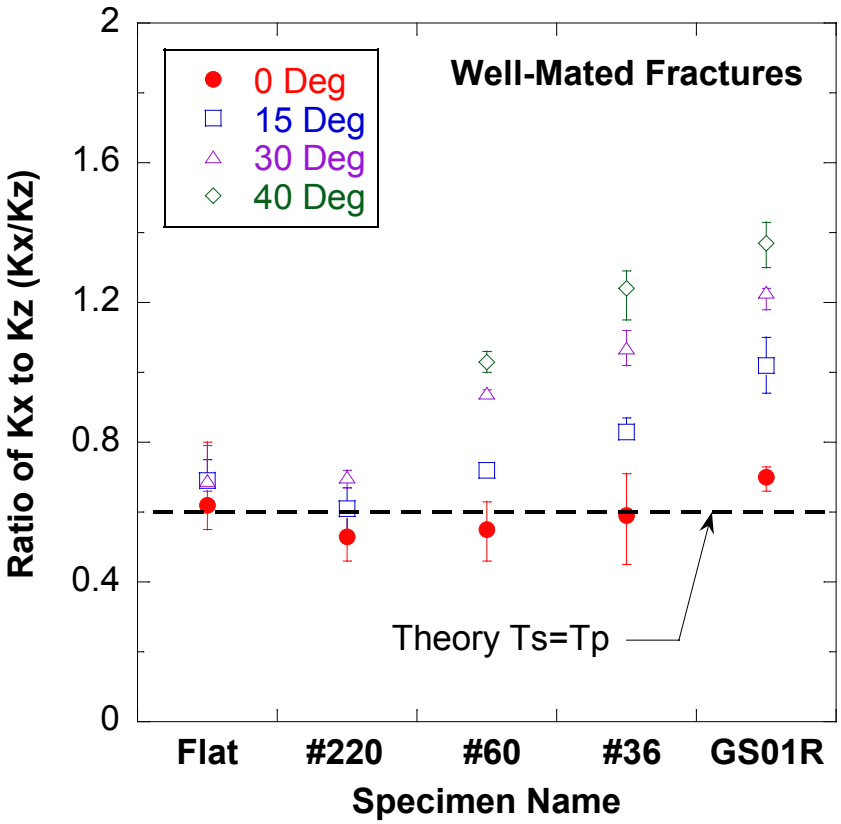

Figure 3.4.4-4. Stiffness ratio averaged over the range of normal stress between 1.5 and 4.0 MPa for the well-mated fracture specimens, as a function of loading path.

3.4.5 Variation of Stiffness Ratio during Shearing

The second stage tests were performed to study the stiffness ratio prior to and during shear failure. In these tests, a specimen was normally compressed first and then sheared at a constant displacement rate until final slip occurred. A normal stress of 4 MPa was applied to the specimens and was held constant during the test. The seismic imaging system constantly monitored the fracture by measuring transmitted and reflected waves through the specimen, as was done in the first stage tests.

3.4.5.1 Mechanical Behavior

In general, the shear displacement - shear stress curve can be divided into three regimes: initial seating, linear, and non-linear regime. The initial seating is the deformation that occurs during load transfer from the loading frame to the specimen. After the seating deformation, a linear increase in shear stress with increasing displacement follows, indicating that the load frame fully transferred the load to the specimen. This linear portion of the stress-displacement curve is usually regarded as elastic. The displacements that occur in this elastic regime are recoverable. The linear portion holds almost up to the peak shear stress, or shear strength of the fracture, after which degradation of the shear strength begins and exhibits a non-linear stress-displacement relation. During this stage, the two fracture surfaces in contact must override each other's asperities and/or the asperities on the fracture surface begin to shear off, causing dilation and degradation of the fracture roughness. In the non-linear regime, non-recoverable plastic deformation occurs (Jaeger et al. (2007)).

Figure 3.4.5-1 contains a graph of shear displacement versus shear stress for the specimens with a well-mated fracture, i.e., gypsum Flat, #220, #60, and #36, all for a normal stress of 4.0 MPa. The displacements shown in Figure 3.4.5-1 were corrected by setting the initial seating deformations to zero displacement. The maximum peak friction angles were, for gypsum #36 $\phi_{peak} > 55°$, for gypsum #60 $\phi_{peak} = 48°$, for gypsum Flat $\phi_{peak} = 39°$, and for gypsum #220 $\phi_{peak} = 36°$, respectively. The displacements at peak shear strength, d_{peak}, are indicated by the downward arrows in Figure 3.4.5-1. As seen in the Figure, while the gypsum #220 and #60 specimens showed a reduction in shear strength, the gypsum Flat did not. For the gypsum #36 specimen, shear failure was not fully induced because the shear load applied to the specimen reached the maximum limit of the loading frame.

3.4.5.2 Shear Strength and Surface Roughness

To characterize shear strength with surface roughness, the concept of 'micro-slope angle' suggested by Park and Song (2013) was adopted. The micro-slope angle θ is defined as the angle, measured in the direction of shear, between the dip β of the slope neighboring asperities and the right angle 90°, i.e., $\theta = \pm(90° - \beta)$. A positive value indicates an upward slope, and a negative sign, a downwards slope (along the direction of shear, as mentioned). Park and Song found that, at the peak shear strength, the areas with positive micro-slope angles composed most of the contact areas. After the peak strength, the areas with the greatest magnitude of positive micro-slope angles remained in contact. They concluded that the contact area during shearing was closely related to the spatial

distribution of the micro-slope angle, and that the more areas with high micro-slope angles, the larger the peak shear strength.

From the surface roughness measurements described in section 3.3.4, the micro-slope angle between neighboring asperities was calculated. Figure 3.4.5-2 shows the spatial distribution of the micro-slope angles for: (a) gypsum Flat; (b) #220; (c) #60: and (d) #36 specimens. The blue and red colors indicate areas with relatively low and high micro-slope angles, respectively. The histograms of the micro-slope angles are included in Figure 3.4.5-3.

The shear strength of the gypsum Flat, #220, #60, and #36 specimens shown in Figure 3.4.5-1 confirmed the conclusion of Park and Song's study (2013) in that the more the areas with high micro-slope angle, the greater the shear strength. For the gypsum Flat and #220 specimens, most of the micro-slope angles ranged between ±5°, as seen in Figure 3.4.5-3. This observation is in agreement with the observation of similar peak shear strength between gypsum Flat and #220 specimens, which had peak friction angles of 39° and 36°, respectively. The gypsum Flat specimen had a higher peak friction angle than the gypsum #220 specimen because the waviness of the fracture surface provided additional strength. The gypsum #36 specimen had more areas with high micro-slope angles than the gypsum #60 specimen, as shown in Figures 3.4.5-2 (c) and (d). Most of micro-slope angles in the gypsum #60 specimen were between ±20°, while for the gypsum #36 specimen, the micro-slope angles were between ±30°, as seen in Figure 3.4.5-3. This is in agreement with the higher peak friction angle for the gypsum #36 specimen.

3.4.5.3 Stiffness Ratio during Shearing

Figure 3.4.5-4 shows the variation of: (a) shear and (b) normal fracture specific stiffness during shearing, as well as the shear stress-displacement curves. The shear and normal fracture specific stiffness shown in Figure 3.4.5-4 are the average of corresponding data. The downward arrows indicate $d_{elastic}$, the displacement at the end of the linear portion of the stress-displacement curve. For the gypsum #220, #60, and #36 specimens, the maximum values of the shear fracture specific stiffness were obtained at (gypsum #220) or before (gypsum #60 and #36) the $d_{elastic}$ for each specimen; the values then decreased with further shear displacement. However, the gypsum Flat specimen had the maximum shear specific stiffness after $d_{elastic}$.

Figure 3.4.5-5 shows the ratio of shear to normal fracture specific stiffness during shearing and the corresponding shear stress-displacement response. The downward and upward arrows indicate $d_{elastic}$ and $d_{max,kx/kz}$, respectively, that denote the displacement at the end of the linear portion of the stress-displacement response and at the maximum stiffness ratio. Table 3.4.5-1 lists the mean asperity size, maximum stiffness ratio, d_{peak}, $d_{elastic}$, $d_{max,kx/kz}$, from tests.

Prior to the application of shear (at -1.0 mm displacement in Figure 3.4.5-5), the stiffness ratios of the gypsum Flat, #220, #60, and #36 specimens ranged from 0.46 to 0.60, close to the theoretical value of 0.6 given by equation (3.2.2-2). In all the tests, as the shear load increased, the stiffness ratio gradually increased until a maximum. The maximum, in most tests was attained during the linear or elastic regime. The only exception was the gypsum Flat specimen, where the maximum ratio 0.82 was obtained at a displacement of 0.92 mm, i.e., the maximum κ_x/κ_z =0.82 occurred at $d_{max,\ kx/kz}$ = 0.92 mm, much larger

than $d_{elastic}$ = 0.42 mm. For the rest of the tests, the results are as follows: the gypsum #220 specimen attained a maximum ratio of 0.75, from an initial ratio of 0.6, at $d_{max, kx/kz}$ = 0.43 mm, which coincided with $d_{elastic}$ = 0.43 mm; the gypsum #60 specimen reached a maximum stiffness ratio of 1.13, from an initial value of 0.46, at $d_{max, kx/kz}$ = 0.29 mm, a displacement smaller than $d_{elastic}$ = 0.38 mm; the gypsum #60 specimen had a maximum ratio of 1.20, from the initial value of 0.56, at $d_{max, kx/kz}$ = 0.33 mm, well within the elastic regime ($d_{elastic}$ = 0.56 mm).

3.4.5.4 Discussion

Figure 3.4.5-6 shows the normalized: (a) shear and (b) normal fracture specific stiffness during shearing for the gypsum Flat, #220, #60, and #36 specimens, as well as the corresponding shear stress-displacement response. The stiffness was normalized with respect to its value prior to shear. As observed in the Figure, the shear fracture specific stiffness changed with shear much more than the normal fracture specific stiffness and its dependency on shear is similar to that obtained for the stiffness ratio (see Figure 3.4.5-5). This suggests that the stiffness ratio during shear strongly depends on the shear stiffness.

Table 3.4.5-1 includes the difference between $d_{elastic}$ and $d_{max, kx/kz}$, i.e. $d_{max, kx/kz} - d_{elastic}$, for all tests. The positive sign of $d_{max, kx/kz} - d_{elastic}$ means that the maximum stiffness ratio was found in the plastic regime, and a negative sign during the elastic regime. The smaller $d_{max, kx/kz} - d_{elastic}$ is, the earlier the maximum stiffness ratio was observed. As the fracture roughness increased from gypsum Flat to gypsum #36, the maximum stiffness ratio occurred earlier, as testified by inspection of $d_{max, kx/kz} - d_{elastic}$, that decreased from

0.50 mm from the gypsum Flat specimen to -0.23 mm for the gypsum #36 specimen. Similar experimental observations were made by Hedayat et al. (2012). In their experiments, the amplitude of the shear waves increased as the shear load increased and reached a maximum prior to the peak shear strength. They regarded the change in the amplitude as 'precursors' to failure, which were detected closer to failure for fractures with a smooth surface (i.e. low friction angle) than with a rough surface (i.e. high friction).

As discussed in section 3.4.4-3, shear fracture specific stiffness for well-mated fractures was sensitive to the application of shear stress. The increase of shear specific stiffness with increasing shear stress was interpreted as the increase of contact area sensitive to shear specific stiffness (Pyrak-Nolte et al. (1996)). Hence, the decrease of the shear specific stiffness may indicate irrecoverable changes or damage to the frictional characteristics of the fracture. As the fracture surface roughness increased, the decrease in shear specific stiffness was found earlier. It indicates that the displacement required to induce irrecoverable damage to a frictional surface decreases with increase of surface roughness. Finally, the stiffness ratio may provide a measure for detecting degradation of the frictional strength of a fracture because the shear specific stiffness dominates the stiffness ratio, at least when shearing at a constant normal stress.

Table 3.4.5-1. Summary of shear experiments.

Specimen	Mean Asperity (μm)	Max. Stiffness Ratio	$d^{**}_{max, kx/kz}$ (mm)	$d^{+}_{elastic}$ (mm)	d^{++}_{peak} (mm)	$d_{max\text{-}kx/kz} - d_{elastic}$ (mm)
Gypsum Flat	59-70	0.82	0.92	0.42	0.90	0.50
Gypsum #220	62-70	0.75	0.43	0.43	0.84	0.0
Gypsum #60	265-267	1.13	0.29	0.38	0.46	- 0.09
Gypsum #36*	335-537	1.20	0.33	0.56	0.56	- 0.23

* Not fully induced shear failure.
** Shear displacement at maximum stiffness ratio
+ Shear displacement at the end of the linear portion of stress-displacement plot
++ Shear displacement at peak shear strength

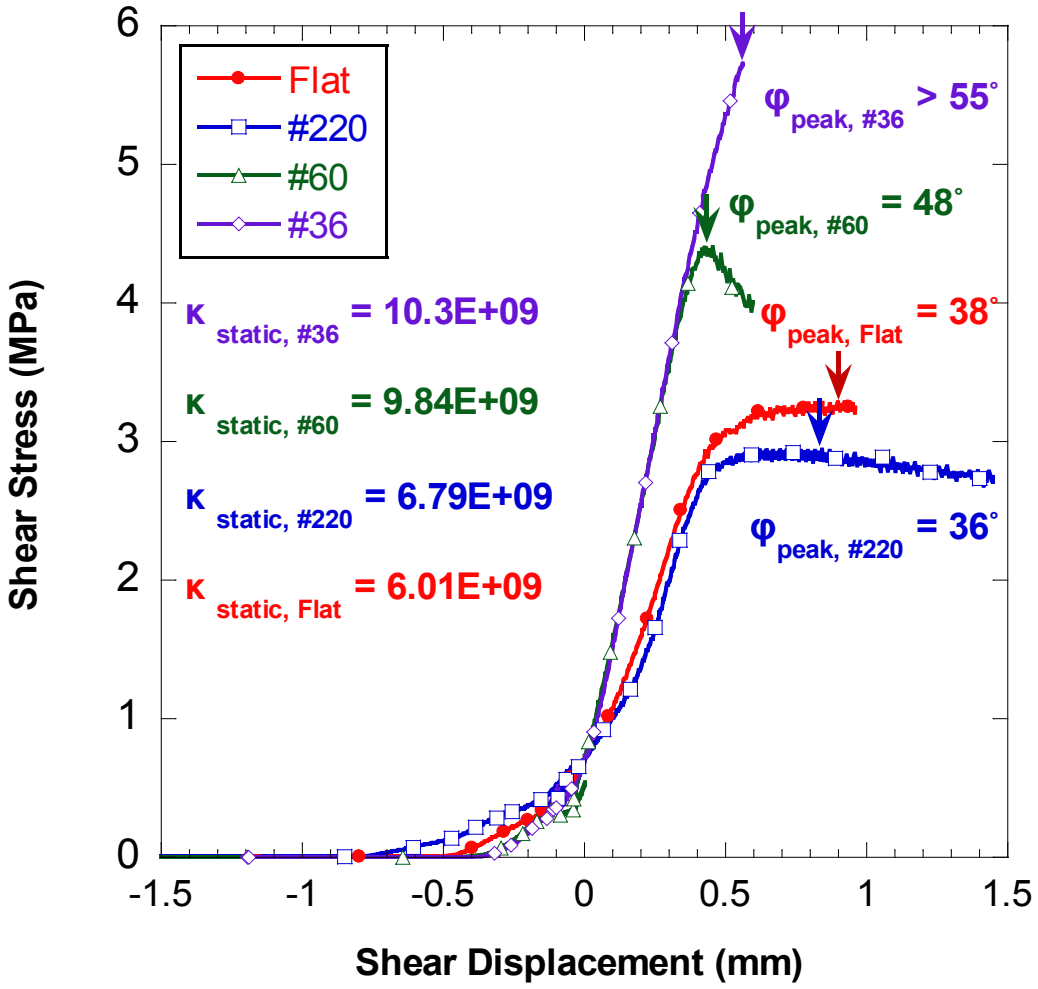

Figure 3.4.5-1. Shear displacement versus shear stress for σ_n = 4.0 MPa. Downward arrows indicate the displacement at peak shear strength, d_{peak}.

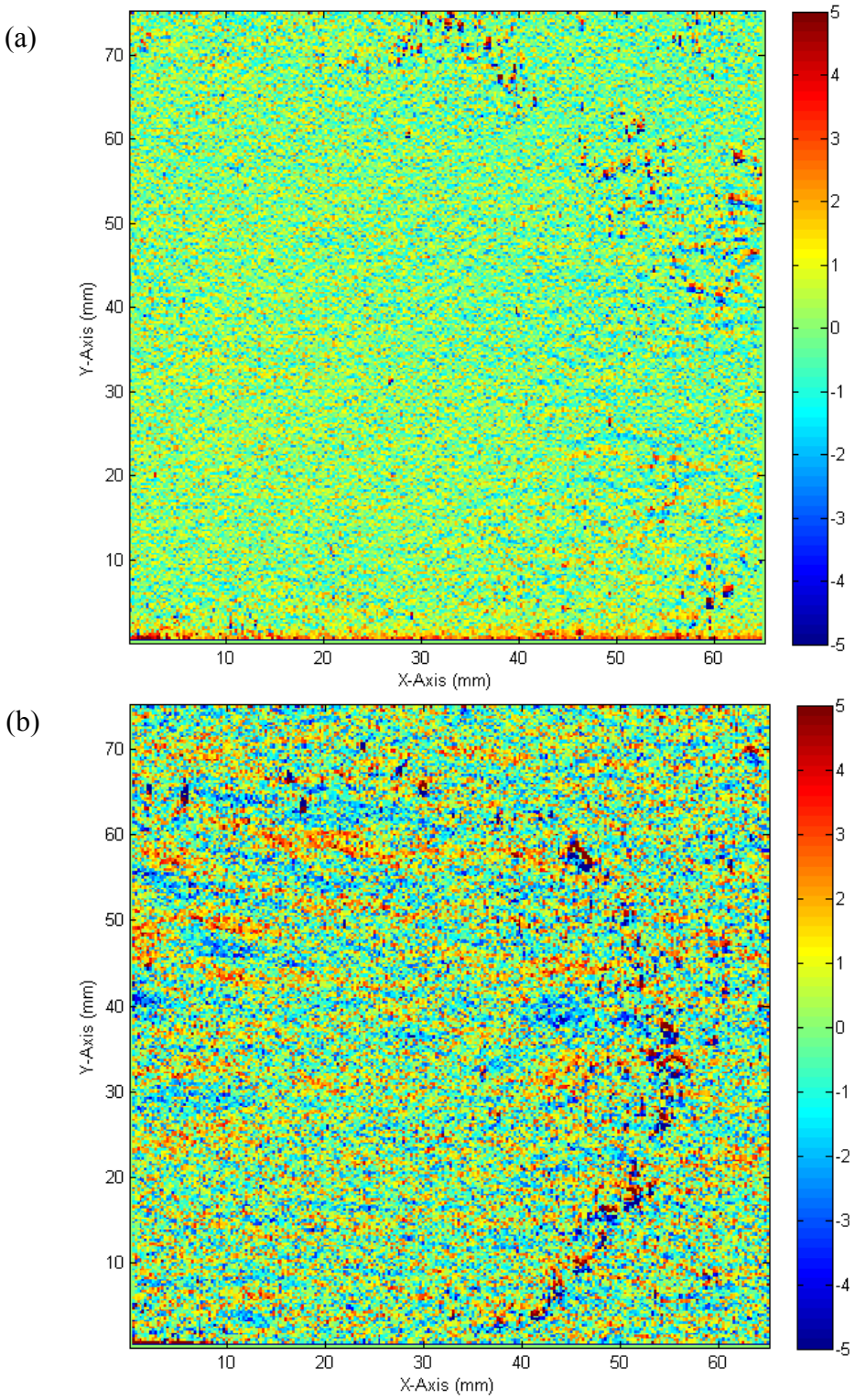

Figure 3.4.5-2. Spatial distribution of micro-slope angles for: (a) gypsum Flat; (b) #220; (c) #60; and (d) #36 specimens. The color bar represents the magnitude of the micro-slope angle in degrees (continued).

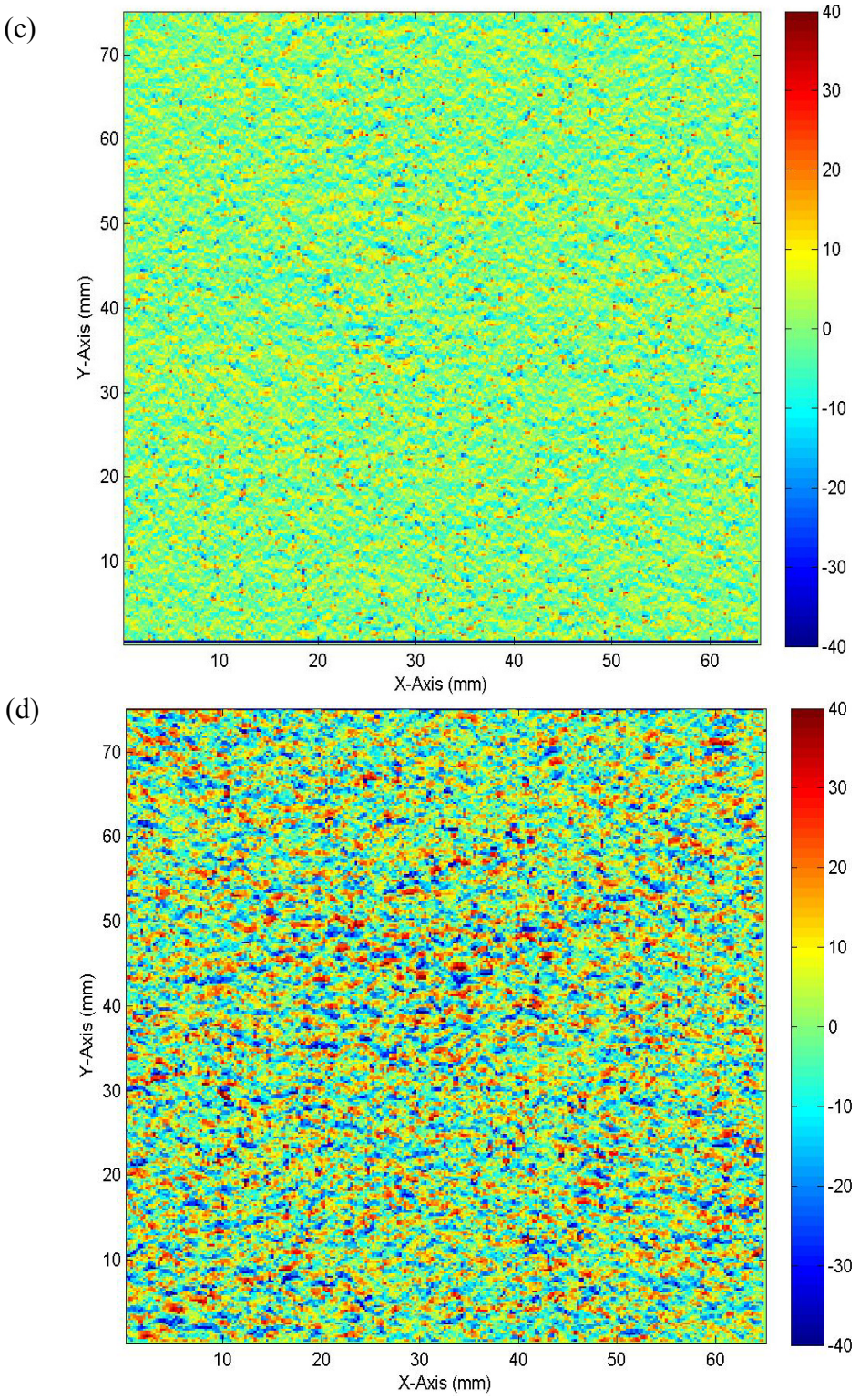

Figure 3.4.5-2. Spatial distribution of micro-slope angles for: (a) gypsum Flat; (b) #220; (c) #60; and (d) #36 specimens. The color bar represents the magnitude of the micro-slope angle in degrees.

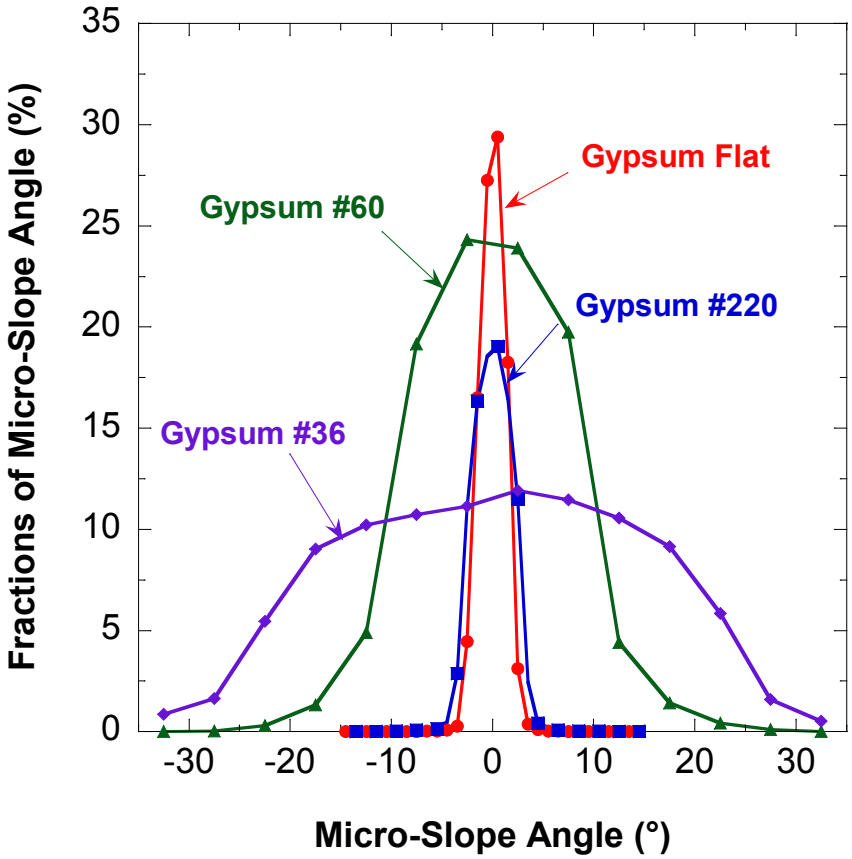

Figure 3.4.5-3. Distribution of micro-slope angle for gypsum Flat, #220, #60, and #36 specimens.

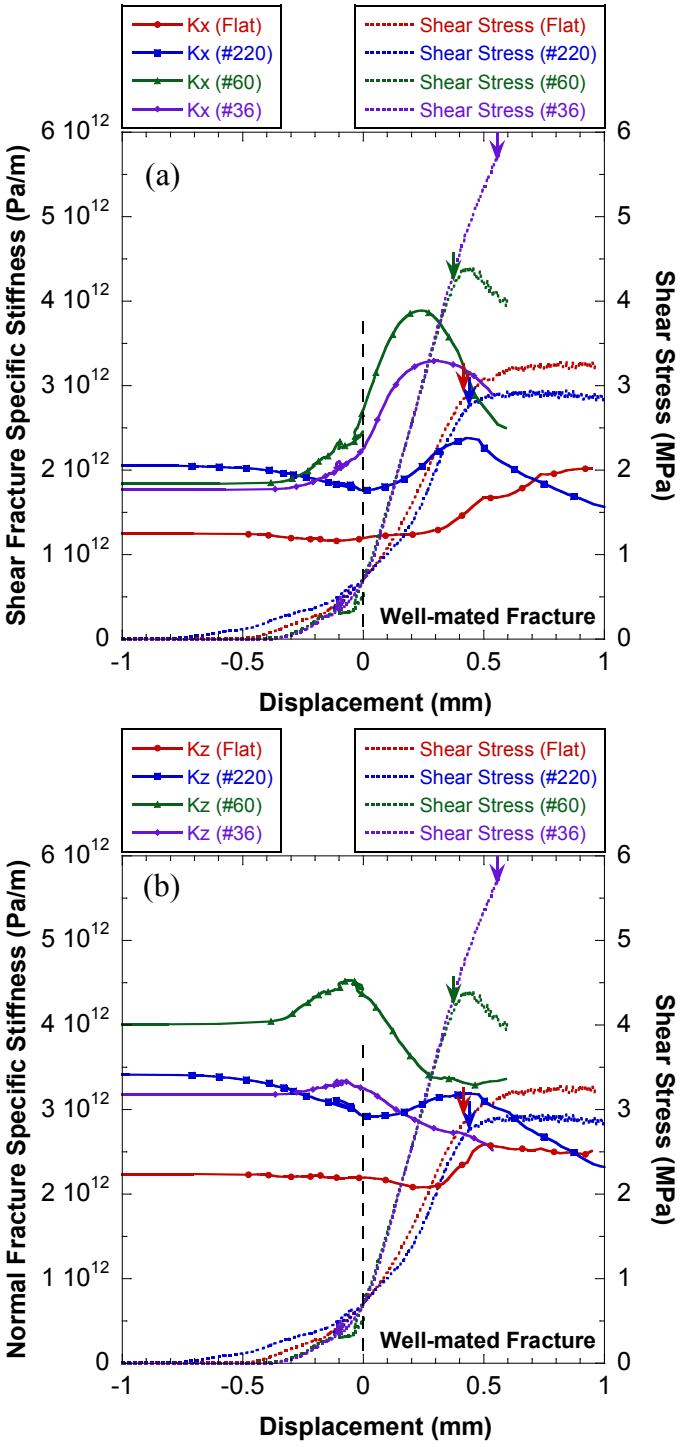

Figure 3.4.5-4. (a) Shear and (b) normal fracture specific stiffness for σ_n = 4.0 MPa for gypsum Flat, #220, #60, and #36 specimens and shear stress-displacement response. The dotted vertical line indicates initial seating deformation and downward arrows the displacement at the end of the elastic regime, $d_{elastic}$.

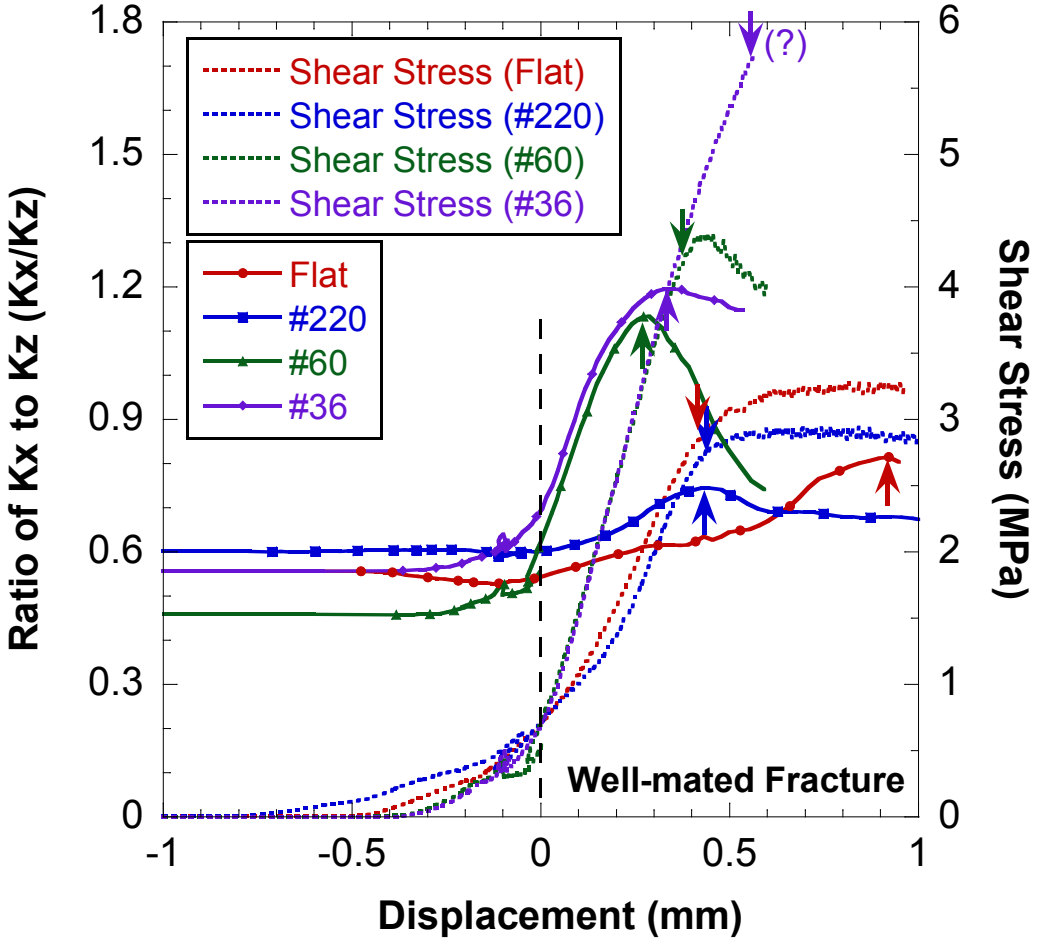

Figure 3.4.5-5. Ratio of shear to normal fracture specific stiffness during shear for gypsum Flat, #220, #60, and #36 specimens at σ_n = 4.0 MPa. The dotted vertical line indicates initial seating deformation and downward and upward arrows the displacement at the end of the elastic regime, $d_{elastic}$, and the displacement at maximum stiffness ratio, $d_{max,kx/kz}$, respectively.

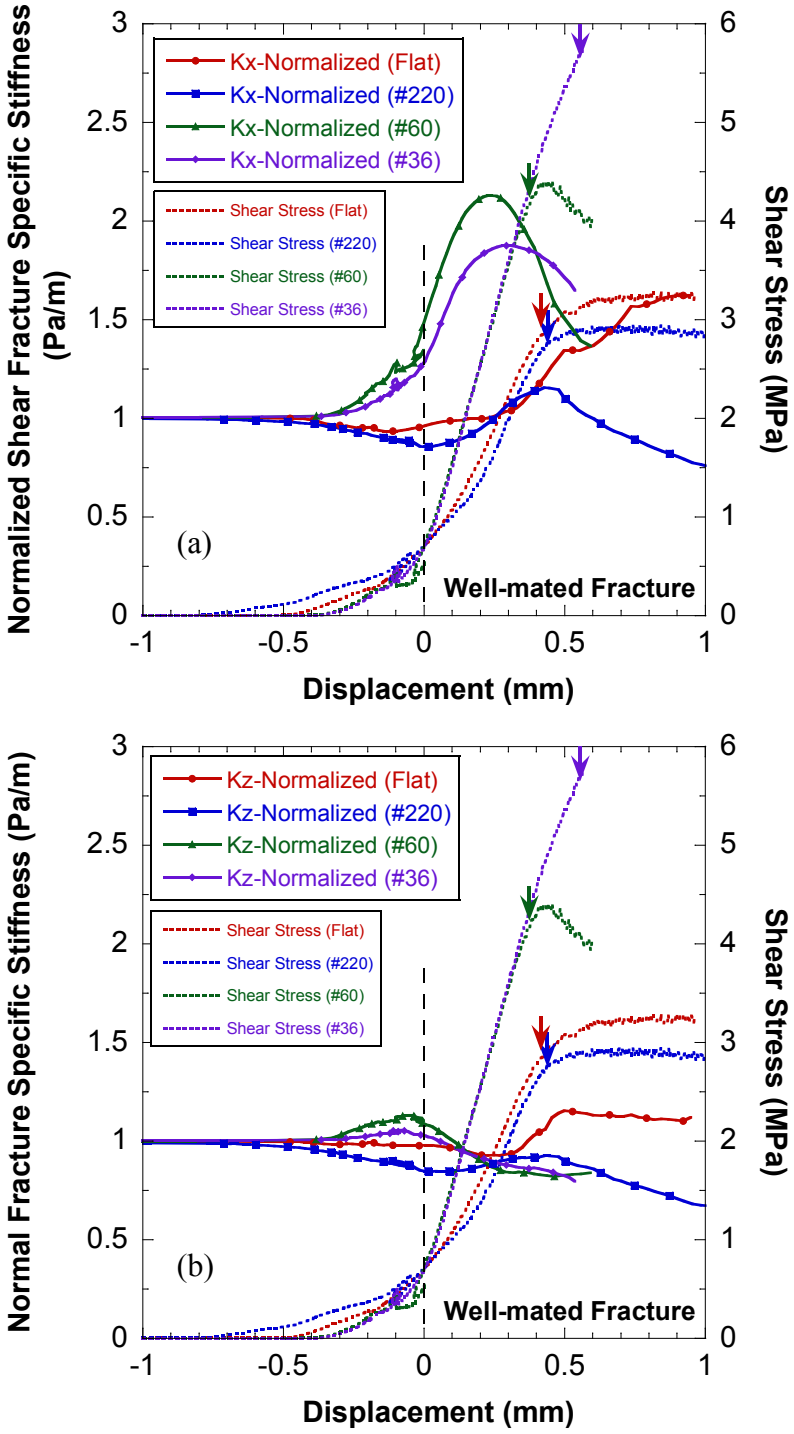

Figure 3.4.5-6. Normalized (a) shear and (b) normal fracture specific stiffness during shearing at σ_n = 4.0 MPa for the gypsum Flat, #220, #60, and #36 specimens and shear stress-displacement response. The dotted vertical line indicates initial seating deformation and downward arrows the displacement at the end of the elastic regime, $d_{elastic}$.

3.5 Summary

A series of experiments were conducted to study the change of fracture stiffness ratio with stress and for two different types of fractures: non-mated and well-mated. Specimens containing a single fracture were subjected to either only normal loading or concurrent normal and shear loading. Measurements of P- and S- waves through the specimens were used to interpret changes of fracture specific stiffness. Based on the experimental results, the following conclusions are drawn:

- The stiffness ratio for non-mated fractures was insensitive to the application of shear stress for fracture surfaces with mean asperity size ≤ 106 μm.
- For well-mated fractures, the stiffness ratio increased with increasing shear stress. A larger increase was observed as the fracture roughness increased.
- The theoretical stiffness ratio given by equation (3.2.2-2) provides a good estimate of the stiffness ratio for non-mated fractures under high normal stresses and for well-mated fractures under only normal stress.
- During shear with constant normal stress, the stiffness ratio is more dependent on the shear fracture specific stiffness than on the normal fracture specific stiffness.
- During shear, the maximum stiffness ratio was observed prior to failure for well-mated fractures with large surface roughness.

CHAPTER 4. SPATIAL DISTRIBUTION OF FRACTURE SPECIFIC STIFFNESS

4.1 Introduction

One of the goals of geophysical characterization of rock is the detection and characterization of the hydraulic and mechanical properties of fractures. Experimental data and numerical simulations have shown that fracture specific stiffness and fluid flow through a fracture are implicitly related through fracture geometry, i.e., aperture and contact area distributions (Bandis et al. (1983), Tsang and Witherspoon (1983), Brown (1987), Pyrak-Nolte et al. (1990), Pyrak-Nolte et al. (1995), Renshaw (1995), Pyrak-Nolte (1996), Pyrak-Nolte and Morris (1996), Lanaro and Stephansson (2003), Liu (2005), and Petrovitch et al. (2013)). This relation is important because fracture specific stiffness can be determined from seismic wave attenuation and velocity (Pyrak-Nolte et al. (1990)).

This Chapter includes seismic measurements performed to determine the spatial variability of fracture specific stiffness in single fractures subjected to normal and shear stress. The objectives of the tests were to: (1) characterize the spatial distribution of fracture specific stiffness; and (2) determine how the spatial distribution of fracture specific stiffness was modified by normal and shear loading.

4.2 Experimental Method

For the investigation of spatial variability of fracture specific stiffness, a series of experiments were conducted on aluminum and granite specimens. In the tests, a specimen was subjected to uniaxial loading while concurrent measurements of transmitted compressional and shear waves were made. Because the fracture was at an angle with the direction of loading, normal and shear stresses were concurrently applied. The angles, measured with the horizontal, that is measured from a direction perpendicular to the loading direction, ranged from 0˚, (i.e. horizontal fracture), to 30˚. Given the expected frictional properties of the fracture, the angles were not large enough to produce slip.

4.2.1 Sample Preparation

4.2.1.1 Granite Specimens

Nine cylinders of granite were cored from a large granite slab. The cylinders measured 150 mm (≈ 6 inches) in diameter and 100 mm (≈ 4 inches) in height. Two diametrically opposed notches were cut along the length of the cylinders 13 mm deep to help induce a single fracture. An aluminum rod with a diameter slightly larger than the width of the notch was placed in each notch. Then, a compressive load was applied to the rods to induce a single fracture in the rock. After inducing the fracture, two flat surfaces were cut on opposite sides of the cylinder to yield the desired fracture orientation relative to the direction of the load. Specimens with fracture orientations of 0˚, 15˚, and 30˚ were produced. Figure 4.2.1-1 shows the fabricated granite samples and Table 4.2.1-1 lists the specimen name and fracture orientation. The angles of the fractures with respect to the

direction of loading were not large enough to induce slip along the fracture, given the expected frictional strength of the joints. The flat surfaces of the sample were polished until they were smooth because these surfaces were in contact with the transducer array.

4.2.1.2 Aluminum Specimens

Two aluminum specimens were also fabricated to have the same external dimensions as the granite specimens. Figure 4.2.1-2 is a photograph of the fabricated aluminum specimens. The aluminum specimens included an intact sample and a sample with a 0˚ (horizontal) fracture. The aluminum specimens were used for baseline tests to compare the transducer response with granite.

Table 4.2.1-1. Granite specimens and their fracture orientation.

Specimen	Fracture Orientation
GS01 / GS04	0°
GS02 / GS05	30°
GS03 / GS06	15°
GS07 / GS08 / GS09	Intact sample

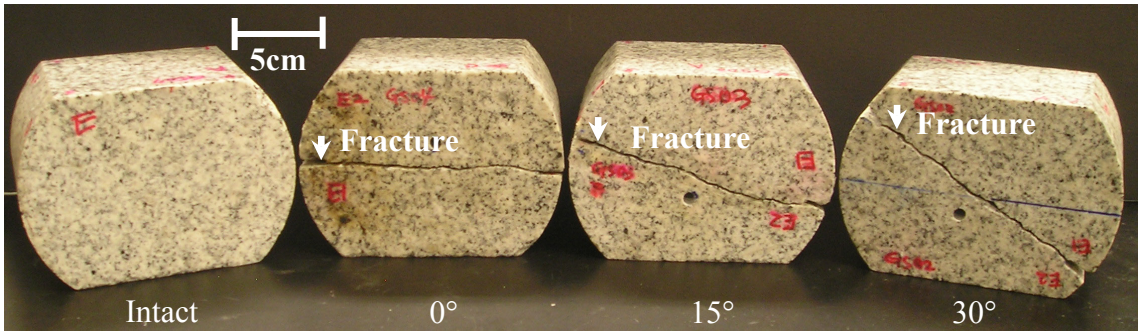

Figure 4.2.1-1. Fabricated granite specimens; intact and fractured specimens with 0˚, 15^{o} and 30˚ angles, measured from the horizontal.

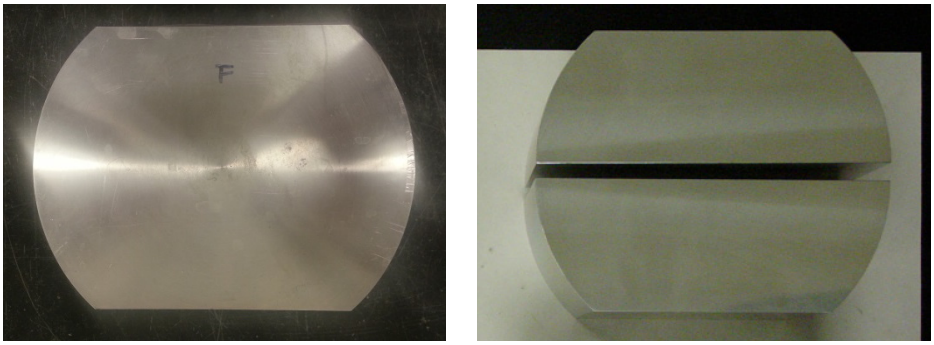

Figure 4.2.1-2. Fabricated aluminum specimens; intact (left) and fractured specimen (right) with an angle of 0˚ (perpendicular to loading).

4.2.2 Experimental Procedure

The procedure for seismic array set-up and data acquisition was standardized to ensure test repeatability. The experimental procedure used for the granite and aluminum specimens was similar to the procedure used for the lucite and gypsum specimens described in section 3.3.3.

The same seismic imaging system described in section 3.3.2 was used to acquire seismic data and the same types of compressional (P-) and shear (S-) wave transducers were also used. The transducers were excited with 400V square waves with a repetition rate of 5 kHz. Figure 4.2.2-1 shows the transducer layout with the polarization direction of the S-wave transducers indicated by the direction of an elongated box. Seven transducers pairs, i.e. seven sources and seven receivers, were used to monitor the seismic response of a fracture during compression loading. Three shear (1S, 2S, and 5S) wave transducers were polarized in the direction of shear and two (4S and 7S) were polarized perpendicular to the direction of shear. Two different polarizations for the shear wave transducers were used to determine if the test specimen exhibited shear wave anisotropy. The data from the S- wave transducers were used to obtain the shear fracture specific stiffness, while the data from the two P-wave transducers (3P and 6P) were used to monitor changes in normal fracture specific stiffness.

Before mounting a specimen on the loading frame, the flat surfaces (located at top and bottom of the specimen) were covered with a thin plastic film and then coupled with the seismic transducers with oven-dried honey. The plastic film prevented penetration of the honey couplant into the pores of the specimen. The specimen was then placed under a 222 kN load to allow the couplant to equilibrate. Transmitted signals were recorded

during 20 hours of equilibration period. The honey-coupling procedure resulted in stable and repeatable transmitted compressional and shear wave signals. After 20 hours, the load was removed and the experiments were performed to measure P- and S- waves across the fracture. The specimen was loaded again from zero up to 222 kN in 10 loading steps, with increments of 22.2 kN. At the end of each loading step, the transmitted P- and S- waves from each transducer pair were recorded. For the 0° fracture specimens GS01 and GS04, the fracture was subjected to only normal compression, while shear and normal loads were imposed on specimens GS02, GS03, GS05, and GS06 that contained angled fractures. The process of unloading and loading was repeated three times to observe if any hysteretic behavior occurred. Figure 4.2.2-2 shows: (a) a schematic diagram of the experimental setup; and (b) a photograph of a specimen mounted on the loading frame with seismic transducers.

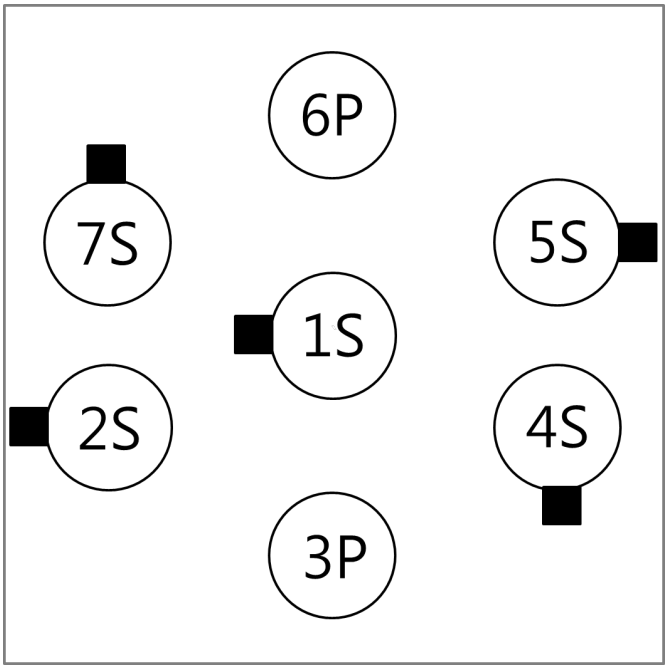

Figure 4.2.2-1. Transducer layout used for aluminum and granite specimens. Elongated box indicates the polarization direction of shear wave transducers.

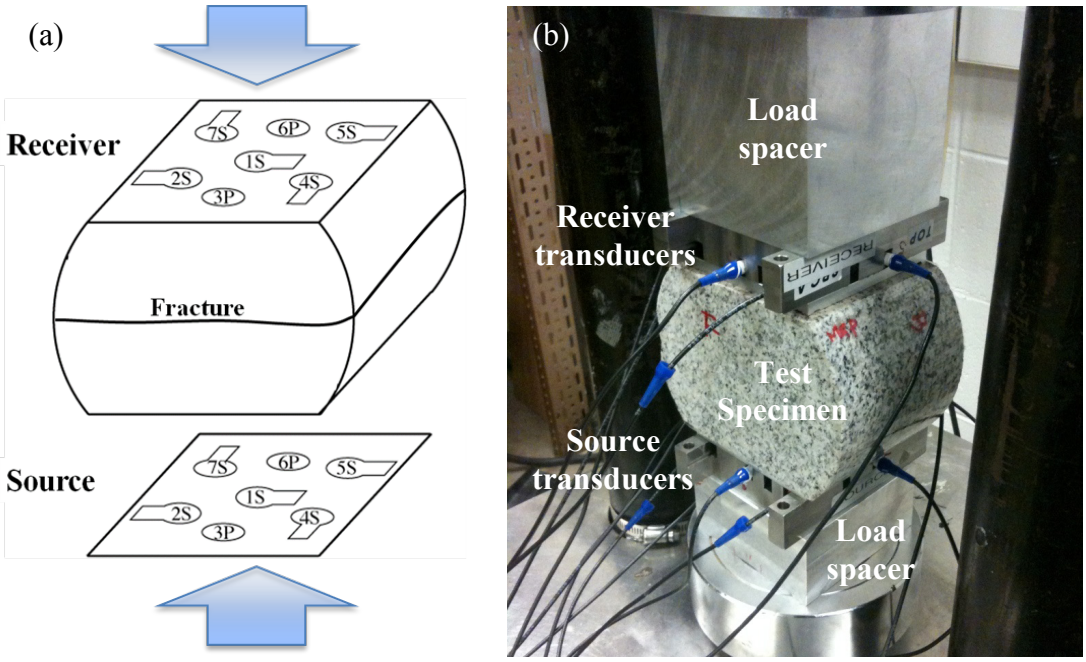

Figure 4.2.2-2. (a) Schematic diagram for experimental setup; and (b) a photograph of an intact granite specimen mounted on the loading frame with seismic transducers housed in load platens. An elongated box in the left indicates the polarization direction of shear wave transducers and the top and bottom arrows represents the applied compressional load.

4.2.3 Roughness and Micro-Slope Angles of Fracture Surface

Before a specimen was mounted in the loading frame, surface roughness measurements were made over the entire area of each fracture surface. Measurements were made in 250 μm increments and in two orthogonal directions using the laser profilometer described in section 3.3.4. The measured data were corrected for positioning errors as explained in section 3.3.4. In this section, the surface roughness measurements and the micro-slope angles on the fracture plane of each granite specimen are presented.

4.2.3.1 Measurement of Surface Roughness

Figure 4.2.3-1 shows the distribution of surface roughness measured from the fractured granite specimens GS01 to GS06. The measured surface roughness was corrected such that the minimum asperity height was zero. Table 4.2.3-1 summarizes the mean value (μ), standard deviation (σ), and coefficient of variance (CV) for the corrected surface roughness measurements. The mean values of the distributions ranged from 2.876 mm to 3.771 mm and the largest asperities ranged from 5.563 mm to 7.101 mm, as listed in the Table. Compared to specimens with a 0° fracture (GS01 and GS04), specimens with an angled fracture (GS02, GS03, GS05, and GS06) had relatively larger standard deviations. The distributions of surface roughness are shown in Figure 4.2.3-1. The specimens with an angled fracture (GS02, GS03, GS05, and GS06) exhibited wider and more skewed asperity height distributions than specimens with 0° fracture specimens (GS01 and GS04). The local surface roughness of the areas sampled by each transducer pair was extracted from the entire surface roughness data. Figures 4.2.3-2 to 4.2.3-7 compare the extracted

local surface roughness distributions with the distribution of the entire fracture surface for specimens GS01 to GS06. The mean values (μ), standard deviation (σ), and coefficient of variance (CV) of the distribution of the local surface are included in Tables 4.2.3-2 to 4.2.3-4. In the tables, the coefficient of variance CV is the ratio between the standard deviation and the mean, σ / μ. The CV is useful to compare the degree of variation from one data series to another (Beck and Arnorld, 1977) since a small CV indicates a narrow distribution and CV is zero for a uniform distribution. For example, the local roughness distributions of the (local) areas under 1S-1S and 2S-2S in GS01 had a CV of 0.100 and 0.376, respectively; see Table 4.3.2-2. As seen in Figure 4.2.3-2 (a), the local roughness distribution under 1S-1S was narrower than under 2S-2S. Hopkins et al. (1987) studied numerically the effect of asperity height distribution on fracture specific stiffness. They found that fracture stiffness increased as the distribution of asperity heights became more uniform, i.e., the more equal the asperity heights were, the stiffer the fracture. The coefficient of variance CV obtained from granite specimens GS01 to GS06 is interpreted with respect to the fracture specific stiffness in section 4.5.

4.2.3.2 Measurement of Micro-Slope Angles

Based on the surface roughness measurements presented in section 4.2.3.1, the distribution of micro-slope angles was obtained. The concept of the micro-slope angle was explained in section 3.4.5.2. Figure 4.2.3-8 shows the distribution of micro-slope angles in GS01 to GS06 fractures. The distributions of the micro-slope angles for the granite specimens were similar to each other and had a bell shape, which was almost

symmetric. Table 4.2.3-5 summarizes the distribution of micro-slope angles for each granite specimen. In the Table, along with the mean value of the micro-slope angles distribution, the maximum micro-slope angle and the fractions of micro-slope angles larger than 20° and 30° are presented. From the micro-slope angles measured in the entire fracture surface, the local micro-slope angles sampled by each transducer pair were extracted. From each of the local micro-slope angles, the maximum and high micro-slope angles corresponding to the top 0.1% to 1.0% of the local distribution were extracted again. These maximum and high micro-slope angles are correlated with shear fracture specific stiffness in section 4.5.2.3. Tables 4.2.3-6 to 4.2.3-8 present the micro-slope angles corresponding to the maximum and the top 0.1% and 1.0% of the local micro-slope angles for every transducer pair, from 1S-1S to 7S-7S for specimens GS01 to GS06. Figures of 4.2.3-9 to 4.2.3-11 present the maximum and high micro-slope angles corresponding to the 0.1% and 1.0% for each local micro-slope distribution. The maximum micro-slope angle generally ranged from 40° to 70°. The micro-slope angles decreased by 20°-30° for the top 1.0%, with respect to the maximum micro-slope angle.

Table 4.2.3-1. Summary of roughness distribution of GS01 to GS06 fractures.

	0° Fracture		15° Fracture		30° Fracture	
	GS01	GS04	GS03	GS06	GS02	GS05
Standard deviation (σ, mm)	0.939	0.927	1.122	0.977	1.065	0.977
Mean (μ, mm)	3.324	3.342	3.509	3.771	3.145	2.876
Coefficient of variance (CV = σ/μ)	0.283	0.277	0.320	0.259	0.339	0.340
Maximum asperity (mm)	6.123	5.718	7.101	6.422	6.999	5.563

Table 4.2.3-2. Local surface roughness, under transducers, for specimens GS01 and GS04, with 0° fracture.

	GS01			GS04		
	σ (mm)	μ (mm)	CV (=σ/μ)	σ (mm)	μ (mm)	CV (=σ/μ)
Entire Surface	0.939	3.324	0.283	0.927	3.342	0.277
1S-1S	0.361	3.602	0.100	0.498	4.025	0.124
2S-2S	1.094	2.911	0.376	0.780	3.570	0.218
5S-5S	0.774	3.087	0.251	0.921	1.775	0.519
3P-3P	0.443	3.116	0.142	0.928	3.650	0.254
6P-6P	0.454	3.691	0.123	0.787	3.660	0.215
4S-4S	0.392	3.819	0.103	0.413	3.339	0.124
7S-7S	1.033	3.082	0.335	0.560	2.794	0.200

Table 4.2.3-3. Local surface roughness, under transducers, for specimens GS03 and GS06, with 15° fracture.

	GS03			GS06		
	σ (mm)	μ (mm)	CV (=σ/μ)	σ (mm)	μ (mm)	CV (=σ/μ)
Entire Surface	1.122	3.509	0.320	0.977	3.771	0.259
1S-1S	0.868	2.430	0.357	0.557	2.439	0.229
2S-2S	0.423	1.753	0.242	0.502	4.540	0.111
5S-5S	0.670	4.144	0.162	0.604	3.528	0.171
3P-3P	0.370	5.388	0.069	0.310	3.489	0.089
6P-6P	0.620	4.198	0.148	0.484	4.645	0.104
4S-4S	0.487	3.568	0.136	0.340	4.014	0.085
7S-7S	0.522	2.806	0.186	0.784	2.863	0.274

Table 4.2.3-4. Local surface roughness, under transducers, for specimens GS02 and GS05, with 30° fracture.

	GS02			GS05		
	σ (mm)	μ (mm)	CV (=σ/μ)	σ (mm)	μ (mm)	CV (=σ/μ)
Entire Surface	1.065	3.145	0.339	0.977	2.876	0.340
1S-1S	0.502	2.594	0.193	0.545	1.673	0.326
2S-2S	0.402	2.250	0.179	0.594	2.775	0.214
5S-5S	0.612	3.442	0.178	0.688	3.420	0.201
3P-3P	0.279	3.022	0.092	0.824	1.682	0.490
6P-6P	0.450	3.471	0.130	0.465	3.225	0.144
4S-4S	0.639	4.300	0.149	0.451	2.773	0.163
7S-7S	0.663	4.856	0.137	0.735	2.812	0.261

Table 4.2.3-5. Summary of micro-slope angle distribution.

	0° Fracture		15° Fracture		30° Fracture	
	GS01	GS04	GS03	GS06	GS02	GS05
Mean (°)	0.060	0.055	0.062	0.015	-0.004	0.040
Maximum (°)	75.8	84.6	78.6	72.5	76.5	75.5
Fractions of Micro-Slope Angle ≥ 20°	0.185	0.133	0.159	0.106	0.140	0.126
Fractions of Micro-Slope Angle ≥ 30°	0.062	0.030	0.049	0.020	0.030	0.025

Table 4.2.3-6. Micro-slope angles corresponding to maximum and top 0.1 % and 1.0 % of the local micro-slope angle distributions, within the area of transducer pairs 1S-1S to 7S-7S for specimens GS01 and GS04, with 0° fracture.

	GS01			GS04		
	Max. (°)	0.1% (°)	1.0% (°)	Max (°)	0.1% (°)	1.0% (°)
1S-1S	67.5	60.7	35.6	62.4	54.6	37.1
2S-2S	66.1	65.1	40.7	63.1	60.4	41.2
5S-5S	56.7	56.0	37	69.5	62.8	37.6
3P-3P	66.2	64.0	37.8	69.0	58.4	45.2
6P-6P	64.9	45.2	35.2	49.6	47.1	33.9
4S-4S	63.7	59.7	34.7	71.6	60.2	36.6
7S-7S	65.3	56.2	39.7	64.3	62.2	40.7

Table 4.2.3-7. Micro-slope angles corresponding to the maximum and top 0.1 % and 1.0 % of the local micro-slope angle distributions, within the area of transducer pairs 1S-1S to 7S-7S for specimens GS03 and GS06, with 15° fracture.

	GS03			GS06		
	Max. (°)	0.1% (°)	1.0% (°)	Max (°)	0.1% (°)	1.0% (°)
1S-1S	73.3	67.6	35.6	71.0	46.9	32.4
2S-2S	73.8	69.7	41.8	50.8	44.7	31
5S-5S	55.3	48.9	35.6	41.8	36.1	30.3
3P-3P	52.9	44.0	32.4	43.9	43.9	34.2
6P-6P	51.6	49.2	38.9	35.7	35.7	29.3
4S-4S	68.1	55.0	37.4	52.6	46.4	35
7S-7S	64.0	57.2	38.2	52.4	45.0	32.7

Table 4.2.3-8. Micro-slope angles corresponding to the maximum, and top 0.1 % and 1.0 % of the local micro-slope angle distributions, within the area of transducer pairs 1S-1S to 7S-7S for specimens GS02 and GS05, with 30° fracture.

	GS02			GS05		
	Max. (°)	0.1% (°)	1.0% (°)	Max (°)	0.1% (°)	1.0% (°)
1S-1S	55.2	45.0	34.6	75.5	61.7	31.2
2S-2S	71.8	55.9	34.4	52.8	42.0	30.2
5S-5S	70.3	63.8	40.6	54.2	40.1	31.2
3P-3P	68.6	62.9	31.6	50.5	48.9	27.5
6P-6P	44.3	38.0	36.2	64.1	47.2	31.7
4S-4S	68.6	59.6	32.7	48.1	45.1	35.6
7S-7S	54.4	43.3	32.7	57.6	52.2	32.3

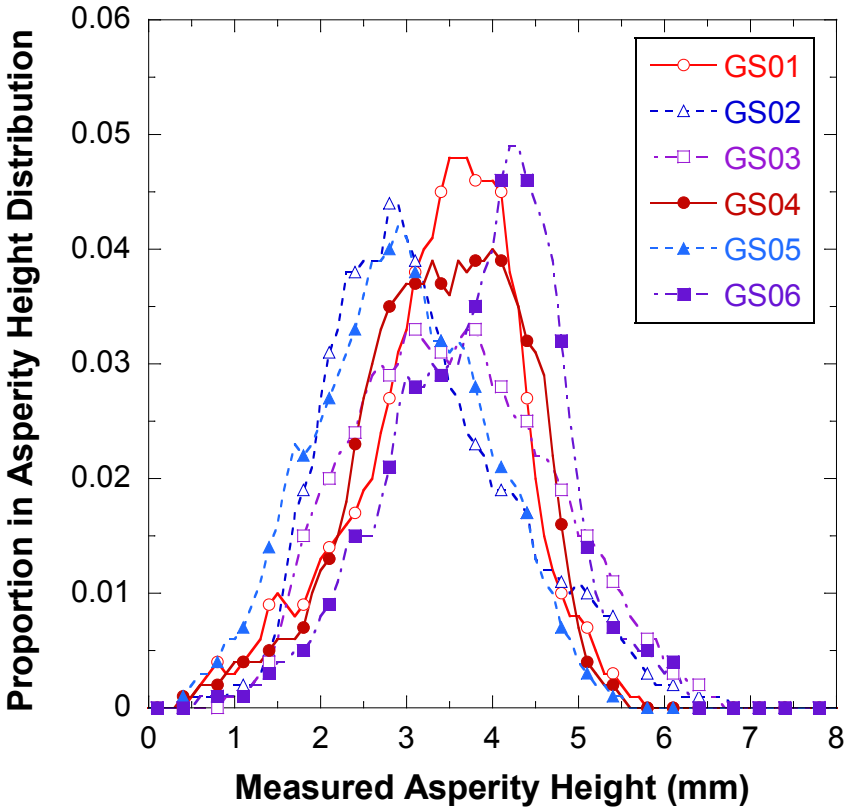

Figure 4.2.3-1. Surface roughness distribution of the entire fracture surface, from GS01 to GS06 specimens.

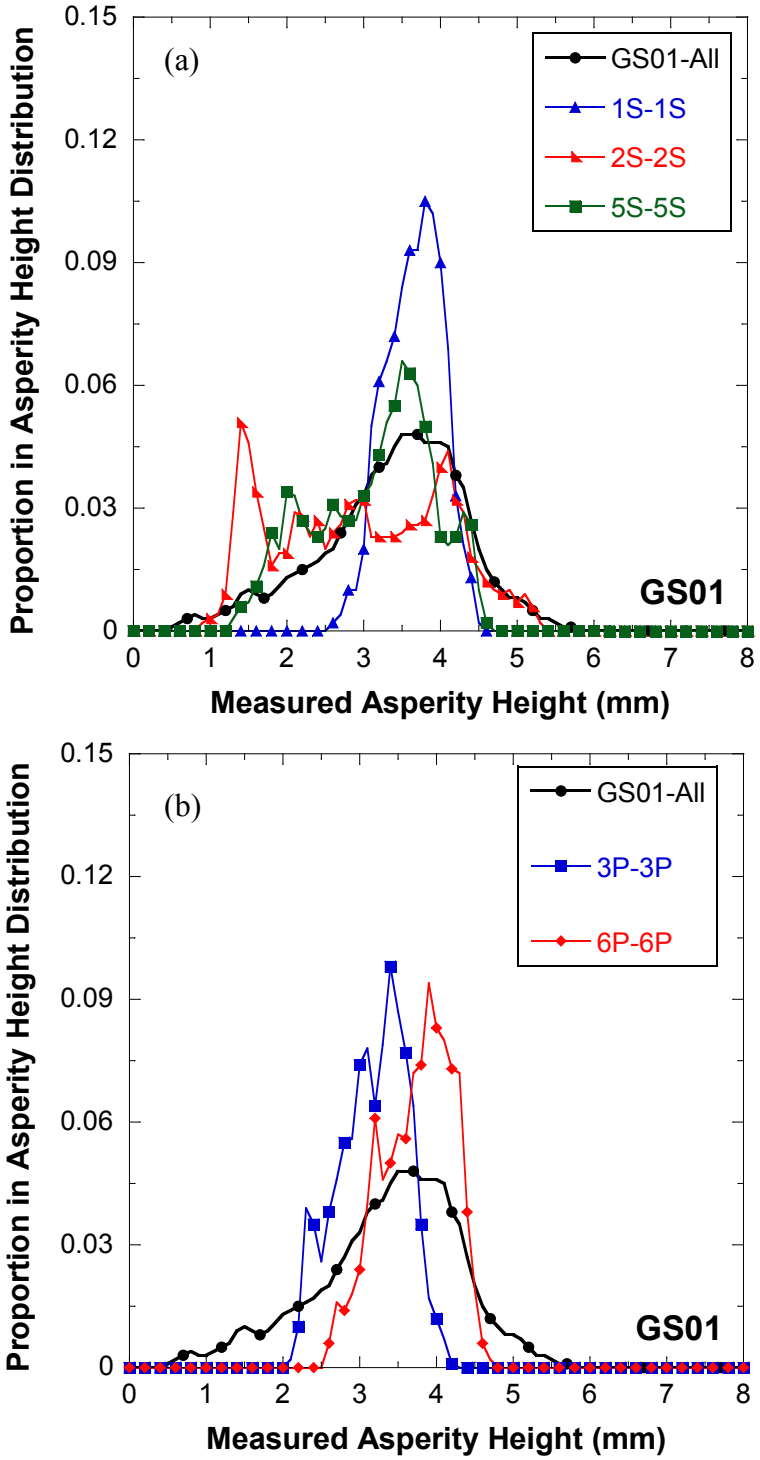

Figure 4.2.3-2. Comparison of entire and local distributions of surface roughness of the areas under transducer pairs: (a) 1S-1S, 2S-2S, and 5S-5S; (b) 3P-3P and 6P-6P; and (c) 4S-4S and 7S-7S, for GS01 with 0° fracture (continued).

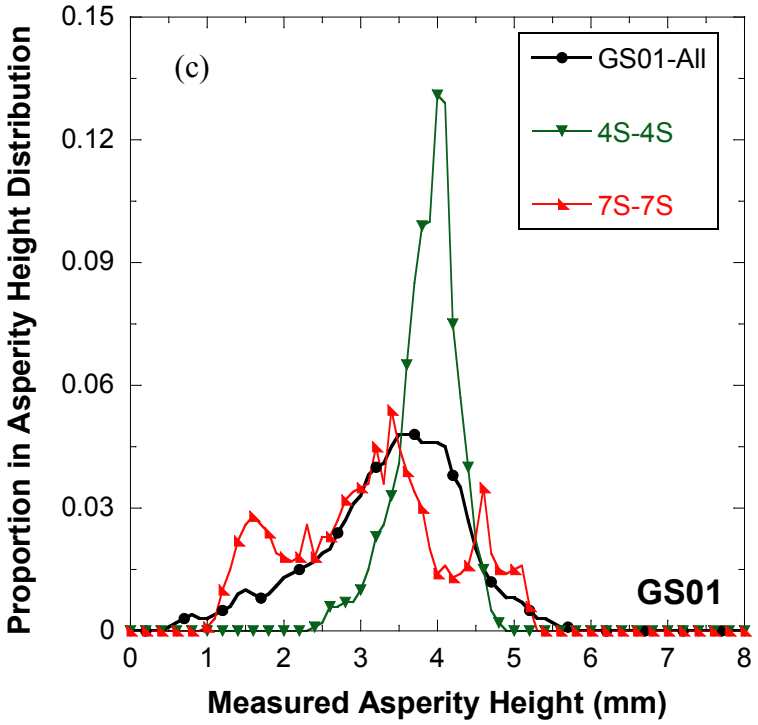

Figure 4.2.3-2. Comparison of entire and local distributions of surface roughness of the areas under transducer pairs: (a) 1S-1S, 2S-2S, and 5S-5S; (b) 3P-3P and 6P-6P; and (c) 4S-4S and 7S-7S, for GS01 with 0° fracture.

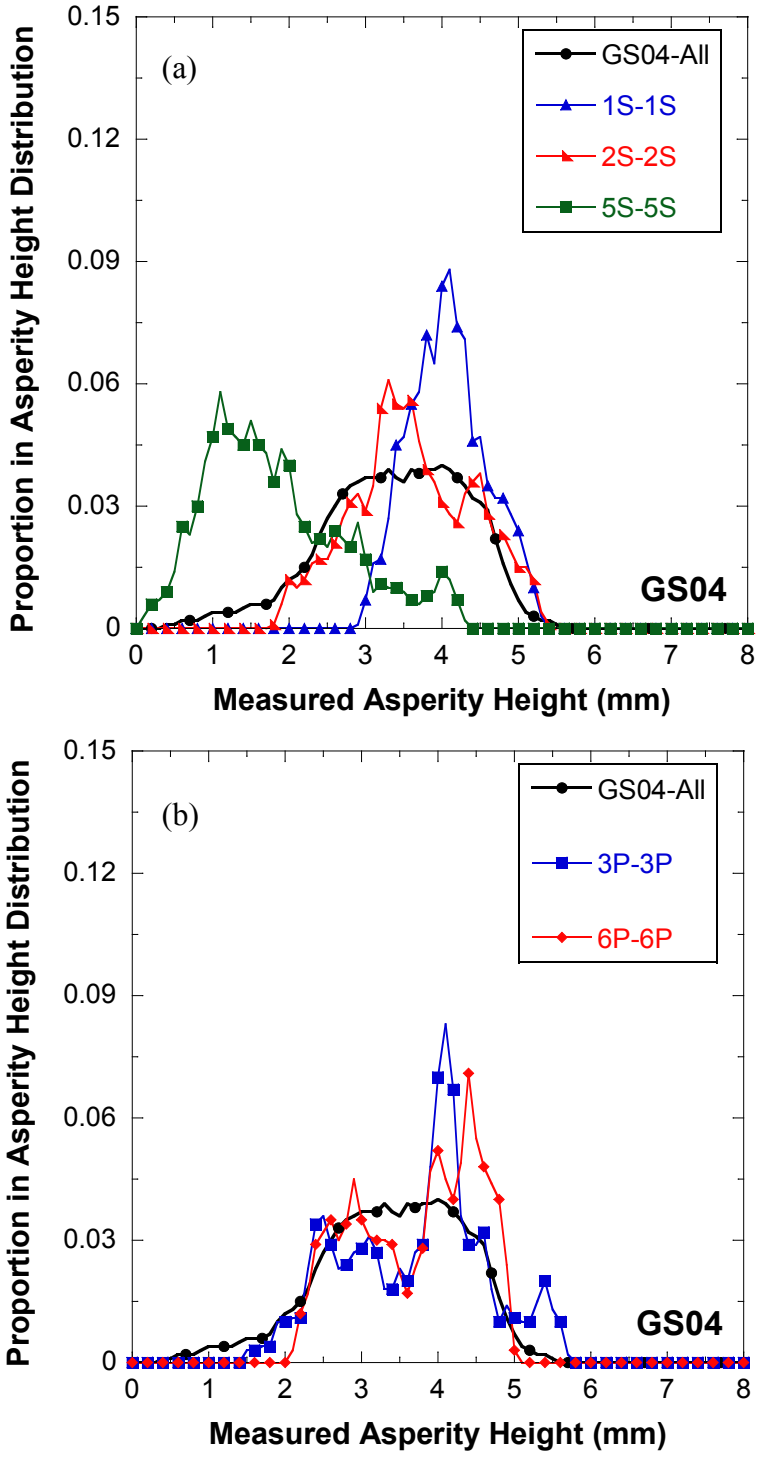

Figure 4.2.3-3. Comparison of complete and local distributions of surface roughness of areas under transducer pairs: (a) 1S-1S, 2S-2S, and 5S-5S; (b) 3P-3P and 6P-6P; and (c) 4S-4S and 7S-7S, for GS04 with 0° fracture (continued).

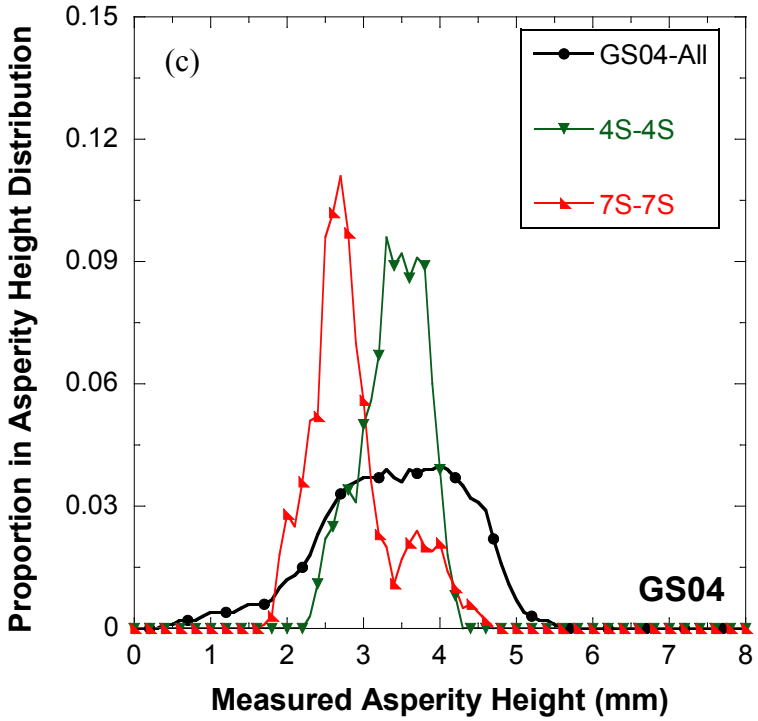

Figure 4.2.3-3. Comparison of complete and local distributions of surface roughness of areas under transducer pairs: (a) 1S-1S, 2S-2S, and 5S-5S; (b) 3P-3P and 6P-6P; and (c) 4S-4S and 7S-7S, for GS04 with 0° fracture.

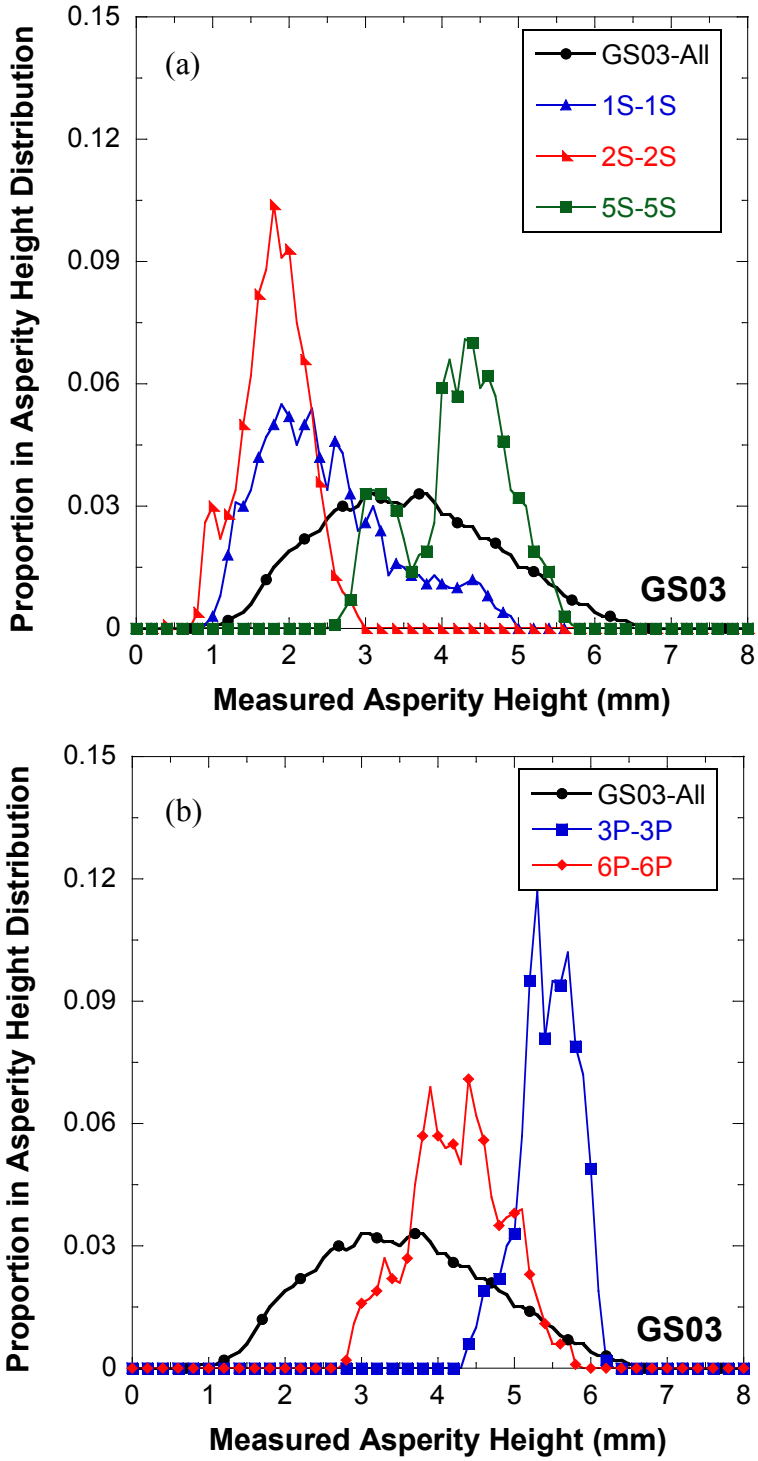

Figure 4.2.3-4. Comparison of complete and local distributions of surface roughness of areas under transducer pairs: (a) 1S-1S, 2S-2S, and 5S-5S; (b) 3P-3P and 6P-6P; and (c) 4S-4S and 7S-7S, for GS03 with 15° fracture (continued).

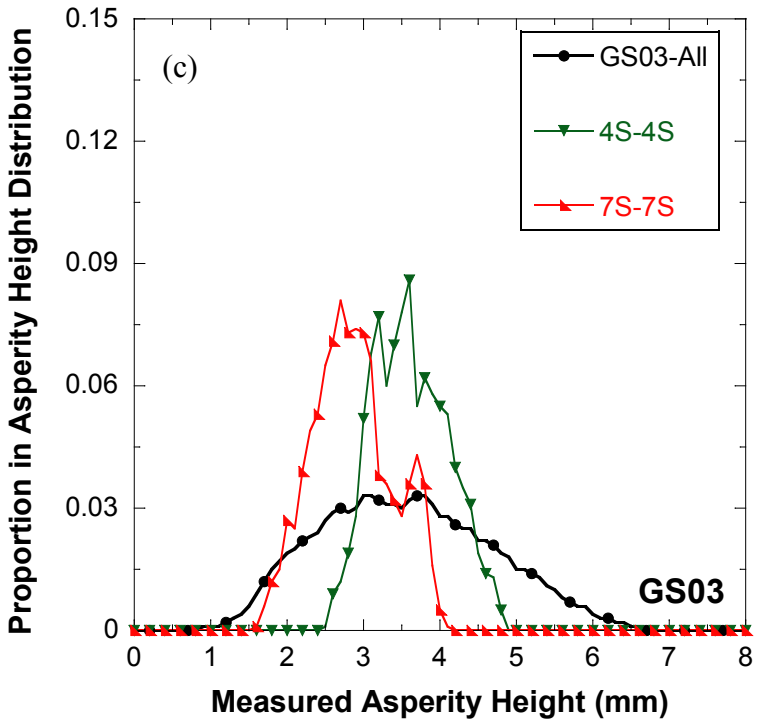

Figure 4.2.3-4. Comparison of complete and local distributions of surface roughness of areas under transducer pairs: (a) 1S-1S, 2S-2S, and 5S-5S; (b) 3P-3P and 6P-6P; and (c) 4S-4S and 7S-7S, for GS03 with 15° fracture.

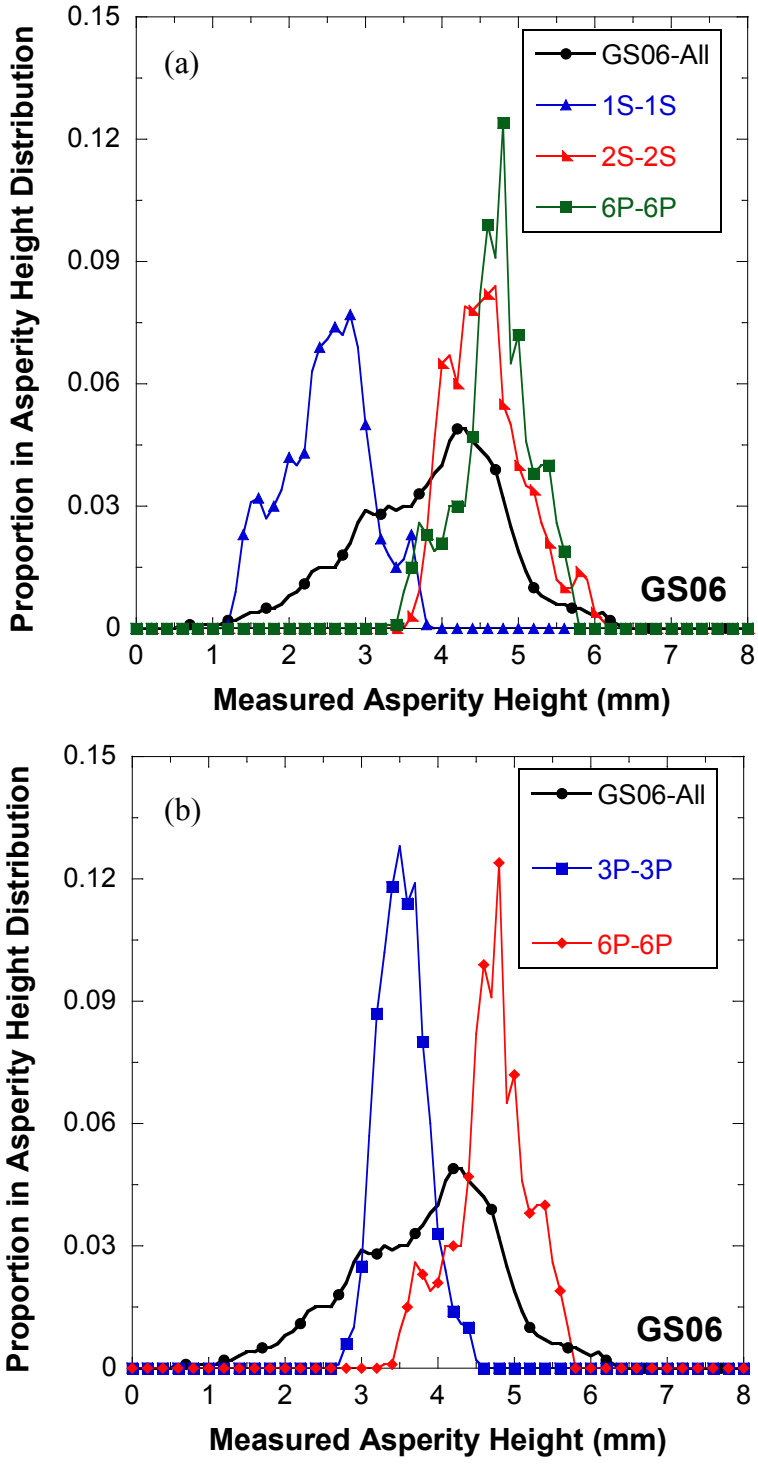

Figure 4.2.3-5. Comparison of complete and local distributions of surface roughness of areas under transducer pairs: (a) 1S-1S, 2S-2S, and 5S-5S; (b) 3P-3P and 6P-6P; and (c) 4S-4S and 7S-7S, for GS06 with 15° fracture (continued).

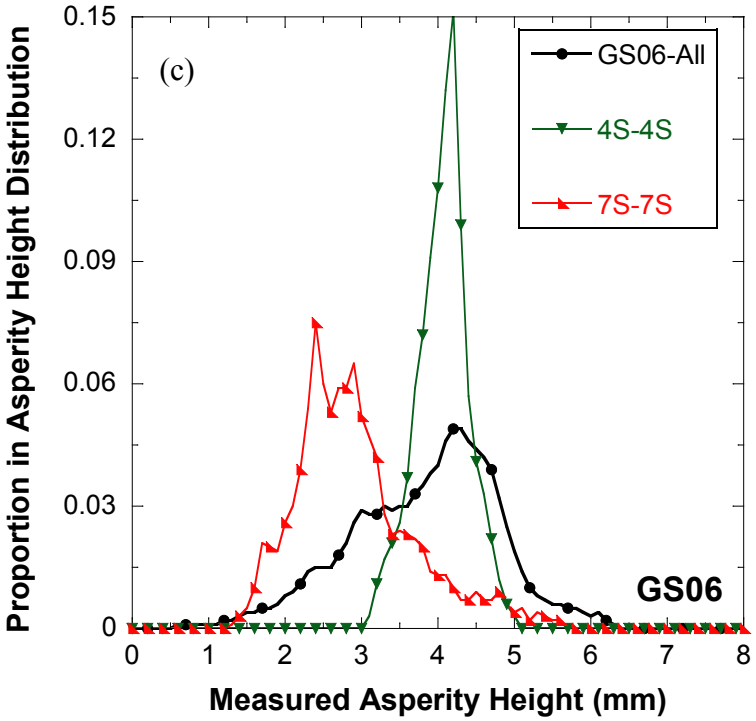

Figure 4.2.3-5. Comparison of complete and local distributions of surface roughness of areas under transducer pairs: (a) 1S-1S, 2S-2S, and 5S-5S; (b) 3P-3P and 6P-6P; and (c) 4S-4S and 7S-7S, for GS06 with 15° fracture.

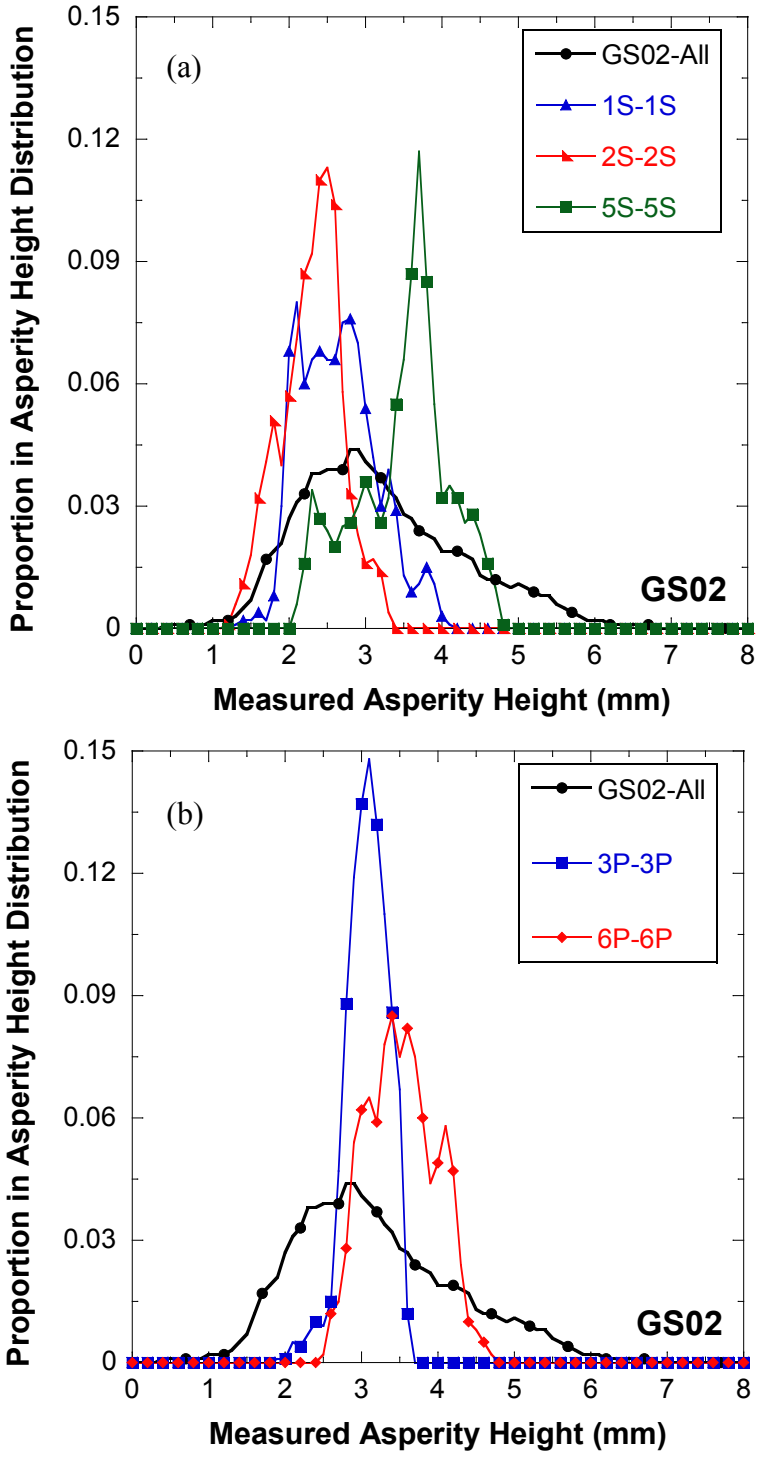

Figure 4.2.3-6. Comparison of complete and local distributions of surface roughness of areas under transducer pairs: (a) 1S-1S, 2S-2S, and 5S-5S; (b) 3P-3P and 6P-6P; and (c) 4S-4S and 7S-7S, for GS02 with 30° fracture specimen (continued).

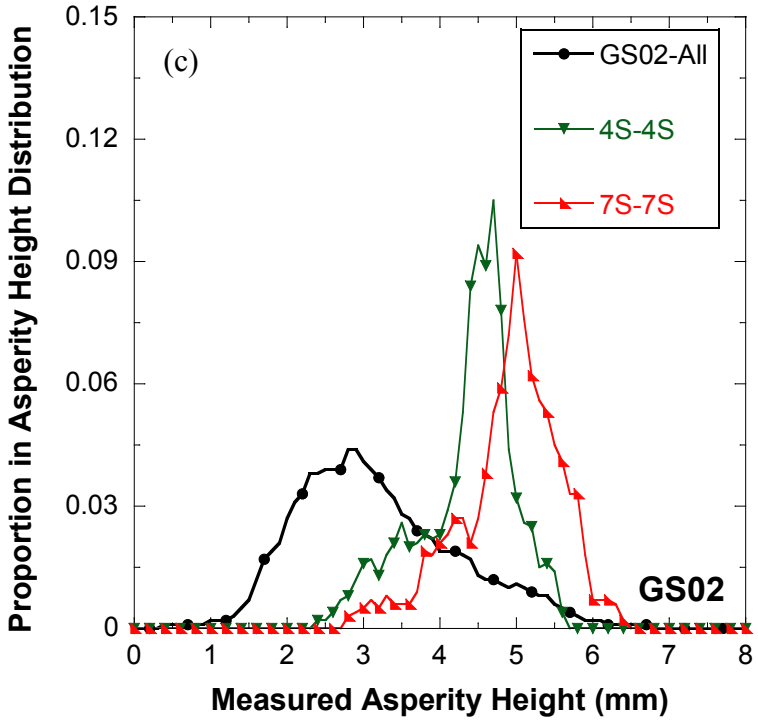

Figure 4.2.3-6. Comparison of complete and local distributions of surface roughness of areas under transducer pairs: (a) 1S-1S, 2S-2S, and 5S-5S; (b) 3P-3P and 6P-6P; and (c) 4S-4S and 7S-7S, for GS02 with 30° fracture specimen.

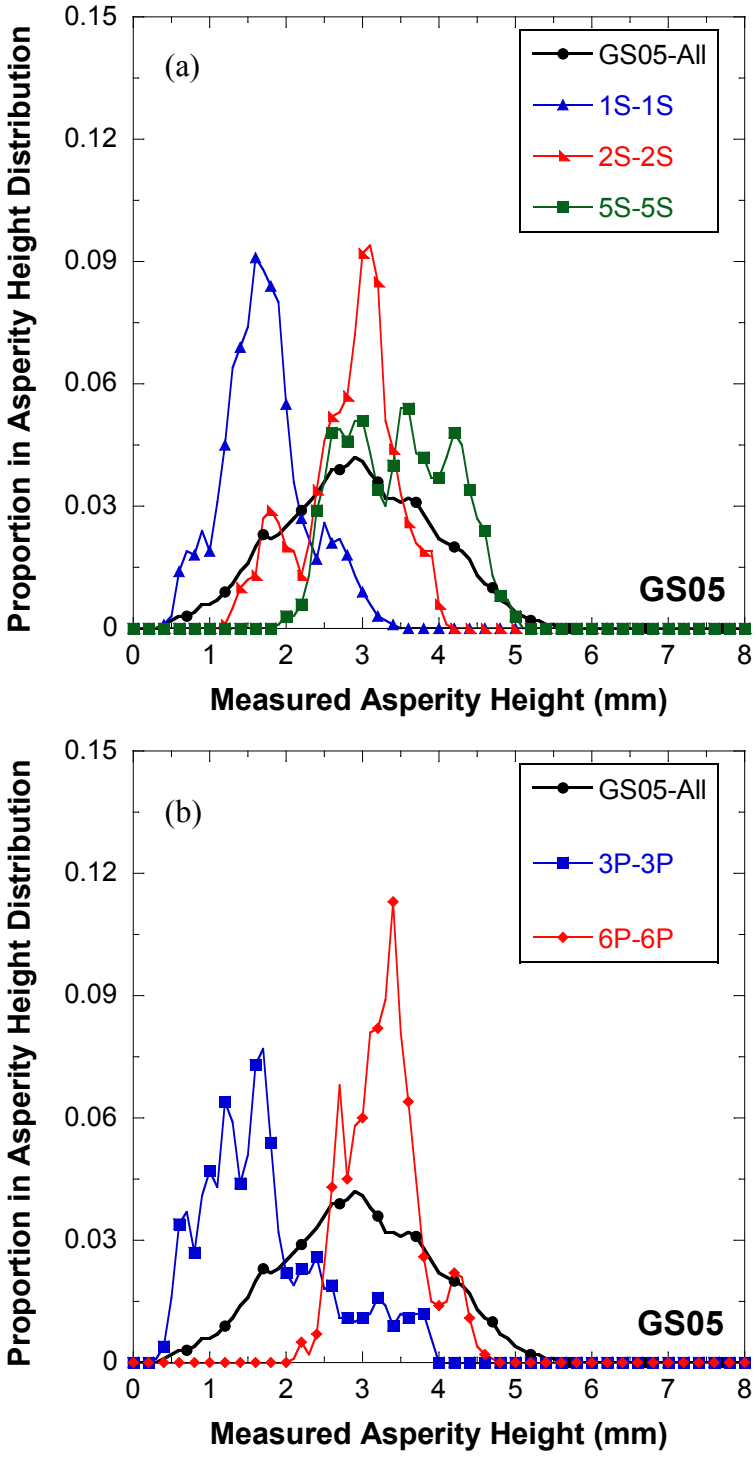

Figure 4.2.3-7. Comparison of complete and local distributions of surface roughness of areas under transducer pairs: (a) 1S-1S, 2S-2S, and 5S-5S; (b) 3P-3P and 6P-6P; and (c) 4S-4S and 7S-7S, for GS05 with 30° fracture (continued).

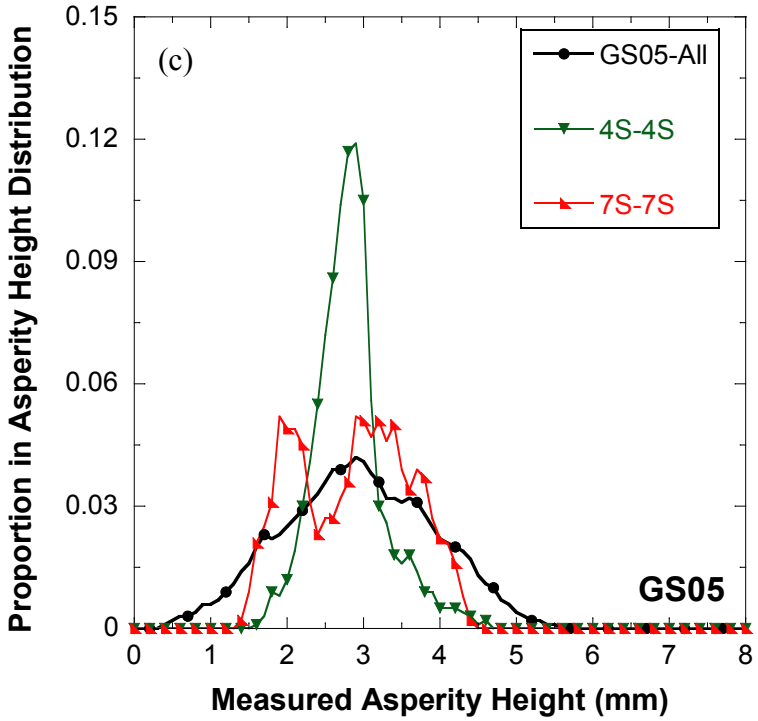

Figure 4.2.3-7. Comparison of complete and local distributions of surface roughness of areas under transducer pairs: (a) 1S-1S, 2S-2S, and 5S-5S; (b) 3P-3P and 6P-6P; and (c) 4S-4S and 7S-7S, for GS05 with 30° fracture.

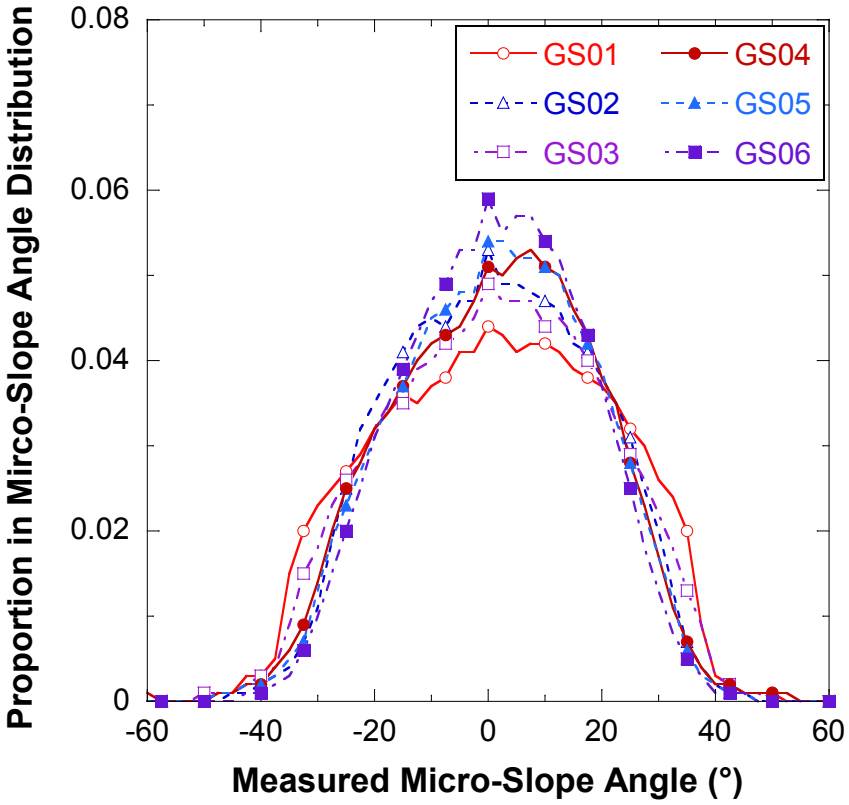

Figure 4.2.3-8. Distributions of micro-slope angle for specimens GS01 to GS06.

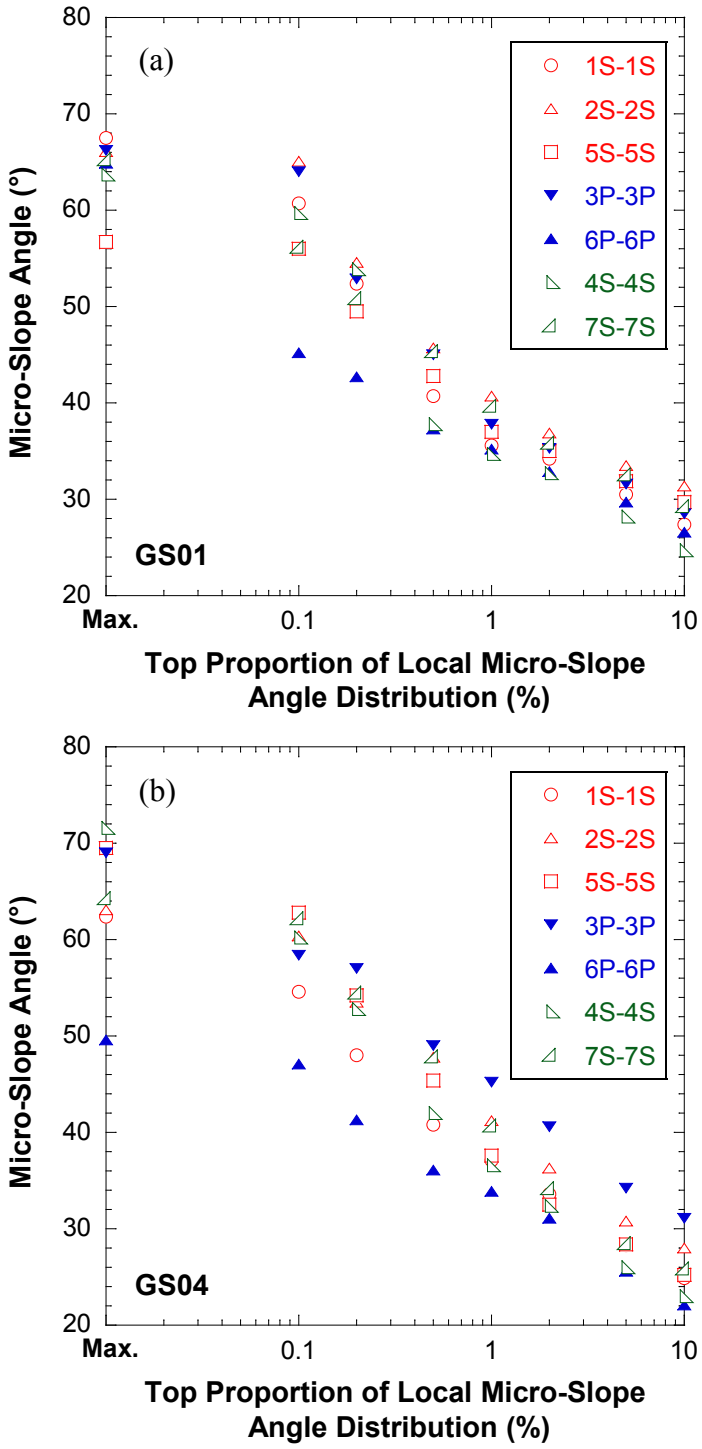

Figure 4.2.3-9. Micro-slope angles for 0° fracture specimens: (a) GS01 and (b) GS04, corresponding to the maximum, and top 0.1% to 10% of the local micro-slope angles under the area of transducer pairs 1S-1S, 2S-2S, and 5S-5S (red), 3P-3P and 6P-6P (blue), and 4S-4S and 7S-7S (green).

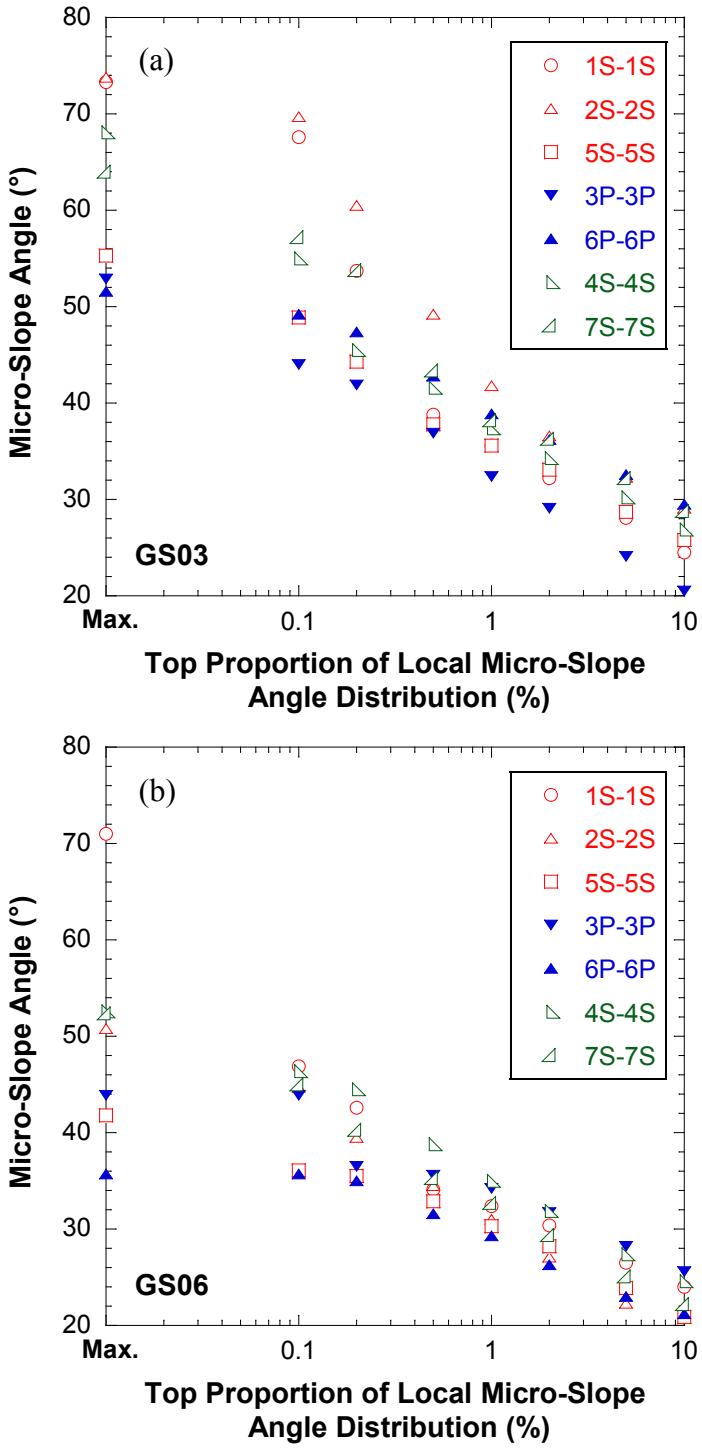

Figure 4.2.3-10. Micro-slope angles for 15° fracture specimens: (a) GS03 and (b) GS06 corresponding to the maximum, and the top 0.1% to 10% of the local micro-slope angles under the area of transducer pairs 1S-1S, 2S-2S, and 5S-5S (red), 3P-3P and 6P-6P (blue), and 4S-4S and 7S-7S (green).

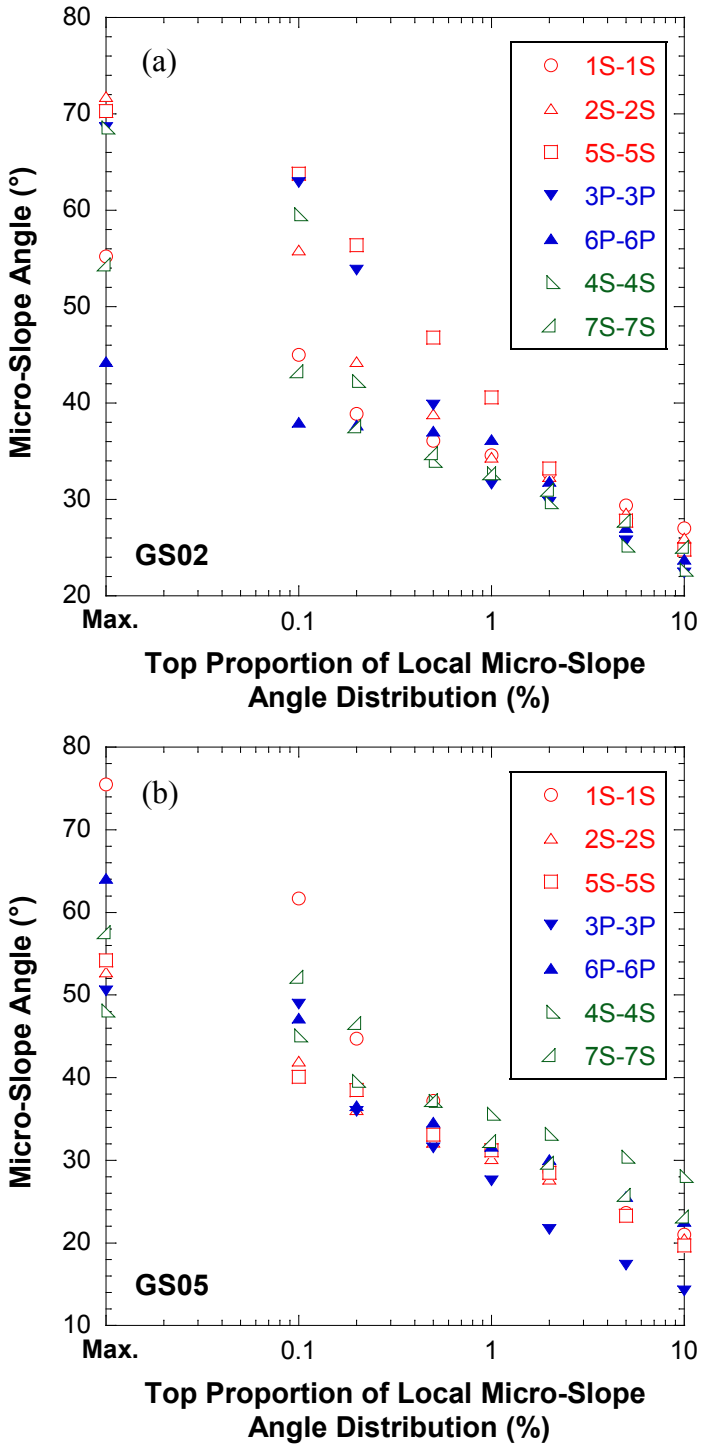

Figure 4.2.3-11. Micro-slope angles for 30° fracture specimens: (a) GS02 and (b) GS05 corresponding to the maximum, and the top 0.1% to 10% of the local micro-slope angles under the area of transducer pairs 1S-1S, 2S-2S, and 5S-5S (red), 3P-3P and 6P-6P (blue), and 4S-4S and 7S-7S (green).

4.3 Seismic Response of Aluminum Specimens

Full waveform measurements were made during the uniaxial compression experiments on aluminum specimens. The seismic measurements obtained from the tests on intact and single-fracture specimens were interpreted using the displacement discontinuity theory.

4.3.1 Intact Aluminum Specimen

The peak-to-peak amplitudes for the solid aluminum specimen are plotted as a function of normal stress in Figure 4.3.1-1, for (a) P-wave and (b) S-wave. The measurements for the intact aluminum specimen were not affected by the load applied because the matrix of the aluminum did not contain micro-cracks. The peak-to-peak amplitudes of P-wave and S-wave were 2.2±0.1V and 0.52±0.04V, respectively. Figure 4.3.1-2 shows (a) P- and (b) S- wave velocities as a function of the stress applied. The wave velocities of P- and S-waves were 6,320 m/sec and 3,080-3,100 m/sec, respectively. The data show no stress-dependence and a small anisotropy in shear wave velocity. The Fourier spectra of 1S-1S and 3P-3P are shown in Figure 4.3.1-3. Both spectra show a very small stress-sensitivity and a constant dominant frequency with stress. For P-waves, the dominant or most probable frequency was 0.7 MHz, and for S-waves, 0.6MHz.

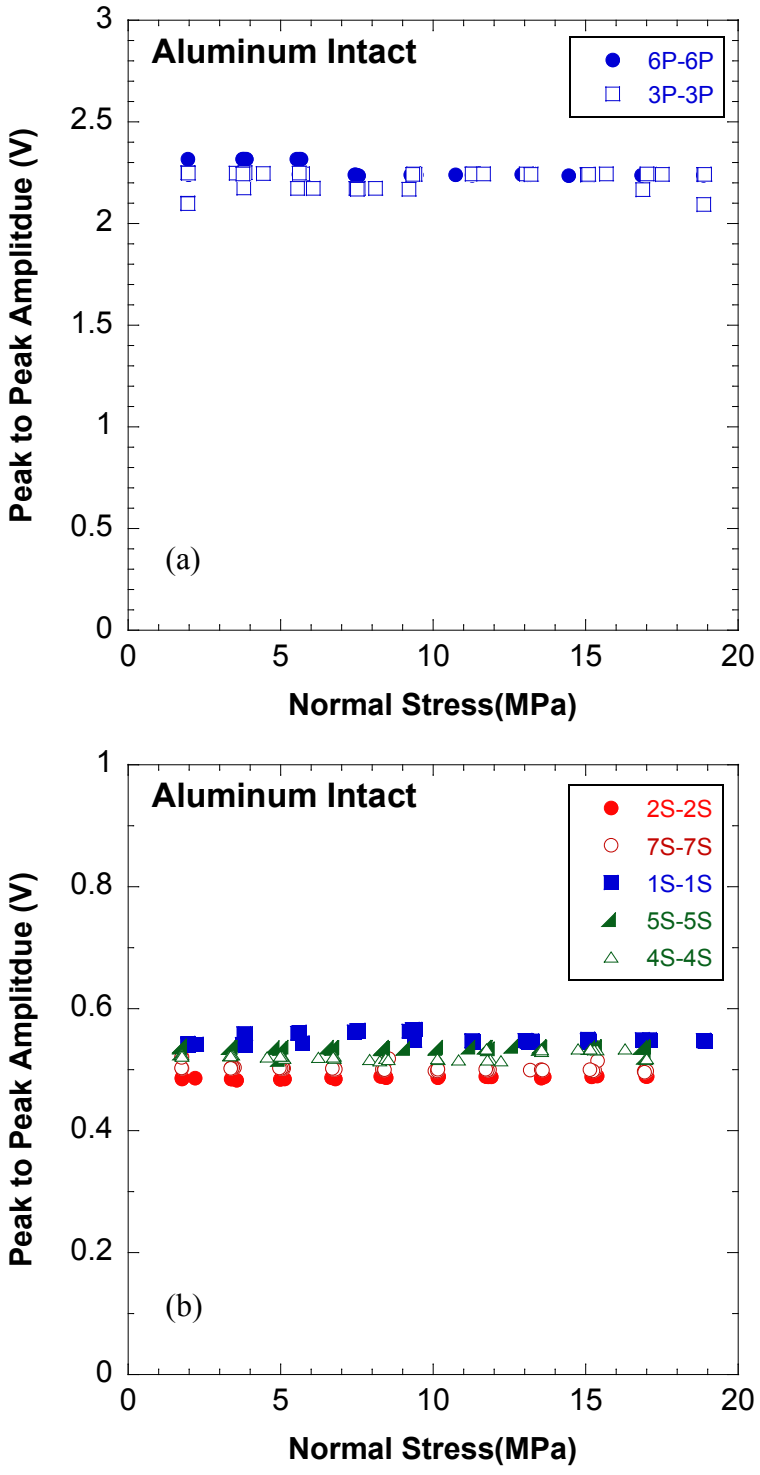

Figure 4.3.1-1. Peak-to-peak amplitude of intact aluminum for: (a) compressional wave; and (b) shear wave, as a function of normal stress.

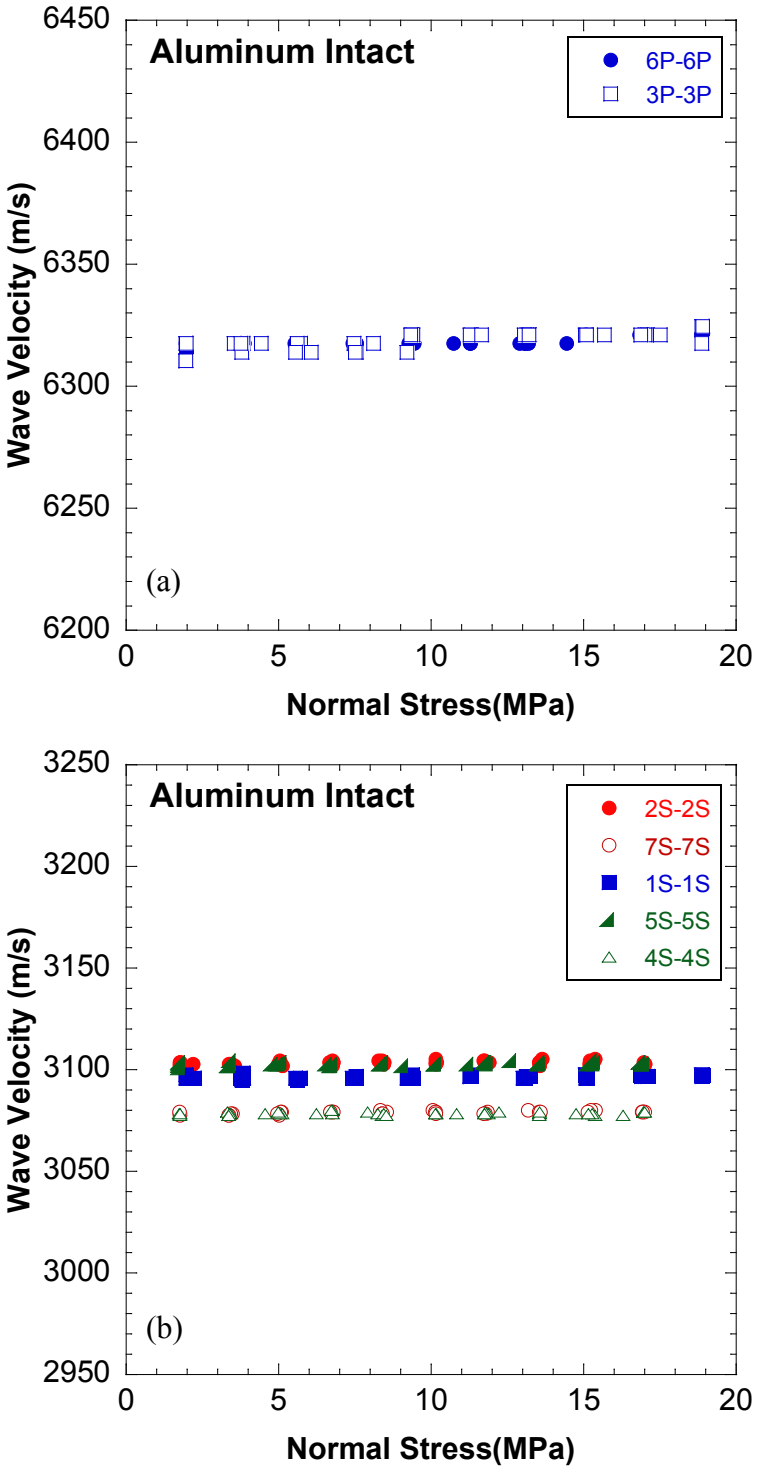

Figure 4.3.1-2. Wave velocity of intact aluminum for: (a) compressional wave; and (b) shear wave, as a function of normal stress.

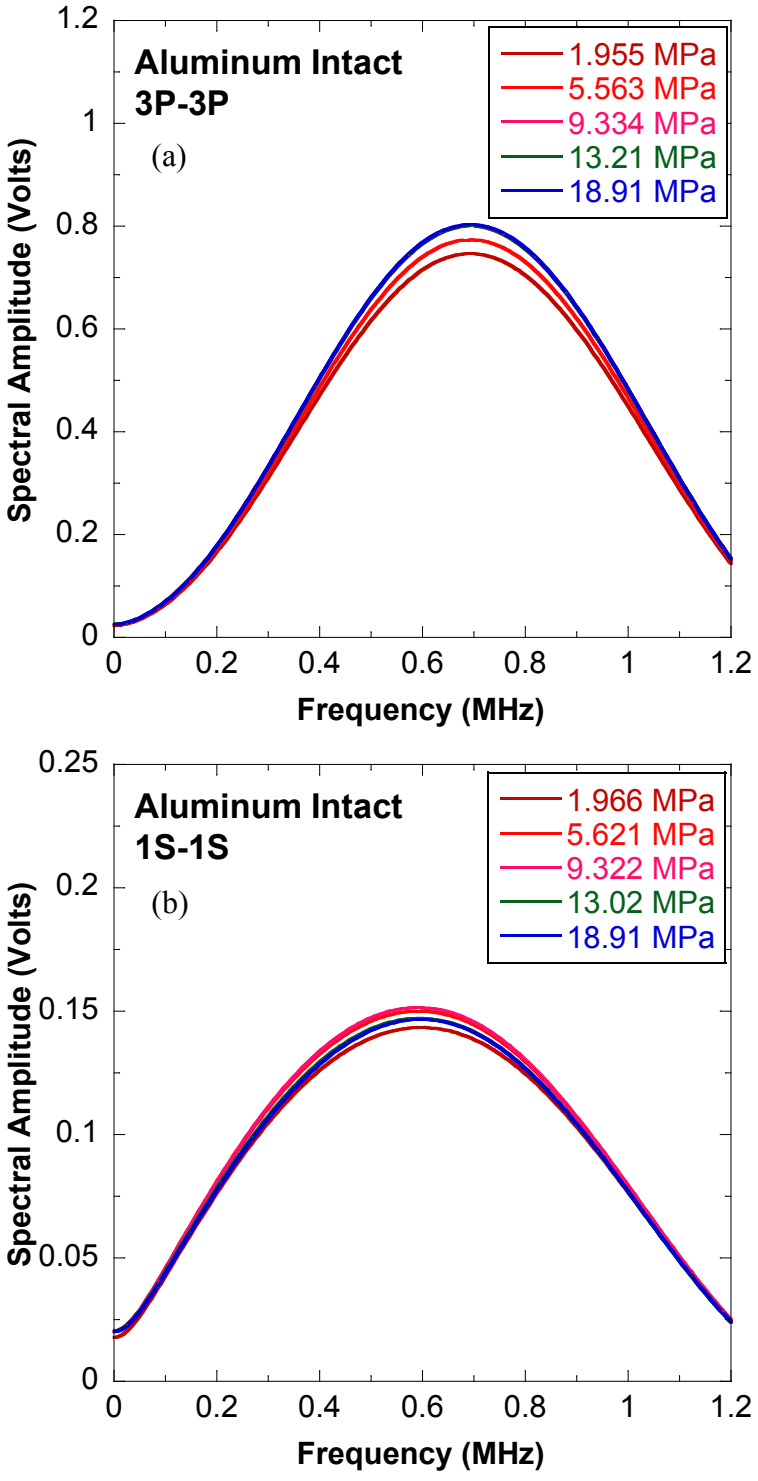

Figure 4.3.1-3. Fourier spectrum of intact aluminum for: (a) compressional wave; and (b) shear wave, as a function of normal stress.

4.3.2 Aluminum Specimen with a Single Fracture

The peak-to-peak amplitude and Fourier spectrum for the aluminum sample with a horizontal fracture are shown in Figures 4.3.2-1 and 4.3.2-2, respectively. As the applied normal stress increased, the peak-to-peak amplitude and spectral amplitude increased and then became constant at around a normal stress 7-8 MPa. At the highest normal stress applied of 18.9 MPa, the peak-to-peak amplitude and spectral amplitude approached those of intact aluminum. The increase in peak-to-peak and spectral amplitudes with normal stress is interpreted as a result of the presence of the fracture. That is, the fracture specific stiffness increased with increasing normal stress until the fracture completely closed, at which time the fracture behaved as intact aluminum.

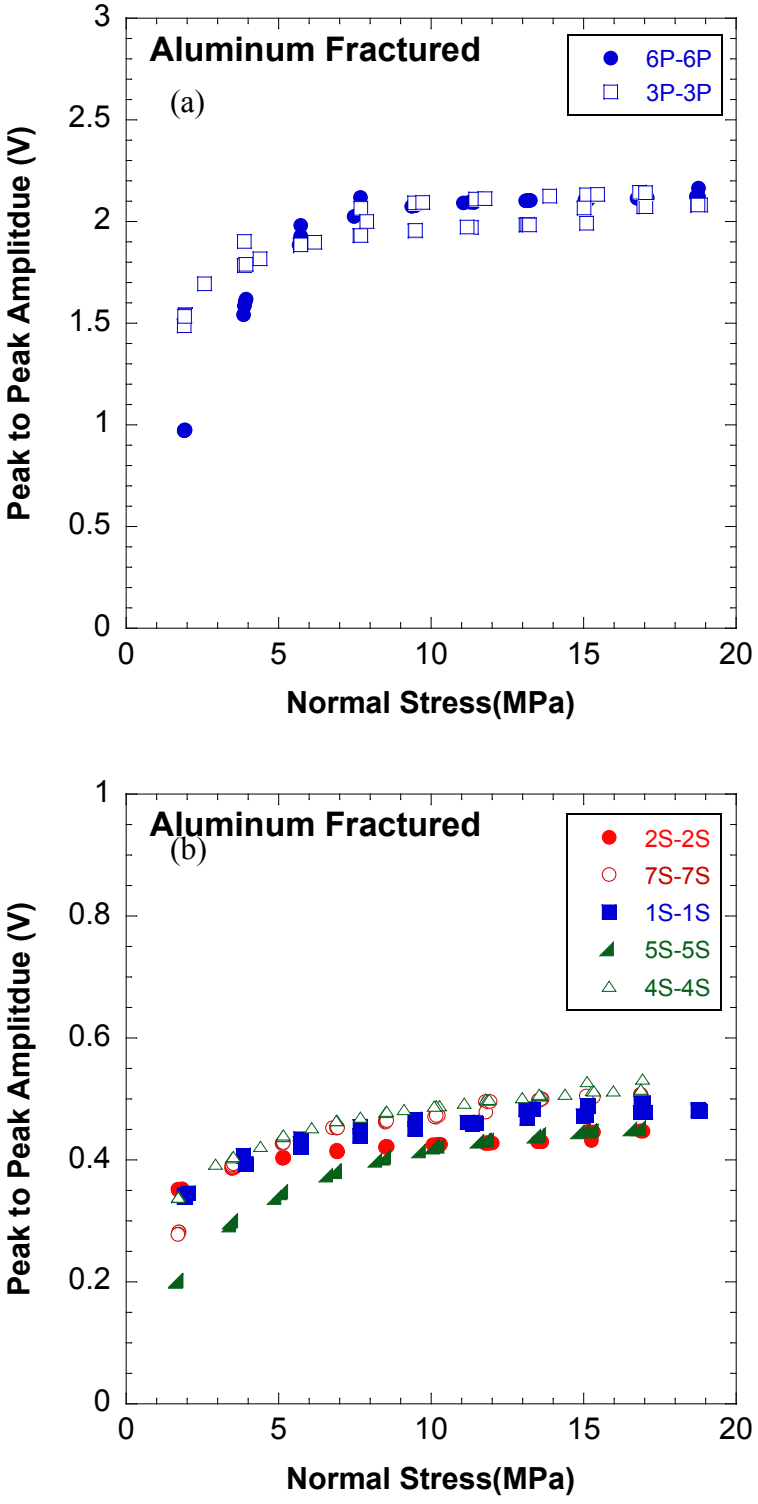

Figure 4.3.2-1. Peak-to-peak amplitude from the fractured aluminum sample for: (a) compressional wave, and (b) shear wave, as a function of normal stress.

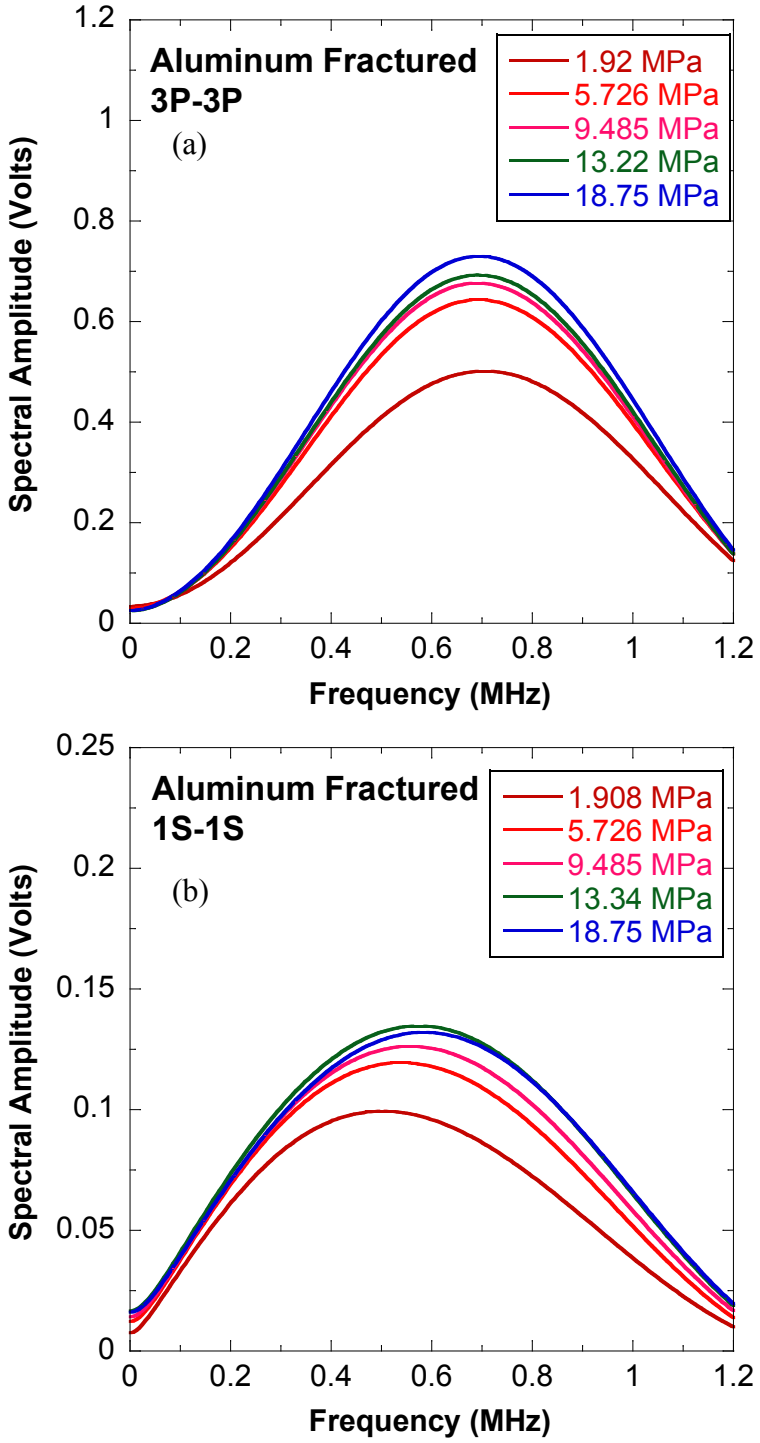

Figure 4.3.2-2. Fourier spectrum from the fractured aluminum sample for: (a) compressional wave, and (b) shear wave, as a function of normal stress.

4.3.3 Error Analysis on Aluminum Specimens

An error analysis on the seismic data from the intact and fractured aluminum specimens was performed to quantify experimental errors and quantify the repeatability of the data acquisition during experiments. Possible sources of error were categorized into three: i) inherent errors of the seismic imaging system, ii) hysteretic behavior of a fracture caused by repetitive loading and unloading, and iii) experimental setup error caused by remounting the specimen in the loading frame.

As described in section 4.2.2, a specimen was subjected to three repetitive cycles of unloading and loading. In the 1st loading cycle, a possible source of error is the inherent errors of the seismic imaging system. The variation in amplitudes recorded during the three repetitive loading and unloading is interpreted as the hysteretic behavior of a fracture. Once the data acquisition from the three repetitive loading cycles was completed (Setup 1), the specimen was dismounted from the loading frame and disassembled from the seismic system. To quantify the error caused by remounting the specimen in the loading frame, the same experiment procedures such as oven-dried honey, 20 hours of honey coupling, and three repetitive loading cycles, were carried out for Setup 2.

The peak-to-peak amplitudes of the transducer pair 1S-1S attached to the intact aluminum specimen recorded during the three repetitive loading cycles, for Setup 1 and 2, are shown in Figure 4.3.3-1. The figure shows: (a) the 1st loading cycle in Setup 1, (b) the repetitive loading cycles of 1st to 3rd cycles in Setup 1; and (c) the 1st to 3rd cycles in Setup 1 and 2. The transducer pair 1S-1S was selected because it exhibited the largest variation in amplitude throughout the experiments. In Figure 4.3.3-1 (a), the amplitudes varied within the range of 0.54 V to 0.57 V, i.e., ±2.5 % variation, during the 1st loading

cycle and for Setup 1. The ±2.5 % variation in amplitude was due to the inherent error of the seismic imaging system. The errors in amplitude slightly increased to ±3.0 % with loading cycles, e.g. from 1st to 3rd, as seen in Figure 4.3.3-1 (b). Between the two different experiment setups, i.e. Setup 1 and Setup 2, the error in amplitude increased to ±4.0 %, as observed in Figure 4.3.3-2 (c)

The source and magnitude of errors associated with the fractured aluminum specimen were similarly analyzed and were quantified based on the same three possible sources. Figure 4.3.3-2 (a) shows the variation in amplitude of transducer pair 4S-4S, which exhibited the largest change in amplitude. At normal stresses 15 MPa and 17 MPa, a small jump in amplitude was recorded due to an error caused by the seismic imaging system. The magnitude of the error was ±2.5 %. For the 1st to 3rd loading cycles, a ±3.0 % error was observed (Figure 4.3.3-2 (b)). Between the two different experimental setups, i.e., from Setup 1 to Setup 2, the errors in amplitude increased up to ±5.0 %, as observed in Figure 4.3.3-2 (c).

The magnitudes of the three possible errors for the fractured aluminum specimen were comparable to those of the intact aluminum, i.e. ±4.0 % and ±5.0 % errors in total for the intact and fracture aluminum specimens, respectively. The magnitudes of the errors for the intact and fractured aluminum specimens were used as a standard to determine the quality of the data from other tests.

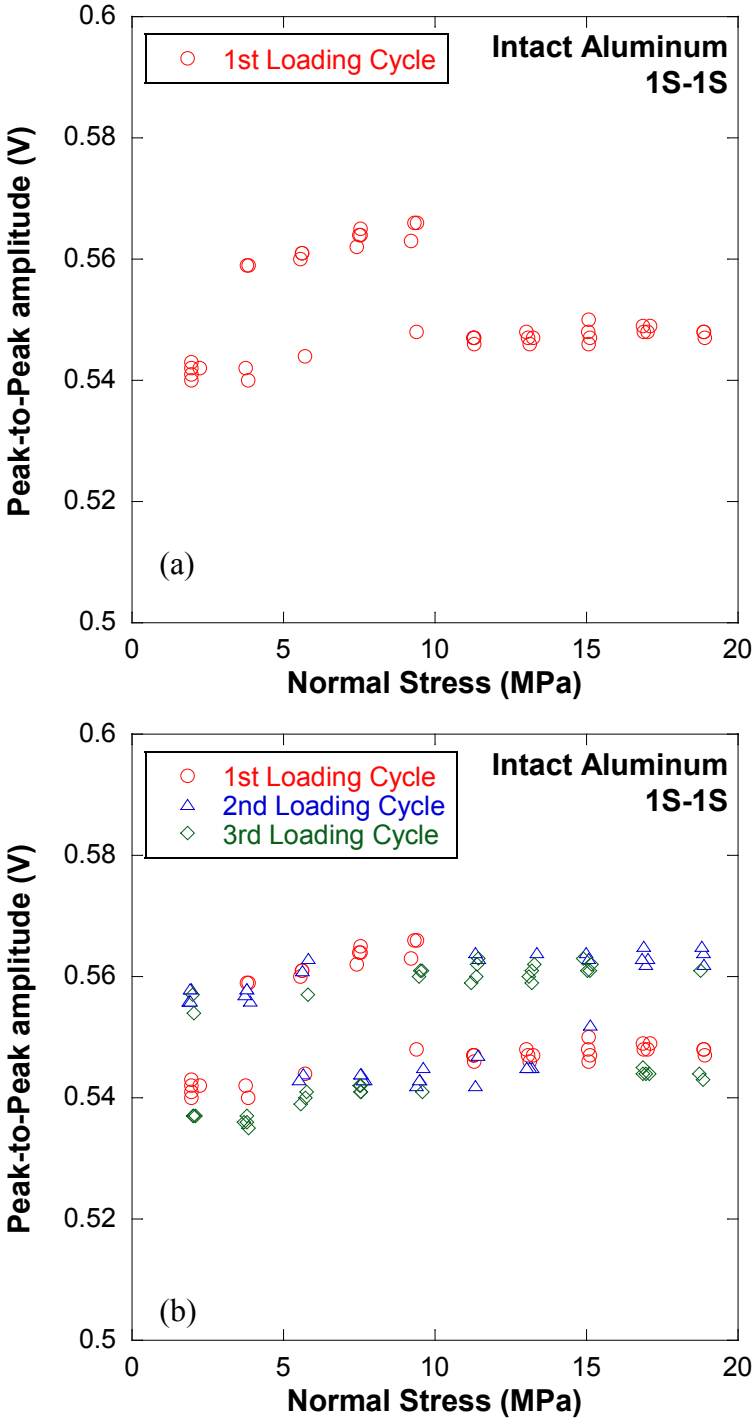

Figure 4.3.3-1. Intact Aluminum specimen. Peak-to-peak amplitude of transducer pair 1S-1S recorded during: (a) 1st loading cycle; (b) loading cycles 1st to 3rd; and (c) two different setups (continued).

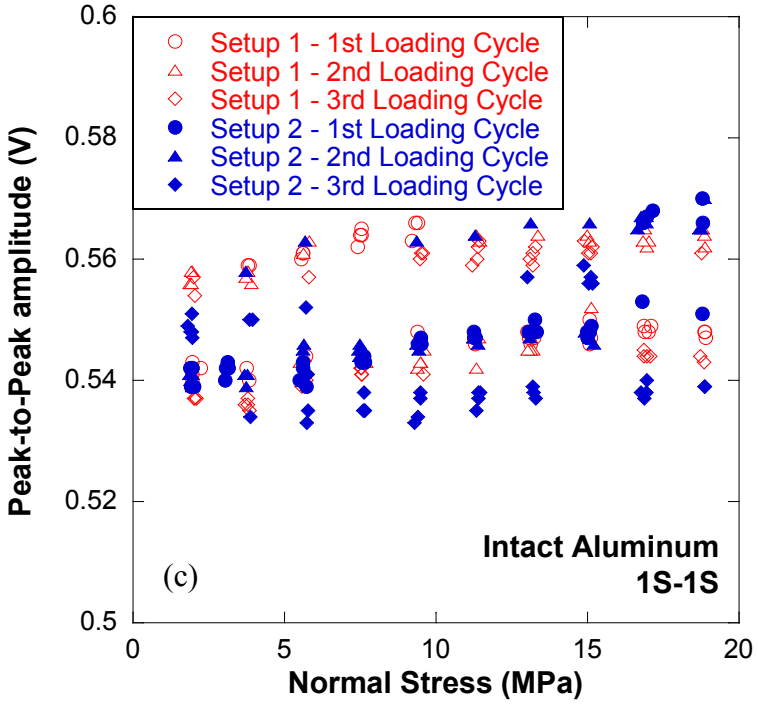

Figure 4.3.3-1. Intact Aluminum specimen. Peak-to-peak amplitude of transducer pair 1S-1S recorded during: (a) 1st loading cycle; (b) loading cycles 1st to 3rd; and (c) two different setups.

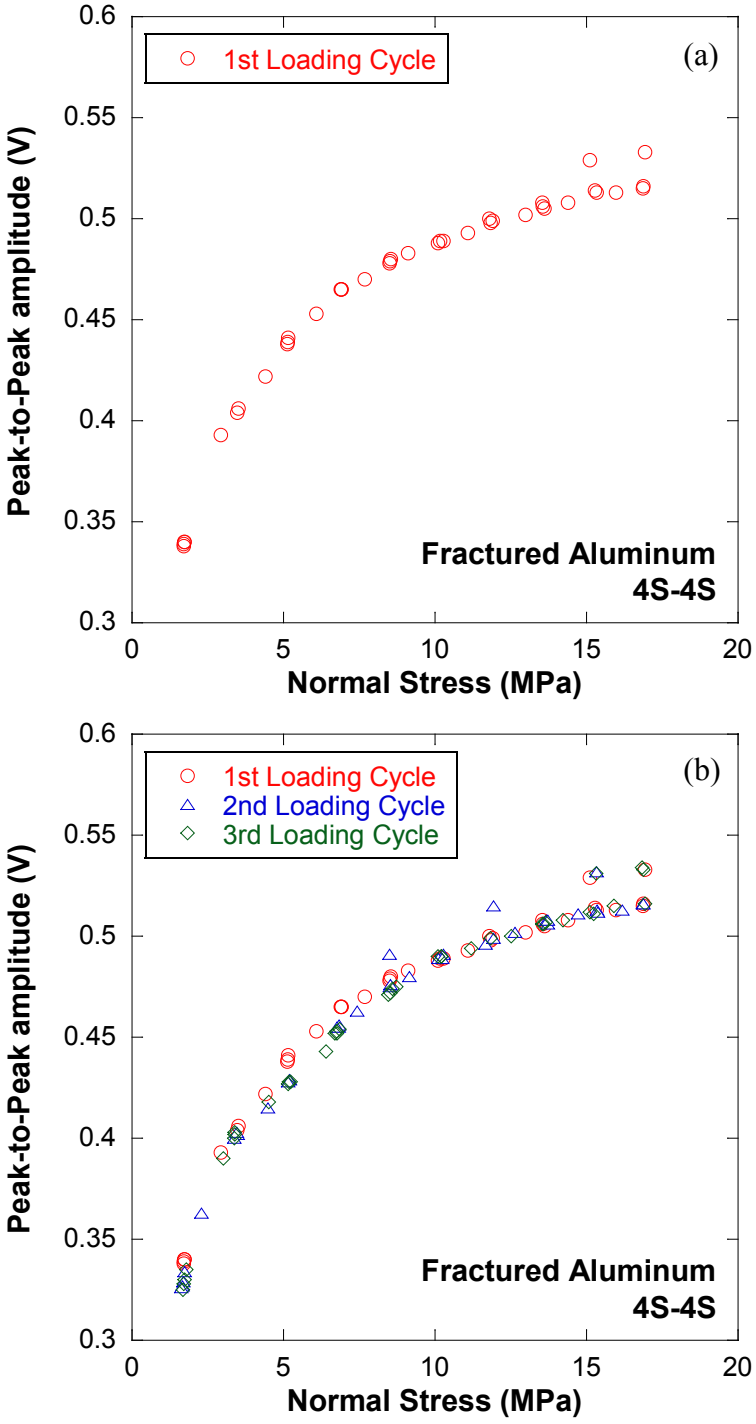

Figure 4.3.3-2. Fractured Aluminum specimen. Peak-to-peak amplitude of transducer pair 4S-4S recorded during: (a) 1st loading cycle; (b) loading cycles 1st to 3rd; and (c) two different setups (continued).

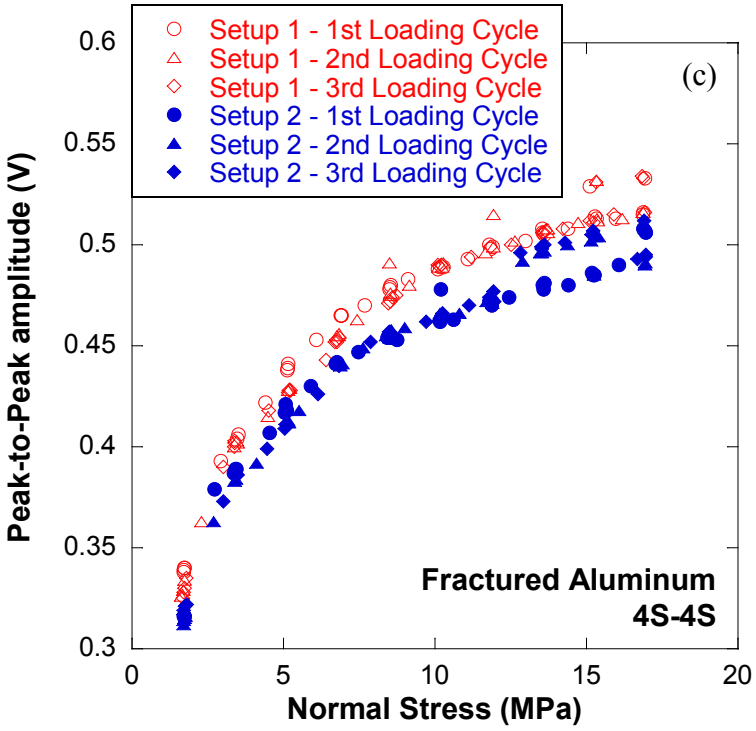

Figure 4.3.3-2. Fractured Aluminum specimen. Peak-to-peak amplitude of transducer pair 4S-4S recorded during: (a) 1st loading cycle; (b) loading cycles 1st to 3rd; and (c) two different setups.

4.3.4 Fracture Specific Stiffness of Fractured Aluminum Specimen

The displacement discontinuity theory was used to estimate the fracture specific stiffness of the fractured aluminum specimen using the measured compressional and shear wave data. The seismic measurements acquired from the intact aluminum specimen were used as a standard to estimate fracture specific stiffness. The seismic impedances were calculated by multiplying the wave velocity obtained from the intact aluminum by the density of the aluminum, which is 2.70 g/cm^3. For the fractured aluminum sample, the angle of incidence of P- and S- waves was 0˚, i.e. normal to the fracture. The estimated normal and shear fracture specific stiffnesses for the fractured aluminum specimen are shown in Figure 4.3.4-1 as a function of the applied normal stress. Error bars in the Figure shows the level of error, about ±5%. For all P- wave transducer pairs, the estimated normal fracture specific stiffness increased with increasing normal stress until a load of 7-8 MPa and then approached an asymptote at higher stresses. The shear fracture specific stiffness is categorized into two groups: group one is for the shear fracture specific stiffness estimated from the shear transducer pairs 1S-1S, 2S-2S, and 5S-5S (which had the same polarization). For these transducers, the fracture specific stiffness increased with increasing normal stress until convergence at around 2.8 TPa/m at the highest normal stress of 18.9 MPa. Group two corresponds to transducers 4S-4S and 7S-7S that had polarization perpendicular to the shear load direction. The shear fracture specific stiffness obtained from these transducers increased with increasing normal stress up to 18.9MPa and did not appear to reach an asymptote. The fracture specific stiffness estimated from each transducer pair showed spatially different values, indicating that the local fracture specific stiffness changed along the fracture plane.

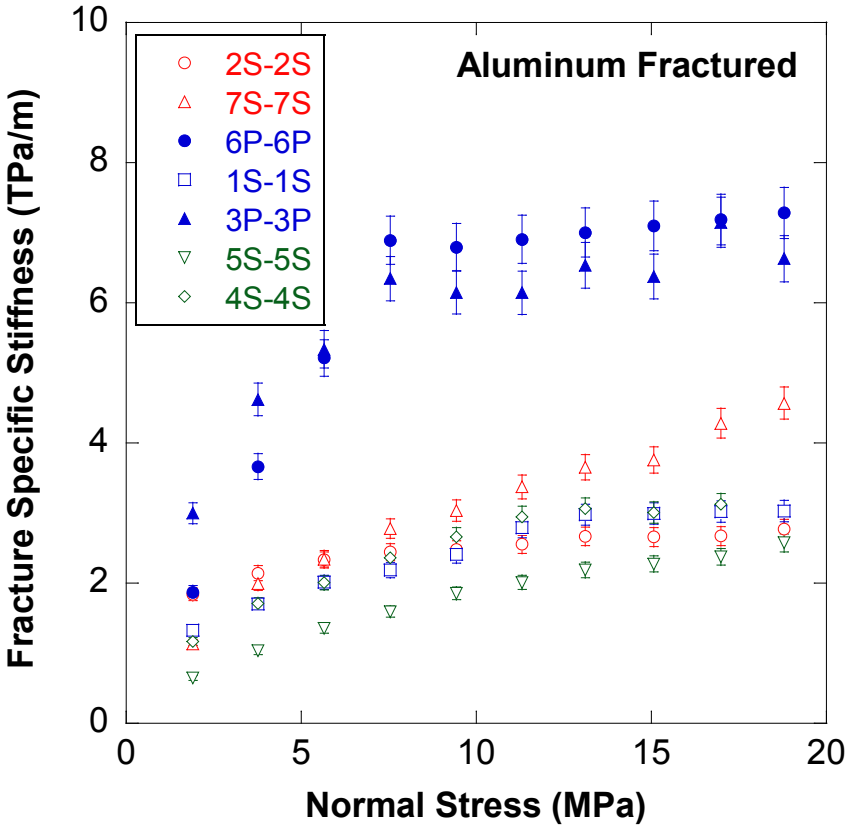

Figure 4.3.4-1. Normal and shear fracture specific stiffness for the fractured aluminum specimen as a function of normal stress. Error bars represent a ±5% error.

4.4 Seismic Response of Granite Specimens

Full waveform measurements were made during uniaxial compression experiments on the following granite specimens: intact specimens GS07, GS08, and GS09; specimens GS01 and GS04 with a 0° fracture (horizontal fracture perpendicular to the load); specimens GS03 and GS06 with a 15° fracture; and specimens GS02 and GS05 with a 30° fracture with the horizontal. The same preparation procedures as in previous tests, that include oven-dried honey, 20 hours of honey coupling, and three repetitive loading cycles were carried out. The seismic measurements obtained from the tests were interpreted using the displacement discontinuity theory.

4.4.1 Intact Granite Specimens

4.4.1.1 Peak-to-Peak Amplitude

Three intact granite samples were prepared as standard for the interpretation of the fracture specific stiffness of the fractured granite specimens. The peak-to-peak amplitudes from GS07, GS08, and GS09 (intact granite specimens) are shown in Figures 4.4.1-1 to 4.4.1-3. In contrast to the intact aluminum, the peak-to-peak amplitudes of all of the intact granite specimens increased with increasing stress. The observed stress-dependence was caused by the presence of micro-cracks in the "intact" granite matrix. The amplitudes from specimen GS07 were significantly lower (by a factor of 2 to 3) than from GS08 and GS09, which were similar to each other. The difference is attributed to the heterogeneity in the rock, i.e. material variability among the samples. This

heterogeneity in the rock is discussed at the end of this section, where the frequency contents obtained from GS07, GS08 and GS09 are compared.

4.4.1.2 Wave Velocity

Figure 4.4.1-4 shows: (a) compressional and (b) shear wave velocity measured from the intact granite specimen GS08. The gradual increase in wave velocity indicates closure of micro-cracks in the matrix. Note that the source-receiver pairs 4S-4S and 7S-7S were polarized at ninety degrees with respect to pairs 1S-1S, 2S-2S, and 5S-5S (see the transducer layout in Figure 4.2.2-1). The ratio of the two orthogonal shear velocities, e.g. 4S/1S, was about 0.9, as seen in Figure 4.4.1-4 (b). This indicates that the granite matrix was anisotropic.

Figure 4.4.1-5 compares the wave velocities measured from GS08 and GS09 for (a) P-, (b) Sv- and (c) Sh waves. The P-wave velocities are based on data from the transducer pairs 3P-3P and 6P-6P. For Sv- and Sh- waves, the wave velocities were computed from the data from 1S-1S, 2S-2S, and 5S-5S, and from 4S-4S and 7S-7S, respectively. As seen in Figure 4.4.1-5, the velocities from GS09 were slightly greater than those from GS08, regardless of the type of wave. The variation in wave velocity between the two intact specimens GS08 and GS09 was ±3-4% at a normal stress of 1.89 MPa and gradually decreased to ±1% at 18.9 MPa. The difference in wave velocity between the two intact specimens is small enough such that it can be neglected. The wave velocities were used to calculate the seismic impedance of the granite matrix as a function of stress. The density of the granite used for stiffness calculations was 2.70 g/cm^3 (Jaeger et al. 2007).

4.4.1.3 Spectral Analysis

The Fourier transforms of the signals from transducer pairs1S-1S and 3P-3P are shown in Figure 4.4.1-6 for different normal stresses. As observed in the peak-to-peak amplitudes and wave velocity, the spectral amplitude increased with increasing stress. A shift in the dominant frequency to higher frequencies with increasing stress is an indicator of the closure of micro-cracks in the granite matrix. For P-waves, the dominant frequency at high stresses was 0.5 MHz, and for S-waves, 0.3MHz. The spectral amplitude and dominant frequency appeared to approach an asymptote at high stress, similar to what was observed for the peak-to-peak amplitude and wave velocities.

The frequency content of all the intact granite samples is compared in Figure 4.4.1-7. In the Figure, the dominant frequency and corresponding spectral amplitude at each loading step is normalized by the maximum dominant frequency and corresponding maximum spectral amplitude, respectively. The normalized spectral amplitudes are plotted with respect to the normalized dominant frequency. Note that the normalized dominant frequency and the normalized spectral amplitude converge to a single line regardless of the type of wave, i.e. compressional or shear, or the location of the source-receiver pair. While GS08 and GS09 specimens exhibited narrower and smaller variations in frequency and amplitude (Figure 4.4.1-7 (b) and (c)), the spectral contents for signals from GS07 exhibited a larger change in frequency and larger increase in amplitude (Figure 4.4.1-7 (a)), which was the result of the heterogeneity of the granite matrix, as mentioned previously. Given these results, the specimen GS07 was excluded as a standard, and GS08 and GS09 were used for stiffness calculations.

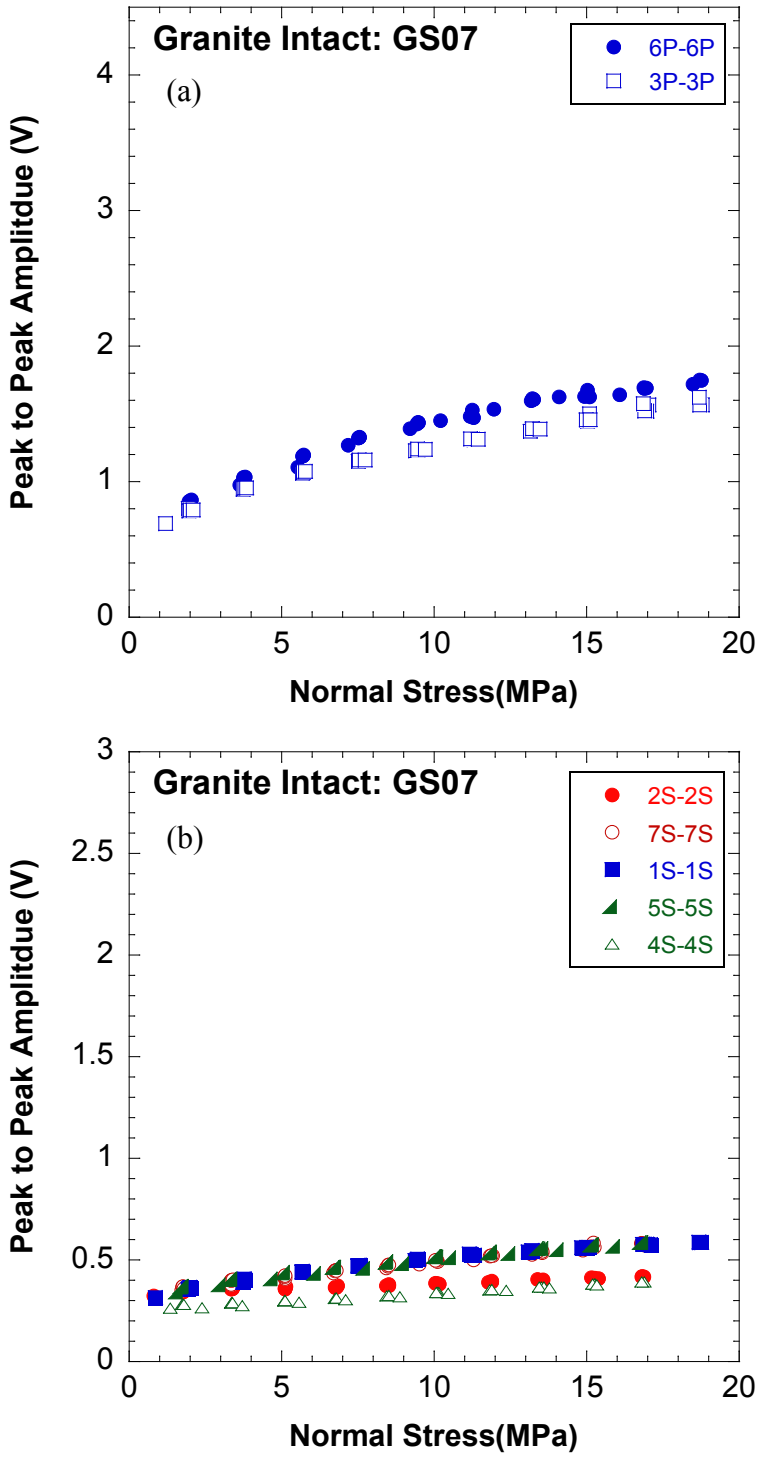

Figure 4.4.1-1. Intact granite sample GS07. Peak-to-peak amplitude for: (a) compressional wave; and (b) shear wave, as a function of normal stress.

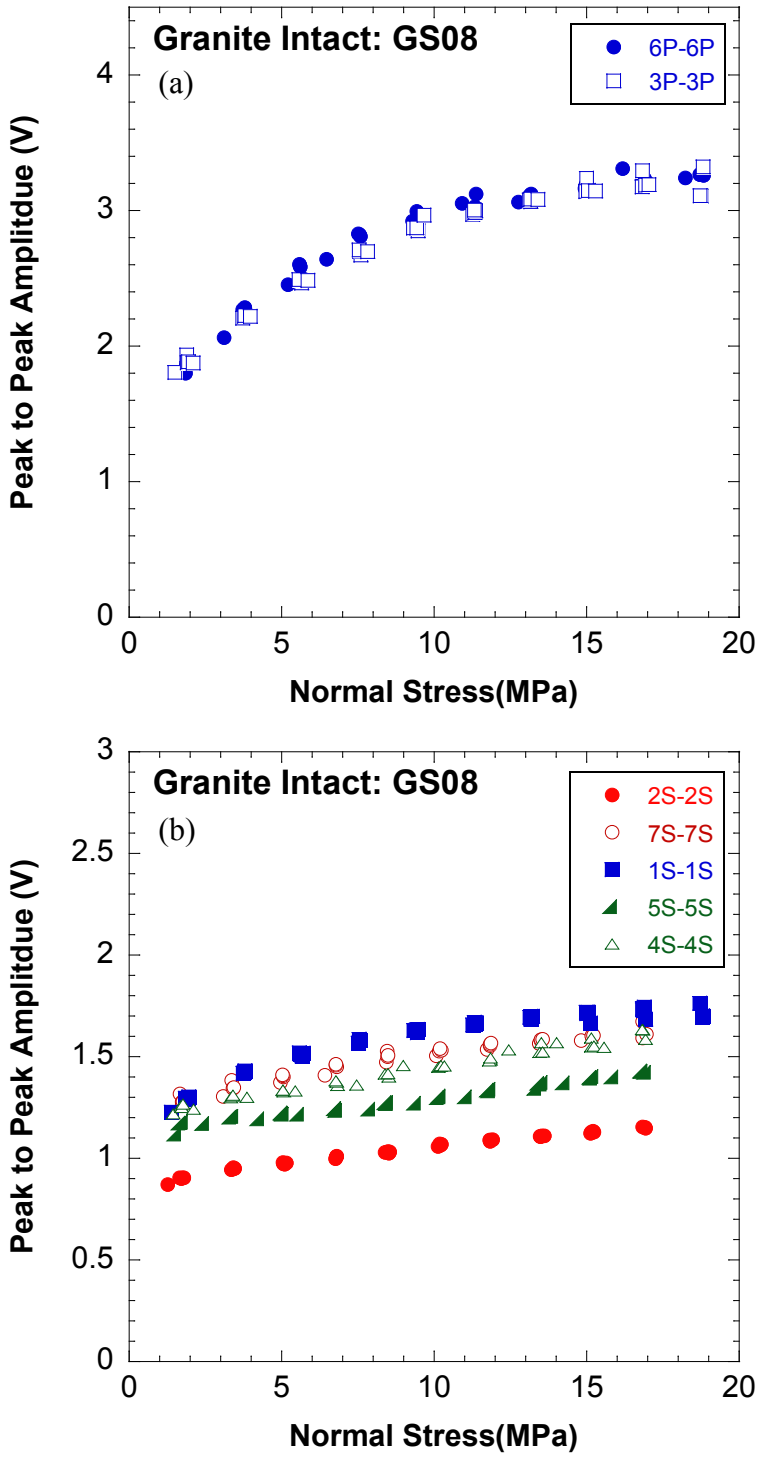

Figure 4.4.1-2. Intact granite sample GS08. Peak-to-peak amplitude for: (a) compressional wave, and (b) shear wave, as a function of normal stress.

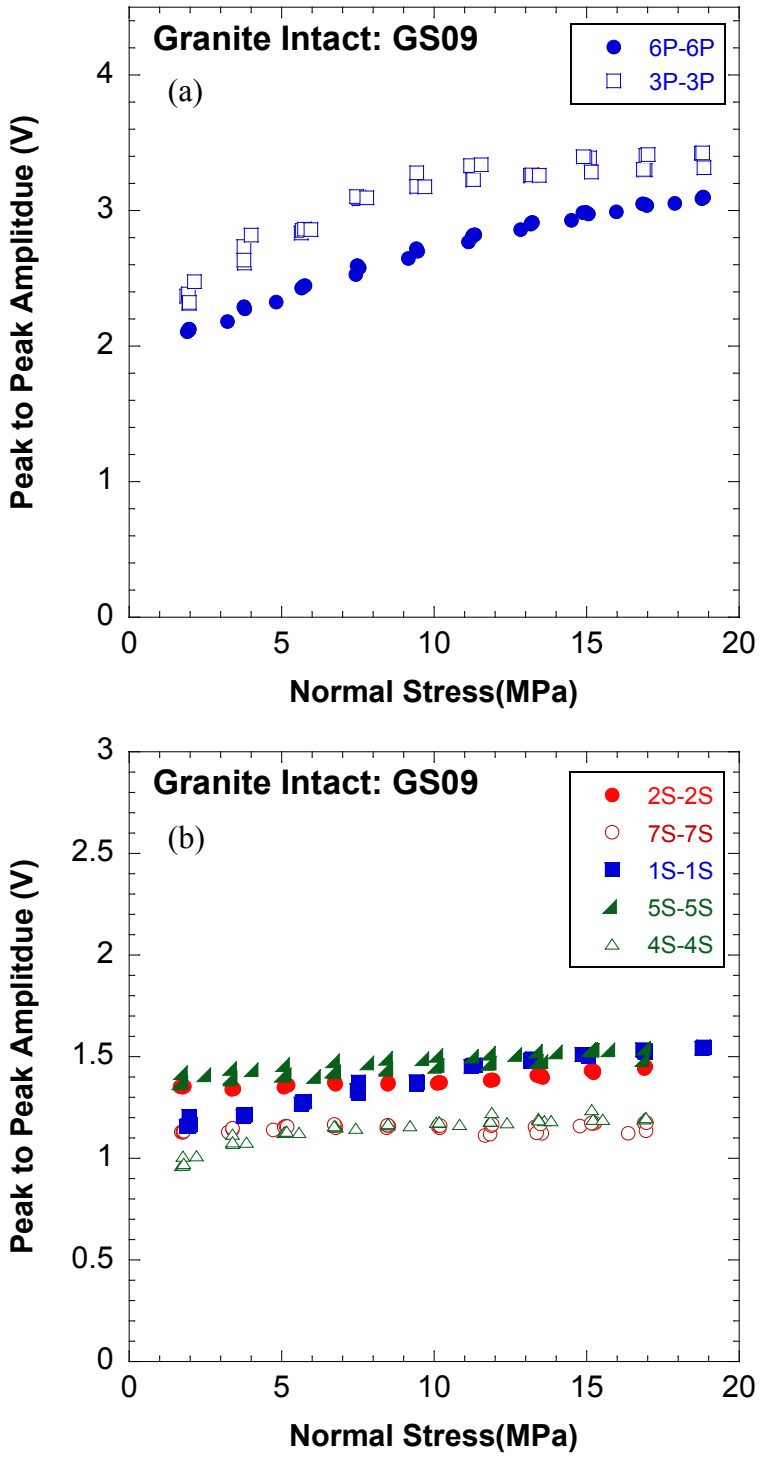

Figure 4.4.1-3. Intact granite sample GS09. Peak-to-peak amplitude for: (a) compressional wave, and (b) shear wave, as a function of normal stress.

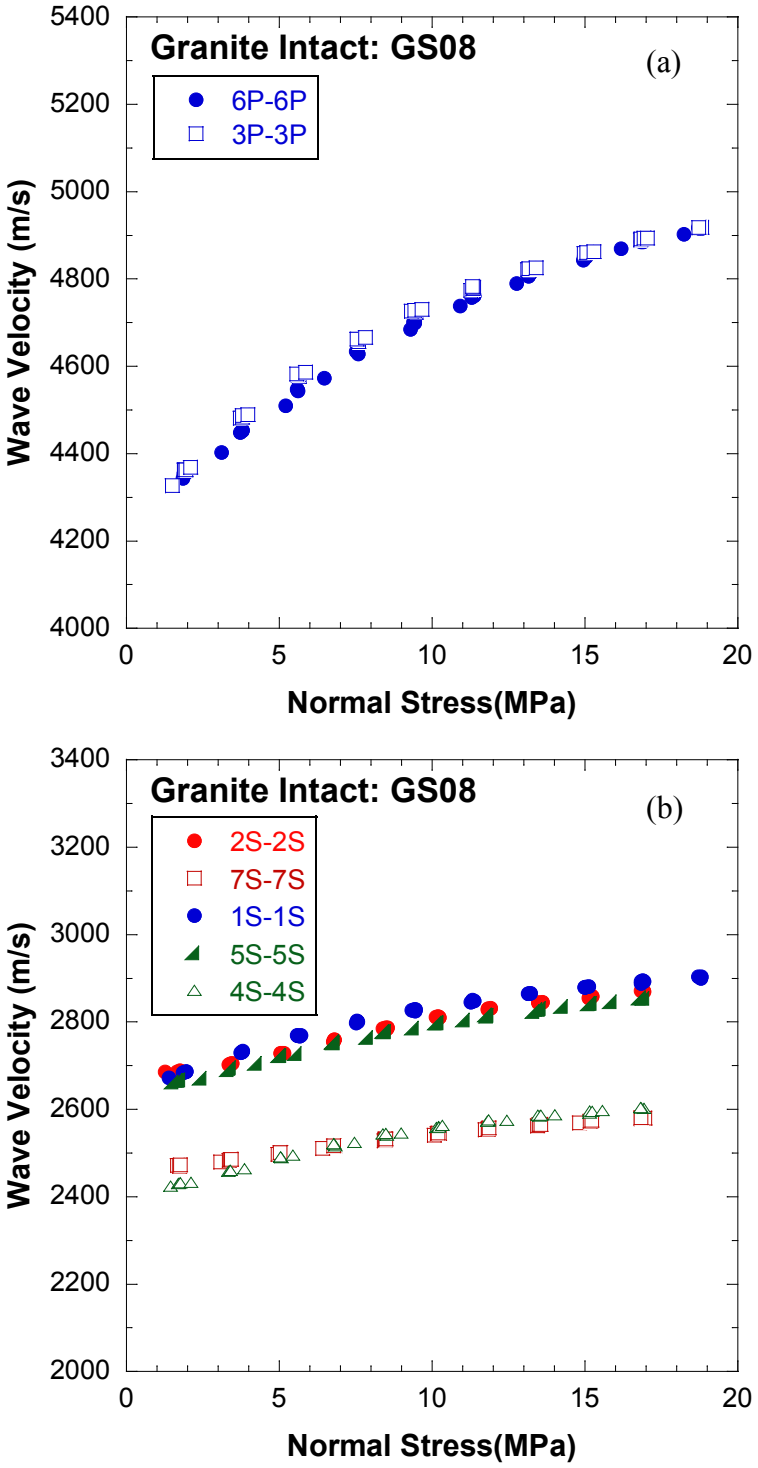

Figure 4.4.1-4. Intact granite sample GS08. Wave velocity for: (a) compressional wave; and (b) shear wave, as a function of normal stress.

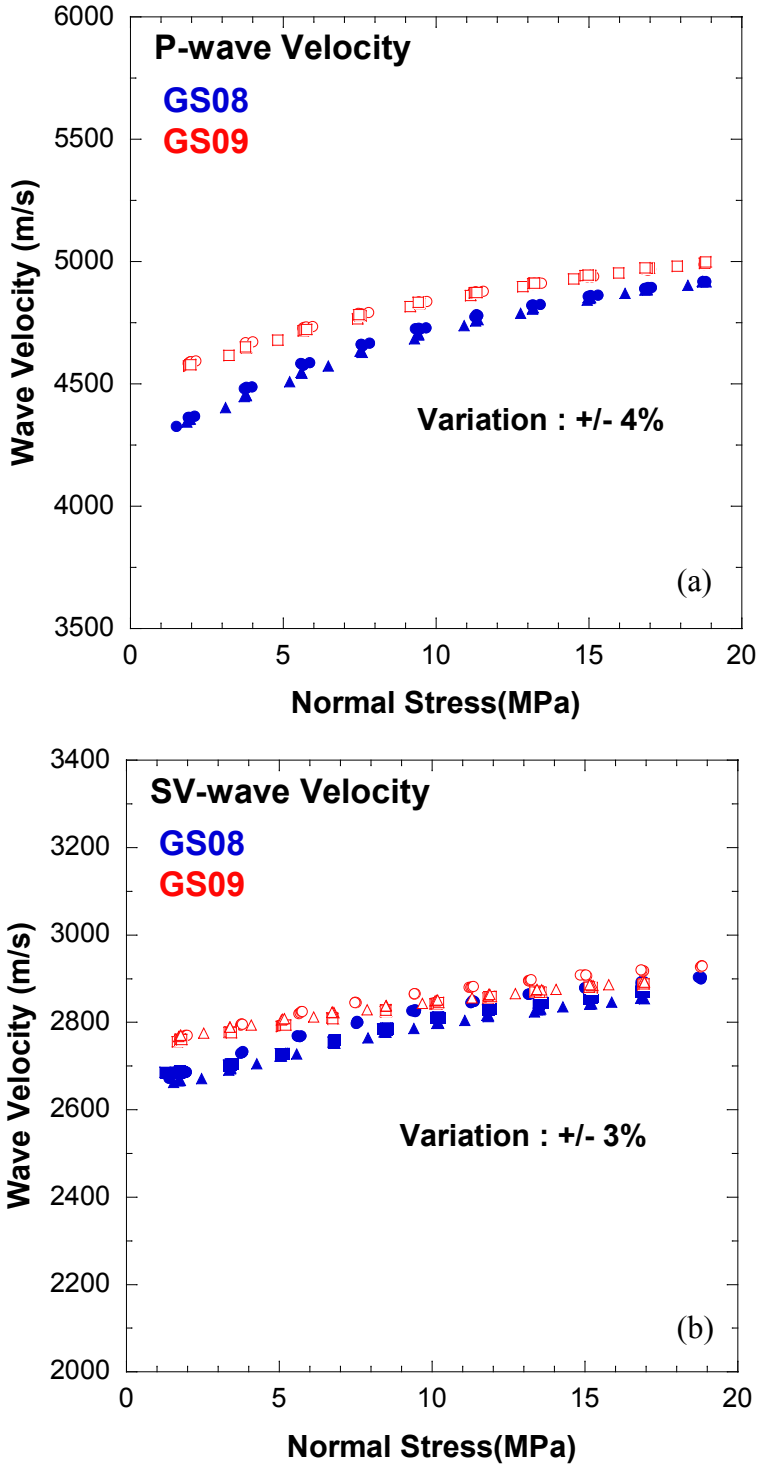

Figure 4.4.1-5. Wave velocities from GS08 (closed blue symbols) and GS09 (open red symbols) for: (a) P-, (b) Sv-,. and (c) Sh- waves. P- wave velocities were measured from 3P-3P and 6P-6P, Sv- wave velocities from 1S-1S, 2S-2S, and 5S-5S; and Sh- wave velocities from 4S-4S and 7S-7S (continued).

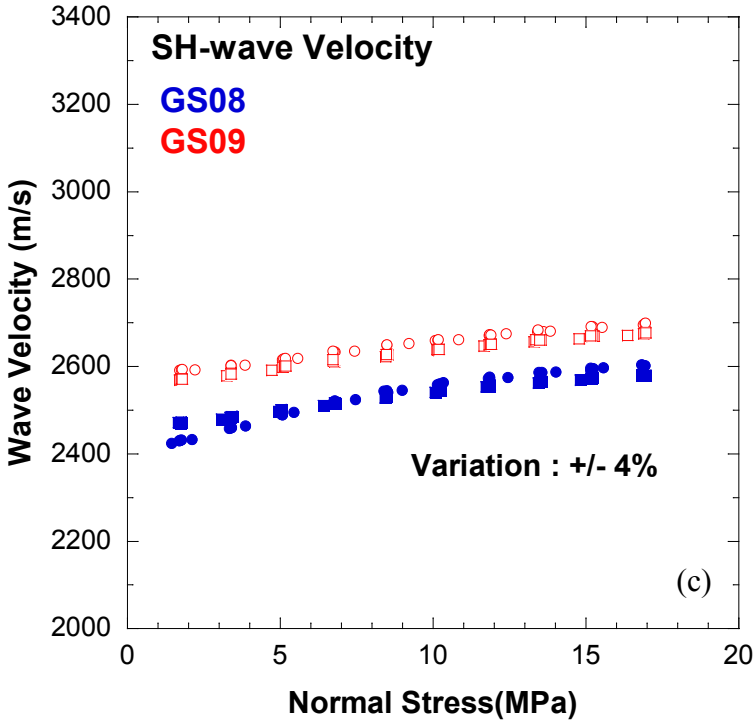

Figure. 4.4.1-5. Wave velocities from GS08 (closed blue symbols) and GS09 (open red symbols) for: (a) P-, (b) Sv-,. and (c) Sh- waves. P- wave velocities were measured from 3P-3P and 6P-6P, Sv- wave velocities from 1S-1S, 2S-2S, and 5S-5S; and Sh- wave velocities from 4S-4S and 7S-7S.

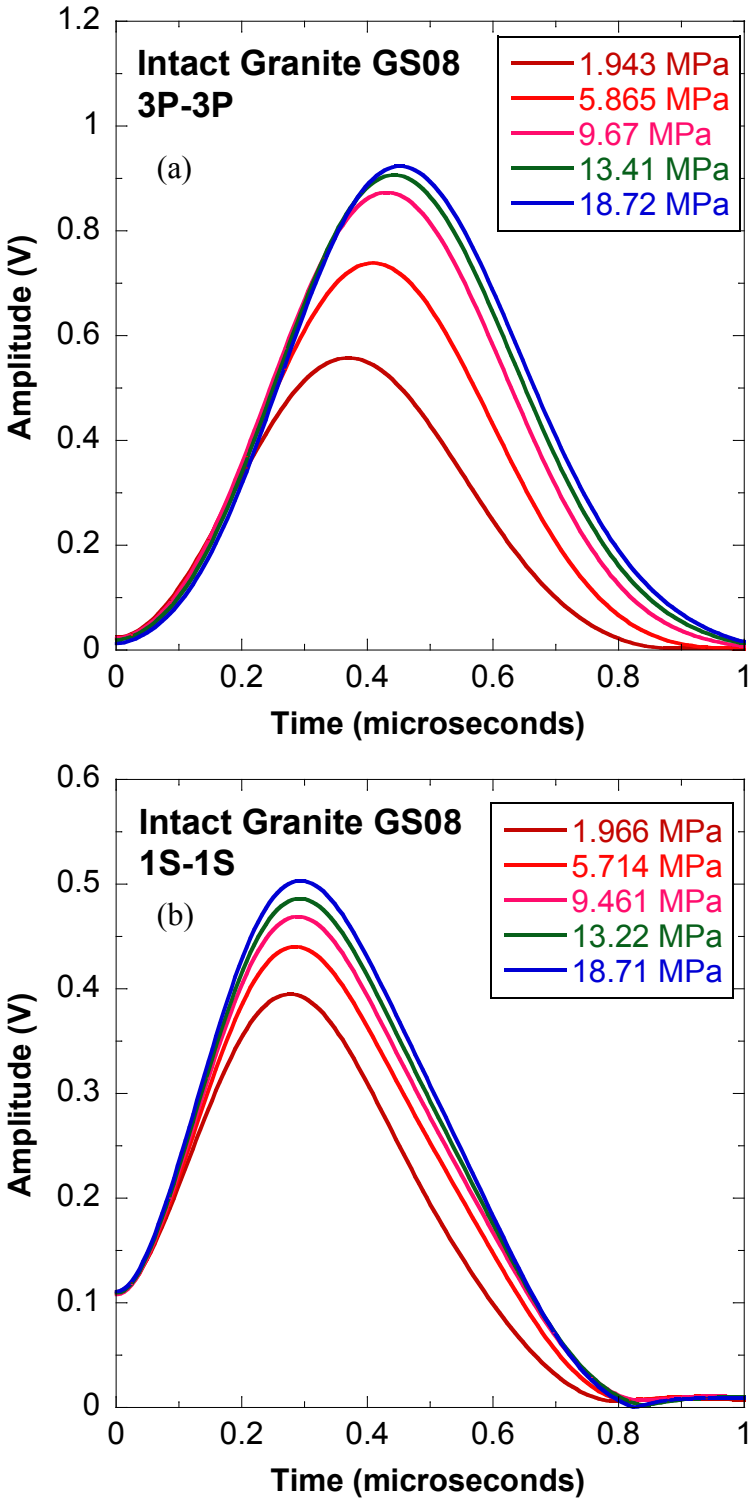

Figure 4.4.1-6. Fractured granite sample GS08. Fourier spectrum for: (a) compressional wave; and (b) shear wave, as a function of normal stress.

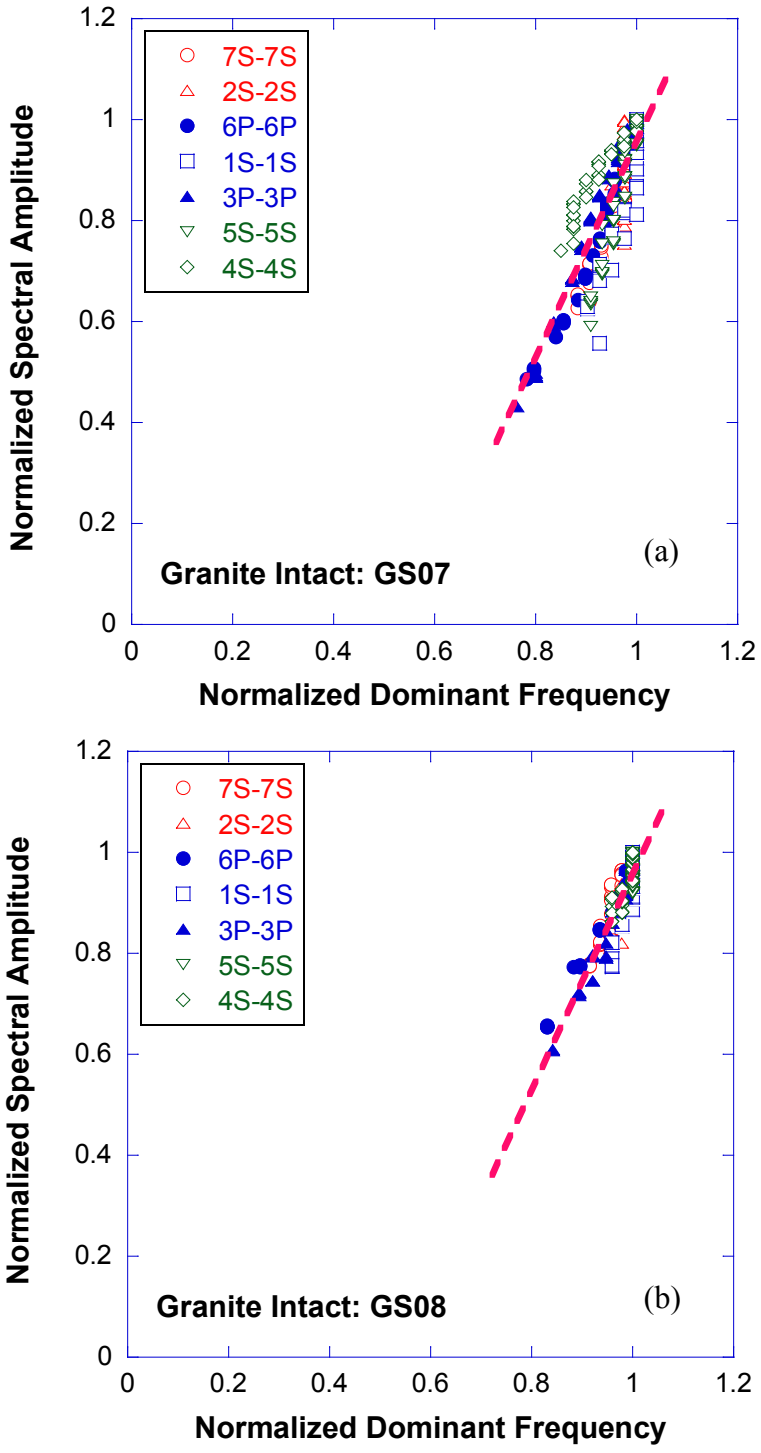

Figure 4.4.1-7. Normalized spectral amplitudes with respect to normalized dominant frequency for intact granite samples: (a) GS07; (b) GS08; and (c) GS09 (continued).

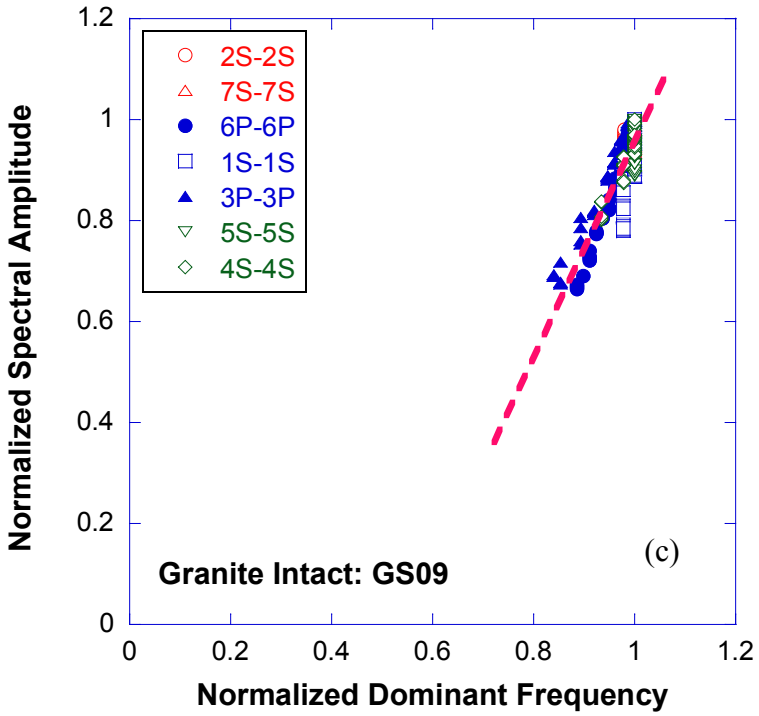

Figure 4.4.1-7. Normalized spectral amplitudes with respect to normalized dominant frequency for intact granite samples: (a) GS07; (b) GS08; and (c) GS09.

4.4.2 Fractured Granite Specimens

Fractured granite specimens were prepared to have three different fracture angles: 0°, 15°, and 30°, with respect to the horizontal; see Table 4.2.1-1. For clarity, the results from specimens GS01 and GS04, with a 0° fracture, are presented first, and then from specimens with an angled fracture.

4.4.2.1 Full Waveforms

Figures 4.4.2-1 and 4.4.2-2 show the compressional and shear waves measured with P- and S- wave transducer pairs 3P-3P and 1S-1S, taken from GS08 (intact specimen) and GS01 (with a horizontal fracture). Figure 4.4.2-1 presents the results from P transducers and Figure 4.4.2.-2 from S transducers. The figures show that both amplitude and wave velocity increased with increasing normal stress. Similar observations can be made for the other intact granite specimen GS09 and for GS04, the granite specimen with a horizontal fracture, as shown in Figures 4.4.2-3 and 4.4.2-4. For intact specimens GS08 and GS09, the increase of peak-to-peak amplitude and wave velocity with increasing stress occurred because of the closure of pre-existing micro-cracks in the granite matrix. For fractured samples GS01 and GS04, the closure of the fracture as well as the closure of the micro-cracks in the granite matrix produced an increase of amplitude and velocity.

Figures 4.4.2-5 to 4.4.2-8 show representative (a) compressional and (b) shear waves measured with transducer pairs 3P-3P and 1S-1S taken from granite specimens with an angled fracture. Note that specimens GS03 and GS06 in Figures 4.4.2-5 and 4.4.2-6 have a 15° fracture, and GS02 and GS05 in Figures 4.4.2-7 and 4.4.2-8 have a 30° fracture.

Similar to the results from GS01 and GS04 with a horizontal fracture, both the amplitude and wave velocity increased with increasing normal stress in granite specimens with an angled fracture. The increase in amplitude and wave velocity arises from the closure of the fracture as well as of the micro-cracks in the granite matrix.

4.4.2.2 Peak-to-Peak Amplitude

A significant increase in the peak-to-peak amplitude was observed in the specimens with a fracture and for all transducer pairs. The increase in amplitude of the signals was larger than in intact specimens GS08 and GS09.

Figures 4.4.2-9 and 4.4.2-10 contain the peak-to-peak amplitude for all transducer pairs used in GS01 and GS04, respectively. For example, the peak-to-peak amplitude of the compressional wave from 3P-3P from specimen GS01 increased from 0.5 to 2.3 (a factor of 4.6) over the range of the applied normal stresses (1.9 MPa to 18.9 MPa), while the amplitudes for the specimen GS08 (intact granite) increased only by a factor of 1.7 over the same range of normal stresses. Figure 4.4.2-11 compares the variation in peak-to-peak amplitudes from GS01 (green), normalized with respect to the amplitudes at a normal stress of 1.9 MPa, with those of GS08 (red) and GS09 (blue). It is clear that the existence of a fracture in GS01 produced a substantial increase of amplitudes. As the normal stress increased, the fracture closed and the transmission of P- and S- waves was enhanced such that the amplitude of the transmitted waves increased. Hence the increasing amplitude of the transmitted wave denotes an increase of fracture specific stiffness.

Figures 4.4.2-12 to 4.4.2-15 present the peak-to-peak amplitudes measured on the specimens with an angled fracture, i.e., 15° fracture (GS03 and GS06) and 30° fracture (GS02 and GS06). Similar to the horizontally fractured specimens, the peak-to-peak amplitudes from specimens with an angled fracture increased with increasing normal stress, indicating the increase of the fracture specific stiffness.

4.4.2.3 Spectral Analysis

Fourier transforms of the recorded signals were performed after applying a taper to isolate the first arrival signal from subsequent reflections. The taper combined an open step function with a duration of 1.28 μsec with one-half close cosine of 3.84 μsec. The Fourier spectral amplitudes for (a) compressional and (b) shear waves from specimens GS01 and GS04 are shown in Figure 4.4.2-16 and Figure 4.4.2-17, respectively, for a range of normal stresses 0-18.9 MPa. The amplitude of the spectrum increased with increasing stress. The spectral content of the compressional (3P-3P) and shear (1S-1S) waves recorded on specimen GS01 shows that the dominant frequency increased with stress compared to the intact specimen GS08. Also, the change in amplitude of the spectra was larger for the fractured specimen than for the intact specimen. For example, for the transducer pair 3P-3P, the dominant frequency increased from 0.39 MHz to 0.47 MHz (21% increase) for intact specimen GS08, while for GS01 it increased from 0.30 MHz to 0.42 MHz (40% increase).

Figure 4.4.2-18 compares the dominant frequency of the signal from fractured specimens GS01 to GS06 with intact specimens GS08 and GS09. In the Figure, the dominant

frequencies for GS08 and GS09 (intact specimens) are represented by a red color, blue for GS01 and GS04 (specimens with a fracture at 0° angle), green for GS03 and GS06 (15° angle), and purple for GS02 and GS06 (30° angle). Figures 4.4.2-18 (a) and (b) show that, for compressional waves (i.e., transducer pairs 3P-3P and 6P-6P), the upper bound of the dominant frequency is the dominant frequency measured from the intact specimens GS08 and GS09 for normal stresses in the range 0-18.9 MPa. The dominant frequency of the intact specimens increased from around 0.4 MHz and approached 0.45-0.48 MHz. For the fractured granite specimens GS01 to GS06, the increase in the dominant frequency of the compressional wave was substantial, changing from 0.28 MHz to 0.48 MHz.

The dominant frequency for shear waves (Figures 4.4.2-18 (c) to (g)) ranged, in general, from 0.2 MHz to 0.3 MHz for normal stresses up to 18.9 MPa. For the intact specimens GS08 and GS09, the dominant frequency of the shear waves remained almost unchanged, roughly at 0.27-0.31 MHz for the normal stress range 0-18.9 MPa. However, the fractured granite specimens GS01 to GS06 had dominant frequencies that increased from 0.2 MHz and approached 0.3 MHz. At the highest normal stress of 18.9 MPa, the dominant frequencies of the intact and fractured specimens were similar and equal to 0.3 MHz.

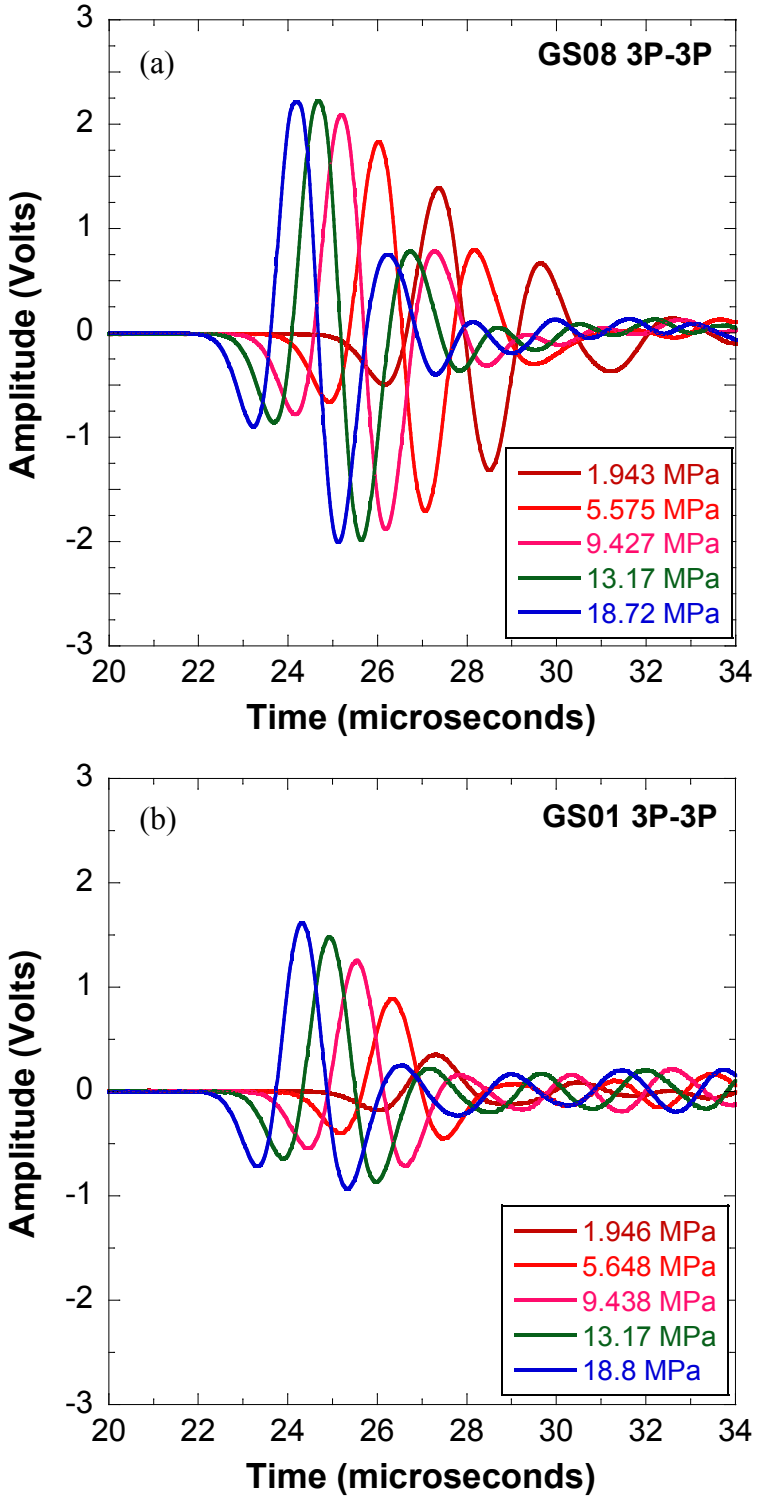

Figure 4.4.2-1. Full waveforms of compressional wave from 3P-3P for: (a) intact granite sample GS08; and (b) GS01 with a 0˚ fracture.

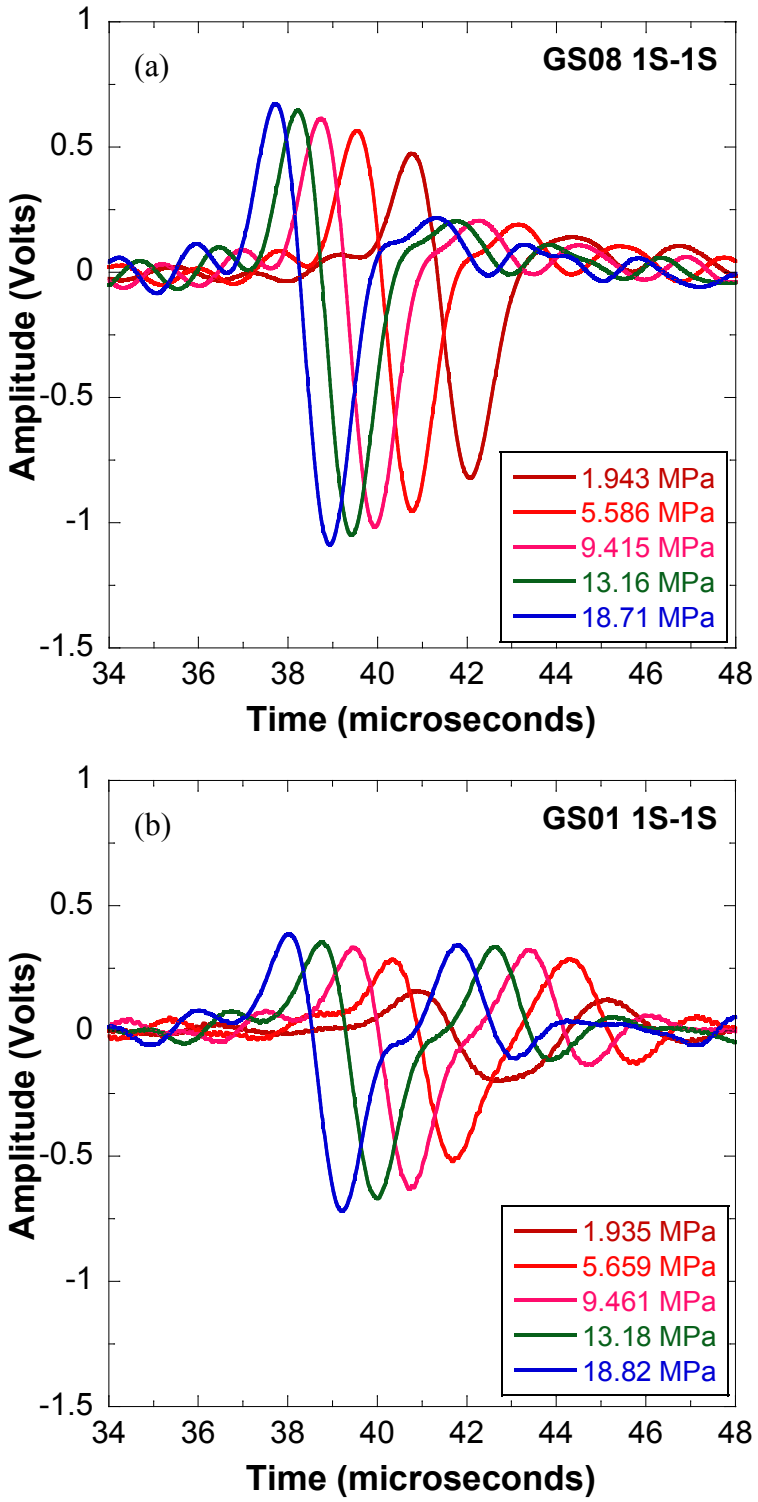

Figure 4.4.2-2. Full waveforms of shear wave from 1S-1S for: (a) intact granite sample GS08 and (b) GS01 with 0˚ fracture.

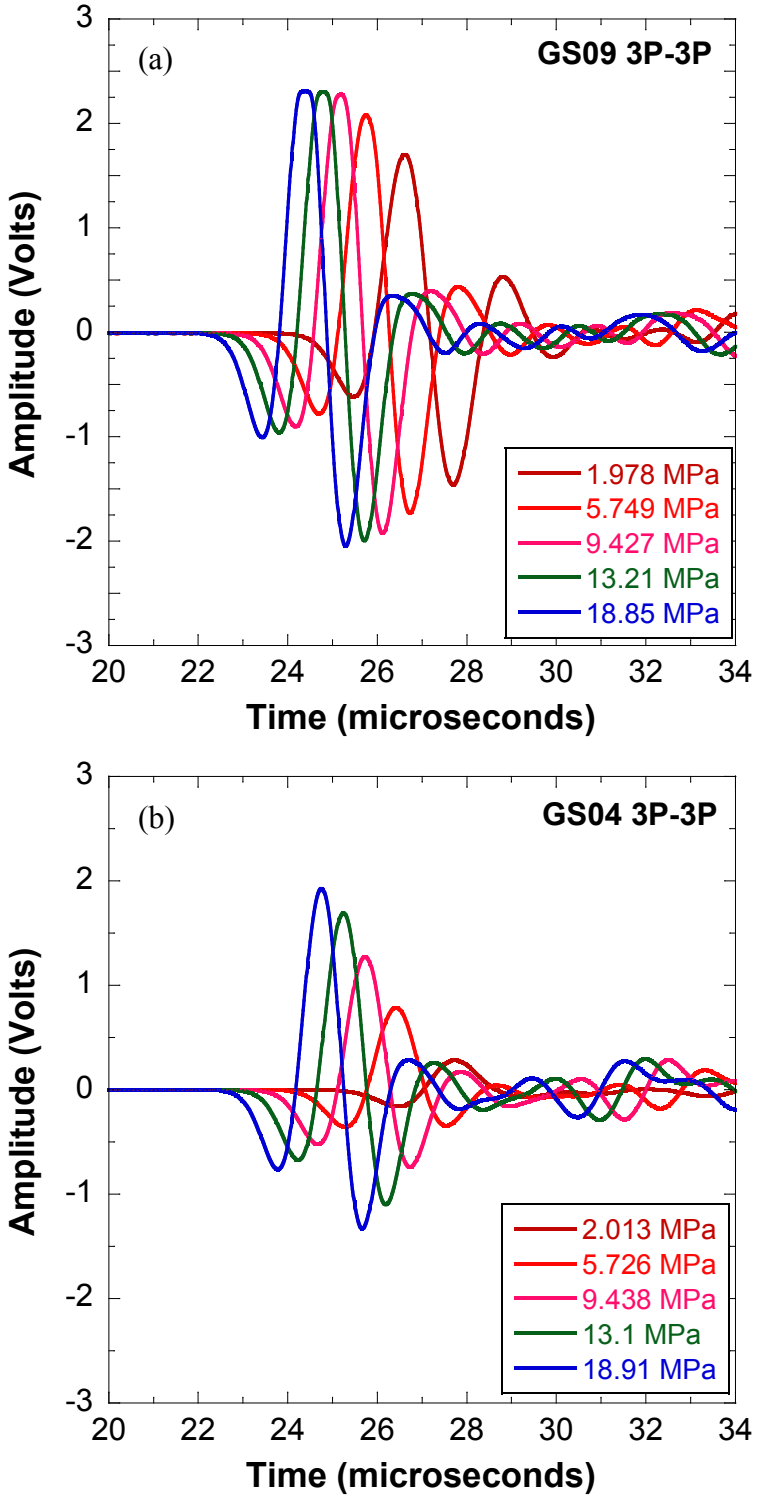

Figure 4.4.2-3. Full waveforms of compressional wave from 3P-3P for: (a) intact granite sample GS09; and (b) GS04 with 0˚ fracture.

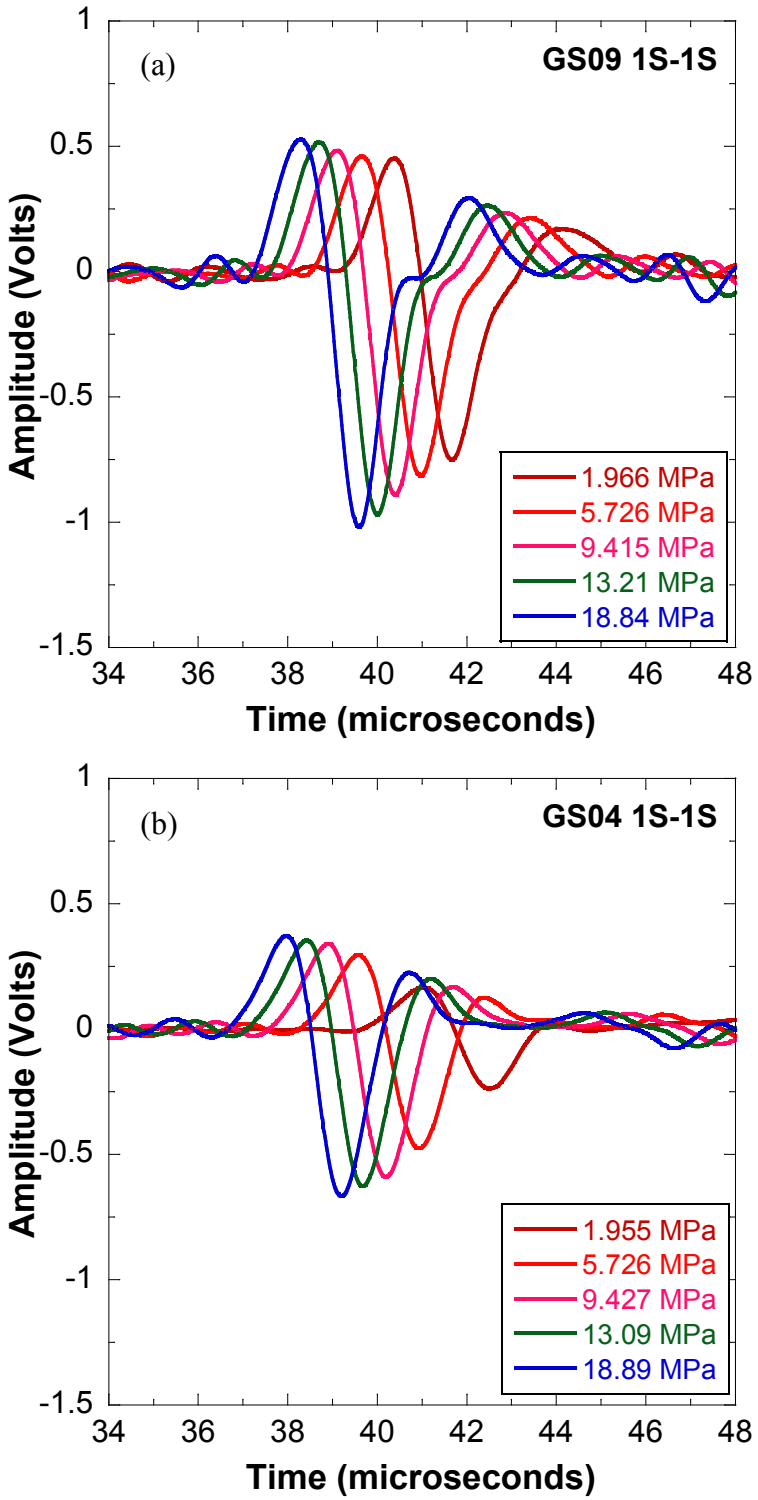

Figure 4.4.2-4. Full waveforms of shear wave from 1S-1S for: (a) intact granite sample GS09; and (b) GS04 with 0˚ fracture.

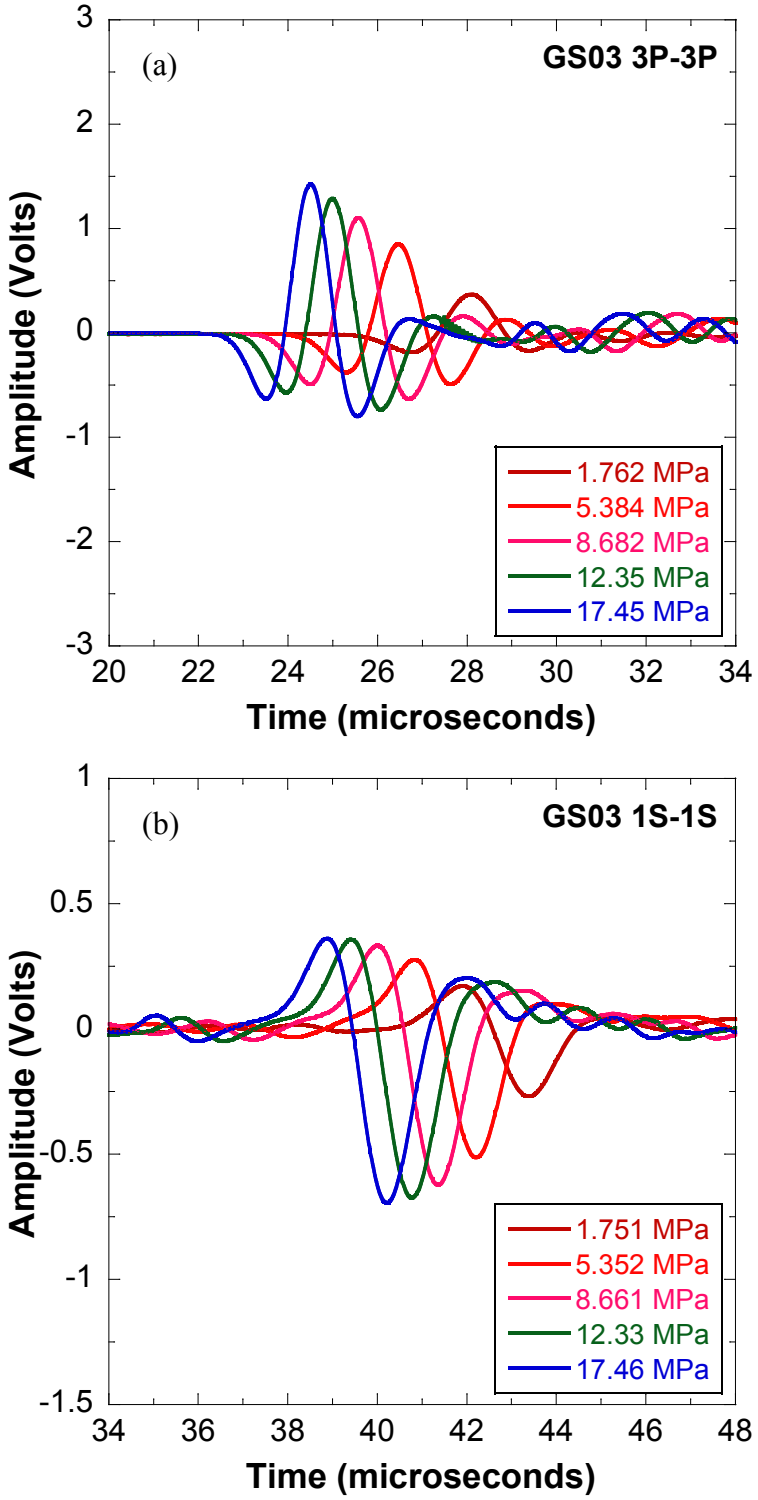

Figure 4.4.2-5. Full waveforms of: (a) compressional wave from 3P-3P; and (b) shear wave from 1S-1S. Specimen GS03 with a 15˚ fracture.

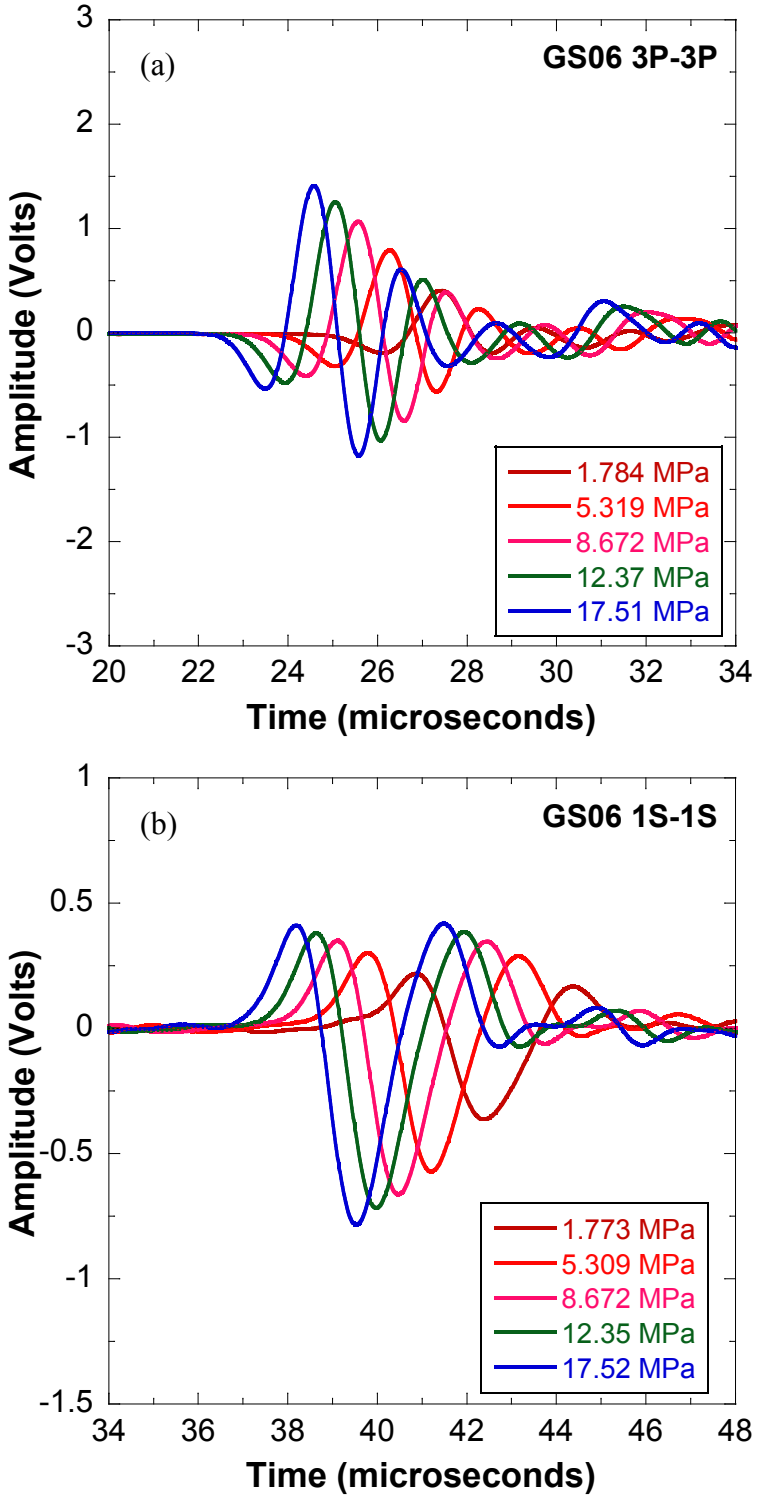

Figure 4.4.2-6. Full waveforms of: (a) compressional wave from 3P-3P; and (b) shear wave from 1S-1S. Specimen GS06 with 15˚ fracture.

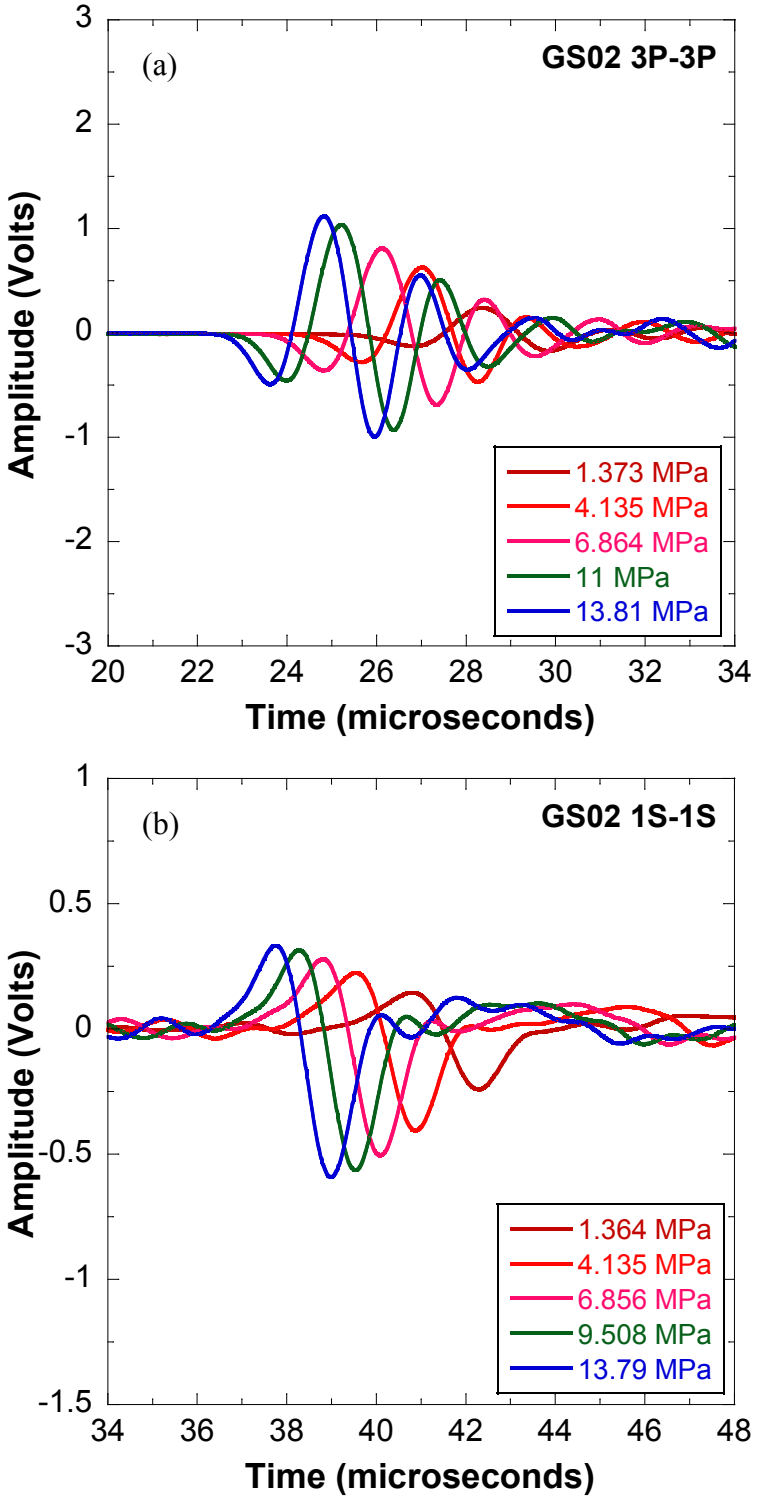

Figure 4.4.2-7. Full waveforms of: (a) compressional wave from 3P-3P; and (b) shear wave from 1S-1S. Specimen GS02 with 30˚ fracture.

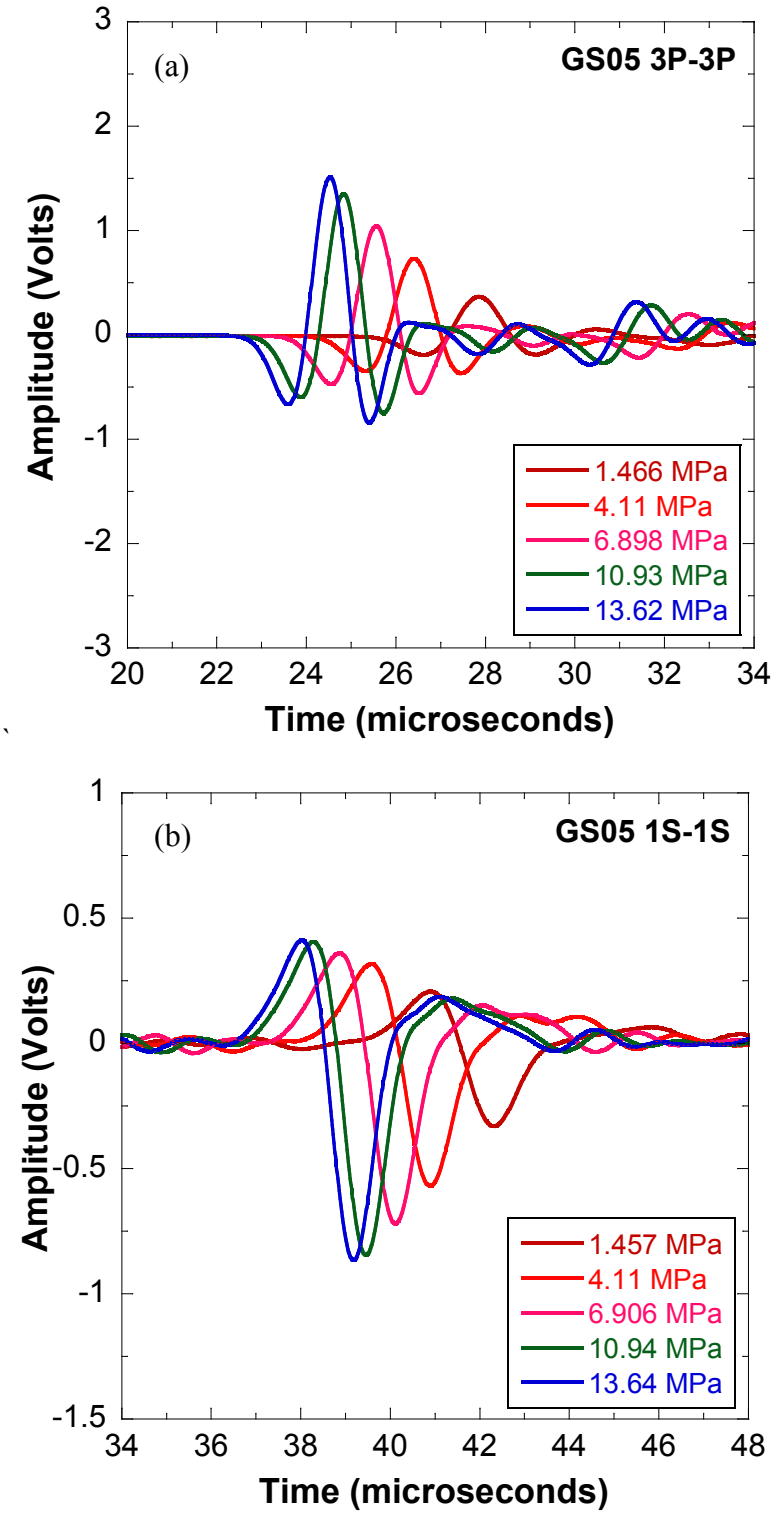

Figure 4.4.2-8. Full waveforms of: (a) compressional wave from 3P-3P; and (b) shear wave from 1S-1S. Specimen GS05 with 30˚ fracture.

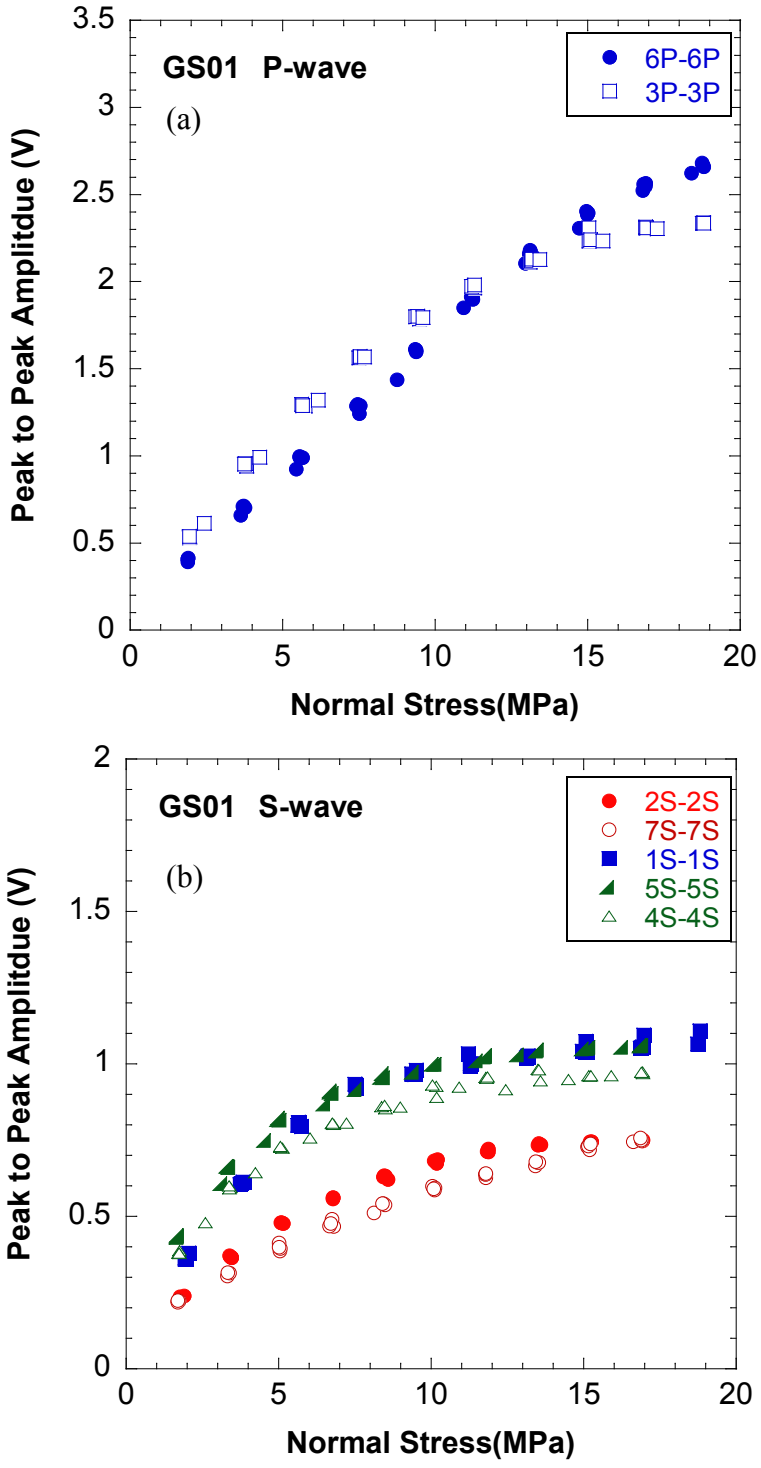

Figure 4.4.2-9. Peak-to-peak amplitude for: (a) compressional wave; and (b) shear wave, with normal stress. Specimen GS01 with 0˚ fracture.

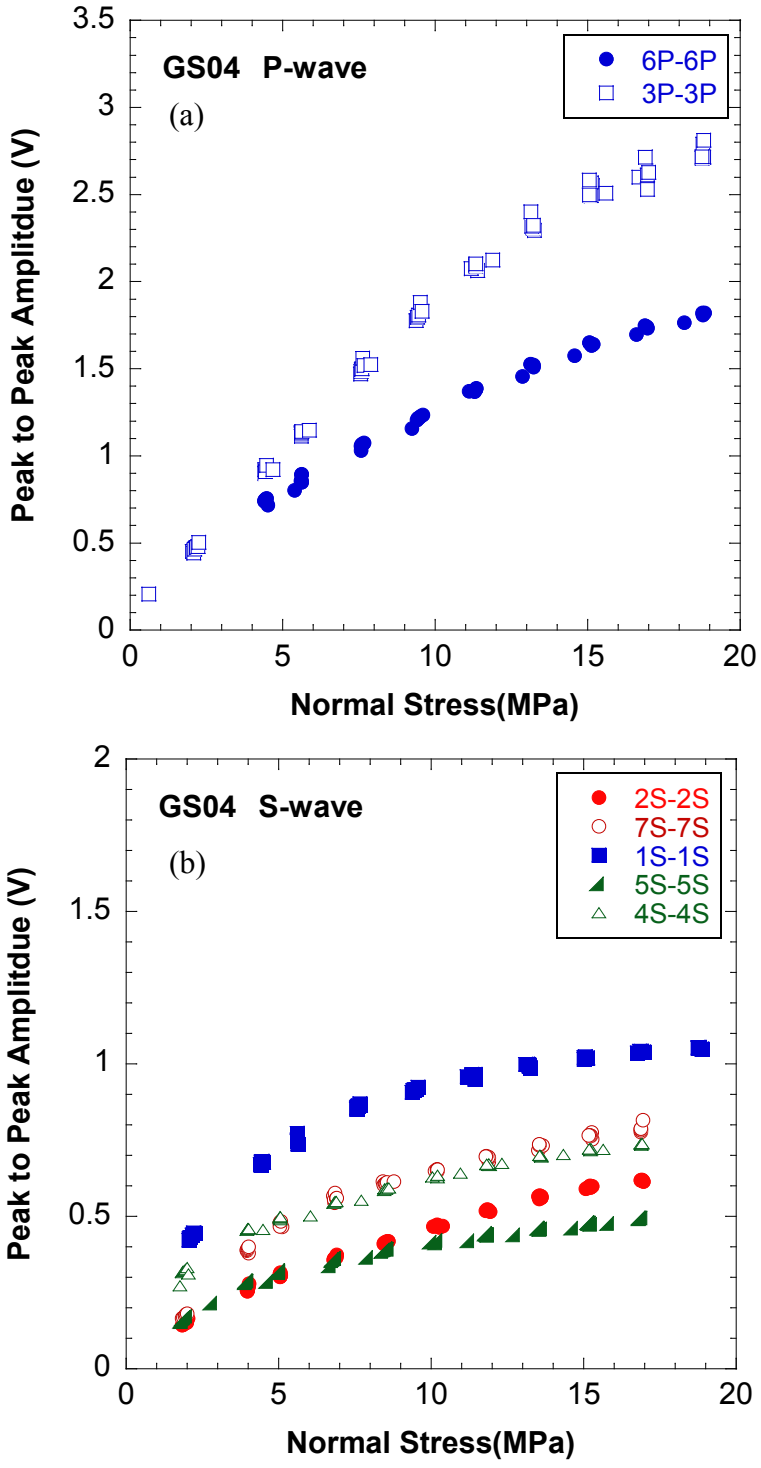

Figure 4.4.2-10. Peak-to-peak amplitude for: (a) compressional wave; and (b) shear wave, with normal stress. Specimen GS04 with 0˚ fracture.

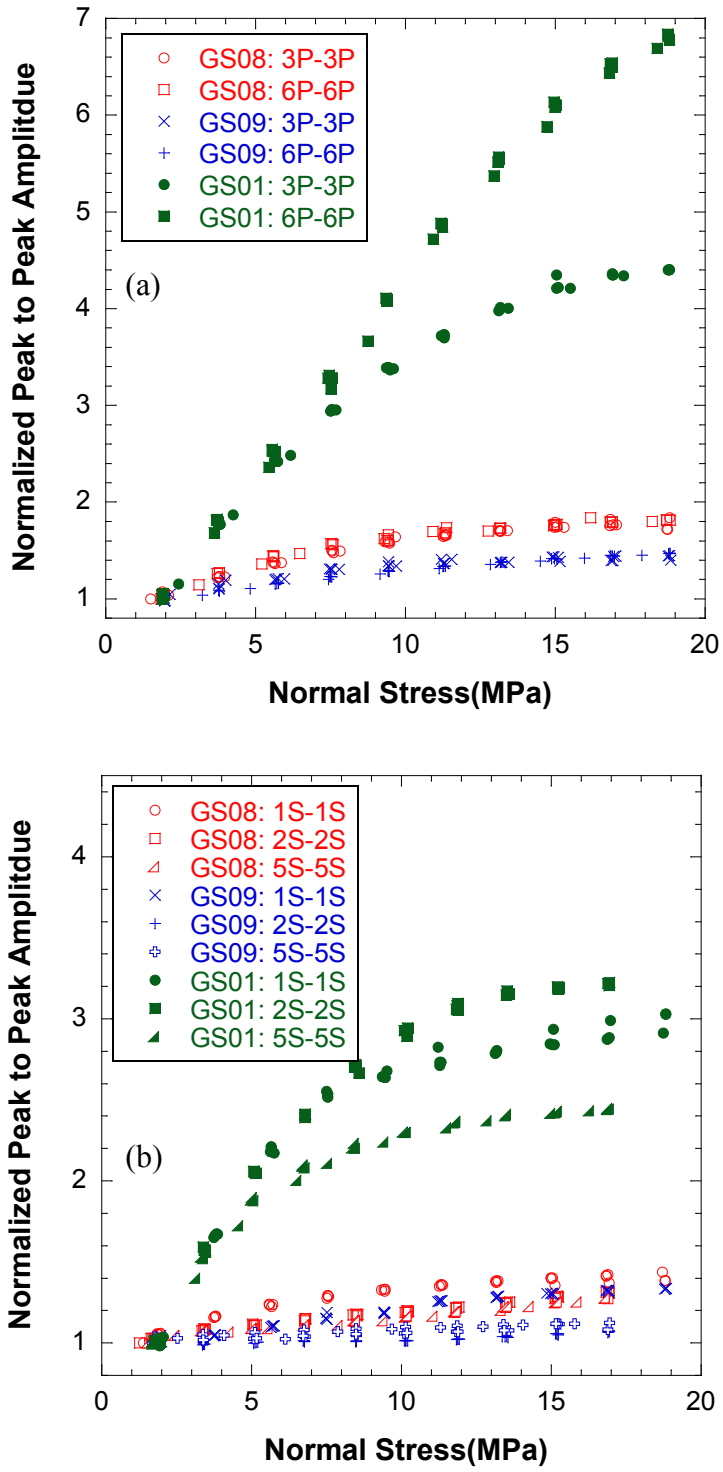

Figure 4.4.2-11. Normalized peak-to-peak amplitudes for (a) P-, (b) Sv-, and (c) Sh-transducer pairs, from GS08 (red), GS09 (blue), and GS01 (green). Amplitudes are normalized with amplitude at 1.89 MPa normal stress (continued).

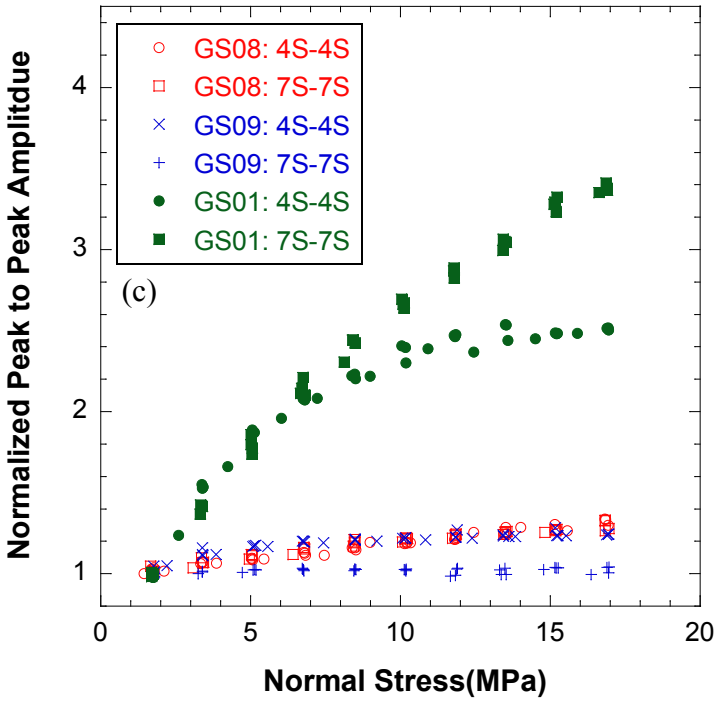

Figure 4.4.2-11. Normalized peak-to-peak amplitudes for (a) P-, (b) Sv-, and (c) Sh-transducer pairs, from GS08 (red), GS09 (blue), and GS01 (green). Amplitudes are normalized with amplitude at 1.89 MPa normal stress.

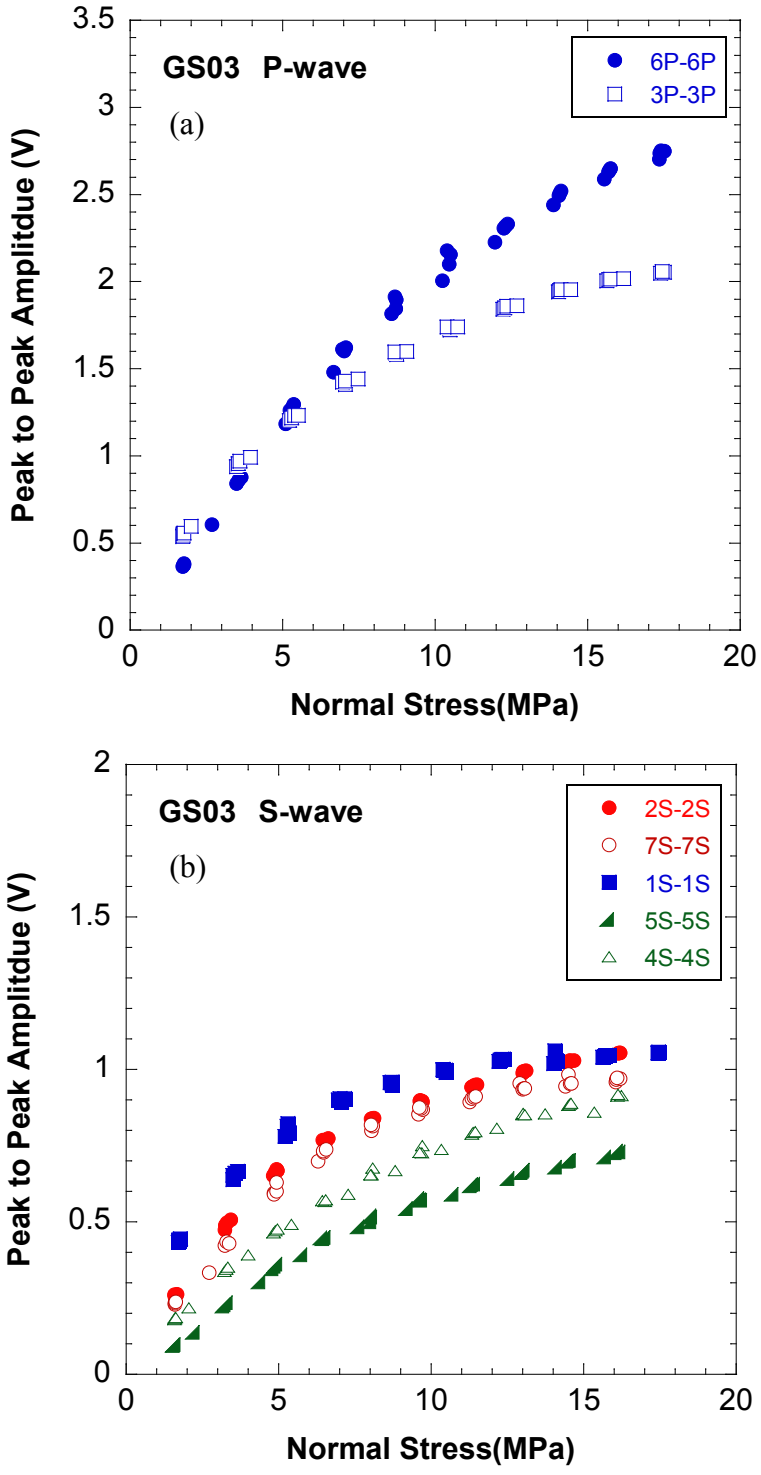

Figure 4.4.2-12. Peak-to-peak amplitude for: (a) compressional wave; and (b) shear wave, with normal stress. Specimen GS03 with 15˚ fracture.

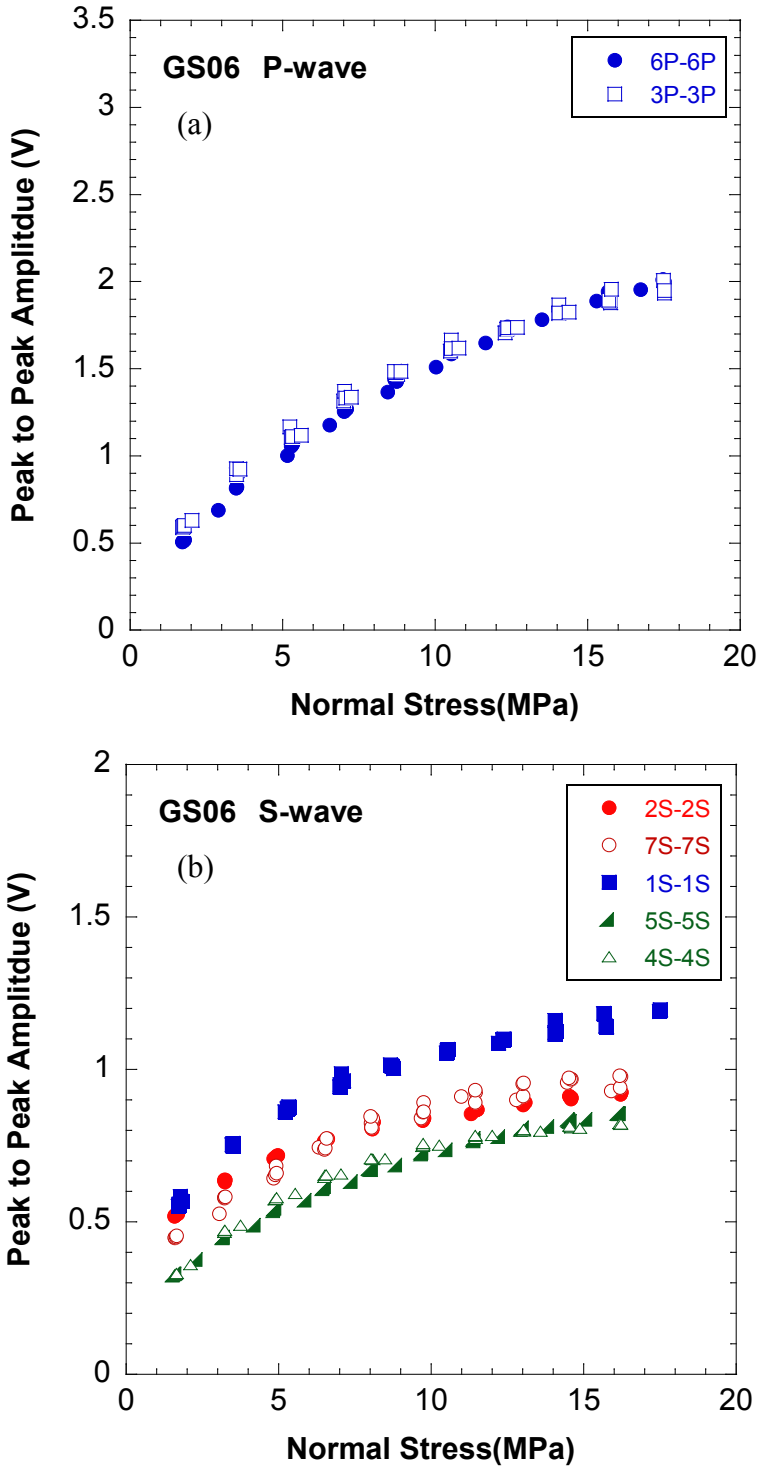

Figure 4.4.2-13. Peak-to-peak amplitude for: (a) compressional wave; and (b) shear wave, with normal stress. Specimen GS06 with 15˚ fracture.

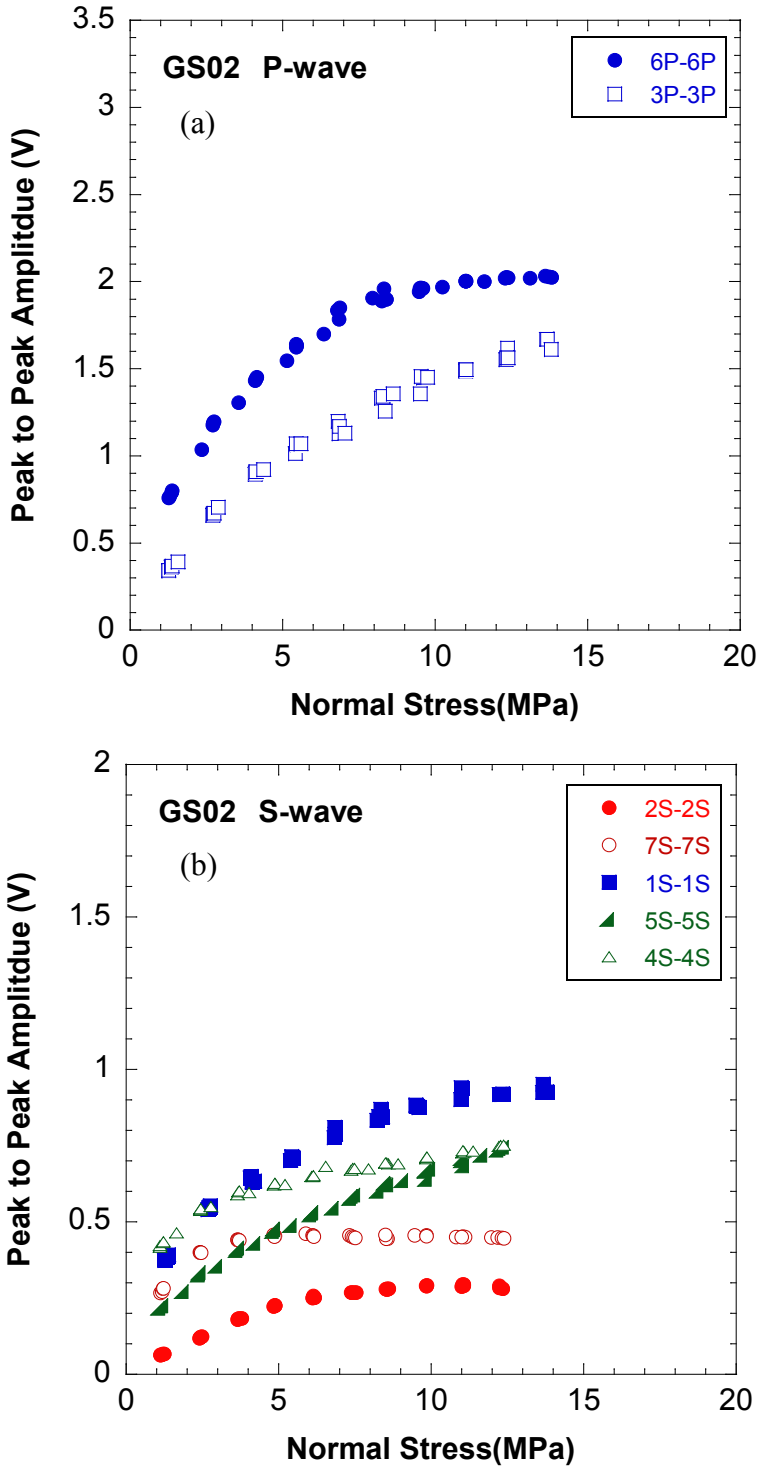

Figure 4.4.2-14. Peak-to-peak amplitude for: (a) compressional wave; and (b) shear wave, with normal stress. Specimen GS02 with 30˚ fracture.

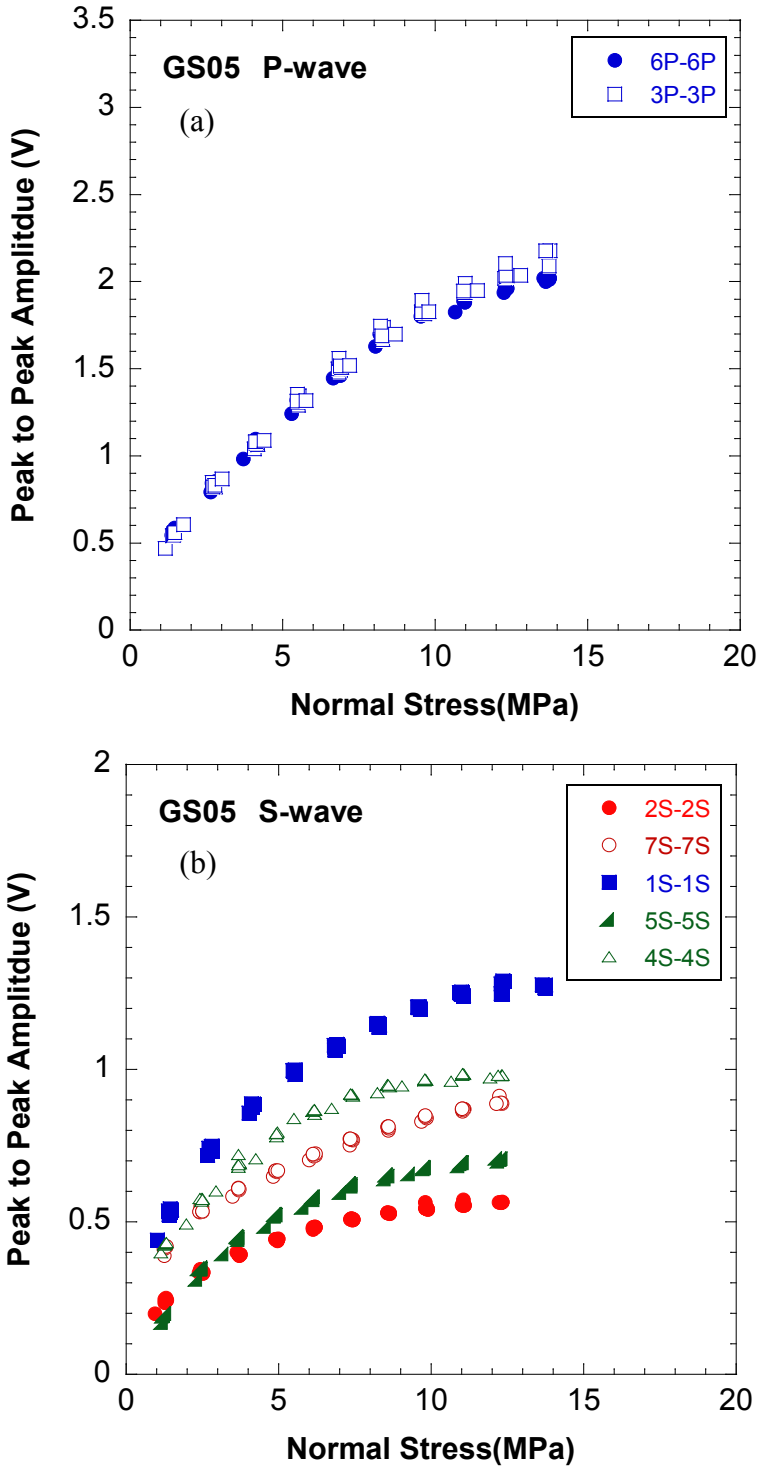

Figure 4.4.2-15. Peak-to-peak amplitude for: (a) compressional wave; and (b) shear wave, with normal stress. Specimen GS05 with 30˚ fracture.

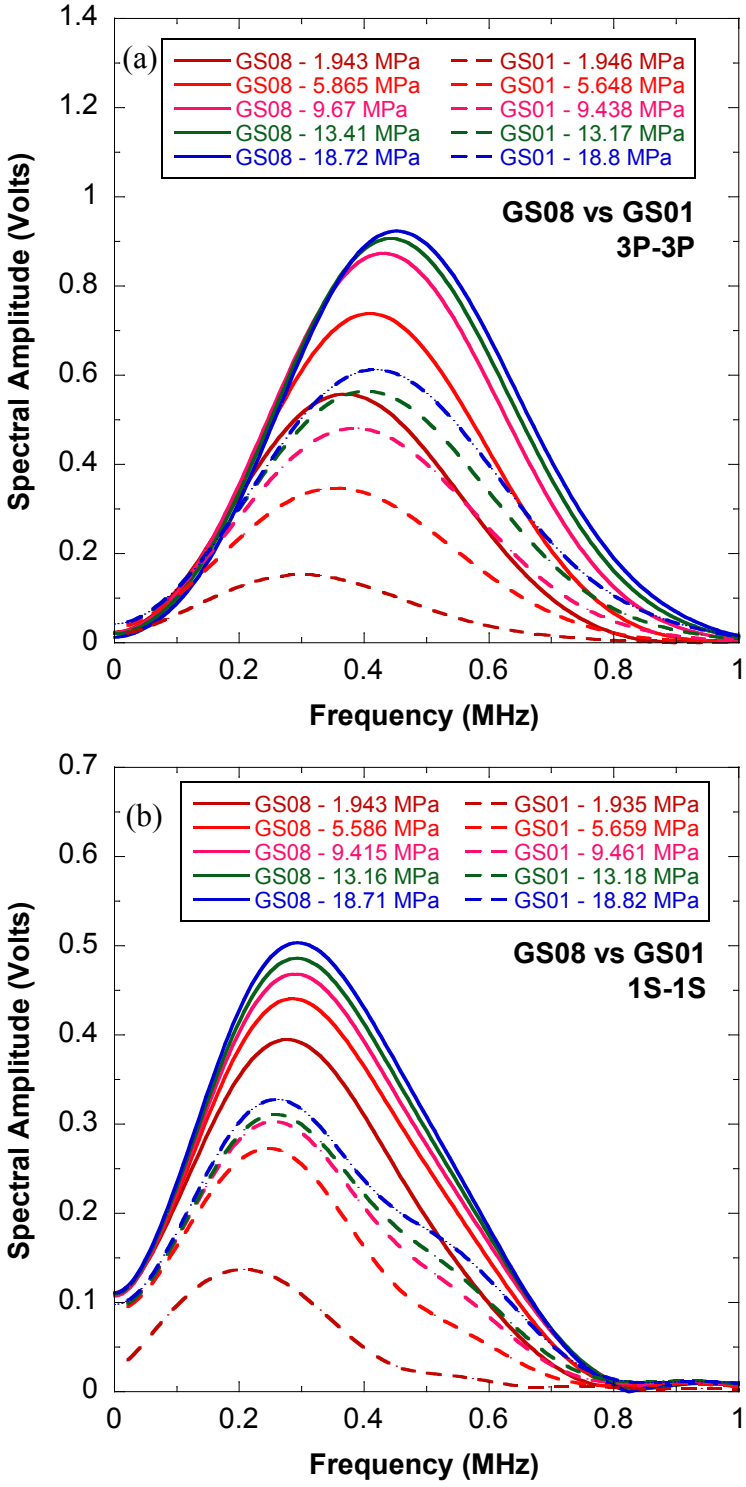

Figure 4.4.2-16. Comparison of Fourier spectra between fractured granite specimen GS01 (dotted line) and intact granite specimen GS08 (solid line) for: (a) compressional (3P-3P); and (b) shear (1S-1S) waves with normal stress.

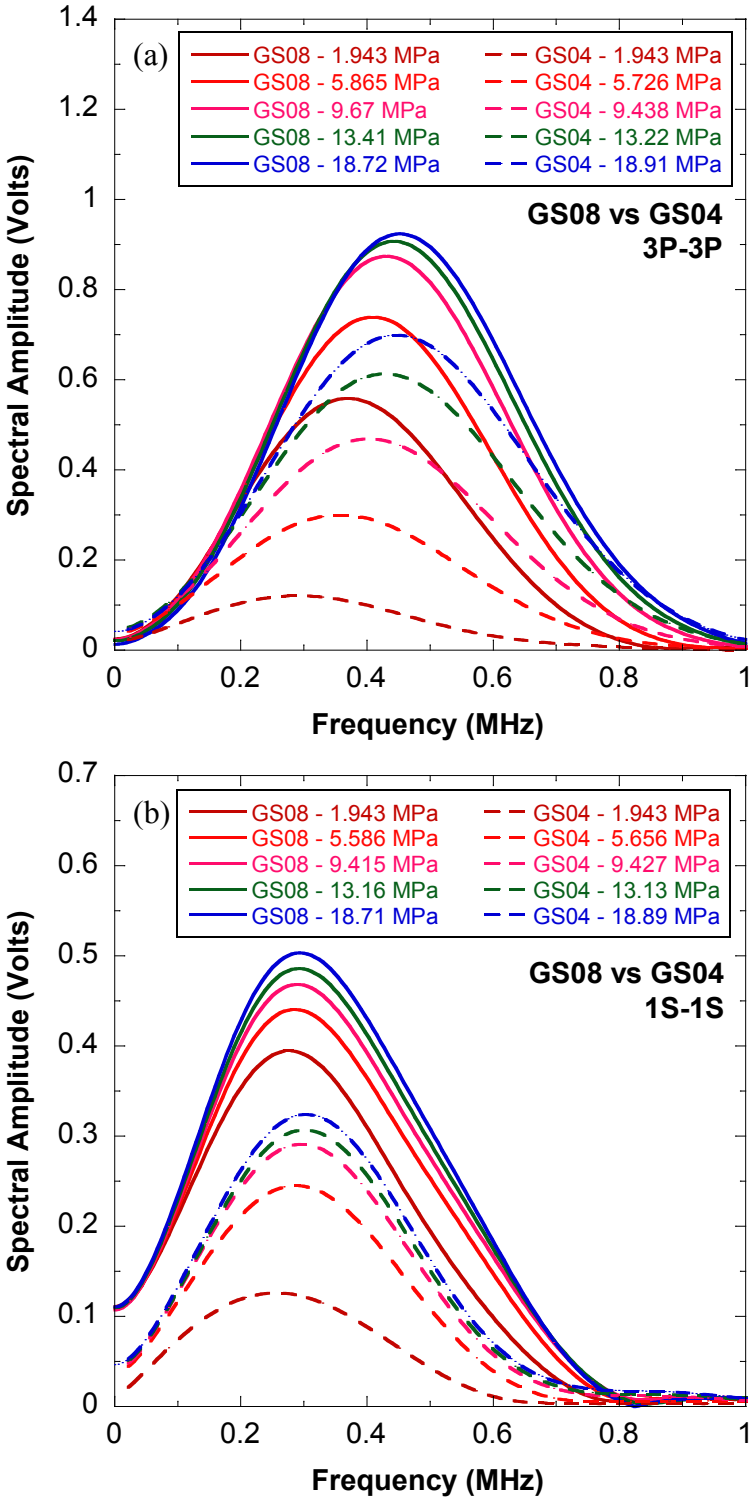

Figure 4.4.2-17. Comparison of Fourier spectra between fractured granite specimen GS04 (dotted line) and intact granite specimen GS08 (solid line) for: (a) compressional (3P-3P); and (b) shear (1S-1S) waves, with normal stress.

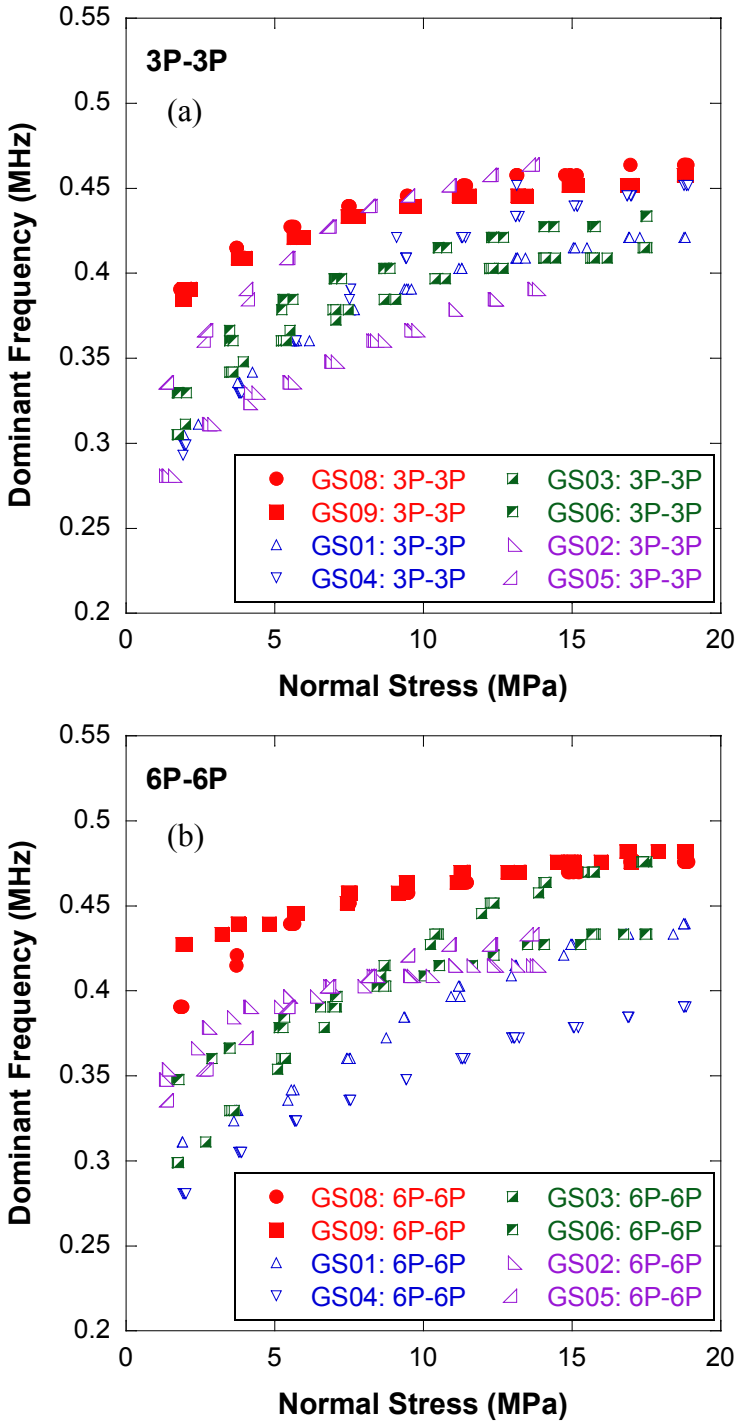

Figure 4.4.2-18. Dominant frequency from intact specimens GS08 and GS09 (red), specimens GS01 and GS04 with 0° fracture (blue), specimens GS03 and GS06 with 15° fracture (green), and specimens GS02 and GS06 with 30° fracture (purple), with normal stress. Data from transducer pairs: (a) 3P-3P; (b) 6P-6P; (c) 1S-1S; (d) 2S-2S; (e) 5S-5S; (f) 4S-4S; and (g) 7S-7S (continued).

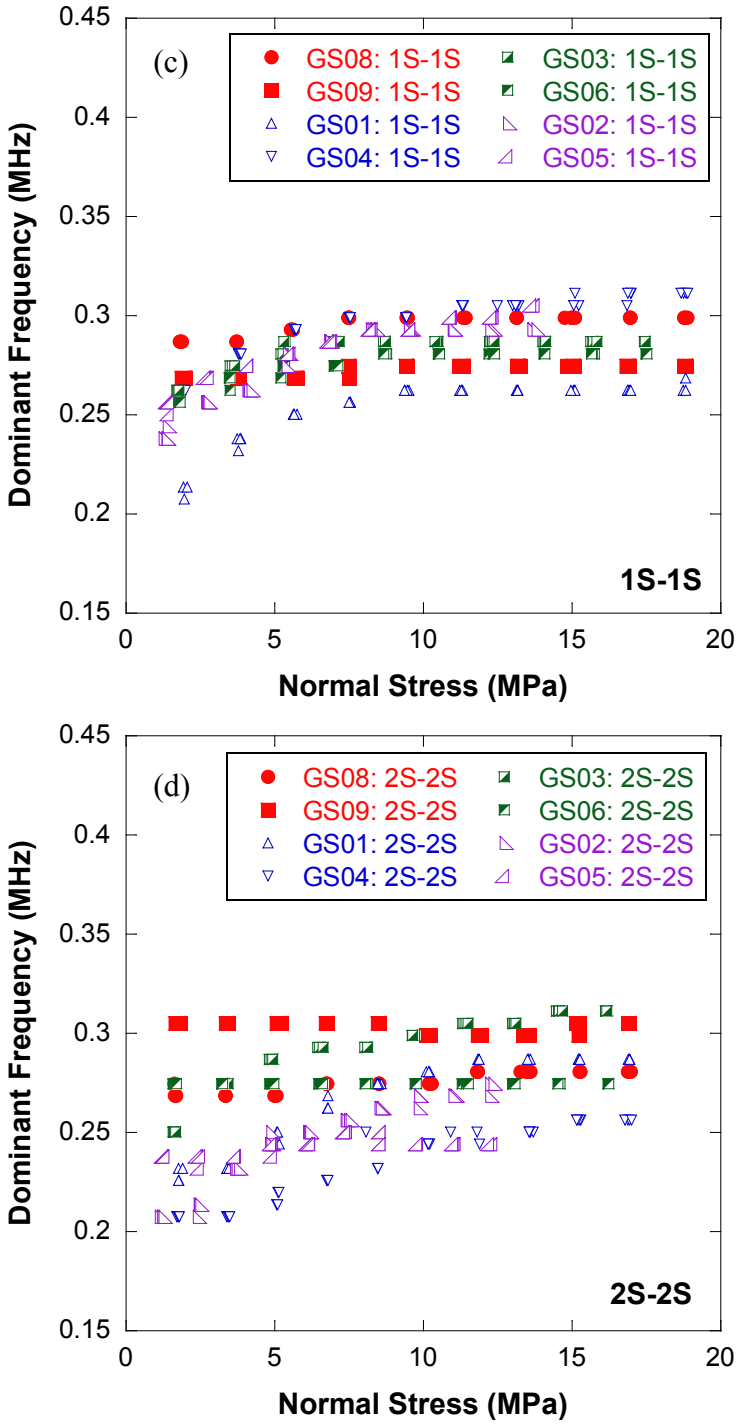

Figure 4.4.2-18. Dominant frequency from intact specimens GS08 and GS09 (red), specimens GS01 and GS04 with 0° fracture (blue), specimens GS03 and GS06 with 15° fracture (green), and specimens GS02 and GS06 with 30° fracture (purple), with normal stress. Data from transducer pairs: (a) 3P-3P; (b) 6P-6P; (c) 1S-1S; (d) 2S-2S; (e) 5S-5S; (f) 4S-4S; and (g) 7S-7S (continued).

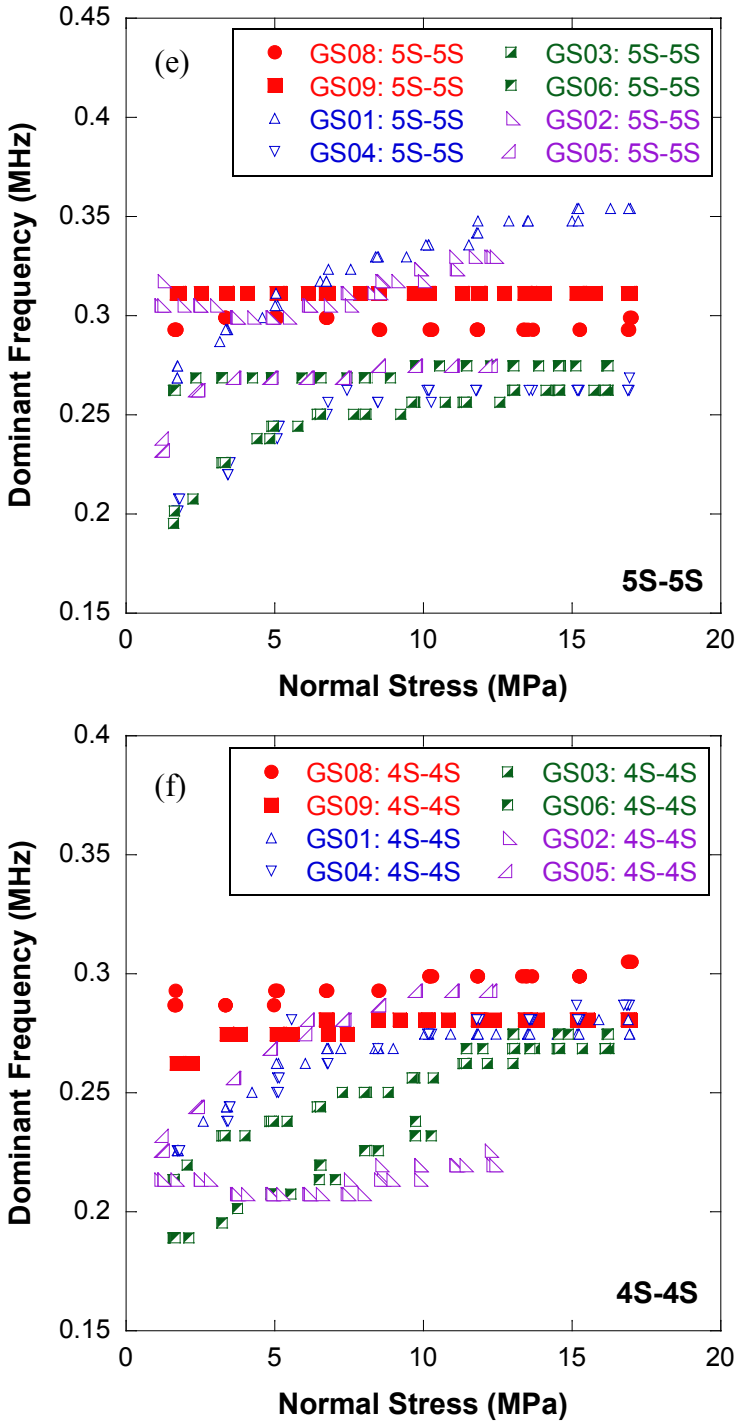

Figure 4.4.2-18. Dominant frequency from intact specimens GS08 and GS09 (red), specimens GS01 and GS04 with 0° fracture (blue), specimens GS03 and GS06 with 15° fracture (green), and specimens GS02 and GS06 with 30° fracture (purple), with normal stress. Data from transducer pairs: (a) 3P-3P; (b) 6P-6P; (c) 1S-1S; (d) 2S-2S; (e) 5S-5S; (f) 4S-4S; and (g) 7S-7S (continued).

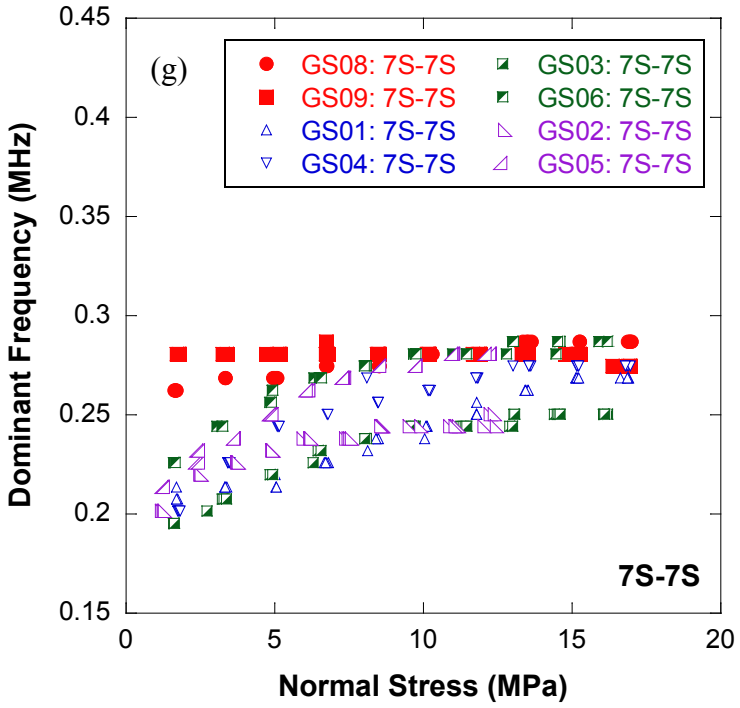

Figure 4.4.2-18. Dominant frequency from intact specimens GS08 and GS09 (red), specimens GS01 and GS04 with 0° fracture (blue), specimens GS03 and GS06 with 15° fracture (green), and specimens GS02 and GS06 with 30° fracture (purple), with normal stress. Data from transducer pairs: (a) 3P-3P; (b) 6P-6P; (c) 1S-1S; (d) 2S-2S; (e) 5S-5S; (f) 4S-4S; and (g) 7S-7S.

4.5 Spatial Distribution of Specific Stiffness in a Fracture

4.5.1 Stiffness Calculation

The normal and shear specific stiffness of granite specimens GS01 to GS06 were estimated using the displacement discontinuity theory using incident P- and Sv- waves (equation (3.2.1-1)) and Sh- waves (equation (3.2.1-2)); see section 3.2.1. For P- and Sv-waves impinging at an angle on a fracture, equation (3.2.1-1) with (2.2.1-11) for P-waves, or equation (2.2.1-12) for Sv- waves, were used to calculate normal (κ_z) and shear (κ_x) fracture specific stiffness. There a total of four equations with six unknowns. The six unknowns are normal (κ_z) and shear (κ_x) fracture specific stiffness, and reflection and transmission coefficients for compressional and shear waves (R_P, R_{SV}, T_P, and T_{SV}). Because the transmission coefficient for compressional (T_P) or shear (T_{SV}) waves was experimentally determined taking the ratio of the spectral amplitude of the transmitted wave for a fractured specimen to that of an intact specimen, the unknowns in the solution matrix reduce to five (κ_z, κ_x, R_P, R_{SV}, and T_{SV} for compressional wave, or κ_z, κ_x, R_P, R_{SV}, and T_P for shear wave). Hence, an additional equation is required to find a complete solution for the five unknowns, such as the ratio of shear to normal fracture specific stiffness (κ_x / κ_z).

As discussed in Chapter 3, the stiffness ratio for a well-mated fracture is sensitive to the size of asperity and the application of shear stress. Of all the gypsum specimens with a well-mated fracture (discussed in Chapter 3), the replica specimen GS01R had the mean asperity height between 2.680 - 2.870 mm, which is comparable to the mean asperity height of 2.876 - 3.771 mm measured from specimens GS01 to GS06. Also, the 15° and

30° loading paths imposed on GS01R were similar to the loading to the 15° fracture specimens (GS03 and GS06) and to the 30° fracture specimens (GS02 and GS05). Thus, it seems reasonable to use the stiffness ratio obtained from the replica specimen GS01R for the stiffness calculation for the 15° and 30° fracture specimens. The specimen GS01R exhibited a stiffness ratio of 1.0 for the 15° loading path ($\kappa_x / \kappa_z = 1.0$) and a ratio $\kappa_x / \kappa_z = 1.2$ for the 30° loading path. Using the stiffness ratio obtained from GS01R, a complete solution was then obtained for the five unknowns.

The intact granite specimens GS08 and GS09 were used as a reference for stiffness calculations. Specimen GS07 was excluded from the calculations because of its heterogeneity, as one can see in Figure 4.4.1-7. The fracture specific stiffness was calculated at the dominant frequency of the spectra from the intact specimens GS08 and GS09. The normal fracture specific stiffness was determined at the dominant frequency 0.5 MHz for compressional waves, and the shear fracture specific stiffness at 0.3 MHz for shear waves. The compressional and shear wave velocities measured from GS08 and GS09 were used to calculate the seismic impedance of the granite matrix, as a function of stress.

4.5.2 Estimation of Fracture Specific Stiffness

4.5.2.1 Uncertainty in Stiffness Calculation

Figure 4.5.2-1 (a) contains the normal fracture specific stiffness estimated from transducer pair 3P-3P and Figure 4.5.2-1 (b) the shear fracture specific stiffness from 1S-1S. Error bars provide the level of uncertainty in estimating fracture specific stiffness.

These two transducer pairs 3P-3P and 1S-1S were selected because they were representative of the uncertainty in estimating normal and shear fracture specific stiffness. The figures show a ±6~8% error originated by the remounting of the transducers on the specimen (i.e. differences due only to dismounting and re-placing the transducers on the same specimen). However the variation in stiffness increases up to ±8~12% when using a different reference standard for the intact rock, i.e. using GS08 instead of GS09. These errors are attributed to the heterogeneity of the granite.

4.5.2.2 Fracture Specific Stiffness in Granite Specimens

Figure 4.5.2-2 (a) gives the normal and shear specific stiffness for specimen GS01 and Figure 4.5.2-2 (b) for GS04. The stiffnesses in Figure 4.5.2-2 were averaged from the values obtained using the two reference standards GS08 and GS09. The shear fracture specific stiffness increased with increasing normal stress until about 10 MPa, and then approached an asymptotic value at higher stresses. The normal fracture specific stiffness increased with increasing stresses from 0-18.9 MPa. The fracture specific stiffnesses estimated from different transducer pairs are different from each other, which indicates that the local fracture specific stiffness changes along the fracture plane.

Spatially non-uniform variations of fracture specific stiffness were also found in specimen GS03 and GS06, which had a 15° fracture, and in GS02 and GS05 with a 30° fracture. Figure 4.5.2-3 shows the variation of fracture specific stiffness for: (a) GS03; and (b) GS06 both with a 15° fracture, and Figure 4.5.2-4 shows the results for: (a) GS02 and (b) GS05, both with a 30° fracture. The specimens with an angled fracture had

variations in fracture stiffness similar to GS01 and GS04. The normal stiffnesses of the fractures in GS02, GS05, GS03, and GS06 increased with increasing normal stress from 0-18 MPa, while the shear stiffnesses gradually approached an asymptote.

4.5.2.3 Surface Roughness and Micro-Slope Angle

In this section, a discussion between fracture specific stiffness, local distribution of fracture asperity height and micro-slope angles is presented. The process for obtaining the local distribution of fracture asperity heights and micro-slope angles under each transducer pair was discussed in sections 4.2.3.1 and 4.2.3.2, and the results listed in Tables 4.2.3-1 to 4.2.3-8.

Figure 4.5.2-5 (a) plots the averaged local normal fracture specific stiffness and Figure 4.5.2-5 (b) the averaged shear fracture specific stiffness, as a function of the coefficient of variance (CV) of the local roughness distribution. The data are taken from specimens GS01 and GS04 (with a 0° fracture). In the Figure, the error bars represent the maximum and minimum fracture specific stiffness for the range of applied normal stresses 0-18.9 MPa. Figure 4.5.2-5 (a) includes the local normal specific stiffness measured from transducer pairs 3P-3P and 6P-6P. Similarly, the local shear specific stiffness from 1S-1S, 2S-2S, 4S-4S, 5S-5S, and 7S-7S is shown in Figure 4.5.2-5 (b), as a function of the CV of the local roughness distribution. The local shear fracture specific stiffness decreased with increasing CV (Figure 4.5.2-5 (b)), which is consistent with the study of Hopkins et al. (1987) that showed that the more uniform the asperity heights are, the stiffer the fracture. For the local normal specific stiffness measured from transducer pairs 3P-3P and

6P-6P, no clear conclusion can be reached, perhaps due to the limited number of data. However, except the one data having 0.25 of CV and 1.4 x 10^{13} Pa/m of normal specific stiffness, the measured local normal specific stiffness increased with decreasing CV (Figure 4.5.2-5 (a)).

A limiting case in Hopkins et al.'s study is the fracture that has only a single asperity height across the fracture plane. In that case, the CV of the surface roughness distribution is zero and the fracture surface is perfectly flat. Hence, the entire fracture surface is always in full contact and has zero aperture; thus the normal specific stiffness of the fracture goes theoretically to infinity. Hence, it makes physical sense that the smaller the CV of the surface roughness distribution, the larger the normal fracture specific stiffness should be when the fracture is subjected to normal stress only.

Figure 4.5.2-6 shows a plot analogous to Figure 4.5.2-5 but for GS03 and GS06 (with a 15° fracture) and Figure 4.5.2-7 for GS02 and GS05 (with a 30° fracture). For the angled fracture specimens, the positive effect of a smaller CV on the shear fracture specific stiffness (i.e., the smaller CV, the larger the shear specific stiffness) does not exist. Fracture specific stiffness appears to increase with increasing CV in Figure 4.5.2-6 (b) and 4.5.2-7 (b). It should be noted that specimens GS02, GS03, GS05, and GS06 were subjected to shear stress as well as normal stress. In the study of Hopkins et al., the relation between CV and fracture specific stiffness was obtained when a fracture was subjected to only normal stress. Given the results from the experiments in this research, it seems that the validity of the relation is limited to a fracture normally compressed.

As shown in Figures 3.4.5-1 and 3.4.5-3, the static shear stiffness from the gypsum specimens increased with increase of the areas with high micro-slope angles. For the

gypsum Flat specimen, the static specific stiffness was 6.01 x 10^9 Pa/m and the micro-slope angles ranged between ±5°, while the gypsum #36 specimen had a static specific stiffness of 10.3 x 10^9 Pa/m with micro-slope angles between ±30°. This observation suggests that that the shear fracture specific stiffness of a fracture subjected to shear stress may be related to the micro-slope angle. This is ascertained by correlating the local shear fracture specific stiffness measured from each shear wave transducer pair (1S, 2S, 4S, 5S, and 7S) with the maximum and the top 0.1%, 1.0% and 10% micro-slope angles under each transducer pair. The correlation is done for specimens GS02, GS03, GS05, and GS06 with an angled fracture.

Figure 4.5.2-8 contains the averaged local shear fracture specific stiffness as a function of the maximum and the top 0.1%, 1.0%, and 10% micro-slope angles taken from the micro-slope angle distributions of the fracture areas under the transducers, for specimens (a) GS03 and (b) GS06 (15° fracture), and (c) GS02 and (d) GS06 (30° fracture). The figures also include the local shear specific stiffness measured from transducer pairs 1S-1S, 2S-2S, 4S-4S, 5S-5S, and 7S-7S. The error bars represent the maximum and minimum specific stiffness for the range of normal stresses used in the tests, which was 0-18.9 MPa. In the figures, the correlation coefficients R^2 are also presented for each correlation. For example, for specimen GS03, a correlation coefficient R^2 of 0.9675 was obtained between the local shear specific stiffness and the top 0.1% micro-slope angle (Figure 4.5.2-8 (a)). Given the correlation coefficients R^2 obtained, the best correlation was found when the shear specific stiffness was correlated with the maximum or the top 0.1% of micro-slope angles. For these cases, the shear fracture specific stiffness increased with the increase of the maximum or the top 0.1% micro-slope angles. This result indicates

that, for a fracture subjected to shear stress, the shear fracture specific stiffness depends on the higher micro-slope angles.

In summary, local fracture geometry, e.g., local surface roughness distribution or local micro slope angles, influences the magnitude of the local shear fracture specific stiffness. Depending on the loading condition imposed on a fracture, the shear fracture specific stiffness is dominated by fracture geometry, i.e., the CV of the surface roughness is a critical factor for fracture under normal compression, while the local micro-slope angle is important for determining the shear fracture specific stiffness when the fracture is subjected to shear. Hence, fracture topology can be instrumental in estimating, or at least understanding, the spatial variability and magnitude of shear fracture specific stiffness.

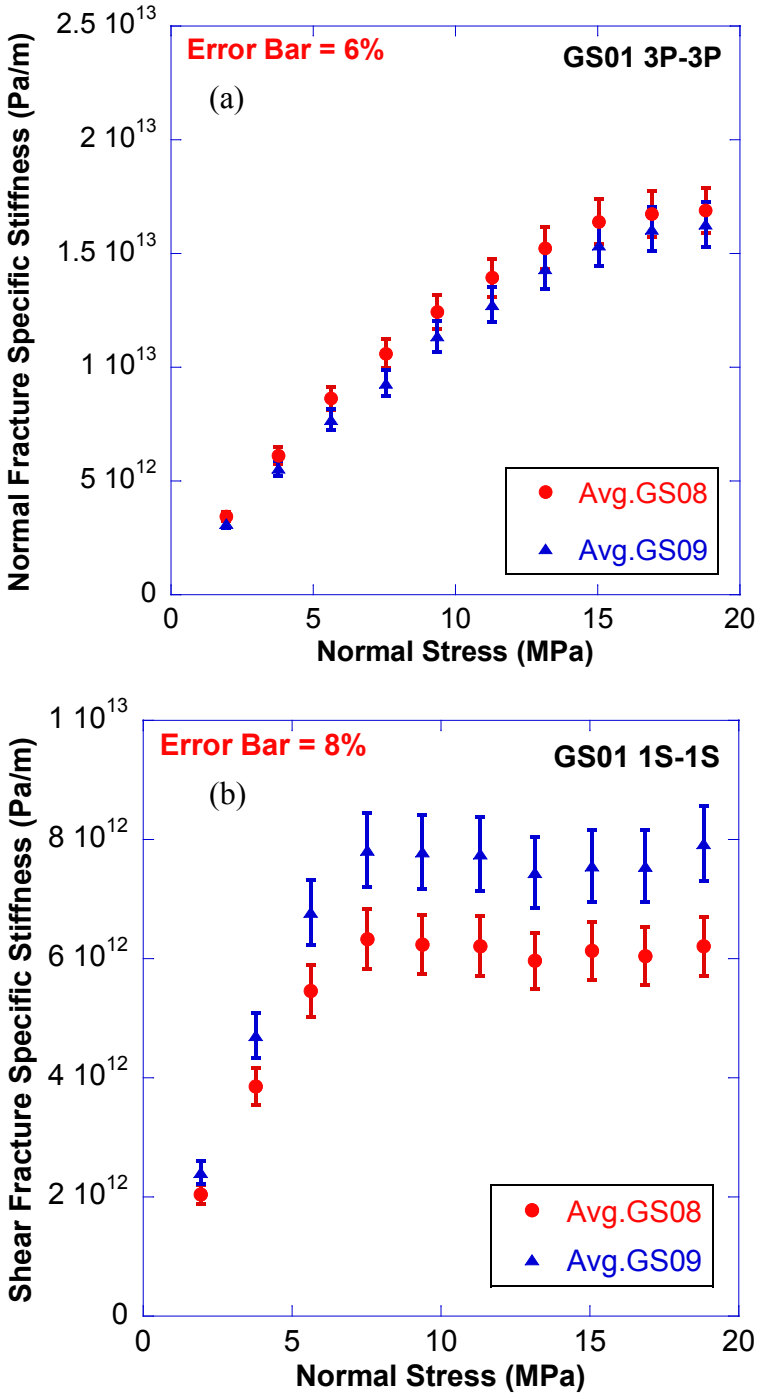

Figure 4.5.2-1. Estimated: (a) normal; and (b) shear fracture specific stiffness based on data from intact granite specimens GS08 and GS09.

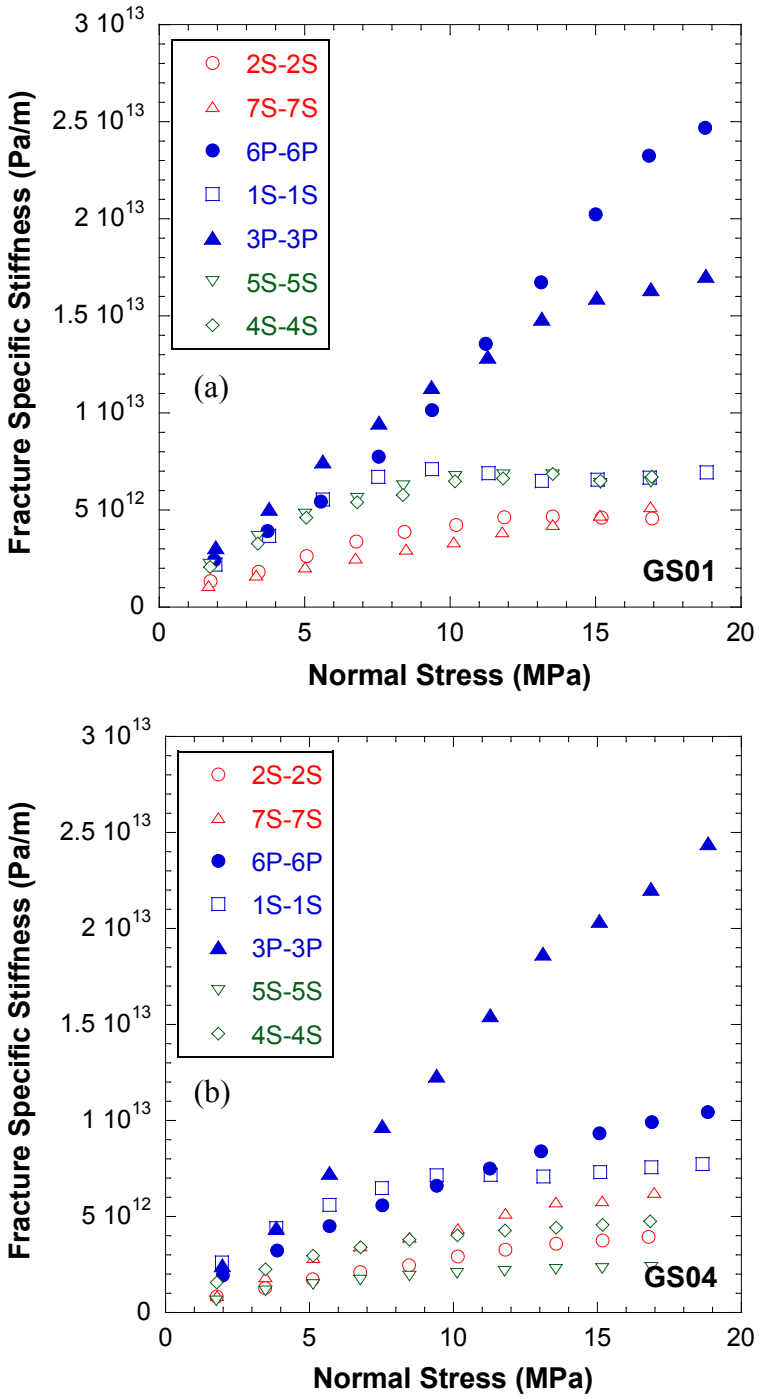

Figure 4.5.2-2. Normal and shear fracture specific stiffness for granite specimens: (a) GS01; and (b) GS04, with a 0° fracture, as a function of stress.

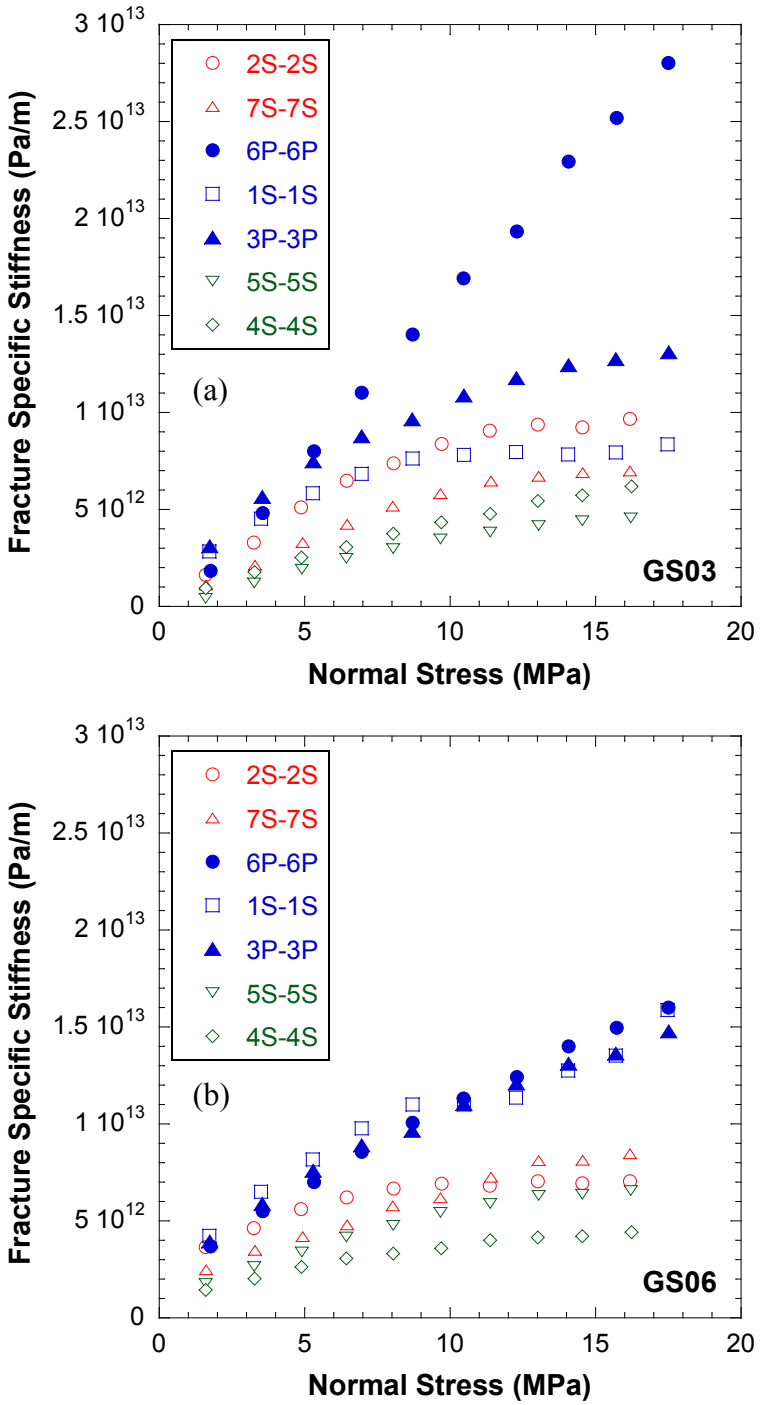

Figure 4.5.2-3. Normal and shear fracture specific stiffness for granite specimens: (a) GS03; and (b) GS06, with a 15° fracture as a function of stress.

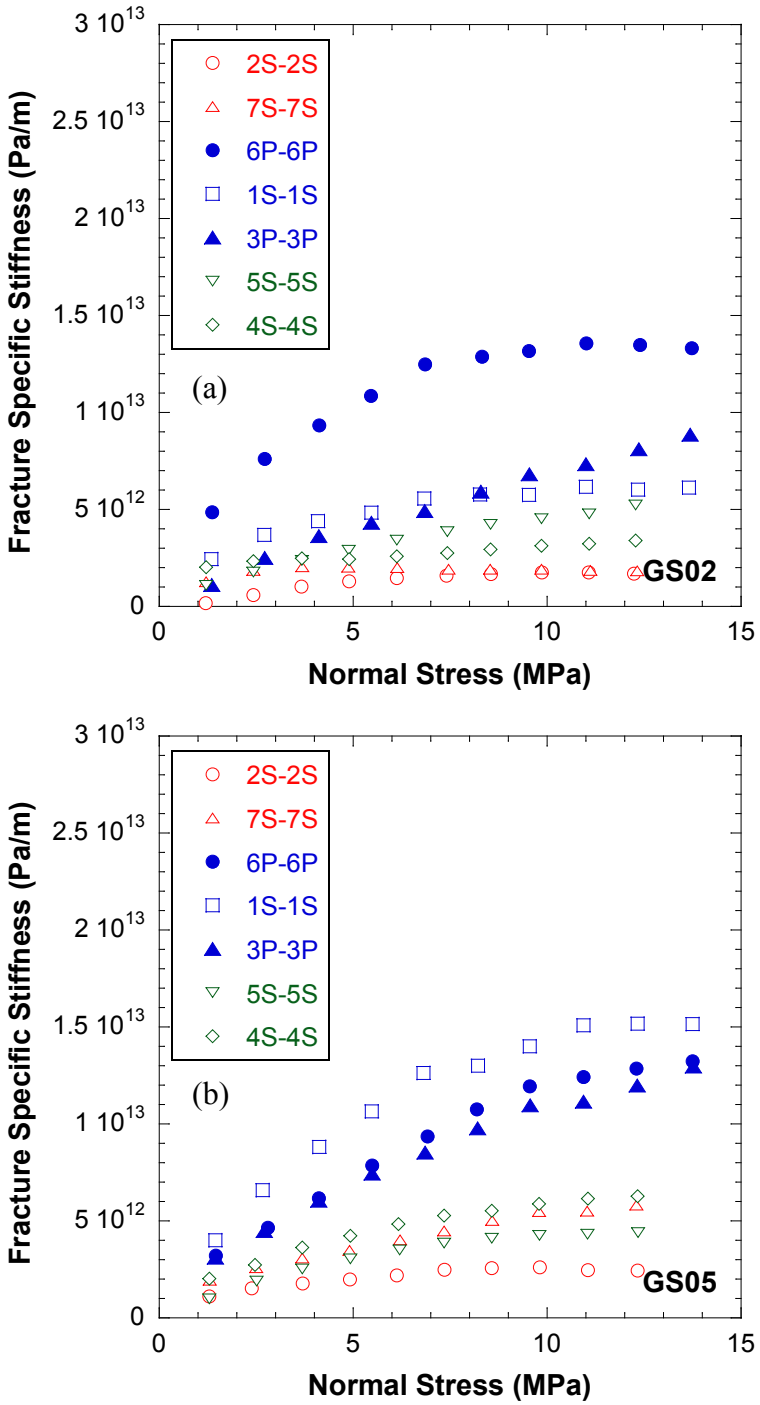

Figure 4.5.2-4. Normal and shear fracture specific stiffness for granite specimens: (a) GS02; and (b) GS05, with a 30° fracture as a function of stress.

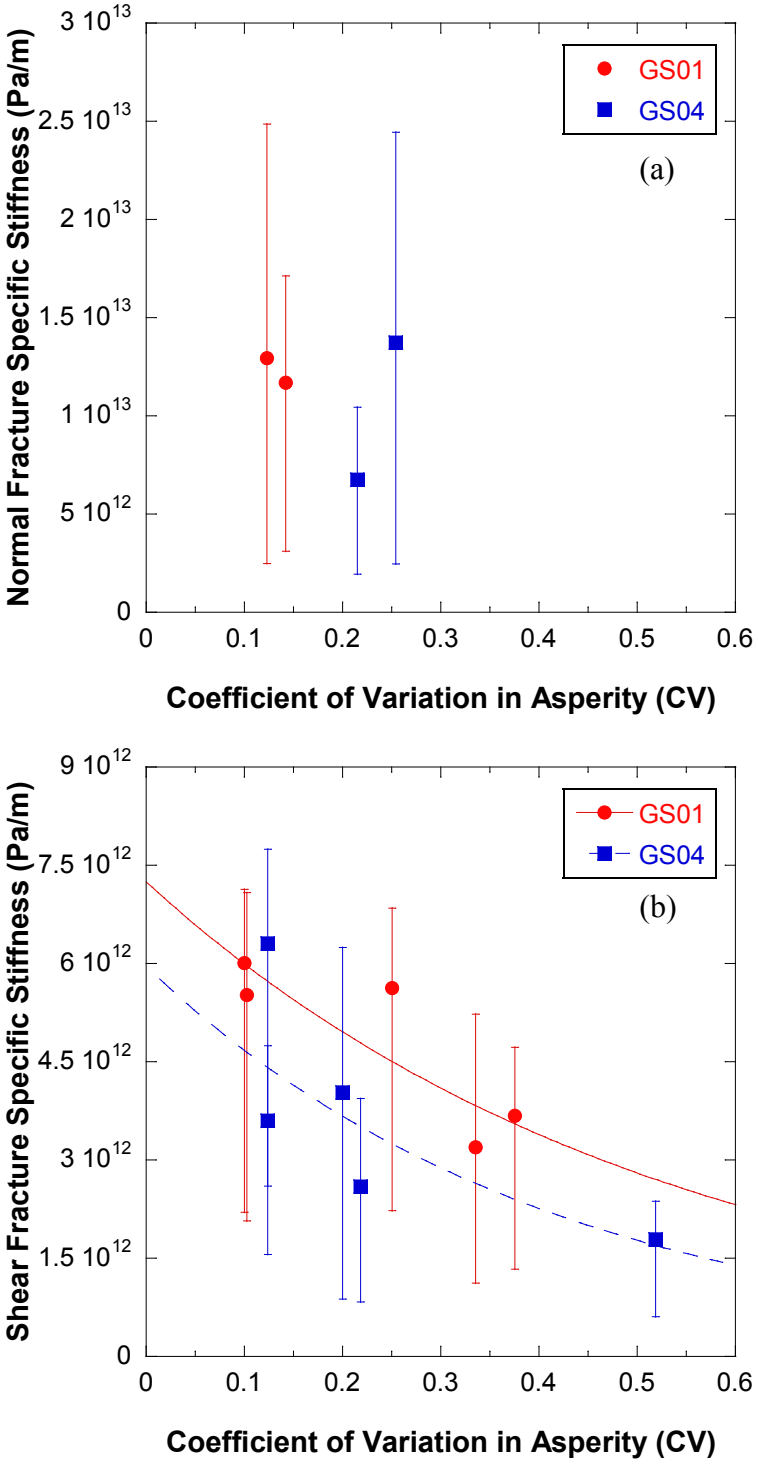

Figure 4.5.2-5. Averaged local: (a) normal; and (b) shear fracture specific stiffness as a function of the coefficient of variance CV of the local roughness distribution. Data from specimens GS01 and GS04 with a 0° fracture. Error bars show the maximum and minimum values.

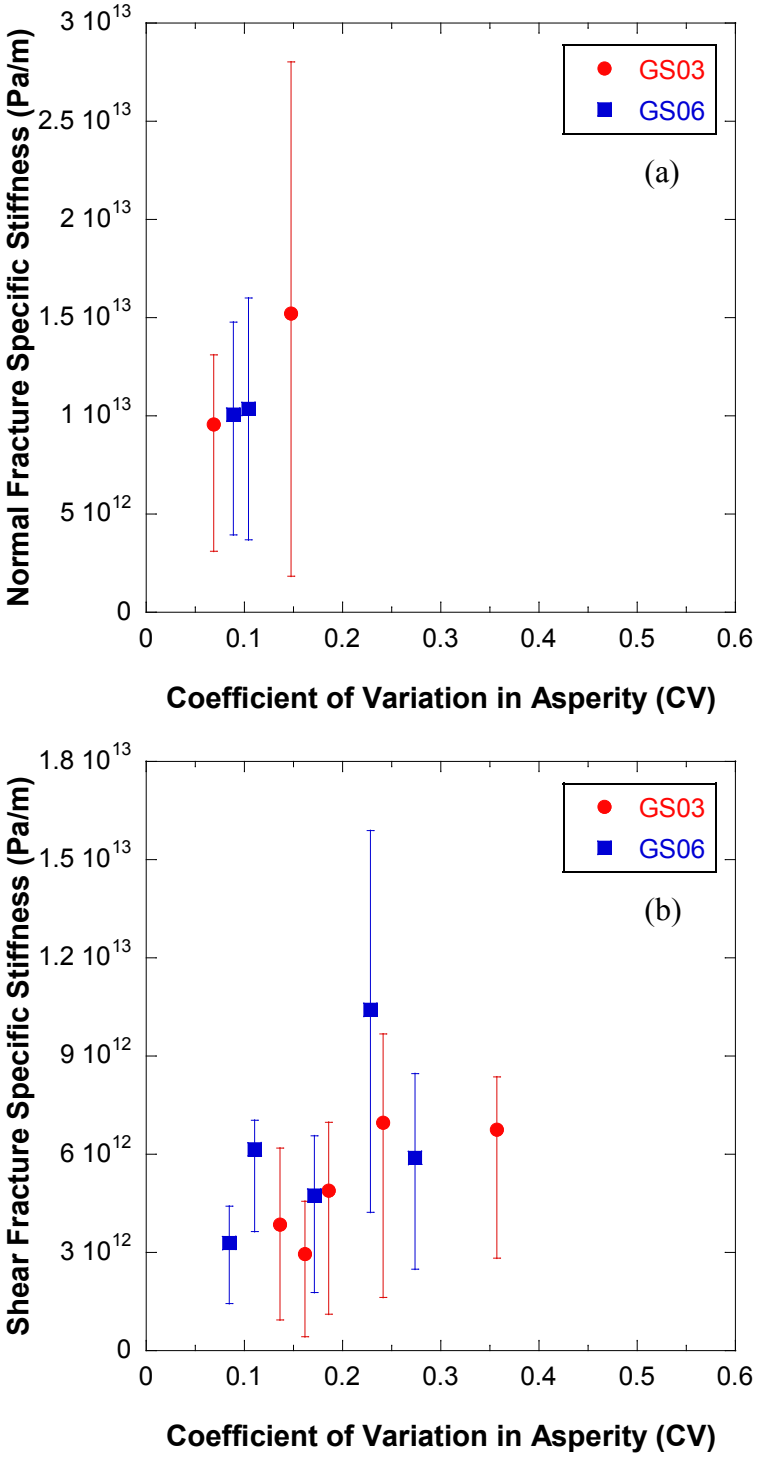

Figure 4.5.2-6. Averaged local: (a) normal; and (b) shear fracture specific stiffness as a function of the coefficient of variance CV of the local roughness distribution. Data from specimens GS03 and GS06 with a 15° fracture. Error bars show maximum and minimum values.

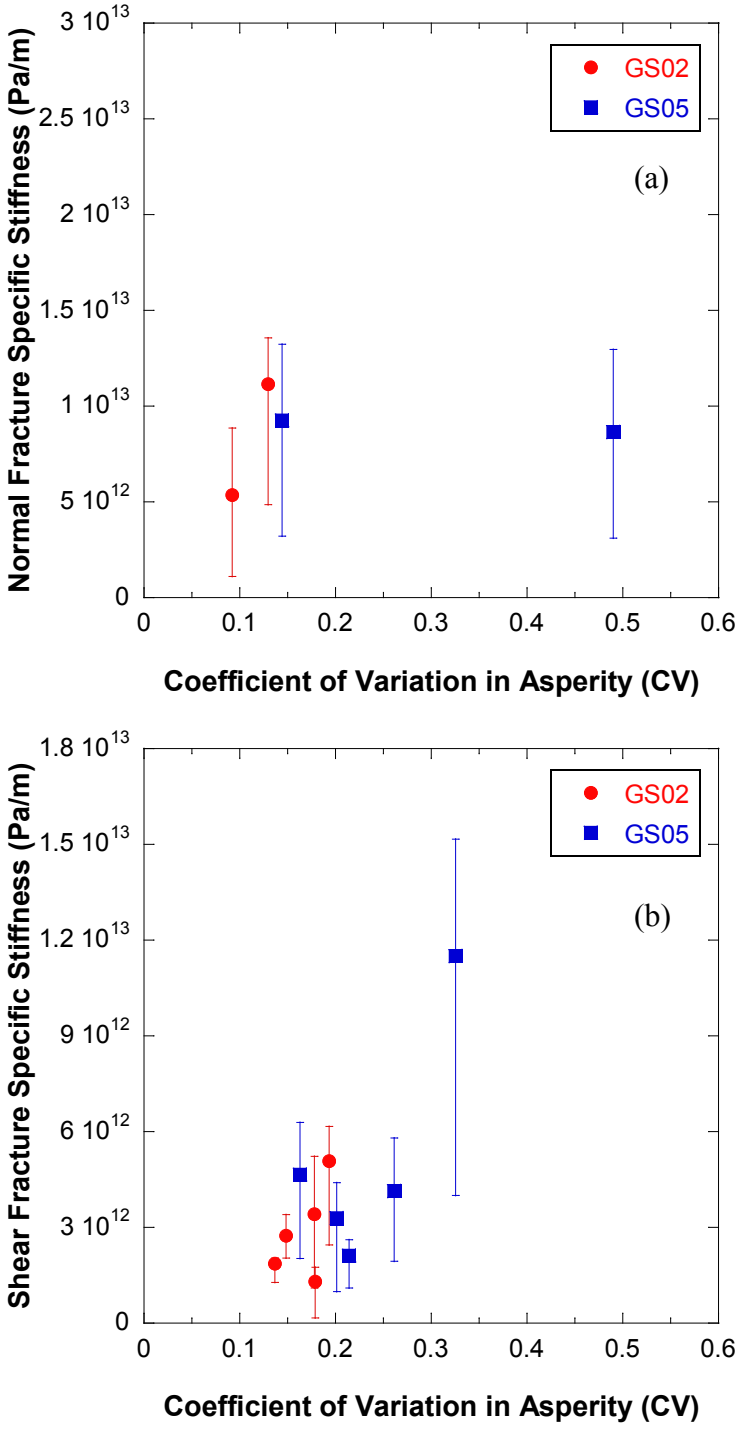

Figure 4.5.2-7. Averaged local: (a) normal; and (b) shear fracture specific stiffness as a function of the coefficient of variance CV of the local roughness distribution. Data from specimens GS02 and GS05 with a 30° fracture. Error bars show maximum and minimum values.

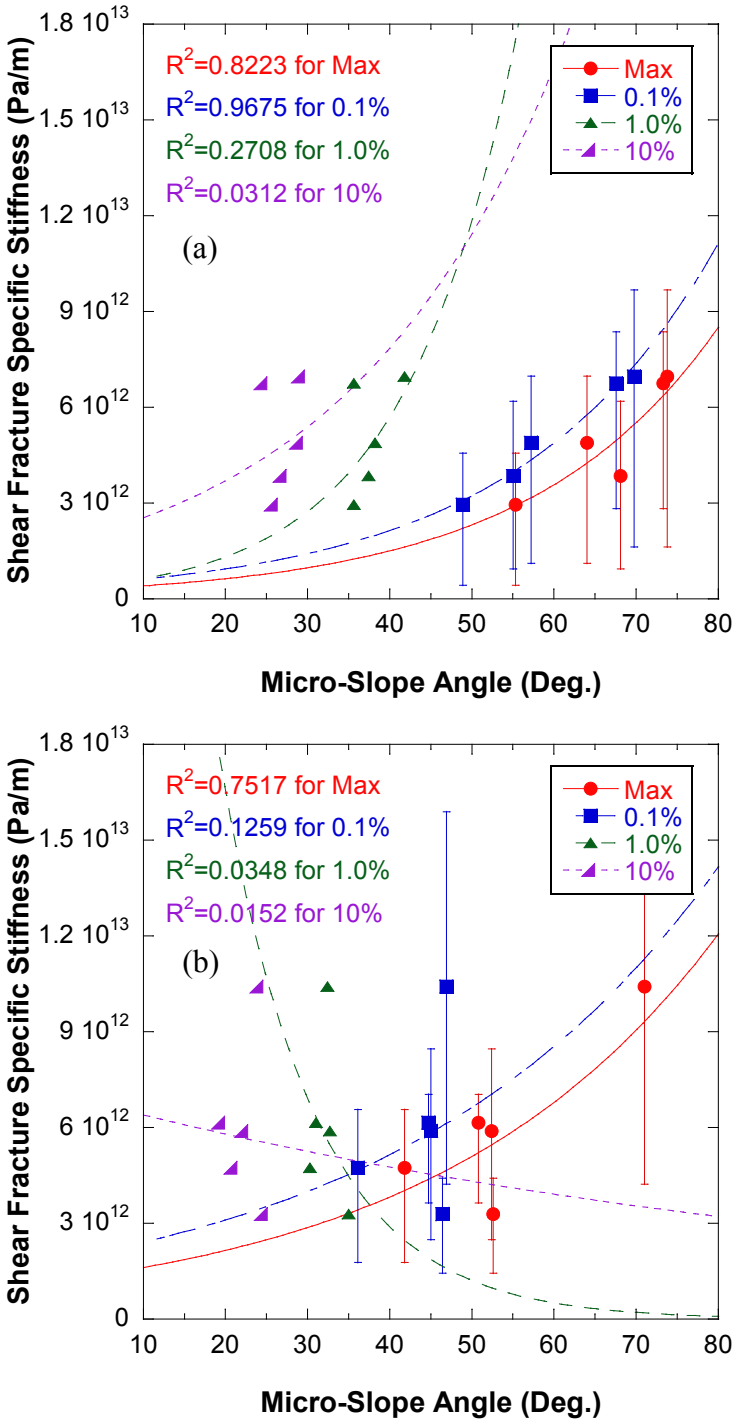

Figure 4.5.2-8. Averaged local shear fracture specific stiffness as a function of the micro-slope angles corresponding to the maximum, the top 0.1%, 1.0%, and 10% of the local micro-slope angle distributions under shear wave transducers for: specimens (a) GS03 and (b) GS06 with 15° fracture; and specimens (c) GS02 and (d) GS05 with 30° fracture. Error bars show maximum and minimum values (continued).

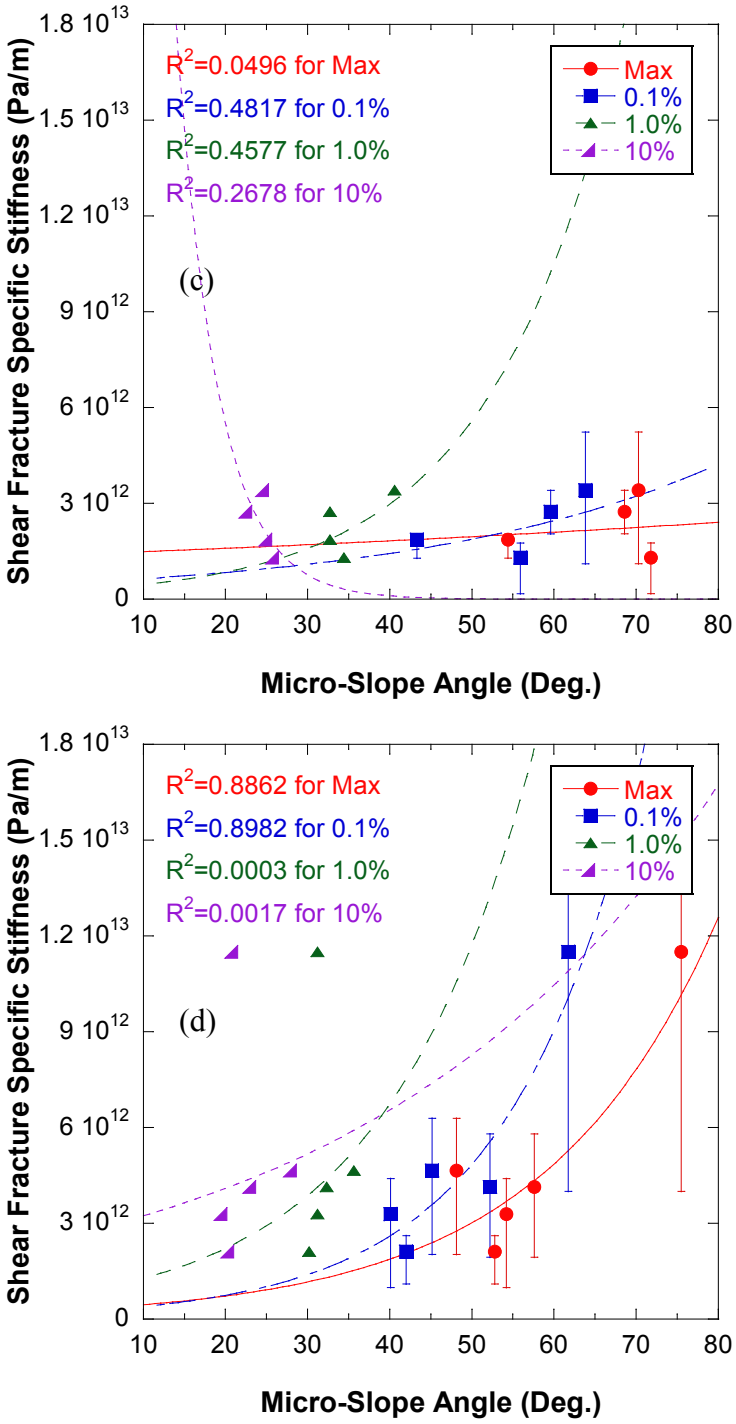

Figure. 4.5.2-8. Averaged local shear fracture specific stiffness as a function of the micro-slope angles corresponding to the maximum, the top 0.1%, 1.0%, and 10% of the local micro-slope angle distributions under shear wave transducers for: specimens (a) GS03 and (b) GS06 with 15° fracture; and specimens (c) GS02 and (d) GS05 with 30° fracture. Error bars show maximum and minimum values.

4.5.3 Spatial Distribution of Fracture Specific Stiffness

One of the goals of this study is to map the spatial distribution of fracture specific stiffness as a function of stress. Figure 4.5.3-1 is a plot of the fracture specific stiffness for specimen GS01 for: (a) 1.9 MPa, (b) 7.6 MPa, and (c) 19.0 MPa normal stress. In the figure, the location of the transducers, the type of transducers, transducer pairs and polarization of the shear waves are shown. The color of the transducer symbol represents the magnitude of the fracture specific stiffness. Again, S-wave transducers sensed shear specific stiffness and P-wave transducers sensed normal specific stiffness. As stress on the fracture increased from 1.9 MPa to 18.9 MPa, the fracture specific stiffness increased non-uniformly across the fracture. The fracture specific stiffness estimated from each transducer pair showed spatially different values, indicating that the local fracture specific stiffness changed along the fracture plane. The shear fracture specific stiffness at the center of the fracture (1S) increased rapidly and approached a limiting value at a stress of 7.6 MPa. With increasing stress, the normal fracture specific stiffness (3P and 6P) continued to increase. The spatial variability of fracture specific stiffness exceeded the variation in stiffness calculation as a result of the heterogeneity of the granite. For example, at normal stress of 19 MPa, the local shear specific stiffnesses of the fracture areas under transducer 2S and 1S were 4.6 TPa/m and 6.9 TPa/m, respectively. The difference between the two fracture specific stiffnesses was 50%, which exceeds the heterogeneity of granite, which is ±8~12%.

In a similar manner, the map of specific stiffness for the rest of the fractured granite specimens, i.e., GS02 to GS06, was prepared. Figure 4.5.3-2 contains the stiffness map for GS04 with a 0° fracture at selected normal stresses. At the normal stress of 1.9 MPa,

the measured fracture specific stiffness ranged from 0.6 - 2.6 TPa/m, represented by dark blue in Figure 4.5.3-2 (a); with normal stress, the stiffness increased, but at different rates depending on location. For example, the fracture specific stiffness measured from transducer pair 4S-4S increased from 1.6 TPa/m at a normal stress of 1.9 MPa to 4.7 TPa/m at 19.0 MPa, a factor of 2.9, while the specific stiffness from 3P-3P increased by a factor of 9.8, from 2.5 TPa/m to 24.4 TPa/m for the same range of normal stresses.

For the specimens with an angled fracture, the fracture specific stiffness had also spatial variation and was stress-dependent, as seen in Figures 4.5.3-3 to 4.5.3-6. Figure 4.5.3-3 is a plot of the stiffness map at normal stresses of: (a) 1.6 MPa, (b) 6.4 MPa, and (c) 16.0 MPa, for specimen GS03. Figure 4.5.3-4 is an analogous plot for GS06. Both specimens had a fracture at 15° with the horizontal. The stiffness maps for GS02 and GS05, with a 30° fracture, are presented in Figures 4.5.3-5 and 4.5.3-6, respectively, at normal stresses of: (a) 1.4 MPa, (b) 5.4 MPa, and (c) 13.8 MPa.

In summary, the estimated fracture specific stiffness is stress-dependent and the fracture exhibits spatial variability of fracture specific stiffness. The spatial variability of specific stiffness exceeded the variation of specific stiffness induced by the heterogeneity of the granite matrix. The fracture specific stiffness increased with increasing normal stress and then approached an asymptote at high stresses. The stiffness maps prepared in this section are compared with the results of fluid invasion tests in the next Chapter.

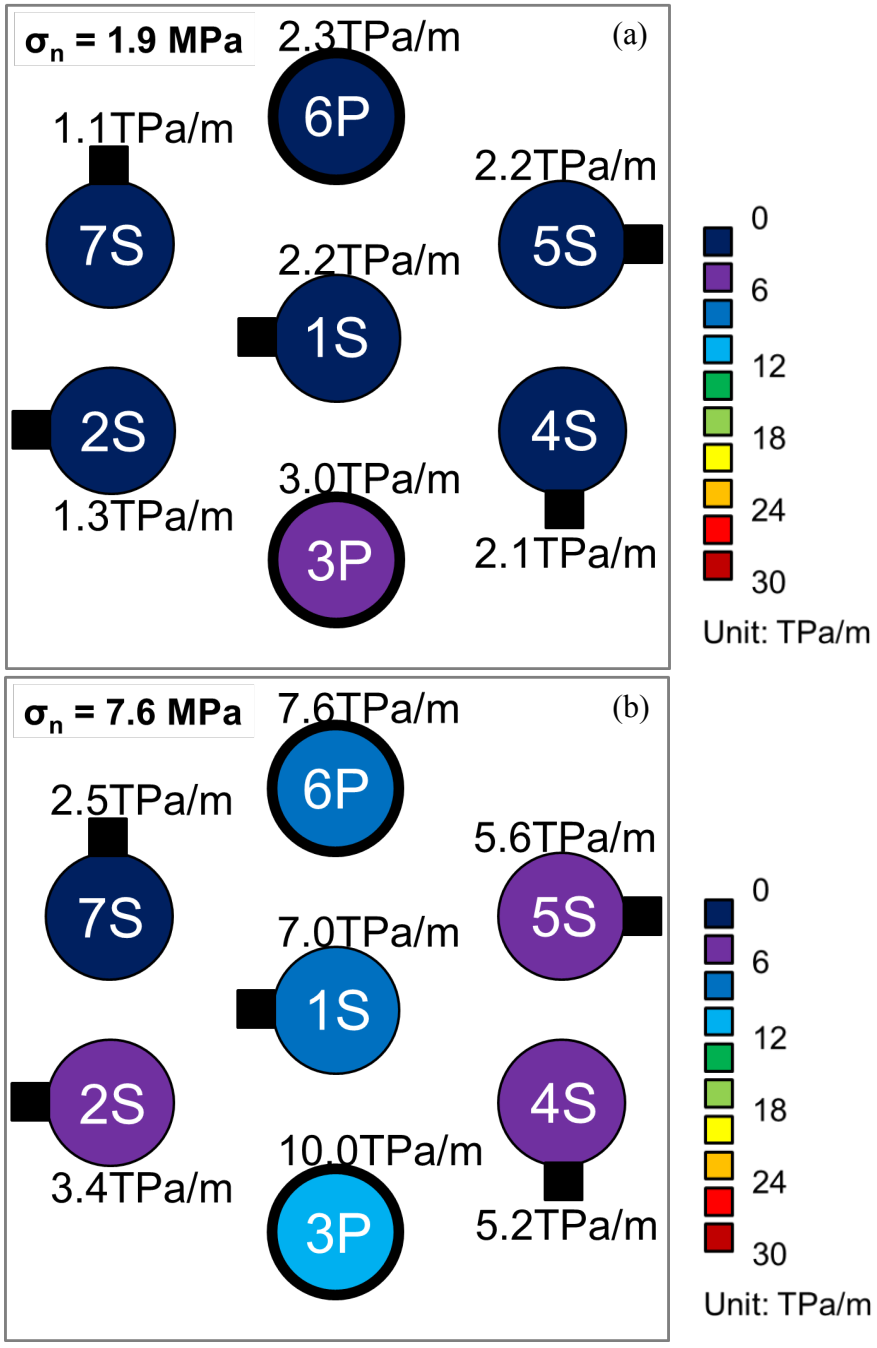

Figure 4.5.3-1. Stiffness map of GS01 with a 0° fracture at: (a) 1.9 MPa; (b) 7.6 MPa; and (c) 19.0 MPa normal stress. Elongated box represents the polarization of shear wave transducers (continued).

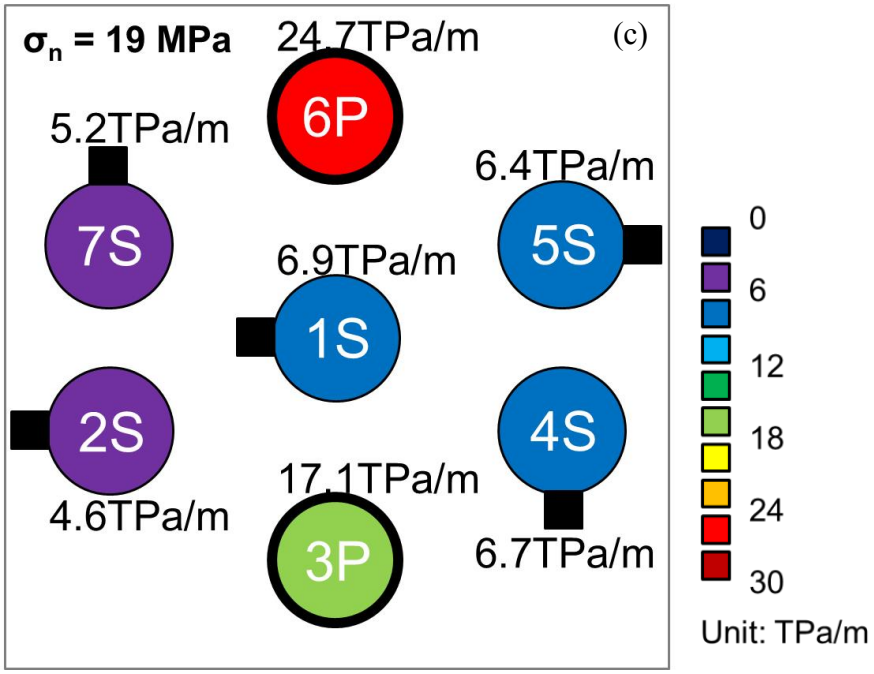

Figure. 4.5.3-1. Stiffness map of GS01 with a 0° fracture at: (a) 1.9 MPa; (b) 7.6 MPa; and (c) 19.0 MPa normal stress. Elongated box represents the polarization of shear wave transducers.

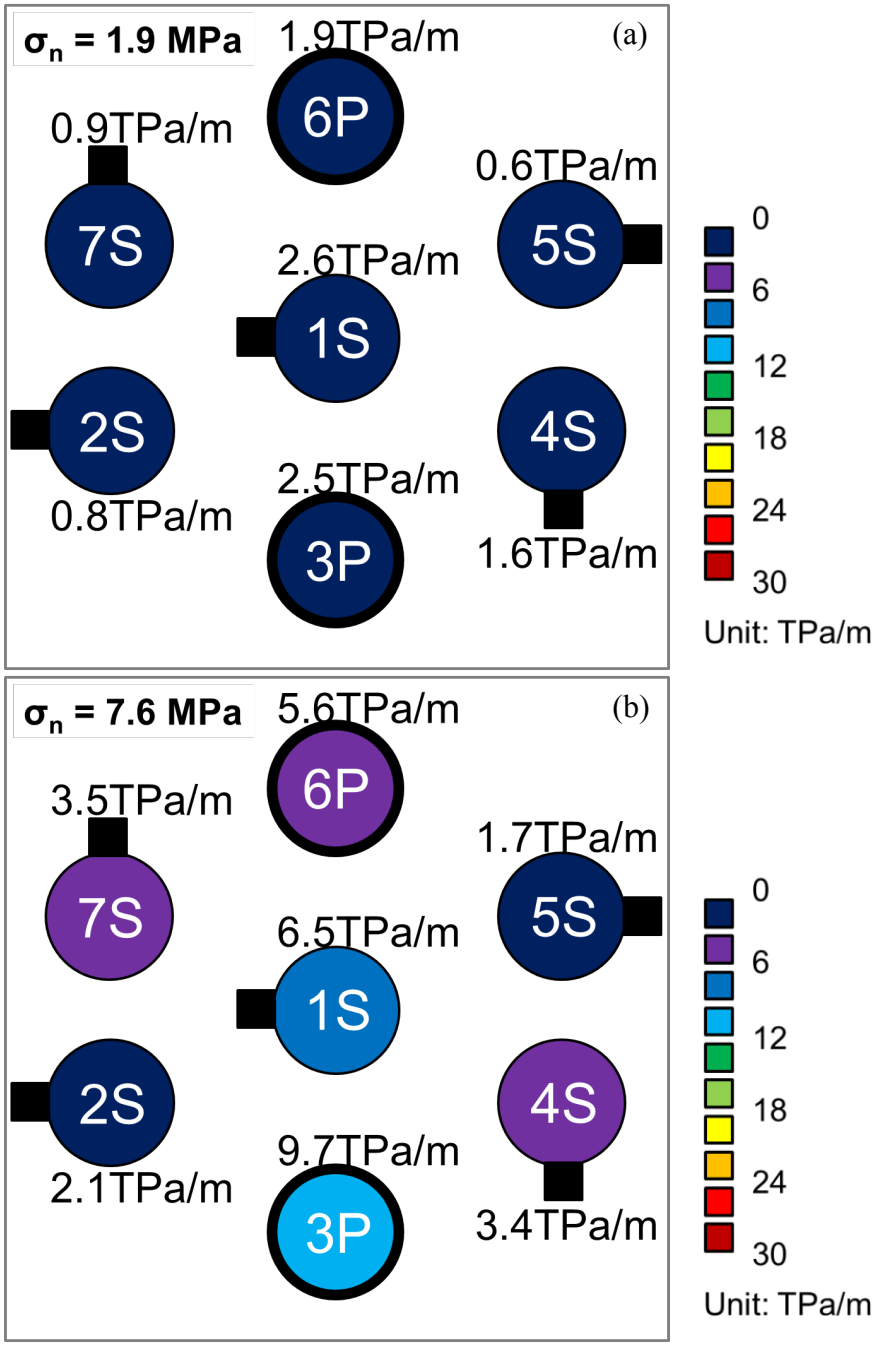

Figure 4.5.3-2. Stiffness map of GS04 with a 0° fracture at: (a) 1.9 MPa; (b) 7.6 MPa; and (c) 19.0 MPa normal stress. Elongated box represents the polarization of shear wave transducers (continued).

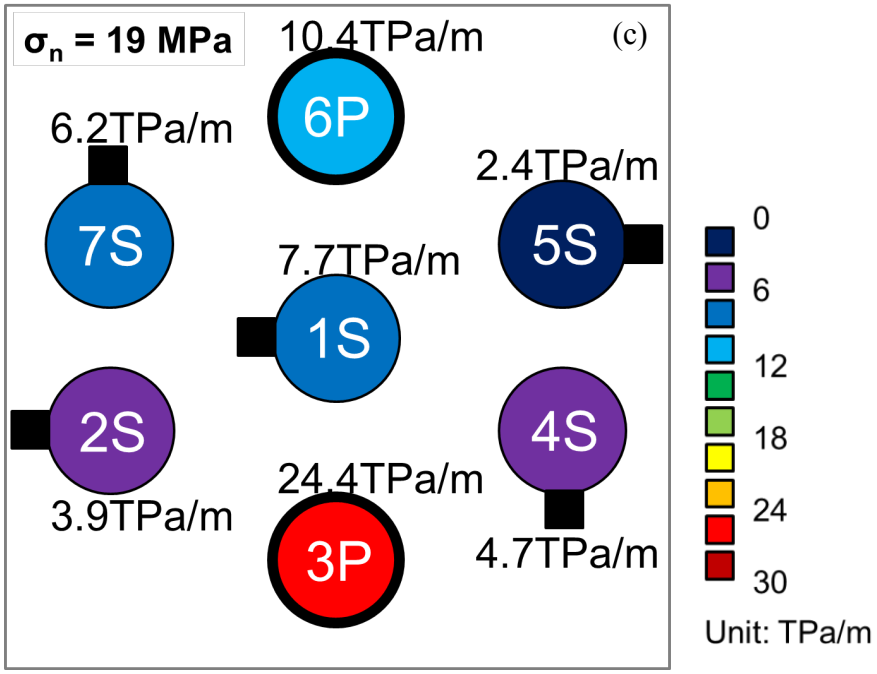

Figure. 4.5.3-2. Stiffness map of GS04 with a 0° fracture at: (a) 1.9 MPa; (b) 7.6 MPa; and (c) 19.0 MPa normal stress. Elongated box represents the polarization of shear wave transducers.

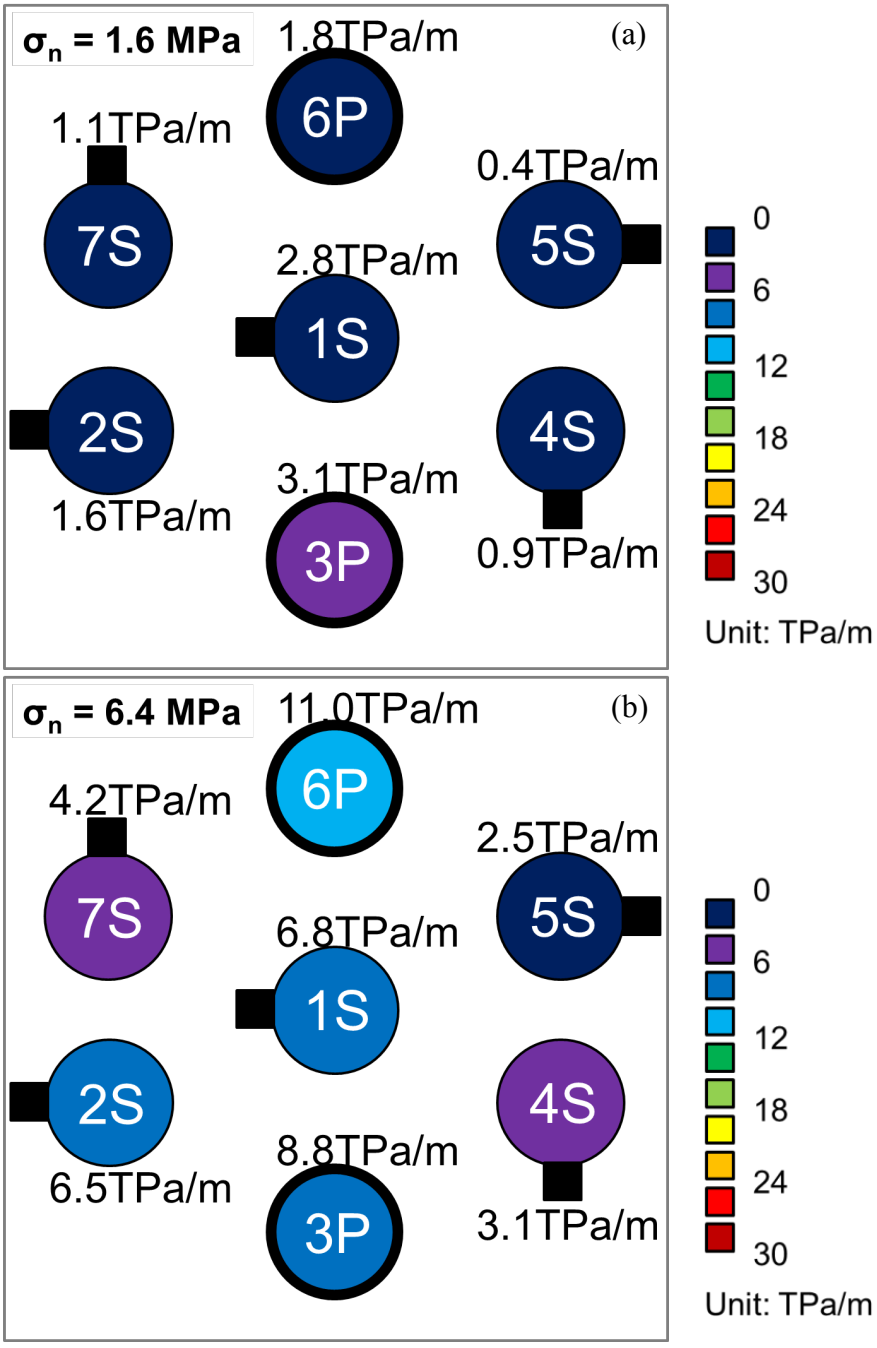

Figure 4.5.3-3. Stiffness map of GS03 with a 15° fracture at: (a) 1.6 MPa; (b) 6.4 MPa; and (c) 16.0 MPa normal stress. Elongated box represents the polarization of shear wave transducers (continued).

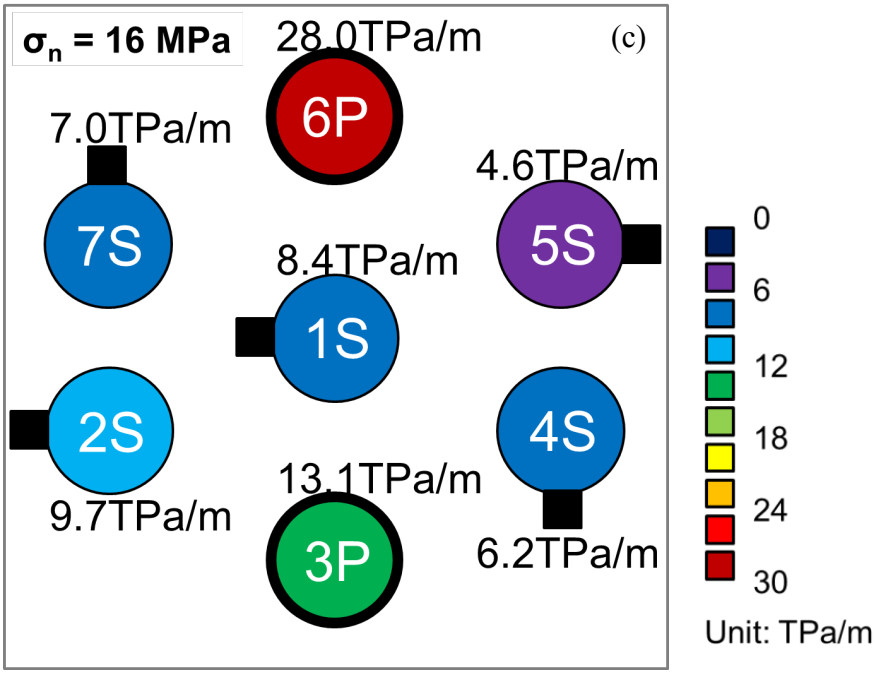

Figure. 4.5.3-3. Stiffness map of GS03 with a 15° fracture at: (a) 1.6 MPa; (b) 6.4 MPa; and (c) 16.0 MPa normal stress. Elongated box represents the polarization of shear wave transducers.

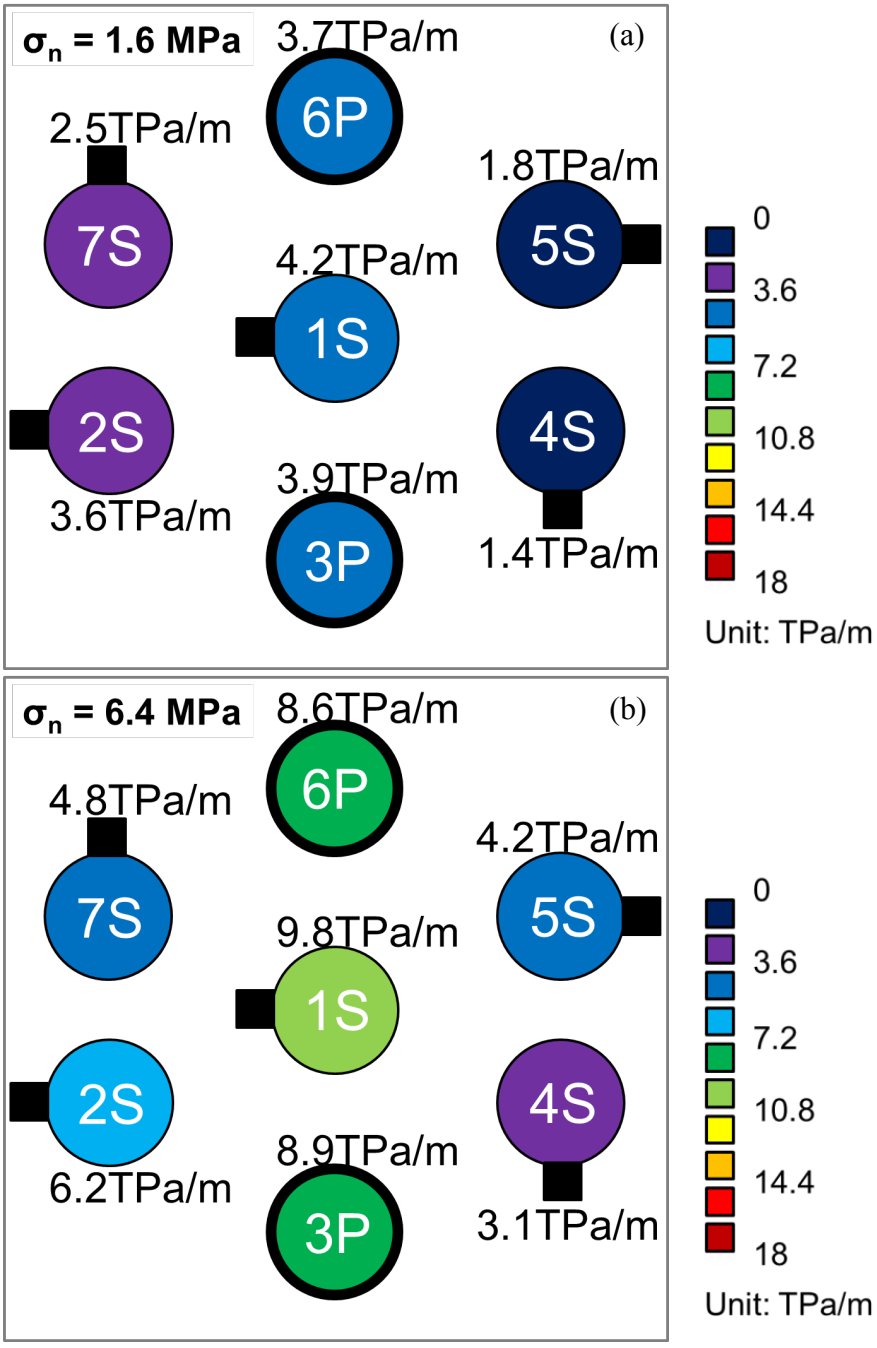

Figure 4.5.3-4. Stiffness map of GS06 with a 15° fracture at: (a) 1.6 MPa; (b) 6.4 MPa; and (c) 16.0 MPa normal stress. Elongated box represents the polarization of shear wave transducers (continued).

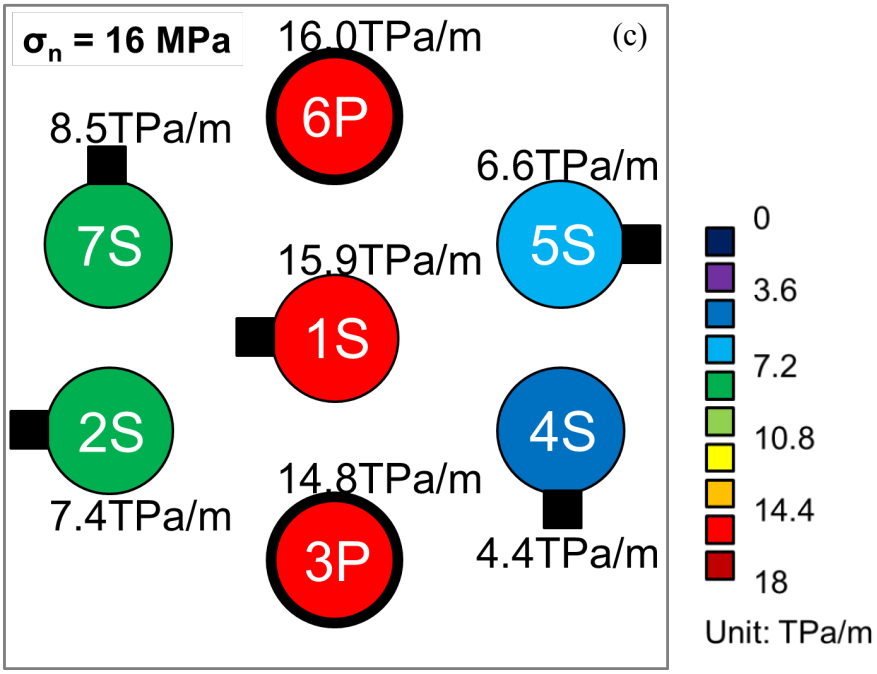

Figure 4.5.3-4. Stiffness map of GS06 with a 15° fracture at: (a) 1.6 MPa; (b) 6.4 MPa; and (c) 16.0 MPa normal stress. Elongated box represents the polarization of shear wave transducers.

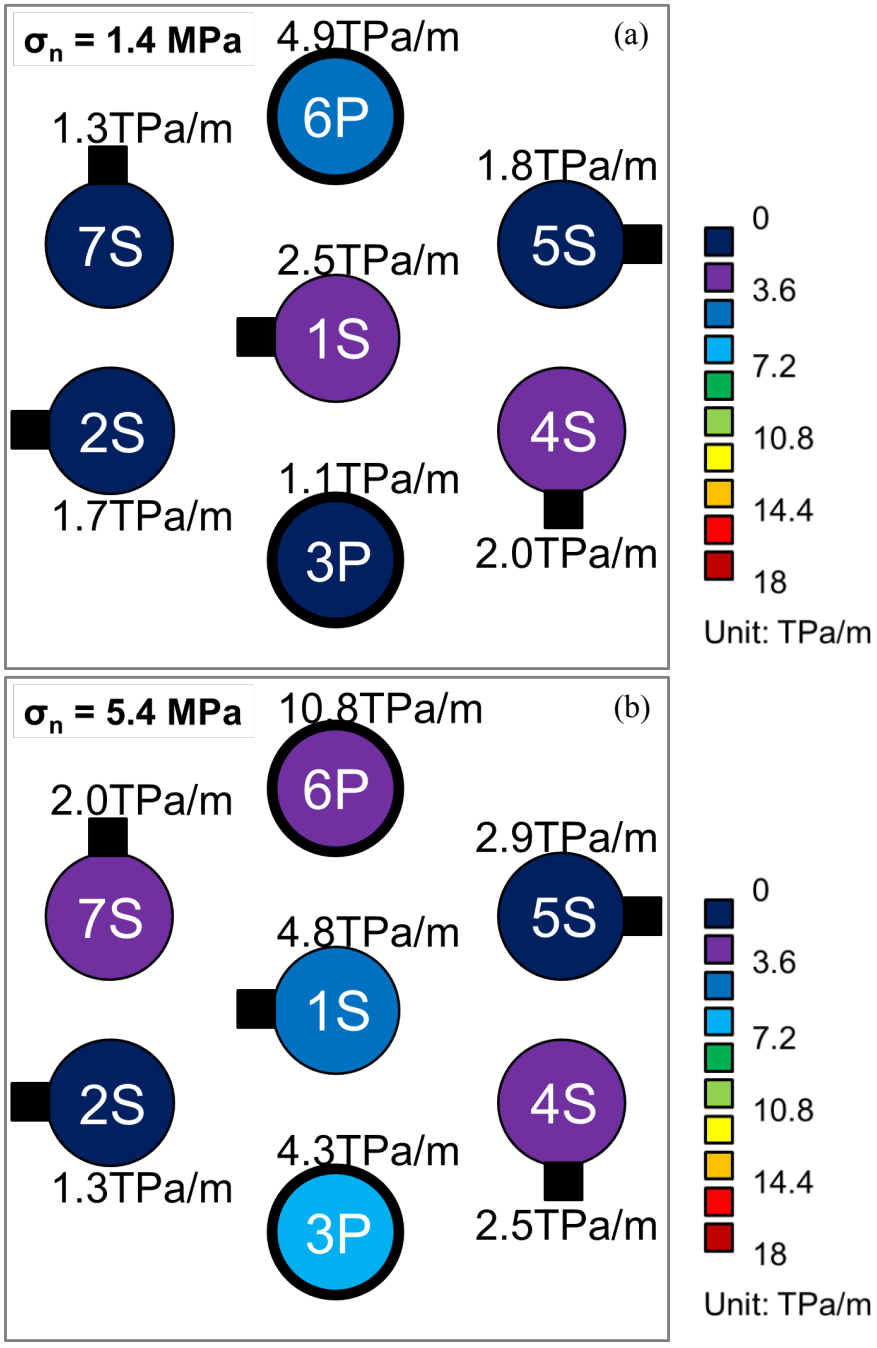

Figure 4.5.3-5. Stiffness map of GS02 with a 30° fracture at: (a) 1.4 MPa; (b) 5.4 MPa; and (c) 13.8 MPa normal stress. Elongated box represents the polarization of shear wave transducers (continued).

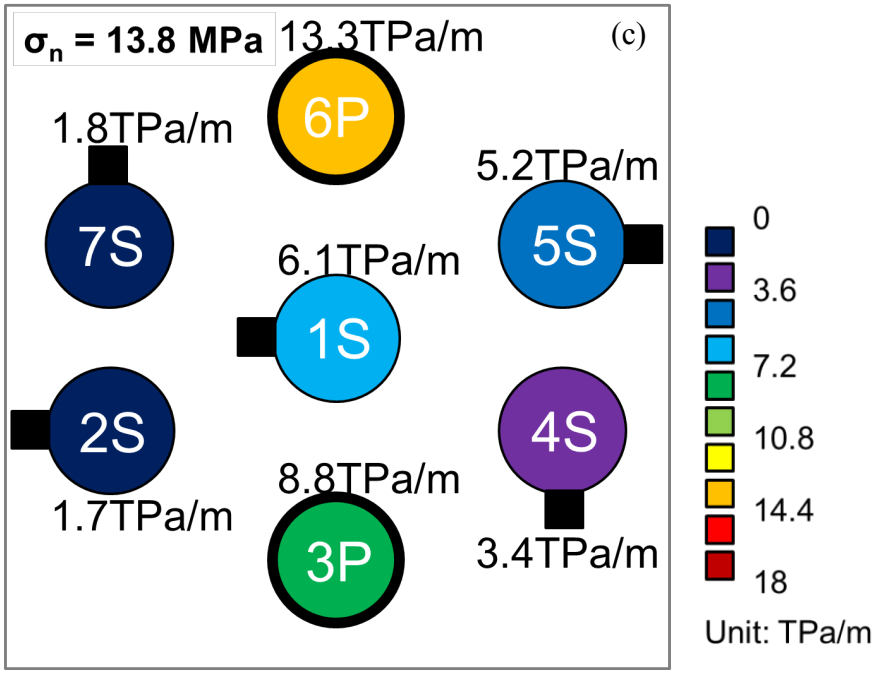

Figure. 4.5.3-5. Stiffness map of GS02 with a 30° fracture at: (a) 1.4 MPa; (b) 5.4 MPa; and (c) 13.8 MPa normal stress. Elongated box represents the polarization of shear wave transducers.

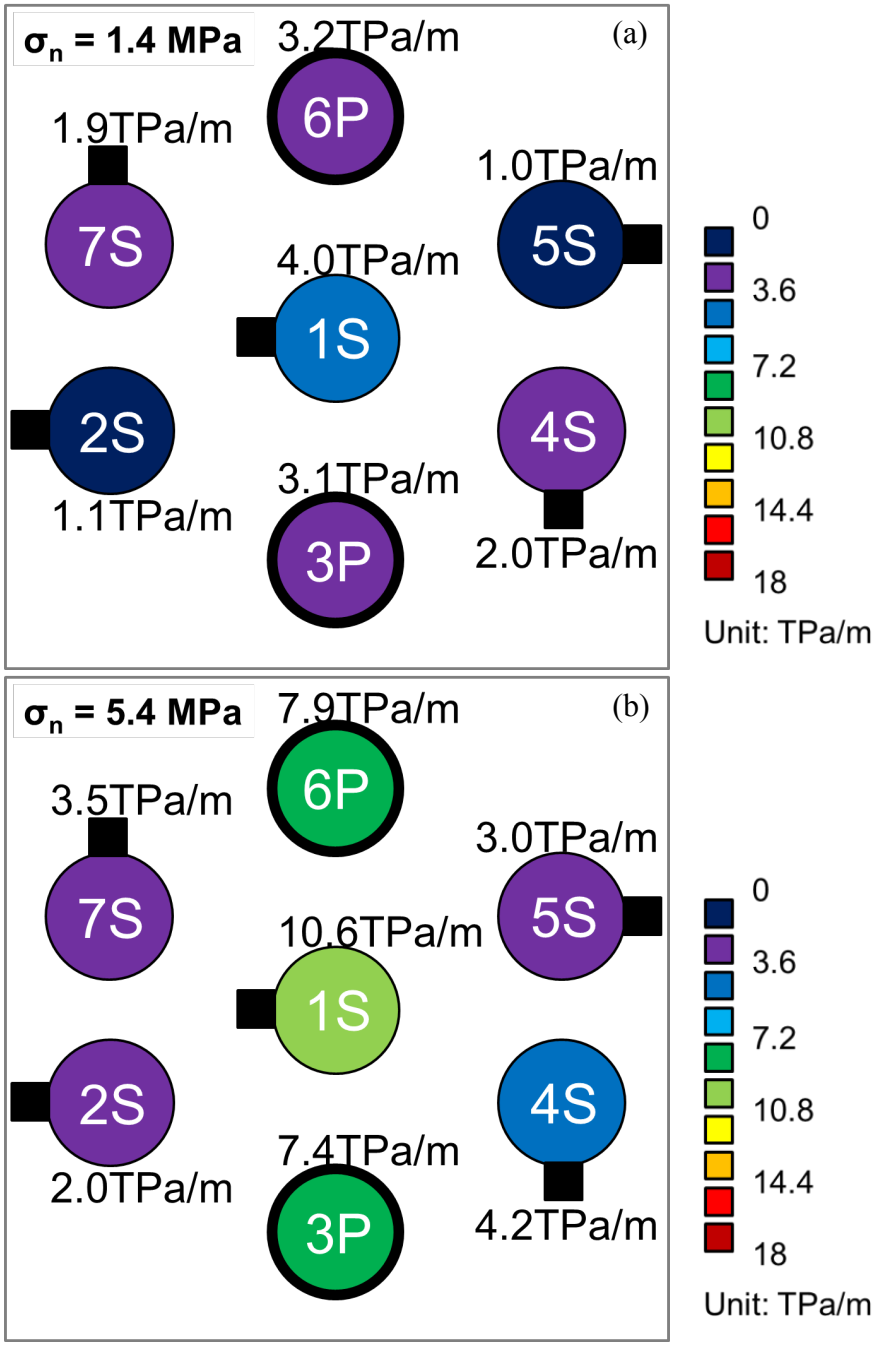

Figure 4.5.3-6. Stiffness map of GS05 with a 30° fracture at: (a) 1.4 MPa; (b) 5.4 MPa; and (c) 13.8 MPa normal stress. Elongated box represents the polarization of shear wave transducers (continued).

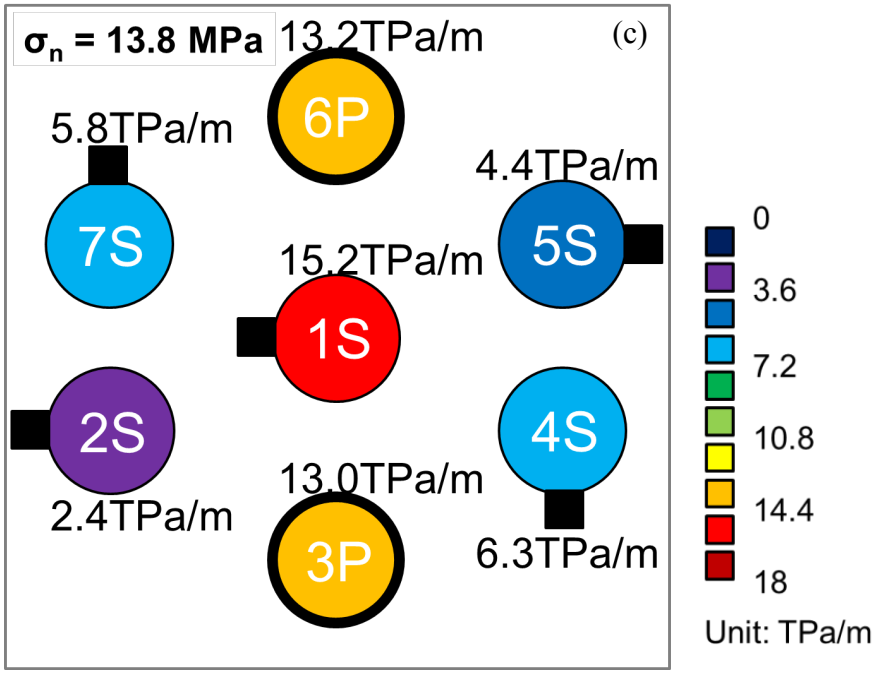

Figure. 4.5.3-6. Stiffness map of GS05 with a 30° fracture at: (a) 1.4 MPa; (b) 5.4 MPa; and (c) 13.8 MPa normal stress. Elongated box represents the polarization of shear wave transducers.

4.5.4 Discussion

As observed in the stiffness maps of specimens GS01 to GS06, the normal fracture specific stiffnesses, measured from 3P and 6P, are greater than the shear fracture specific stiffnesses from 1S, 2S, 4S, 5S, and 7S. This is because the normal fracture specific stiffness depends on the compressional wave velocity (see the section 2.2.1) that, for the granite matrix used in the experiments, ranged from 4,300 to 4,900 m/s while the shear wave velocity ranged from 2,400 to 2,600 m/s (Figure 4.4.1-4). The values result in a seismic impedance for compressional waves larger than that of the shear waves, by about 60-90%.

An important finding, based on the stiffness maps, is that fracture specific stiffness spatially changed across the fractures. Given that a non-uniform stress distribution on the fracture can affect local specific stiffness (the experimentally-found dependency of stiffness on normal stress), a numerical analysis was performed to quantify the normal and shear stress distribution on a fracture under uniaxial load ranging from 0 to 222 kN. In the numerical analysis, linear 3-noded triangular elements were used. The analysis was elastic and two-dimensional plane stress. The elastic modulus and Poisson's ratio were 50 GPa and 0.25, respectively, which were estimated from the compressional and shear wave velocities shown in Figure 4.4.1-4. Figure 4.5.4-1 (a) shows a sketch of the boundary conditions applied to the numerical model. Vertical and horizontal displacements were constrained at the bottom and at the center of the model, respectively, due to the symmetry of the specimen. The model was compressed up to 222 kN applying a downward constant velocity displacement at the top of the model. In the simulation, compression is negative. Because of symmetry, normal and shear stresses under 2S, 7S,

4S, and 5S should be the same. Figure 4.5.4-1 (b) highlights the locations where normal and shear stresses were calculated for each transducer and for each specimen with a 0°, 15°, and 30° fracture.

Figure 4.5.4-2 shows the normal (σ) and shear (τ) stresses on (a) 0°, (b) 15°, and (c) 30° fracture plane; red closed symbols stand for center transducers (1S, 3P, and 6P), and black open symbols for side transducers (2S, 4S, 5S, and 7S). As the fracture angle increases, the normal stress imposed on the fracture decreases, while the shear stress increases for all transducers. Both normal and shear stresses for center transducers are greater than for side transducers, but the difference is small. The normal stress for center transducers is larger than for side transducers by about 8-12%. The shear stress on the 0° fracture was zero, as expected. For the angled fractures (15° and 30°), the differences in shear stress between center and side transducers were only about 1-7%. The results of the numerical analysis indicate that the normal and shear stress distribution across a fracture plane are fairly uniform, suggesting that the stress distributions imposed on the fractures in specimens GS01-GS06 do not cause a large variation of fracture specific stiffness. It is noted that the numerical simulation did not consider the complex fracture geometry such as the variation of asperities along the fracture surface or the aperture in the fracture. However, because the specimens GS01-GS06 had a well-mated fracture, the average normal and shear stresses on the fracture plane was not expected to be significantly different from the numerical results.

Experimental results on fractured specimens GS01-GS06 show that the local variability of shear fracture specific stiffness can be correlated with the local distribution of asperity heights and with the maximum or the top 0.1% of the local micro-slope angles (see

section 4.5.2.3). For normally compressed fractures (GS01 and GS04) a local roughness distribution with small CV results in large shear fracture stiffness (Figure 4.5.2-5 (b)). For the specimens with an angled fracture (GS02, GS03, GS05, and GS06), shear fracture specific stiffness increased with an increase of the maximum or the top 0.1% micro-slope angles (Figure 4.5.2-8). These results suggest that the magnitude of the local shear fracture specific stiffness is related to the local fracture geometry, which can be quantified using surface roughness or micro-slope angles. Finally, the spatial variability of the shear fracture specific stiffness is interpreted as the result of the variation of fracture geometry across the fracture.

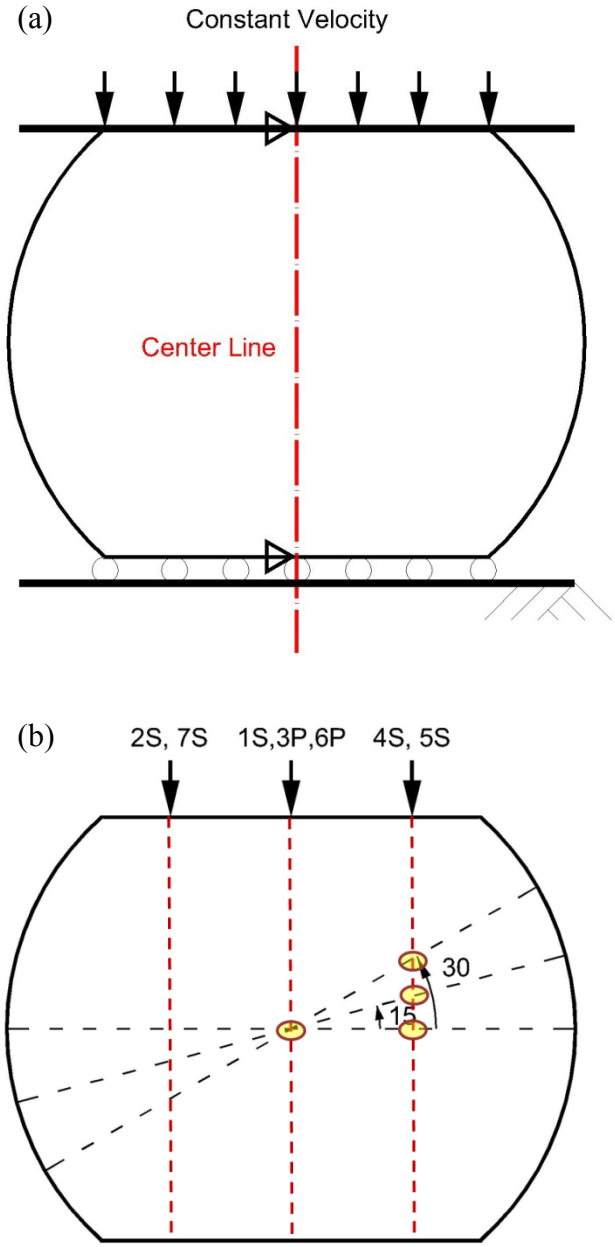

Figure 4.5.4-1. (a) Applied boundary conditions in the numerical model. The vertical displacement is constrained at the bottom of the model and the horizontal displacement is constrained at the center of the model. A downward constant velocity is used at the top of the model to apply compression; (b) Highlighted areas indicate the locations of the 0°, 15°, and 30° fracture planes where normal and shear stress are calculated. The dotted lines indicate the 0°, 15°, and 30° fracture planes.

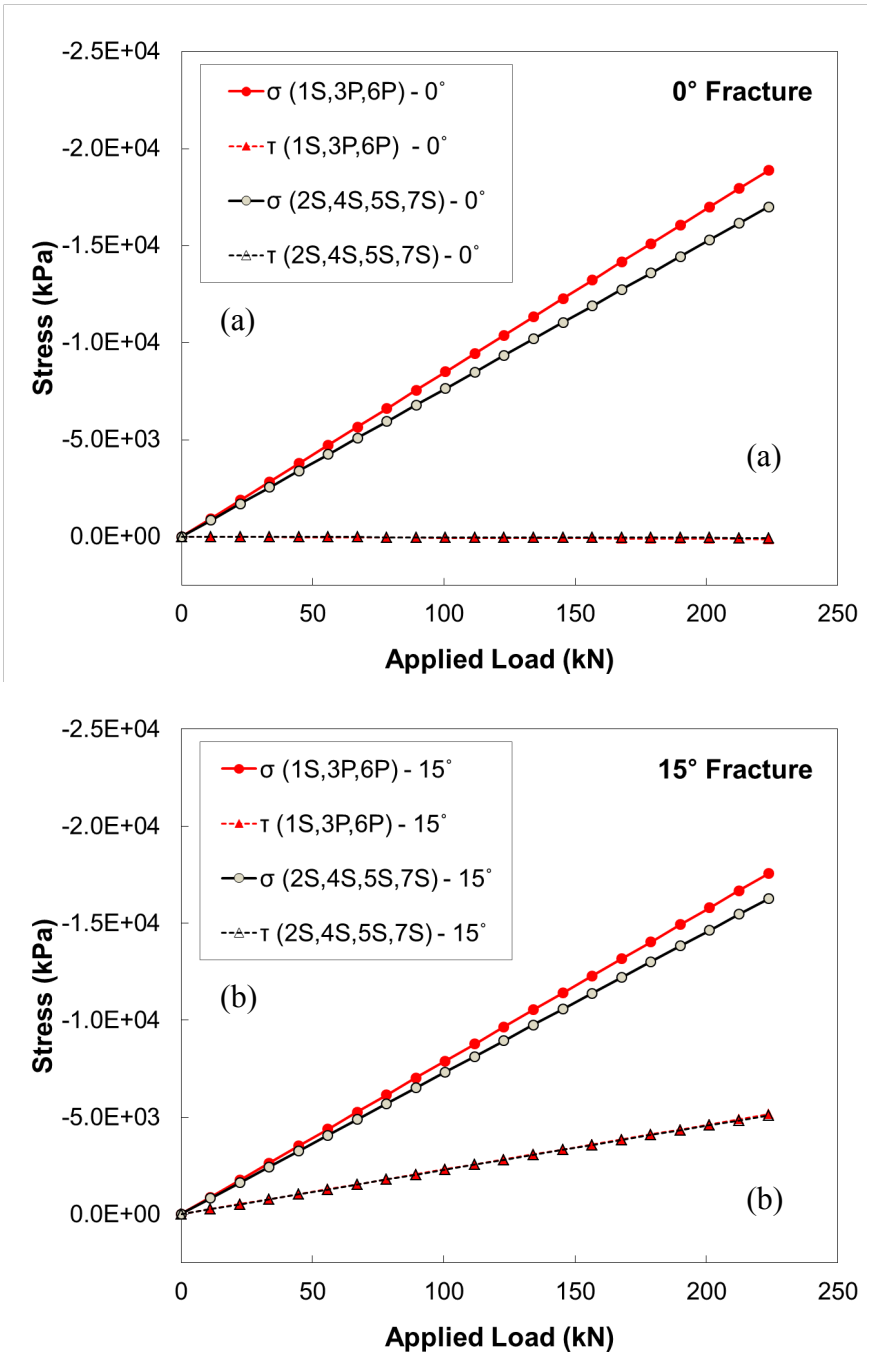

Figure 4.5.4-2. Computed normal (σ) and shear (τ) stresses imposed on: (a) 0°; (b) 15°; and (c) 30° fracture planes for center transducers 1S, 3P, and 6P (red closed symbols), and side transducers 2S, 4S, 5S, and 7S (black open symbols) (continued).

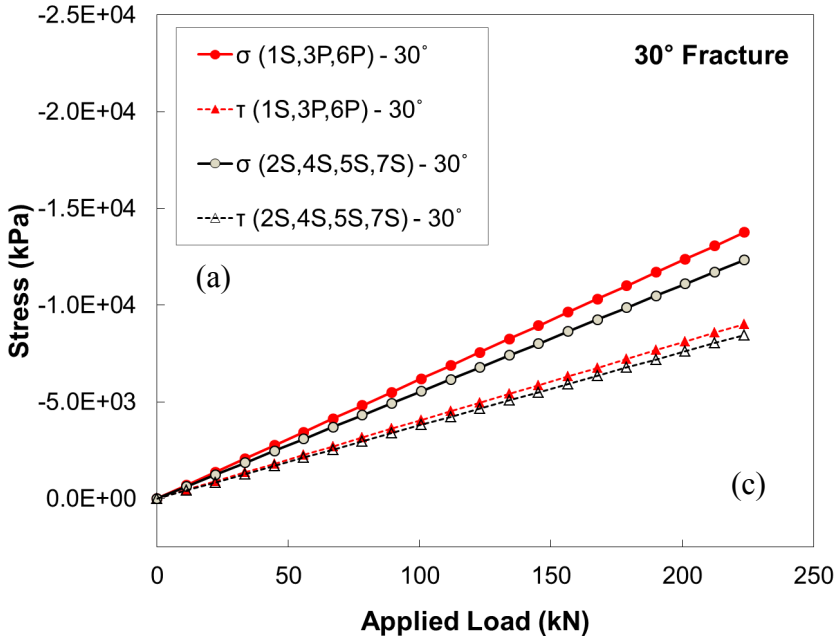

Figure 4.5.4-2. Computed normal (σ) and shear (τ) stresses imposed on: (a) 0°; (b) 15°; and (c) 30° fracture planes for center transducers 1S, 3P, and 6P (red closed symbols), and side transducers 2S, 4S, 5S, and 7S (black open symbols).

4.6 Summary

Seismic measurements were made on intact and fractured granite specimens as a function of stress. Specimens with three different fracture angles, namely 0°, 15°, and 30°, were prepared. Based on the displacement discontinuity theory, the normal and shear fracture specific stiffness were calculated from the measurements of transmitted compressional and shear waves. Stiffness maps showed the spatial distribution of fracture specific stiffness. Based on the experimental results, the following conclusions are drawn:

- The existence of micro-cracks in the granite matrix resulted in stress-dependent seismic behavior of the intact granite specimens GS07 to GS09.
- The granite matrix was weakly anisotropic with an anisotropic ratio of about 0.9 for shear wave velocities in two orthogonal directions.
- Transmission of seismic waves across a fracture depends on the magnitude of the fracture specific stiffness, as the displacement discontinuity theory predicts.
- Fracture specific stiffness increases with increasing stress, inducing the increase of the dominant frequency of transmitted waves.
- The heterogeneity of the granite material resulted in a ±8~12% variation in stiffness calculation, depending on the selection of the intact standard.
- The more uniform the asperity heights are the stiffer the fracture, but only when the fracture is subjected to normal loading.
- High micro-slope angles strongly influence the shear fracture specific stiffness, when the fracture is subjected to shear stress.

- Local variation in fracture geometry induces spatial variability in shear fracture specific stiffness.
- The normal fracture specific stiffness tends to be larger than the shear fracture stiffness. This is due to the greater wave velocity in compression than in shear.
- The fracture specific stiffness is stress-dependent and varies spatially along the fracture.

CHAPTER 5. FLUID FLOW AND FRACTURE SPECIFIC STIFFNESS

5.1 Introduction

A series of experiments had been carried out on fractured granite samples with concurrent measurements of transmitted compressional and shear waves, as well as of fluid flow through their fracture. During the experiments, the fluid front in the fracture was identified through changes of transmitted compressional and shear waves. The results are interpreted in relation to the spatial distribution of fracture specific stiffness. In addition to the fractured granite samples, two granite column samples were prepared to characterize the seismic behavior of the granite matrix when invaded by the fluid. These tests were needed to interpret the results of the tests on fractured granite samples where invasion occurred both through the fracture and through the matrix. From surface roughness measurements of the fracture, the aperture distribution was numerically reconstructed, which was expected to provide information on the spatial distribution of fracture specific stiffness and distribution of fluid flow through the fracture. The objective of the experiments was to investigate the relationship between fluid flow and fracture stiffness when a fracture was subjected to normal and shear stress simultaneously.

5.2 Experimental Method

Fluid flow experiments were performed on granite specimens by injecting pressurized water into the fracture. During the tests, changes of transmitted compressional and shear waves were observed while the fluid front propagated in the fracture plane. In addition, fluid flow through the fracture was measured as a function of stress.

5.2.1 Sample Preparation

5.2.1.1 Granite Column Specimens

The peak-to-peak amplitude and wave velocity measured on intact specimens GS07, GS08, and GS09 were stress-dependent due to the existence of micro-cracks in the rock matrix as discussed in the section 4.4.1. The micro-cracks allow invasion of fluid into the rock matrix, which influences the seismic behavior of the granite. This requires the characterization of the seismic behavior of the granite matrix when invaded by the fluid (water). Two prismatic granite specimens were fabricated with dimensions 2 inches x 2 inches x 4 inches (width x depth x height) for the invasion test. Specimen C01 did not have a fracture (intact specimen), while specimen C02 contained a single fracture orthogonal to the long axis of the prism. Compressional and shear wave transducers were directly attached to the surface of each specimen to measure the transmitted compressional and shear waves across the granite matrix or the fracture during the fluid invasion. Figure 5.2.1-1 shows a photograph of the specimens and the arrangement of the seismic transducers. Figure 5.2.1-1 (a) depicts the intact specimen C01 and Figure 5.2.1-1 (c) the specimen C02 with the fracture. Four pairs of compressional and shear wave

transducers were attached to the four sides of each sample to monitor seismic behavior as fluid was permeated. One additional shear wave transducer pair was added to the top and bottom of the C02 specimen to monitor the seismic behavior of the fracture when invaded by the fluid.

5.2.1.2 Fractured Granite Specimens

The fractured granite specimens (GS01-GS06) that were tested to characterize the spatial distribution of fracture specific stiffness, as described in section 4.4.2, were used again for the fluid invasion tests. In order to spread the flow across the fracture immediately after the point of injection and to concentrate the flow into the outlet tubing, two reservoirs were placed adjacent to the inlet and outlet. The reservoirs were made with two pairs of parallel cuts into one of the fracture surfaces (Figure 5.2.1-2). One set of reservoirs was parallel to the direction of shear loading (*x*- direction) and the other one was perpendicular to it (*y*- direction). These two pairs of reservoirs in the *x*- and *y*- directions enabled us to control the direction of fluid flow. A hole was drilled from the outside of the specimen into each of the reservoirs and was connected to tubing to enable fluid flow into and out of the fracture. The inlet was connected to a flow pump to provide the desired flow rate and hydraulic head. To prevent fluid leakage, the sample was sealed by placing silicon around the fracture perimeter and then covered with the commercial sealing foam 'Great Stuff Pond'. This sealing strategy enabled the application of water pressure up to 100 kPa to the specimen without leaking.

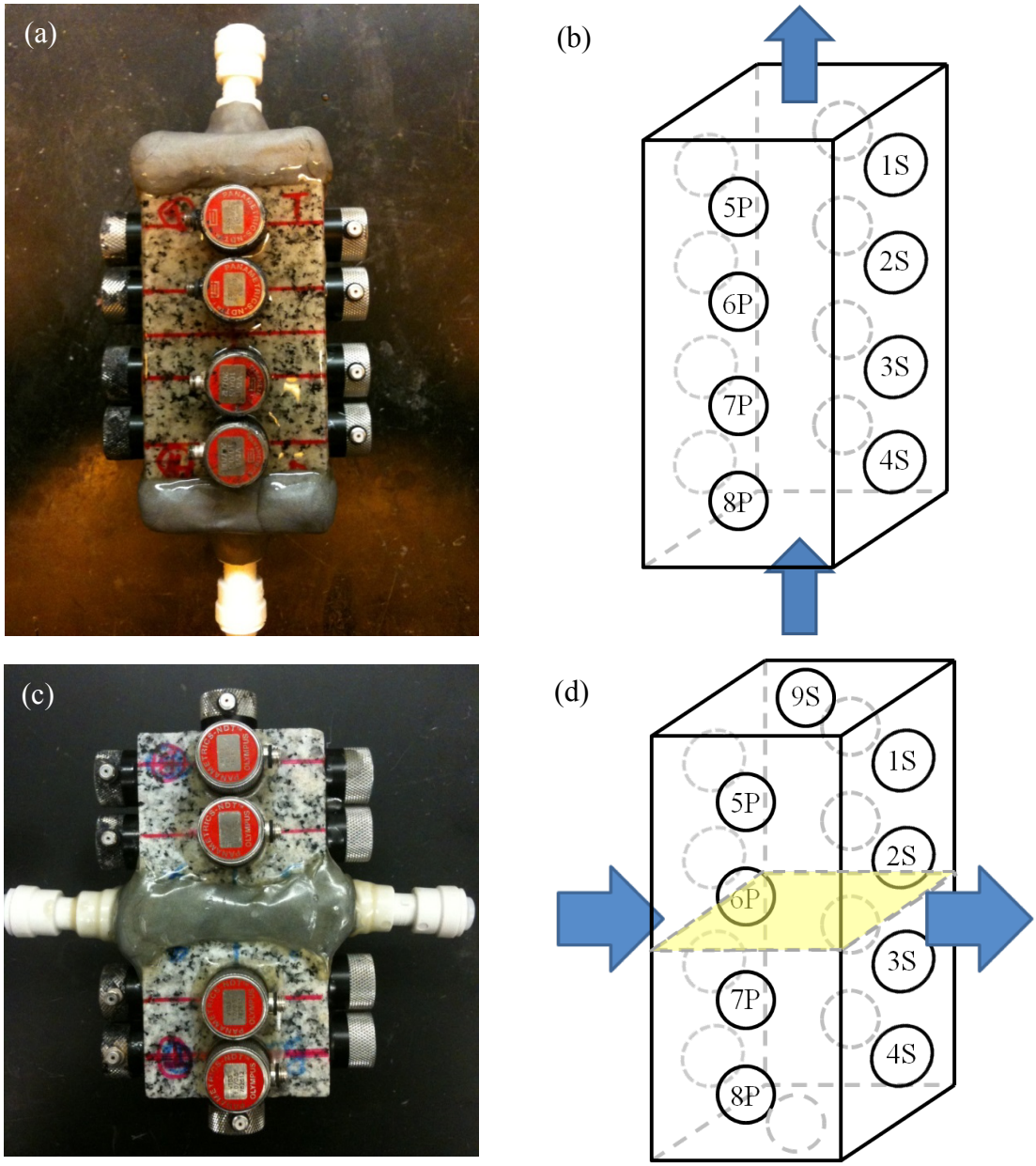

Figure 5.2.1-1. Photographs of granite column samples with seismic transducers: (a) intact C01 specimen; and (c) fractured C02 specimen. Layout of compressional (P) and shear (S) wave transducers for: (b) C01; and (d) C02 specimens. Blue arrows indicate the intended flow direction and the yellow plane represents the fracture in the middle of specimen C02.

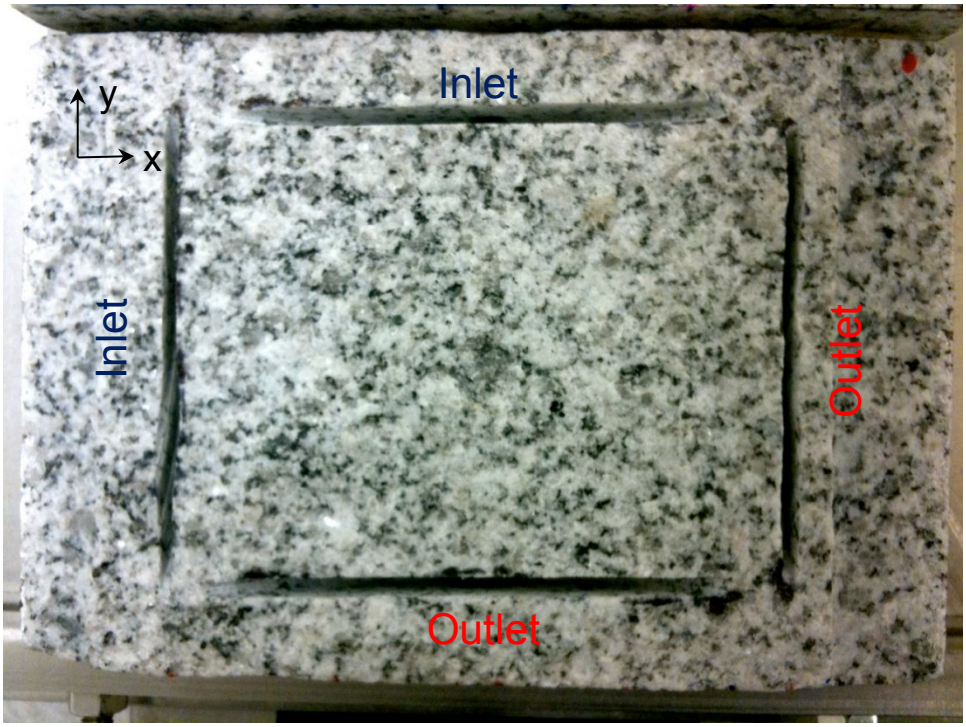

Figure 5.2.1-2. Fluid reservoirs cut into the fracture surface to induce uniform flow in and out of the fracture.

5.2.2 Experimental Procedure

5.2.2.1 Fluid Invasion Tests on Granite Column Specimens

The specimens were first oven-dried for several days before the test. During the experiments, seismic measurements from compressional and shear wave transducers were made to monitor the seismic response of the granite matrix and fracture. The seismic imaging system described in section 3.3.2 was utilized to measure and record the seismic data. The measurements of transmitted compressional and shear waves made with the dry specimen (no flow) were compared with those obtained during the fluid (water) injection. A computer-controlled flow pump (GEOTAC), that recorded the variation of fluid pressure and flow rate with time, was used to inject water into the specimens. For the intact specimen C01, water was injected from the bottom of the sample. As the water permeated upwards into the granite matrix, compressional and shear waveforms were obtained and used to detect the fluid front. For the fractured specimen C02, water was directly injected into the fracture. In this case, water filled the void spaces in the fracture and permeated the rock matrix at the same time. From the experimental results, the invasion velocity in the granite matrix was computed and used to determine the setup time for fluid invasion tests on the fractured granite samples.

5.2.2.2 Flow Tests on Fractured Granite

Prior to each fluid flow experiment, the specimen was oven dried at 95˚C for several days. After drying, the inlet reservoir of the fracture was connected to the flow pump to provide pressurized water to the fracture plane. The water outflow was collected in an external

reservoir and the outflow was estimated by measuring the weight of the water exiting the fracture at given time intervals. For all tests, a constant load was applied to the specimen that was normal to the fracture. Concurrent measurements of fluid flow and seismic wave transmission were performed to examine the fracture stiffness - fluid flow behavior. Changes of peak-to-peak amplitudes and compressional and shear wave velocities were used to detect the fluid front along the fracture, and the arrival time of the fluid front was in turn correlated with the spatial distribution of the fracture specific stiffness. Table 5.2.2-1 lists the fluid invasion tests, i.e., Test-I to Test-IV, and includes information about the applied normal stress and water pressures. The seismic imaging system measured and stored full waveforms of transmitted P- and S- waves every 0.5 minutes for Test-I and every 0.1 minutes for Tests II to IV. The direction of fluid flow in the invasion tests was in the *x*- direction, as shown in Figure 5.2.1-2.

Table 5.2.2-1. Fluid invasion tests.

Test	Specimen	Normal stress (MPa)	Water pressure (kPa)	Time interval for seismic data acquisition (sec)
Test-I	GS01	1.9	10	30
Test-II		7.6	100	6
Test-III	GS03	7.6	100	6
Test-IV	GS06	7.6	100	6

5.2.3 Reconstruction of Aperture Distribution

The aperture distribution of the fractures was reconstructed from the surface roughness measurements. Surface roughness measurements of the fractured granite specimens GS01-GS06 and the fractured granite column C02 were made prior to fluid invasion tests. From the surface measurements data, the aperture distribution was reconstructed numerically using a Matlab code written for this purpose. The fracture surface roughness data were corrected for misalignment by applying three orthogonal rotations and translations to minimize errors from positioning the specimen in the specimen holder of the laser profilometer system (Sharifzadeh et al. (2008)). The corrections for rotations in the *x*- and *y*- axes (the fracture plane was assumed to be on the *x*-*y* plane) were performed first. The rotation angles for the *x*- and *y*- directions were obtained by forcing the edges of the fracture to be horizontal. To determine the optimum position of the upper half of the specimen with respect to the lower half, i.e. the location of the origin of coordinates of the *x*- and *y*- axes, the upper and lower surfaces of the fracture were rotated relative to each other in increments of $\Delta\theta = 0.25^{\circ}$ (i.e. a number of rotations were performed about the *z*-axis with increment $\Delta\theta$). For each increment $\Delta\theta$, the corrected two surfaces of the fracture were mated. At this point a number of translations of the *x*- and *y*- axes were performed and a two-dimensional cross-correlation was applied to each translation to find the optimum position of the *x*- and *y*- axes. The two-dimensional cross-correlation is a measure of similarity of two surfaces, and estimates how the shapes of the two surfaces match. The optimum position of the *x*- and *y*- axes (i.e. the origin of coordinates of the axes) is determined when the value of the cross-correlation is maximized (Santamarina and Fratta (2005)). After this was done for each *z*- rotation, the apertures of the fracture

were calculated by measuring the distance between the two corrected surface roughness data. The standard deviation of each aperture distribution was calculated. The best estimate for the position of each half of the specimen with respect to each other is found for the *z*-rotation, and associated position of the *x*- and *y*- axes, that gives the smallest standard deviation of the aperture distribution.

5.3 Results and Analysis

5.3.1 Aperture Distribution

5.3.1.1 Validation of Optimum Aperture Distribution Procedure

Reconstruction of the aperture distribution of a fracture from surface roughness measurements requires two key steps: i) finding the optimum position in the *x*- and *y*-axes based on the maximum value of the two-dimensional cross-correlation between the two surface roughness data, and ii) determination of the best estimate of the aperture distribution based on the smallest standard deviation. The validity of these two key assumptions in reconstructing the aperture distribution was tested on two synthetic fractures, which were perfectly mated to each other such that the aperture was zero. The surface roughness *z* in the synthetic fracture was assumed to be a function of the coordinates *x* and *y*. An arbitrary surface roughness *z* is given by the following mathematical expression:

$$z = \frac{1}{4}xy \cdot \exp((-x^2 - y^2)) + \frac{1}{8}\sin(2\pi x) + \frac{1}{8}\sin(\frac{\pi y}{2}) + 0.005xy \qquad (5.3.1\text{-}1)$$

where, x and y are the coordinates on the plane of the fracture.

The size of the synthetic fracture was 4 mm x 4 mm and the surface roughness z was calculated at increments of 0.025 mm in the x- and y- directions. It was assumed that the center of the synthetic fracture was located at the origin of the coordinates and that the fracture was perfectly mated with zero lag distances in x- and y- directions and zero rotations in z- directions. Figure 5.3.1-1 contains the: (a) bottom and (b) top surfaces of the synthetic fracture. Figures 5.3.1-1 (c) and (d) show a three-dimensional representation of the bottom and top surfaces, respectively, of the synthetic fracture.

The first procedure to be validated was the 2-dimensional cross-correlation technique that determined the optimum position of x- and y- directions. Figure 5.3.1-2 (a) shows the variation of the intensity of the 2-dimensional cross-correlation values between the two surface roughness data of the synthetic fracture as a function of lag distance in x- and y- directions. Here, the lag distance is a distance shifted relative to each fracture surface. The maximum intensity was obtained at a lag of zero in the x- and y- directions, which indicates that the optimum position is at the origin of coordinates. The aperture obtained at the optimum position with zero lag is shown in Figure 5.3.1-2 (b) and, as expected, the calculated optimum apertures were uniformly zero throughout the fracture plane.

The second procedure consisted of the selection of the best estimate of the aperture distribution from the distributions calculated at different z- axis rotation (angle θ). For the synthetic fracture, the best estimate of the aperture distribution should give zero aperture throughout the fracture plane, which would result in zero standard deviation of the aperture distribution. Figure 5.3.1-3 (a) shows the variation of the aperture distribution as a function of the z- rotation. The angles for the z- rotation relative to each other were

±15°. For 0° rotation in the *z*- direction, uniform zero apertures were obtained throughout the fracture plane. However the aperture distributions for fractures misaligned in the *z*-axis, i.e., deviated from the 0° rotation in the *z*- direction, had wider distributions; the more the fracture was misaligned in the *z*-axis, the wider the aperture distribution was. Figure 5.3.1-3 (b) shows the variation of the standard deviation for each aperture distribution calculated for different *z*- rotation angles. For the fracture with θ=0°, the minimum standard deviation of the aperture distribution was obtained. As seen in Figures 5.3.1-3 (a) and (b), the optimum aperture distribution with uniform zero aperture and the minimum standard deviation were found at θ=0°

In addition to the synthetic fracture, which was perfectly mated and thus had zero aperture, an synthetic fracture that had in its surface roughness a random noise was also used for validation. The roughness of the new fracture was defined by adding a random term to equation (5.3.1-1). Equation (5.3.1-2) provides the final roughness:

$$z = \frac{1}{4}xy \cdot \exp((-x^2 - y^2)) + \frac{1}{8}\sin(2\pi x) + \frac{1}{8}\sin(\frac{\pi y}{2}) + 0.005xy + Amp \cdot rand(x, y) \quad (5.3.1\text{-}2)$$

where, *rand(x, y)* is a random number based on the *x* and *y* coordinates, and *Amp* is a constant that gives the magnitude of the noise. The magnitude of noise was chosen to give up to a 40% of the maximum amplitude in equation (5.3.1-1). The random noise was provided by the random number function in Matlab (*rand*) that generates random numbers drawn from a standard uniform distribution on the open interval (0, 1). Figure 5.3.1-4 shows the synthetic fracture with the random noise. The new roughness resulted

in deviations from the previous surface roughness, as one can see by comparing Figure 5.3.1-4 with Figure 5.3.1-1.

Figure 5.3.1-5 (a) presents the variation of intensity of the two dimensional cross-correlation between the two surface roughness as a function of lag distance in *x*- and *y*-directions and Figure 5.3.1-5 (b) the best estimate of aperture distribution at the lag of zero in the *x*- and *y*- coordinates. The optimum position was found for zero lag distance, similar to the previous case. The optimum aperture distribution determined at the zero lag shows the randomly distributed aperture throughout the fracture plane. Figure 5.3.1-6 (a) shows the aperture distribution for the synthetic fracture as a function of the *z*- rotations relative to each other within ±15°. The apertures at 0° rotation in the *z*- direction had a distribution close to uniform and had the smallest standard deviation (Figure 5.3.1-6 (b)). As the rotation in the *z*- direction deviated from 0°, the aperture distribution broadened.

Based on the results of the verification tests, it was concluded that the optimum position in *x*- and *y*- directions and the best estimate of aperture distribution can be determined from the procedures that included a first step based on finding the maximum 2-dimensional cross-correlation and a second step based on determining the minimum standard deviation of the aperture distribution.

5.3.1.2 Aperture Distribution of the Fractured Granite Specimens

The technique for determining the best estimate of fracture aperture described in the preceding section was applied to all the fractured granite samples GS01-GS06. The effect that misalignment about the z-axis had on the aperture distribution is shown in Figure 5.3.1-7. The figure shows the aperture contour maps for specimen GS01 for relative

rotations about the z-axis of θ = -2.5˚ and θ = -1˚ (Figures 5.3.1-7 (a) and (b)), and for the optimum alignment (θ = -0.25˚ Figure 5.3.1-7 (c)). At θ = -2.5˚, a radial pattern was observed that arose from misalignment of the two fracture surfaces; the pattern was removed when the two surfaces were aligned at θ = -0.25˚. The standard deviations of the aperture distributions corresponding to each *z*- rotation were calculated and are plotted in Figure 5.3.1-8 (a). The best estimate for aperture distribution was then selected based on the smallest standard deviation. Note that the exact magnitude of the aperture cannot be determined because there is no standard reference plane between the two surfaces that compose the final fracture geometry. For specimen GS01, the aperture distribution at θ = -0.25˚ was chosen as the best estimate. This is so because, as the *z*- rotation angle deviated from θ = -0.25˚, the aperture distribution had a larger standard deviation and larger mean aperture than the values for θ = -0.25˚. Figure 5.3.1-8 (b) shows the variation of aperture distribution as a function of *z*- rotation.

Table 5.3.1-1 contains the rotation angles of all three axes that provided the best estimates for each specimen. In addition to the fractured granite specimens (GS in the Table), the procedure was also used for gypsum specimens (GY in the Table). Because gypsum had a smaller grain size than granite, it was thought necessary to check the applicability of the procedure to gypsum. For that purpose, four fractured gypsum specimens were fabricated with a single fracture oriented at 0˚, 15˚, or 30˚ with respect to the horizontal. The fracture was induced in a manner similar to the granite specimens (Jaeger et al. (2007)). The specimens had the same external dimensions as the granite specimens. Surface measurements of the fracture in the gypsum specimens were made in the same manner, and the same technique to reconstruct the aperture distribution was

utilized. Table 5.3.1-1 contains the results of the optimization technique for the four gypsum specimens GY03, GY04, GY05, and GY07.

Figure 5.3.1-9 compares the aperture distribution between granite and gypsum specimens. It is interesting to note that, as expected, both the most probable aperture, which is the aperture having the largest fraction in the aperture distribution, and the standard deviation of the gypsum fractures were smaller than those of granite. Table 5.3.1-2 summarizes the most probable aperture and the standard deviation of the aperture distribution for all the granite and gypsum specimens.

Table 5.3.1-1. Correction angles for best estimate of aperture distribution.

Specimen	Fracture angle (˚)		Correction for misalignment (˚)		
			X	Y	Z
GS01	0˚	Lower fracture	-0.3991	-0.2712	-0.25
		Upper fracture	0.2576	0.5405	
GS02	30˚	Lower fracture	0.3672	1.9672	0
		Upper fracture	-0.2535	3.7711	
GS03	15˚	Lower fracture	0.4201	2.3081	0.25
		Upper fracture	0.6856	0.9292	
GS04	0˚	Lower fracture	0.6941	-3.4738	-0.25
		Upper fracture	-1.4174	-3.8518	
GS05	30˚	Lower fracture	2.8256	-1.6247	-1
		Upper fracture	-2.3905	-1.3378	
GS06	15˚	Lower fracture	2.4398	-4.1932	-0.75
		Upper fracture	-2.7616	-3.2683	
GY03	0˚	Lower fracture	-1.3285	2.0791	-1.75
		Upper fracture	1.3334	1.9151	
GY04	0˚	Lower fracture	-1.2501	2.8355	-0.75
		Upper fracture	1.1628	2.5653	
GY05	15˚	Lower fracture	0.2154	0.5458	-0.25
		Upper fracture	-0.0644	0.329	
GY07	30˚	Lower fracture	-0.7153	3.2124	-1
		Upper fracture	0.0769	3.0168	

Table 5.3.1-2. Most probable aperture and standard deviation of aperture distribution of all fractures.

Specimen	Fracture orientation	Most probable aperture (mm)	Standard deviation
GS01	0˚	0.6	0.131
GS02	30˚	0.6	0.156
GS03	15˚	1.15	0.179
GS04	0˚	0.8	0.153
GS05	30˚	1.3	0.197
GS06	15˚	0.75	0.133
GY03	0˚	0.2	0.0625
GY04	0˚	0.1	0.058
GY05	15˚	0.5	0.13
GY07	30˚	0.1	0.0378

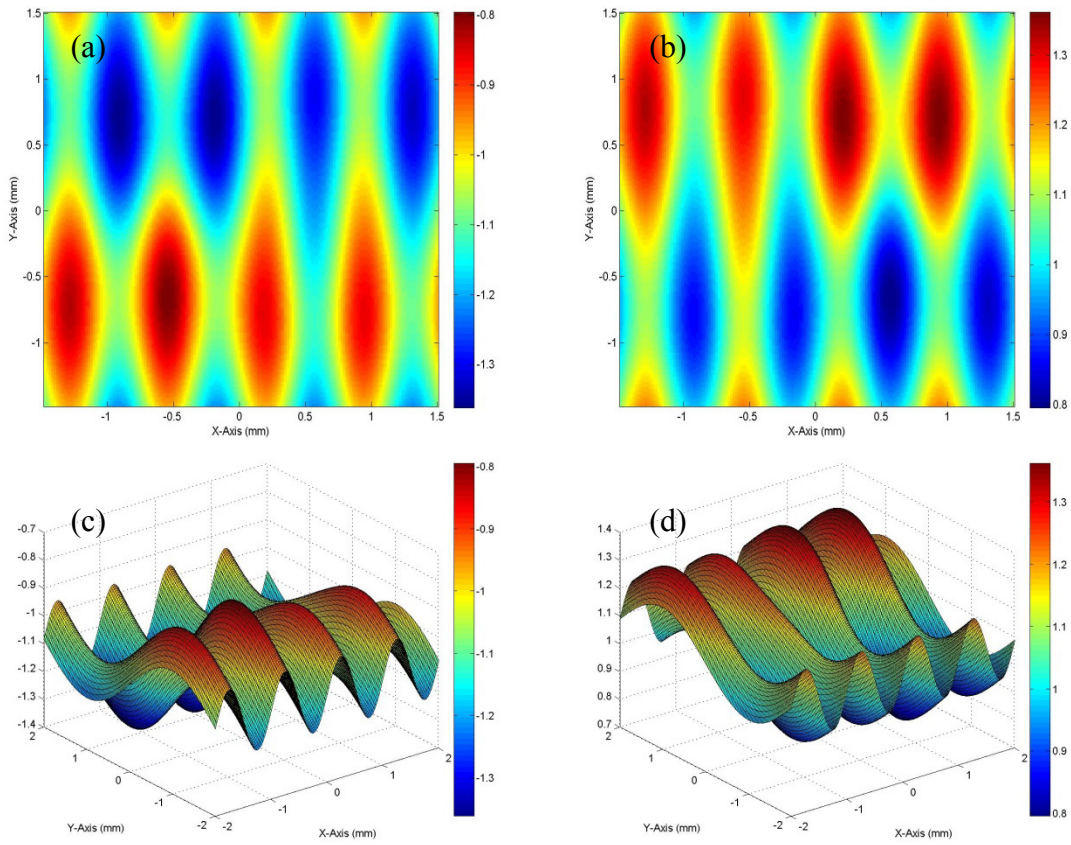

Figure 5.3.1-1. Synthetic fracture. Two dimensional plot of surface roughness for (a) bottom surface; and (b) top surface. Three dimensional representation of surface roughness: (c) bottom surface; and (d) top surface. The color bars on the right represent the height of asperities in mm.

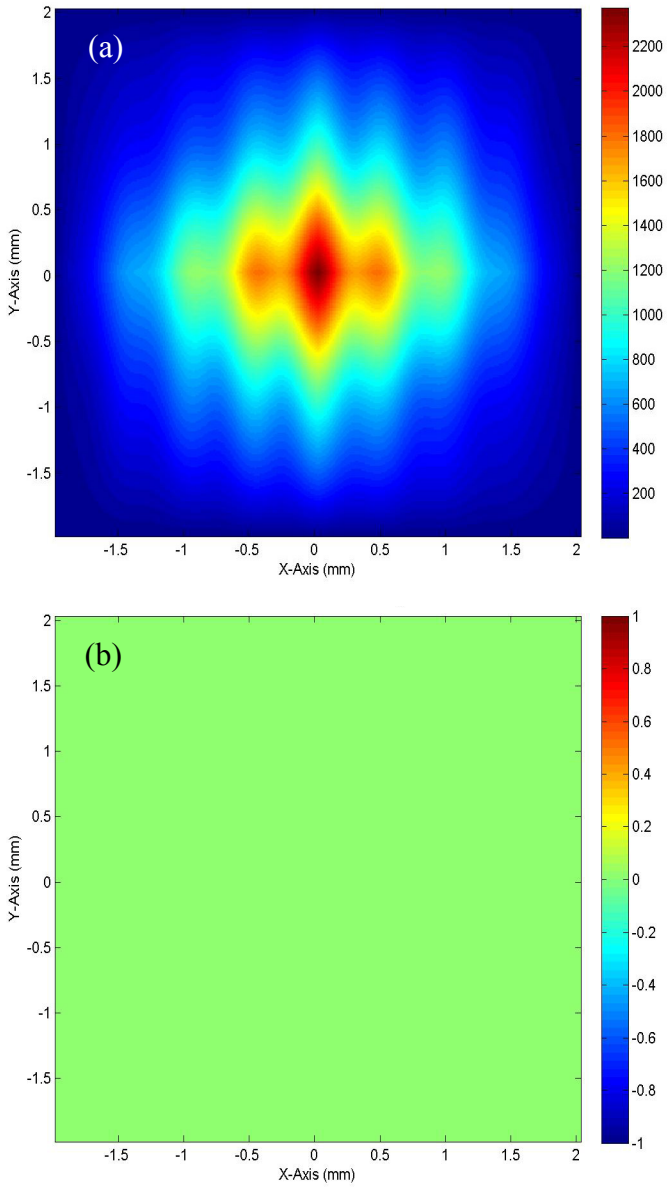

Figure 5.3.1-2. Synthetic fracture. (a) 2-dimensional cross-correlation between the two surface roughness as a function of lag distance in *x*- and *y*- directions; (b) Aperture distribution at a lag of zero. The color bars show aperture in mm.

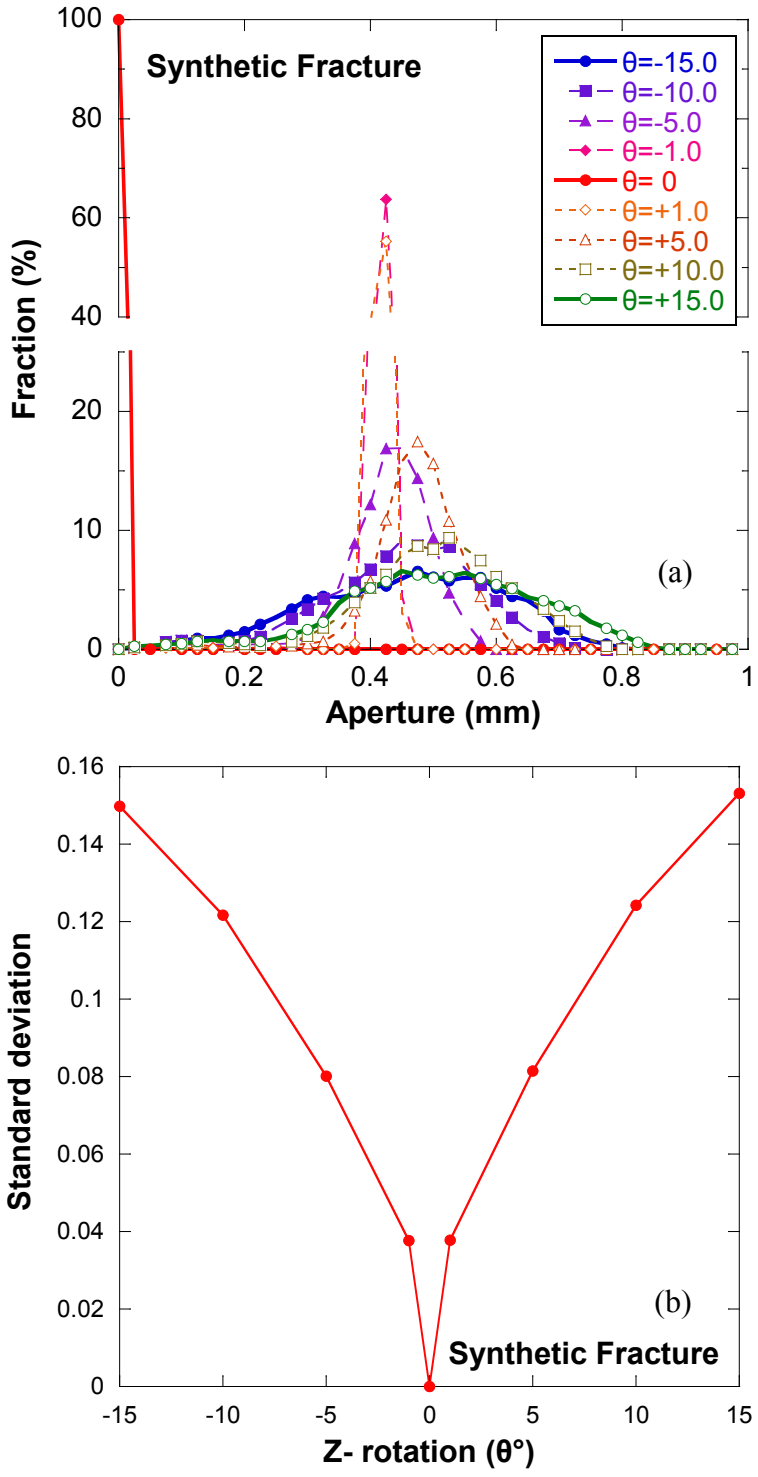

Figure 5.3.1-3. Determination of the optimum aperture distribution for synthetic fracture. (a) Aperture distribution; and (b) standard deviation with z- rotation. The optimum distribution had zero aperture and zero standard deviation.

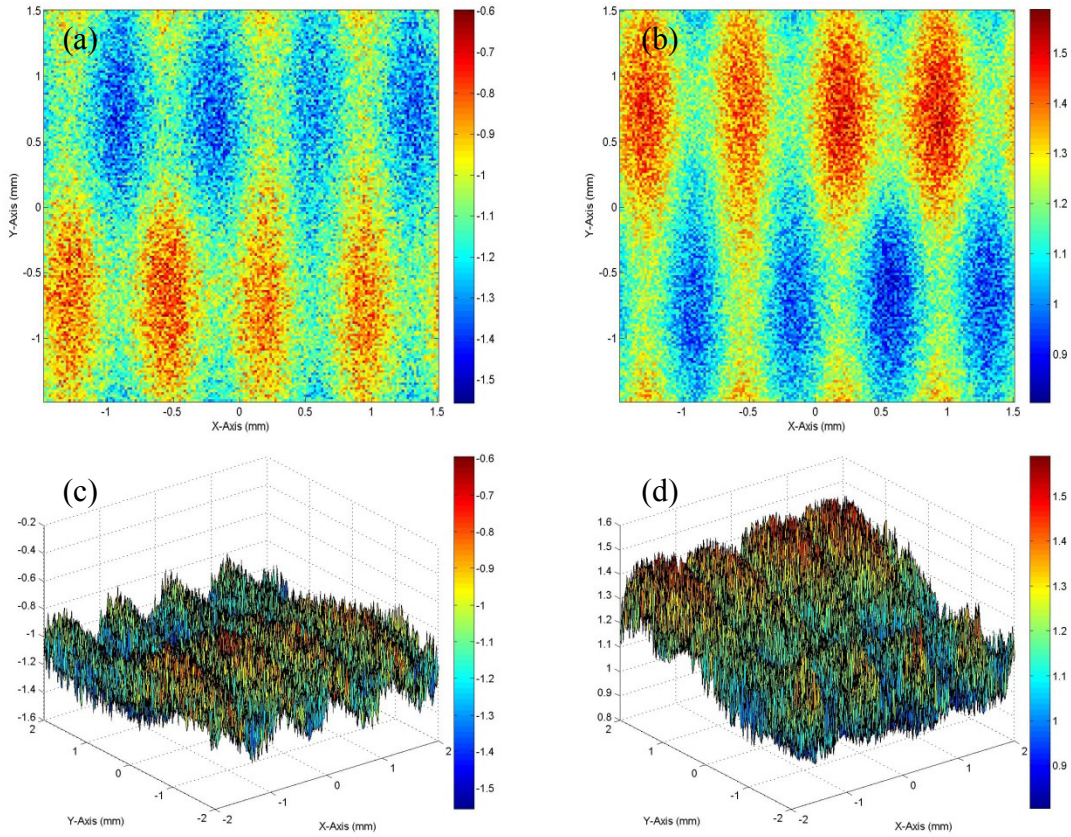

Figure 5.3.1-4. Synthetic fracture with added noise. Two dimensional plot of surface roughness for (a) bottom surface; and (b) top surface. Three dimensional representation of surface roughness: (c) bottom surface; and (d) top surface. The color bars on the right represent the height of asperities in mm.

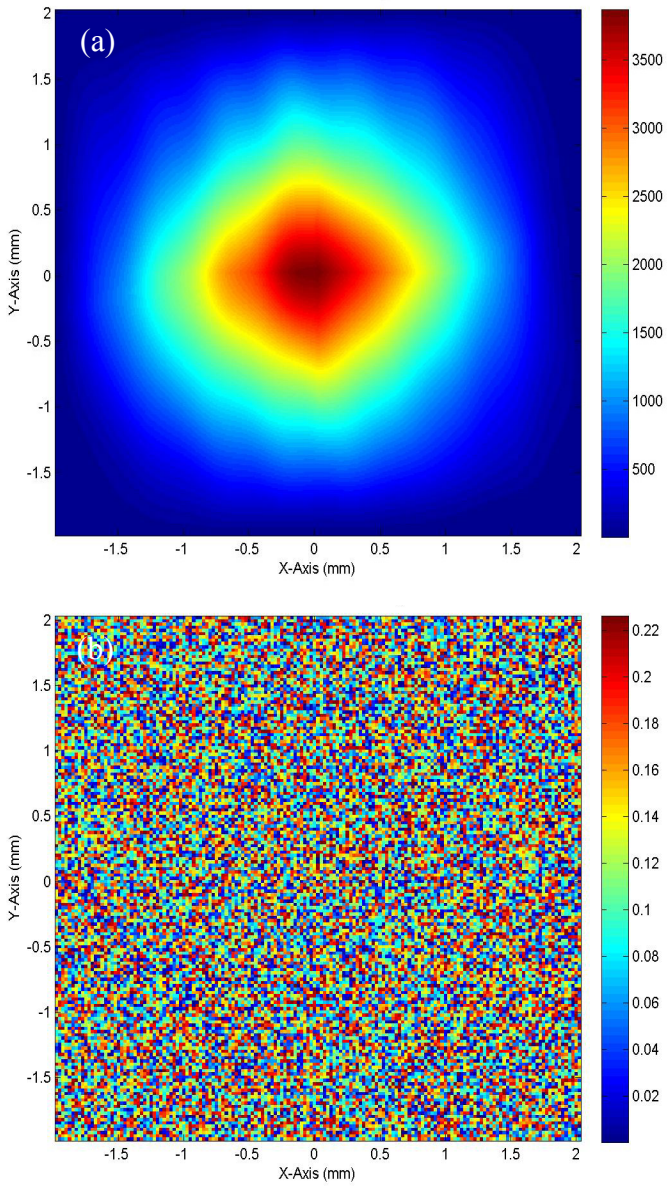

Figure 5.3.1-5. Synthetic fracture with added noise. (a) 2-dimensional cross-correlation between the two surface roughness as a function of lag distance in *x*- and *y*- directions; (b) aperture distribution at a lag of zero. The color bars show aperture in mm.

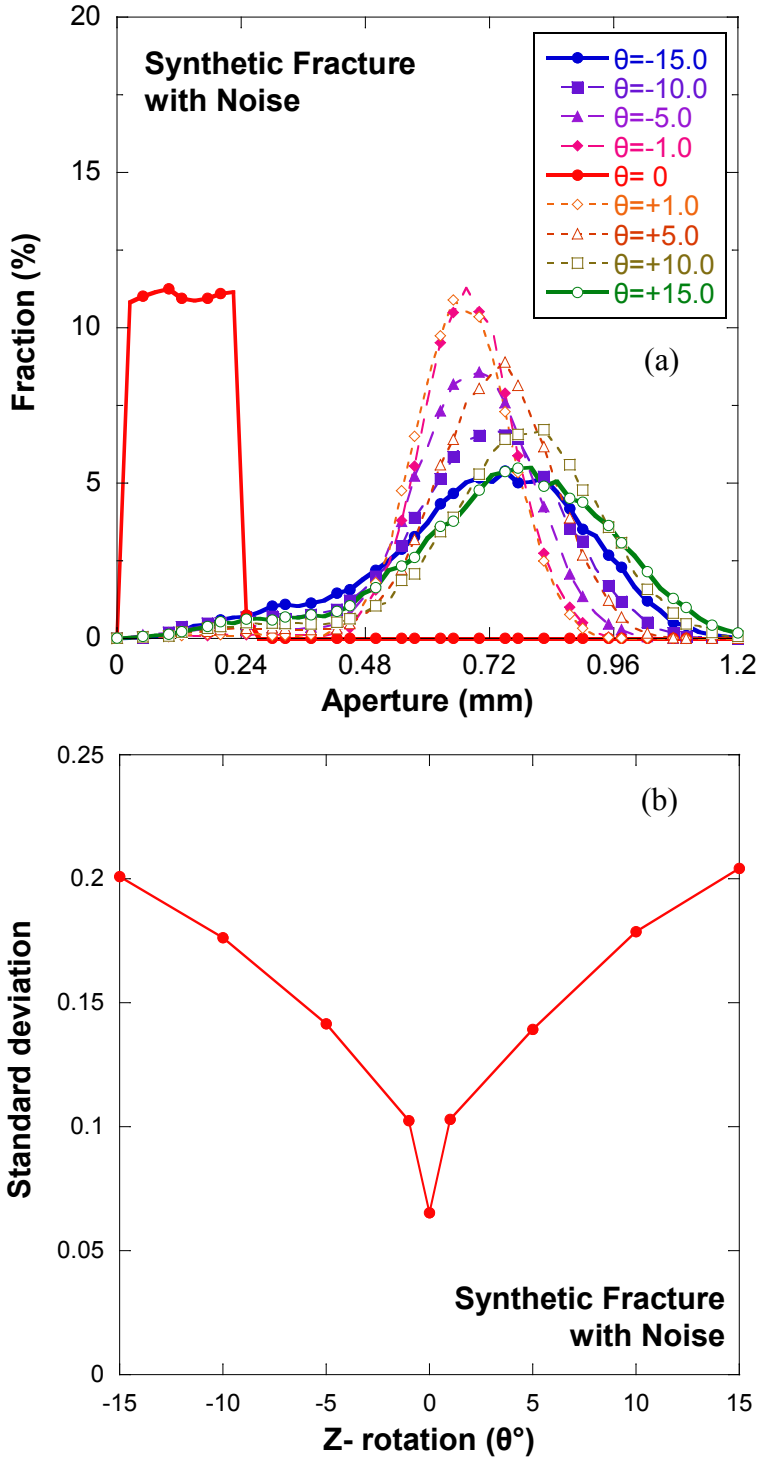

Figure 5.3.1-6. Determination of the optimum aperture distribution for synthetic fracture with added noise. (a) Aperture distribution; and (b) standard deviation with z- rotation. Optimum distribution had zero aperture and zero standard deviation.

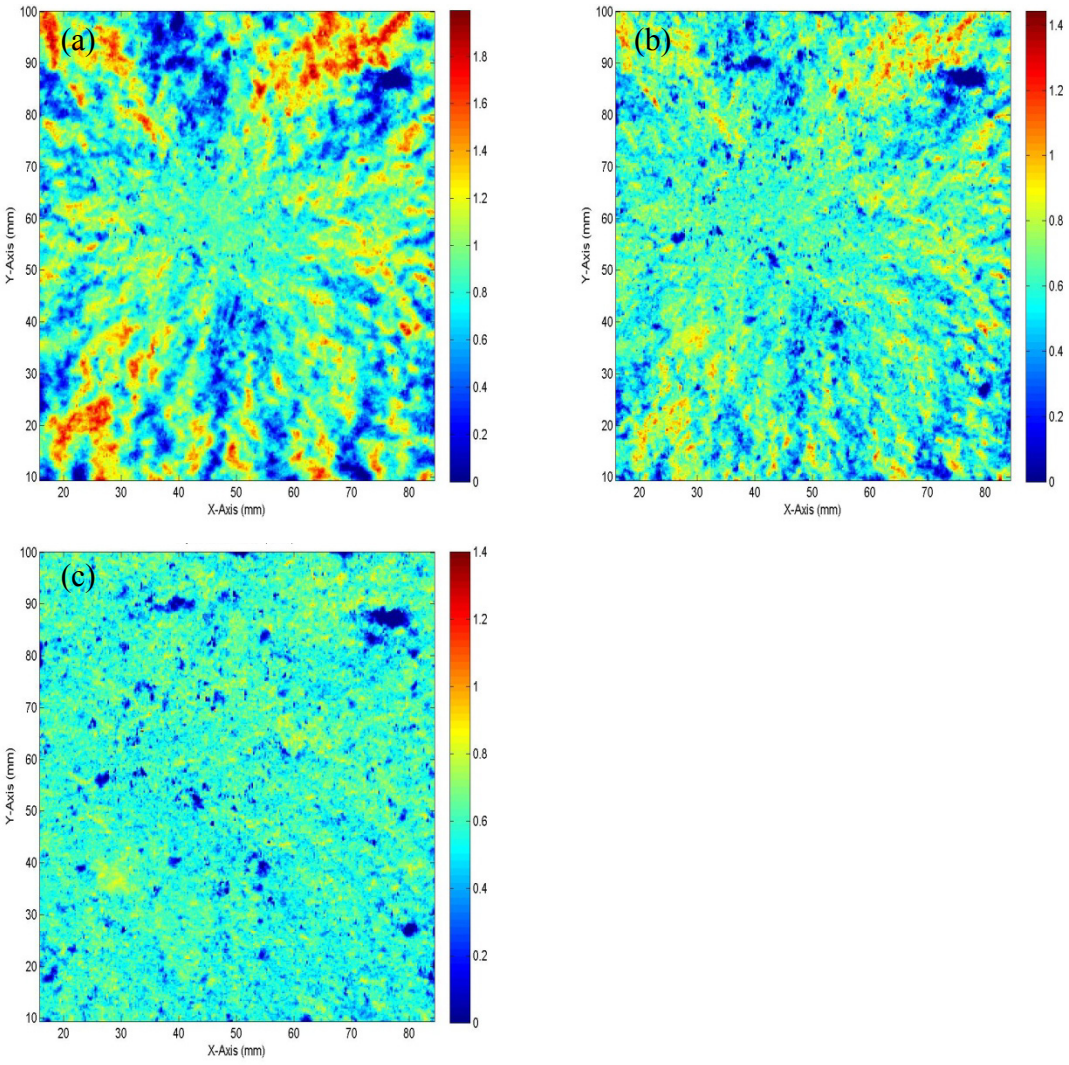

Figure 5.3.1-7. Aperture contour map when rotation in *z*- direction is: (a) -2.5˚, (b) -1˚; and (c) -0.25˚ for GS01 specimen. The color bars represent aperture size in mm.

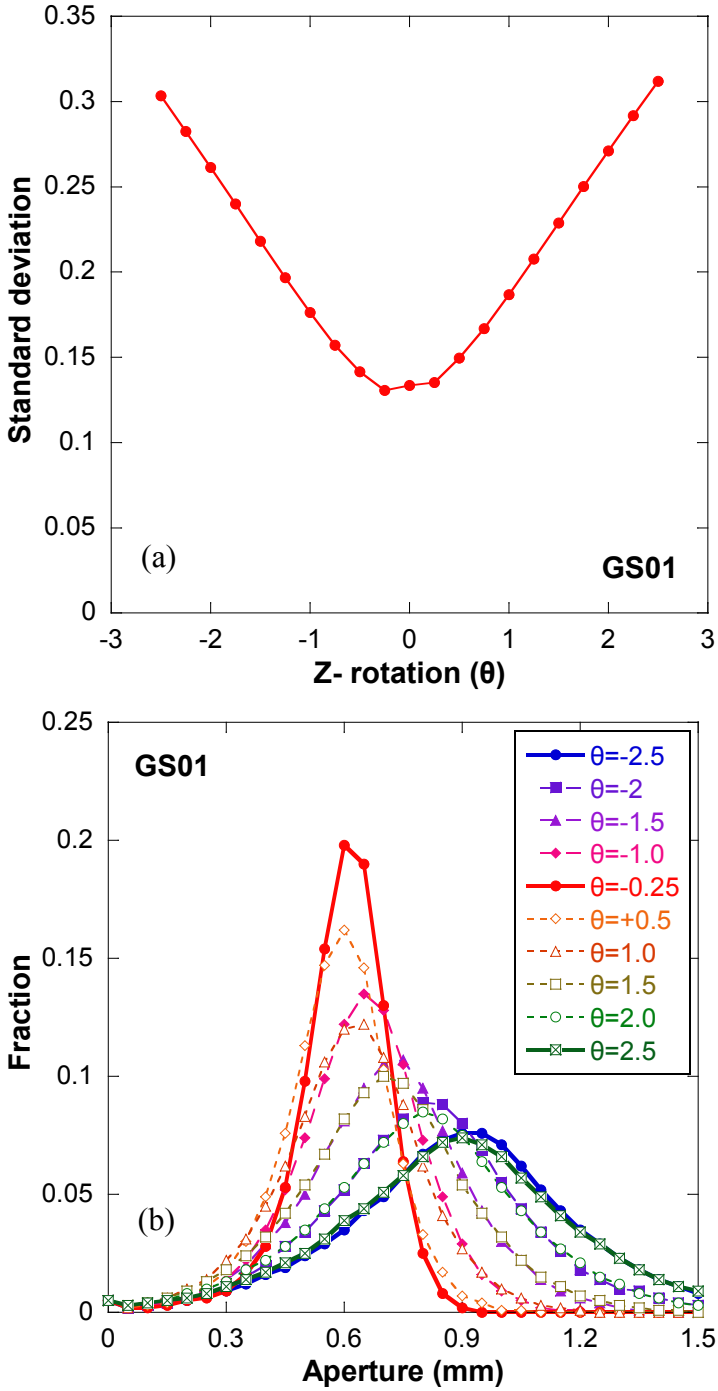

Figure 5.3.1-8. Determination of the optimum aperture distribution. (a) Standard deviation of aperture distribution corresponding to each z- rotation; and (b) aperture distribution with *z*-rotation, for GS01 specimen. The optimum distribution was selected such that it had the smallest standard deviation (θ = -0.25˚).

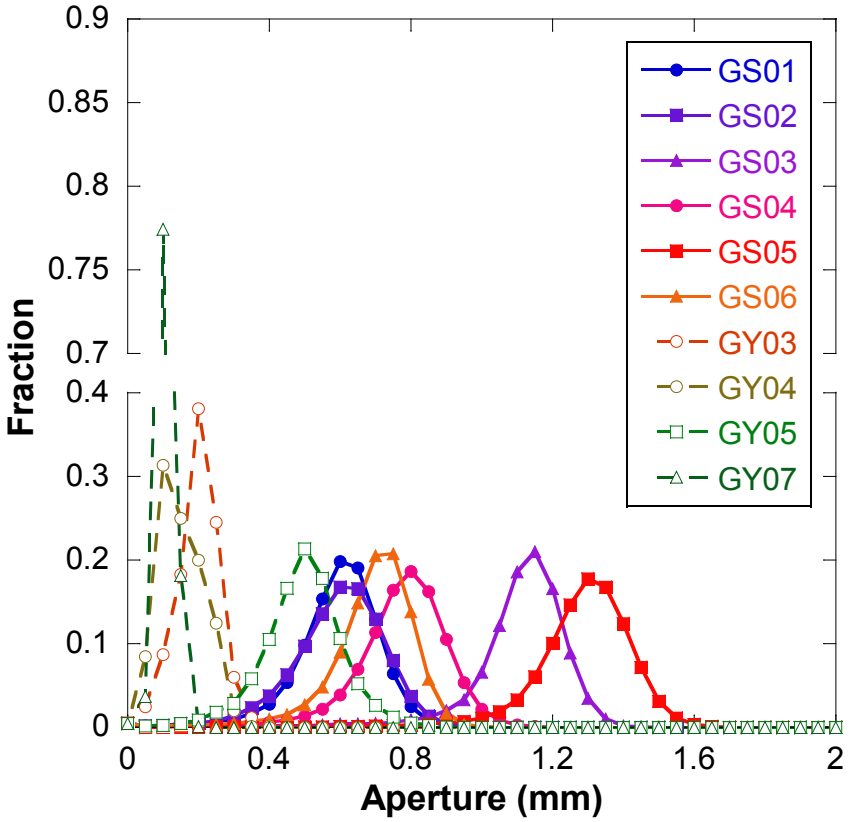

Figure 5.3.1-9. Aperture distributions for fractured granite and gypsum specimens.

5.3.2 Fluid Invasion of Granite Matrix

5.3.2.1 Intact Granite Column Specimen

Distilled water was injected from the bottom of the C01 (intact) specimen. Transmitted compressional (P-) and shear (S-) waves were used to detect the fluid front. The fluid front was assumed to be between a source-receiver pair when the signal amplitude decreased by 50% with respect to its initial value (when the specimen was dry) (Li (2011)). This assumption is based on a Fresnel diffraction study of an invading fluid in a fracture by Pyrak-Nolte et al. (2006). They showed that constructive interference occurred when the invading fluid front was placed at 7 to 8 wavelengths away from the source-receiver line (an imaginary line between the centers of the source and receiver). The seismic diffraction at the tip of the fluid front resulted in an increase in transmission. As the front passed between the source and the receiver, the transmission decreased rapidly. As the water-air front advanced from the source-receiver line, the transmission reached a constant value. To recognize the arrival of the fluid front easily, the peak-to-peak amplitude of a measured signal was normalized with respect to its initial value (when the sample was dry).

Figure 5.3.2-1 contains the normalized peak-to-peak amplitudes of each source-receiver pair. The fluid front was detected first, almost at the same time, at 4S-4S and 8P-8P, which are the transducers closest to the inlet. The first detection occurred at 180-200 minutes after the experiment began. The fluid front propagated to 3S-3S and 7P-7P, and was detected 458-487 minutes after the start of the fluid invasion. The arrival of the fluid front was also identified by 2S and 6P at 1,010-1,120 minutes, and then by 1S and 5P at

1,720 and 1,780 minutes. A significant decrease in the normalized amplitude was observed at all the source-receiver pairs when the fluid front passed the source-receiver line. The normalized peak-to-peak amplitude reached constant values after 2 days (=2,880 minutes) for all transducer pairs. The arrival of the fluid front identified at each source-receiver pair is plotted with distance from the inlet in Figure 5.3.2-2. From the Figure, the invasion velocity into the rock matrix was estimated. The computed invasion velocity is 5.9×10^{-7} m/sec.

Figure 5.3.2-3 (a) shows the variation in spectral amplitudes for representative shear waves and Figure 5.3.2-3 (b) for compressional waves during fluid invasion into the granite matrix. The spectral amplitudes were measured with transducer pairs 3S-3S, for Figure 5.3.2-3 (a) and with 7P-7P for Figure 5.3.2-3 (b). Upon wetting of the granite matrix, the spectral amplitudes of both shear and compressional waves decreased. The dominant frequency moved to a frequency lower than when the specimen was dry. However, the shift of dominant frequency was larger for shear waves than for compressional waves. The dominant frequency for shear waves decreased from 0.41 MHz to 0.29 MHz while for compressional waves it decreased only from 0.42 MHz to 0.40 MHz. This indicates that the shear waves high frequency components were attenuated more than the compressional waves.

5.3.2.2 Fractured Granite Column Specimen

A drop of normalized peak-to-peak amplitude, similar to what was observed for the intact specimen, was observed for specimen C02 when the fluid front passed a source-receiver

line. Figure 5.3.2-4 contains the normalized peak-to-peak amplitudes as a function of invasion time. The Figure shows a decrease in normalized amplitude with fluid invasion, suggesting that the transducers closest to the fracture, 2S, 3S, 6P, and 7P were the first to detect the arrival of the fluid front. The first detection occurred 65-75 minutes after start of the test. At time 265-309 minutes the front was detected at 1S, 4S, 5P, and 8P. The normalized amplitudes of the transducer pair 9S-9S, which was located at the top and bottom of the specimen and monitored the fracture, reduced to 60% of the initial value during the first 50 minutes and reached a constant value after about 6 hours (= 360 minutes). This indicates that the granite matrix reached a steady-state saturation after 6 hours. The arrival of the fluid front detected by each source-receiver pair is plotted with distance from the inlet in Figure 5.3.2-5. The estimated invasion velocity was 16.3×10^{-7} m/sec. The invasion velocity for the C02 specimen was about three times larger than of C01. The larger invasion velocity for C02 could be caused by additional fracturing, perhaps due to the Brazil test (tensile fracture) procedure. Fracturing can generate micro-cracks in the rock matrix, resulting in an increase of permeability of the rock matrix. The other possible explanation is the difference in boundary conditions of the invasion tests. For the C01 specimen, the distilled water was injected from bottom (inlet) to top (outlet) with a pressure of 10 kPa. The hydraulic head between inlet and outlet decreased linearly from 1.02 m (=10 kPa / 9.81 kN/m^3) to 0 m. However, for the C02 specimen, water was directly injected into the fracture. The hydraulic head distribution along the fracture plane was not uniform, resulting in a non-uniform invasion of water into the rock matrix.

5.3.2.3 Summary and Discussion

From the experimental results of the column specimens C01 and C02, it was found that the transmission of compressional and shear waves decreased rapidly as the granite matrix became filled with fluid (water). In addition to a decrease in amplitude, the dominant frequency was reduced upon saturation of the rock matrix. The attenuation of the high frequency components of the shear waves was larger than of the compressional waves. From the reduction of amplitudes at each seismic transducer pair, the location of the fluid front was determined and the invasion velocity of the fluid in the granite matrix was evaluated. The invasion velocity obtained from specimens C01 and C02 was in the range 5.9 - 16.3 x 10^{-7} m/sec.

Figure 5.3.2-6 shows the full waveforms monitored by transducer pair 9S-9S during the first 25 minutes of fluid invasion, for the fractured column specimen C02. For the first 4 minutes, there was no change in the waveforms. However, it was observed at 4.5 minutes after invasion that the wave velocity increased, indicating that transducer pair 9S-9S detected the invading water front. Given the extremely low fluid invasion velocity 5.9 - 16.3 x 10^{-7} m/sec in the rock matrix, the fluid invaded the void spaces in the fracture during the early stages of the test and much later permeated into the rock matrix. Hence fluid invasion into a granite fracture can be seismically detected during early stages because the fluid propagates dominantly into the voids of the fracture.

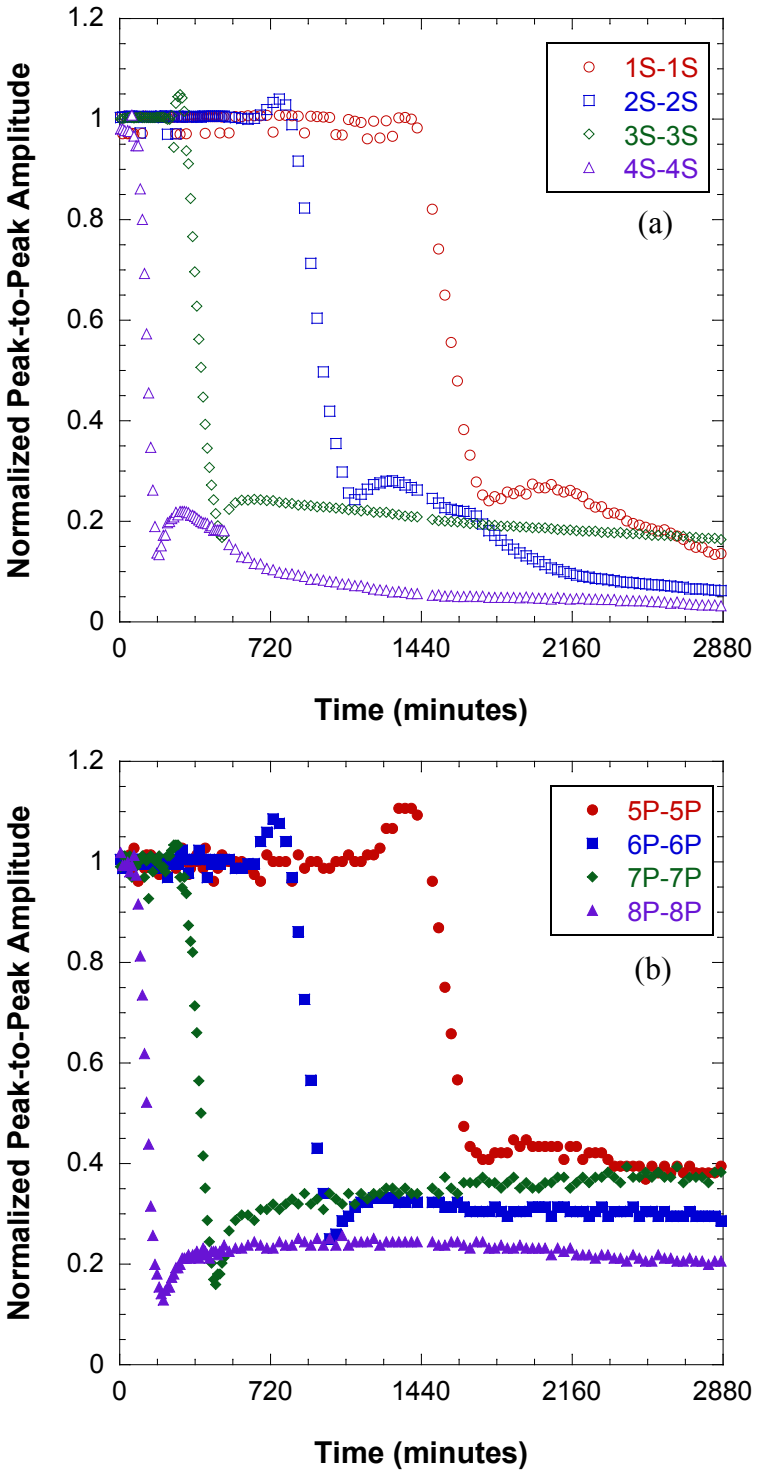

Figure 5.3.2-1. Intact column specimen C01. Normalized peak-to-peak amplitude of: (a) shear; and (b) compressional waves with invasion time. The fluid inlets are closer to 4S and 8P, and the outlets to 1S and 5P.

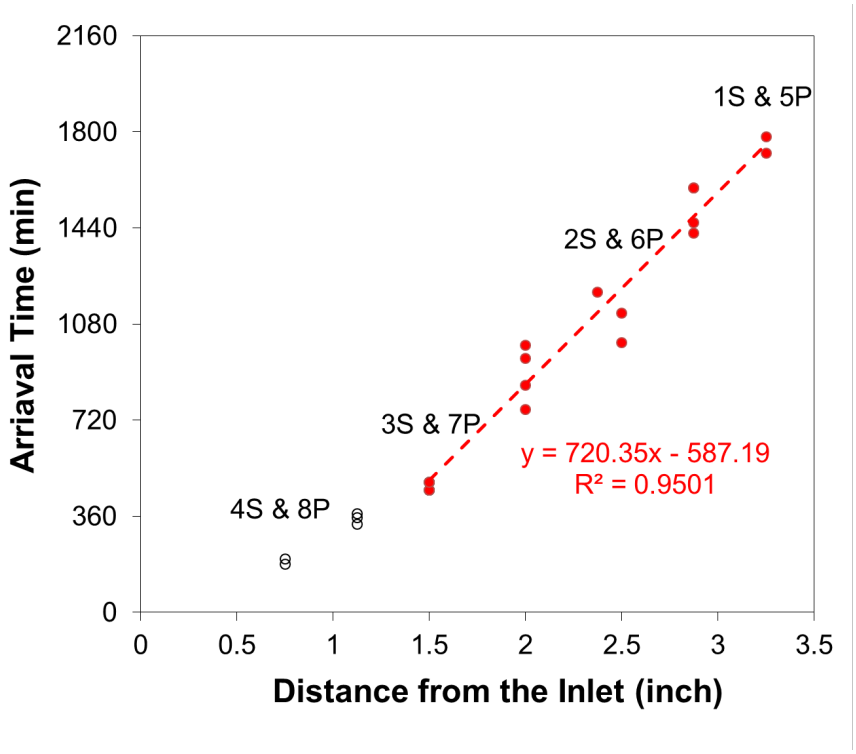

Figure 5.3.2-2. Intact column specimen C01. Estimated arrival time of fluid front at a given source-receiver pair.

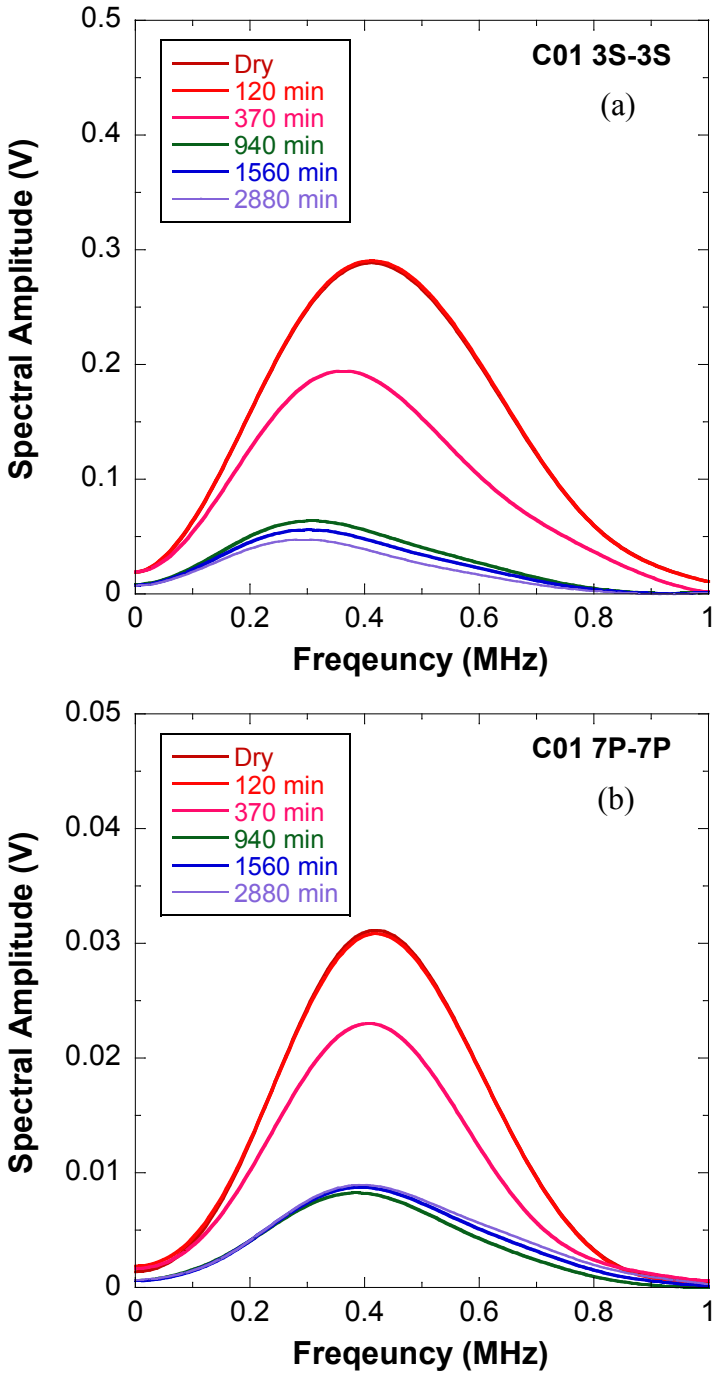

Figure 5.3.2-3. Intact column specimen C01. Spectral amplitudes for representative: (a) shear (3S-3S); and (b) compressional (7P-7P) waves during fluid invasion.

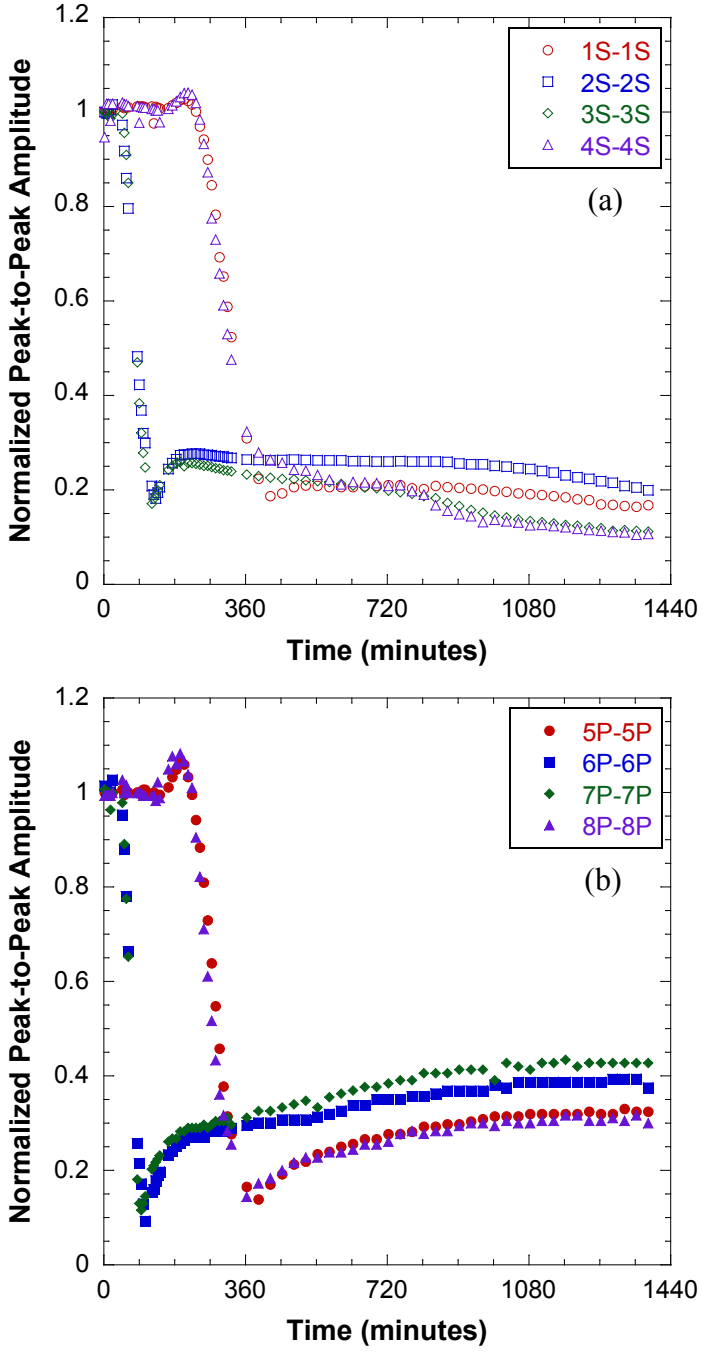

Figure 5.3.2-4. Fractured specimen C02. Normalized peak-to-peak amplitude of: (a) shear; and (b) compressional waves measured from transducers attached to the sides of the specimen; and (c) normalized peak-to-peak amplitude of shear wave attached to top and bottom of specimen, with invasion time. Transducer pairs 2S, 3S, 6P and 7P are closer to the fracture and 9S is on the top and bottom of the specimen (continued).

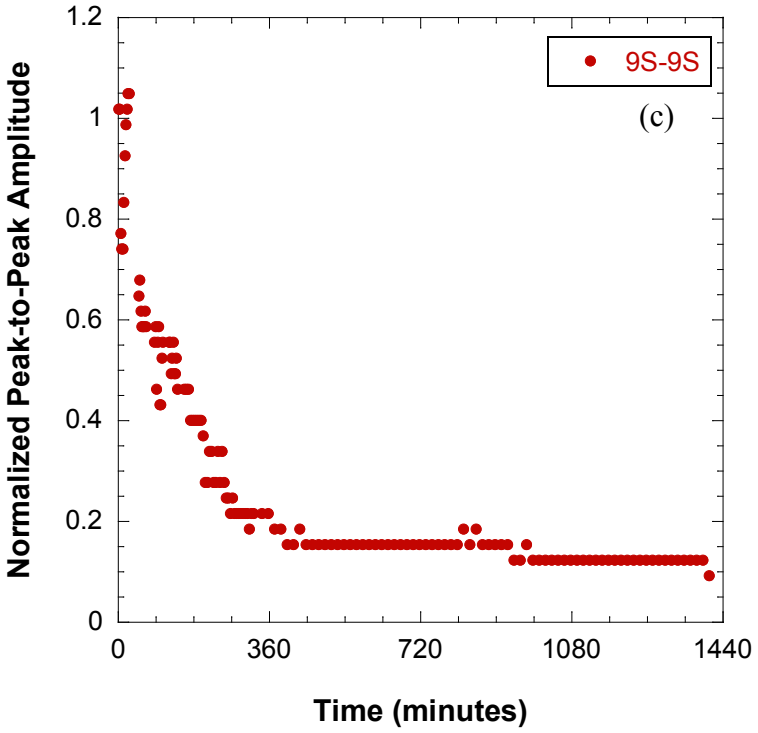

Figure 5.3.2.-4. Fractured specimen C02. Normalized peak-to-peak amplitude of: (a) shear; and (b) compressional waves measured from transducers attached to the sides of the specimen; and (c) normalized peak-to-peak amplitude of shear wave attached to top and bottom of specimen, with invasion time. Transducer pairs 2S, 3S, 6P and 7P are closer to the fracture and 9S is on the top and bottom of the specimen.

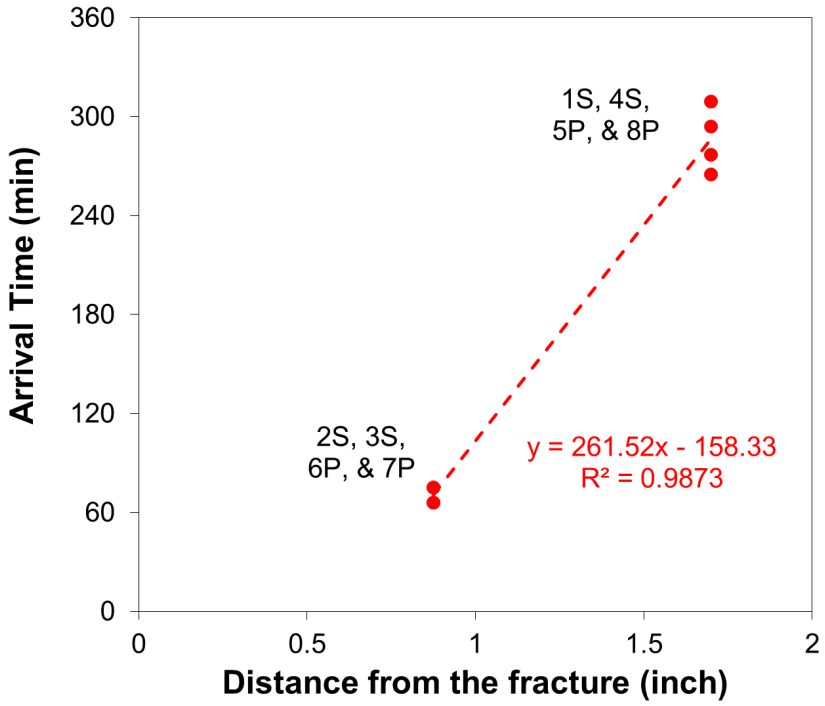

Figure 5.3.2-5. Fractured specimen C02. Estimated arrival time of fluid front at a given source-receiver pair.

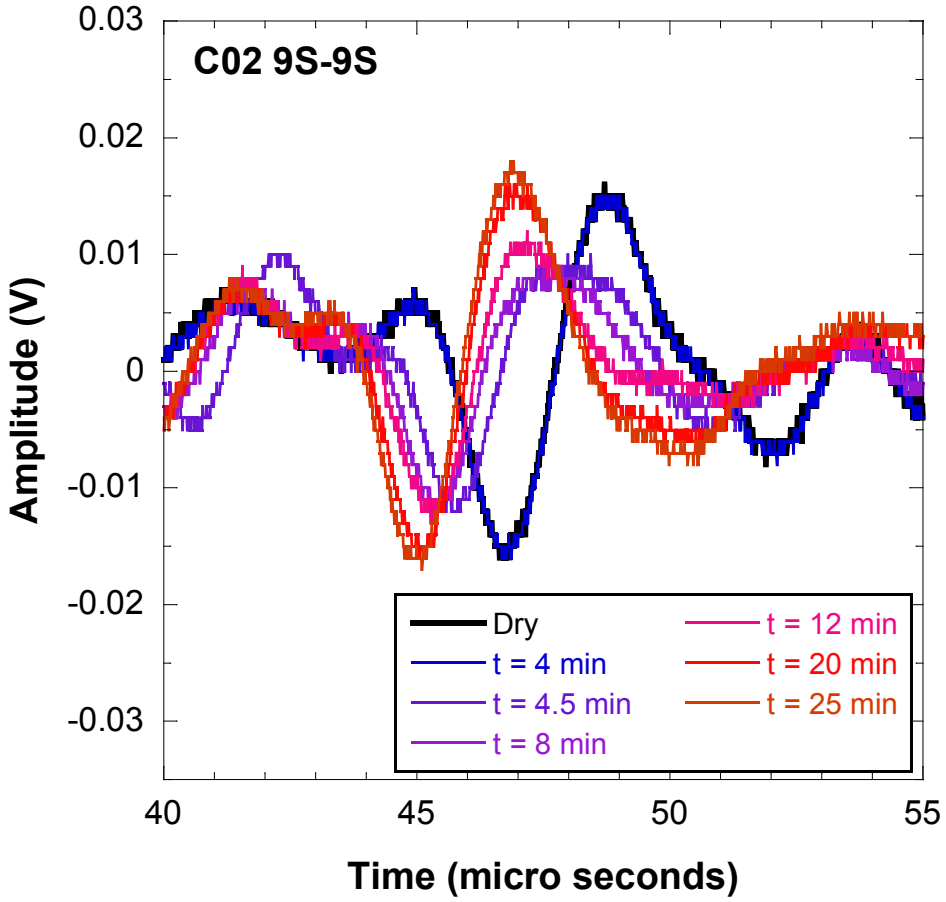

Figure 5.3.2-6. Fractured specimen C02. Full waveforms monitored by the transducer pair 9S-9S during the first 20 minutes of fluid invasion.

5.3.3 Fluid Invasion in a Fracture

As discussed in section 5.3.2, the change of peak-to-peak amplitudes and wave velocities of both compressional and shear waves was used to determine the arrival of the fluid front. As the fluid reached a transducer location, the arrival time of the signal decreased and the amplitude of the signal increased first and then decreased abruptly. The changes in the waveforms were interpreted as the presence of the fluid-air front (Pyrak-Nolte et al. (2006)).

Figures 5.3.3-1 (a) and (b) show the waveforms recorded from transducer pairs 2S-2S and 7S-7S, respectively, during the first 10 minutes of the fluid invasion on GS01 (Test-I; see Table 5.2.2-1). Transducer pairs 2S-2S and 7S-7S were the closest to the inlet. In the figure, time t = 0 means that the fracture plane was dry. During the first 2.5 minutes, there was no change in the recorded signals for both 2S-2S and 7S-7S. At around t = 3.0 minutes, it was observed that the wave velocity started to increase, indicating that transducer pairs 2S-2S and 7S-7S detected the invading fluid front. A similar decrease in arrival time was observed by transducer pairs 6P-6P and 1S-1S at t = 3.5 minutes (Figure 5.3.3-1 (c) and (d)). At around t = 5.0 minutes, it was observed that the wave velocity for transducer pair 3P-3P increased (Figure 5.3.3-1 (e)). Finally, the fluid front spread to transducer pair 5S-5S at t = 10 minutes (Figure 5.3.3-1 (f)). The transmitted S- waves from transducer 4S did not change during the first 10 minutes, indicating that the fluid front did not reach 4S (Figure 5.3.3-1 (g)).

By tracking the detection times of the fluid front at each location of the transducer pairs, the flow path of the fluid can be inferred. The detected arrival times of the fluid front for GS01 during Test-I and Test-II are shown along with the transducer layout in Figures

5.3.3-2 (a) and (b). The flow direction for both tests was from inlet to outlet, as shown in Figures 5.3.3-2. The small black boxes in the figure represent the polarization direction of the S- wave transducers and the numbers above the transducers are the arrival time of the fluid front in minutes.

The fluid front detection times for Test-III (GS03) and Test -IV (GS06) are shown in Figure 5.3.3-3 (a) and (b). Similar to the invasion of the fracture in GS01, the fluid front propagated non-uniformly through the fracture plane in GS03 and GS06. The time for the fluid to travel from inlet to outlet in GS03 and GS06 can be compared with the most probable aperture. The most probable aperture of GS03 was 1.15 mm, which was larger than GS06, which was 0.75mm (see Table 5.3.1-2). For GS03, the fluid front took 2.9 - 3.3 minutes to arrive at the location of transducer pairs 5S and 4S, while it took 5.6 - 6.8 minutes to reach the same locations in GS06. These results are consistent with the concept that larger apertures result in less time for a fluid to flow through a fracture.

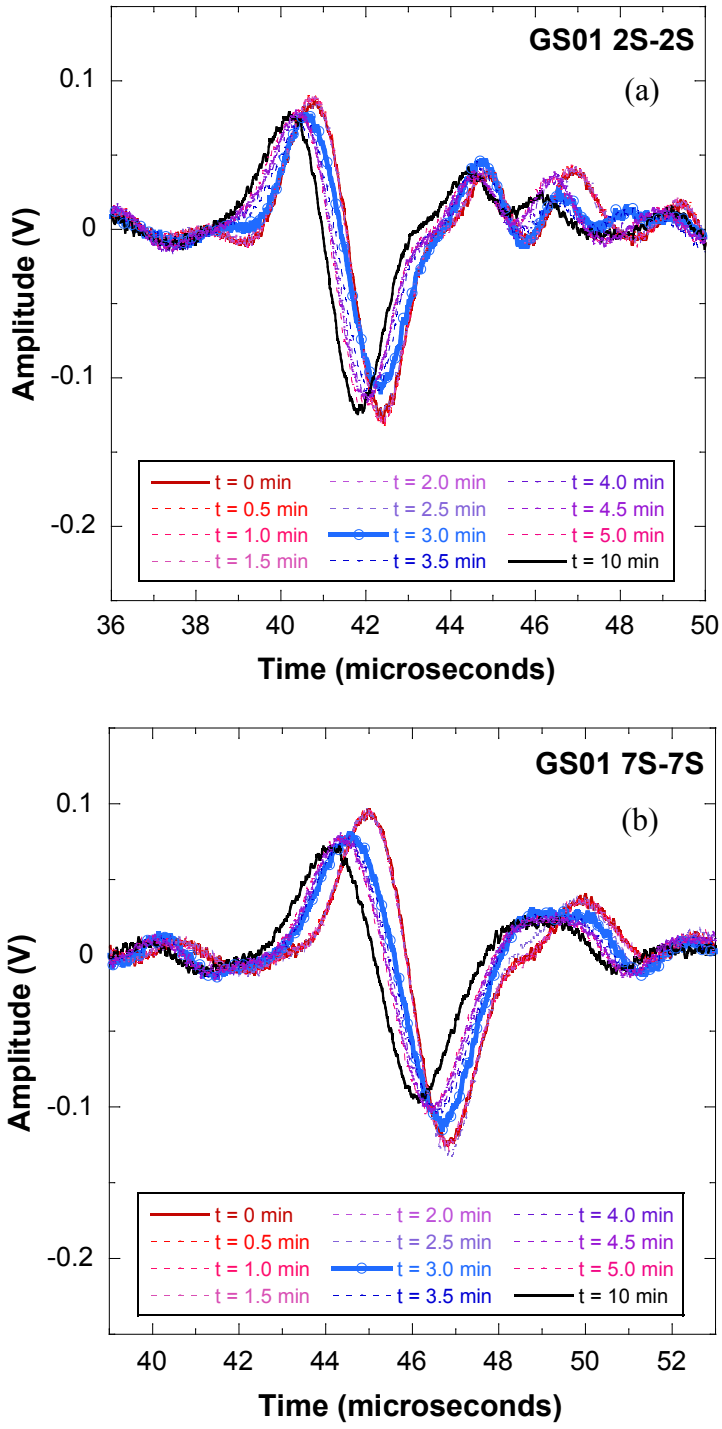

Figure 5.3.3-1. Recorded waveforms from GS01 specimen from transducer pair: (a) 2S-2S; (b) 7S-7S; (c) 6P-6P; (d) 1S-1S; (e) 3P-3P; (f) 4S-4S; and (g) 5S-5S during Test I (continued).

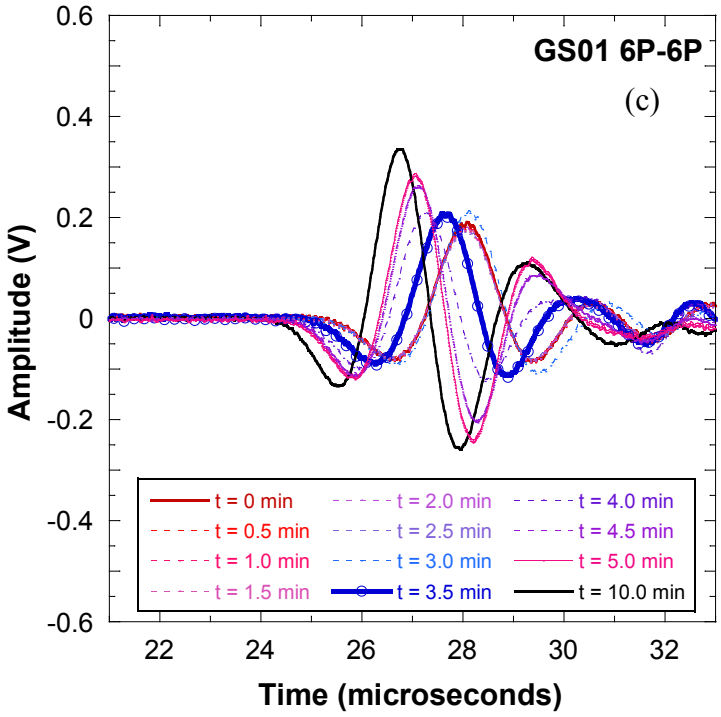

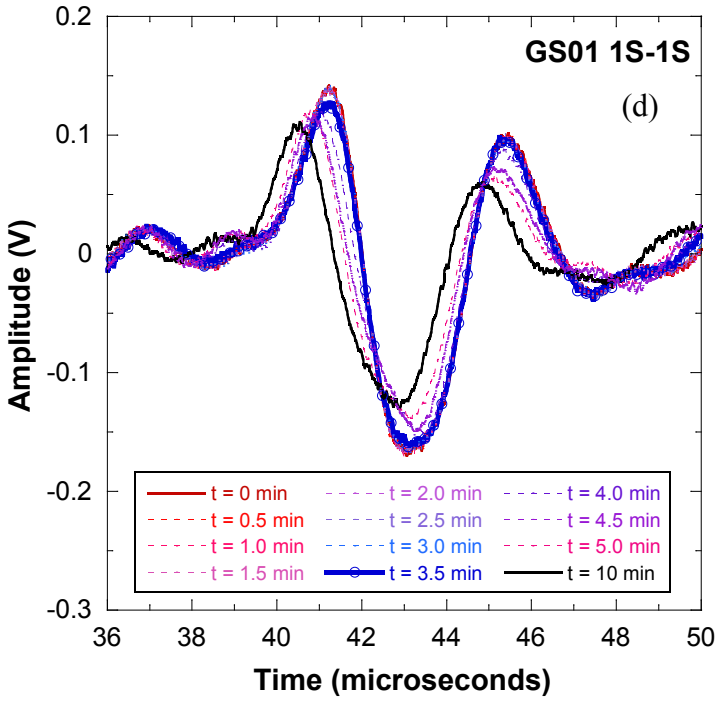

Figure 5.3.3-1 Recorded waveforms from GS01 specimen from transducer pair: (a) 2S-2S; (b) 7S-7S; (c) 6P-6P; (d) 1S-1S; (e) 3P-3P; (f) 4S-4S; and (g) 5S-5S during Test I (continued).

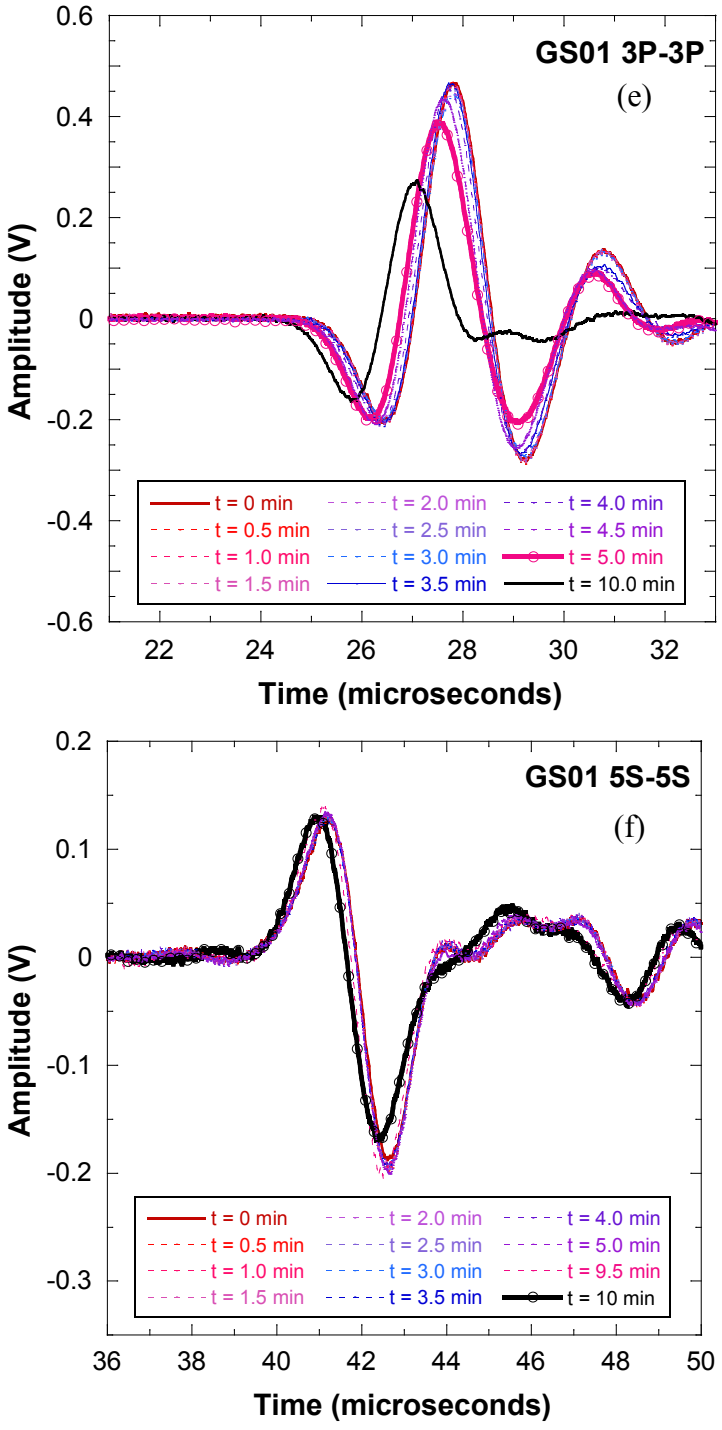

Figure 5.3.3-1 Recorded waveforms from GS01 specimen from transducer pair: (a) 2S-2S; (b) 7S-7S; (c) 6P-6P; (d) 1S-1S; (e) 3P-3P; (f) 4S-4S; and (g) 5S-5S during Test I (continued).

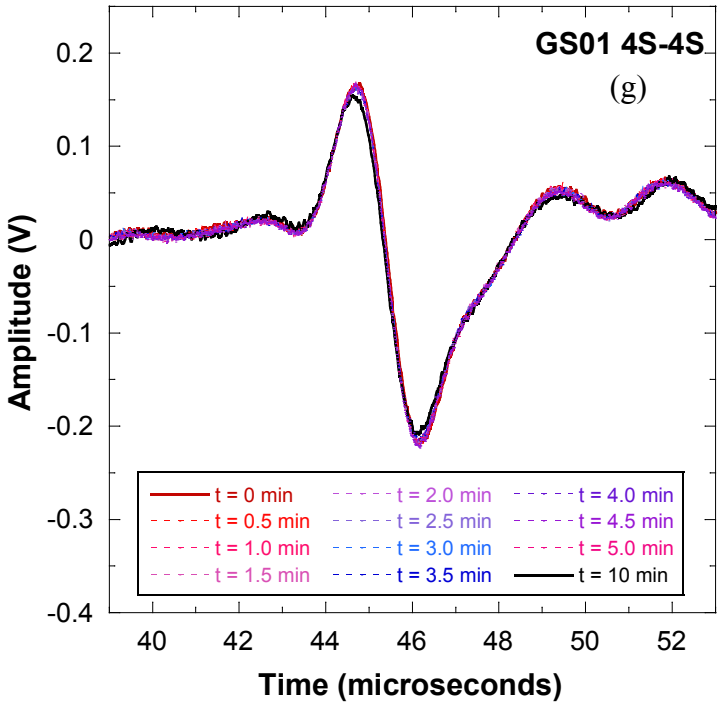

Figure 5.3.3-1 Recorded waveforms from GS01 specimen from transducer pair: (a) 2S-2S; (b) 7S-7S; (c) 6P-6P; (d) 1S-1S; (e) 3P-3P; (f) 4S-4S; and (g) 5S-5S during Test I.

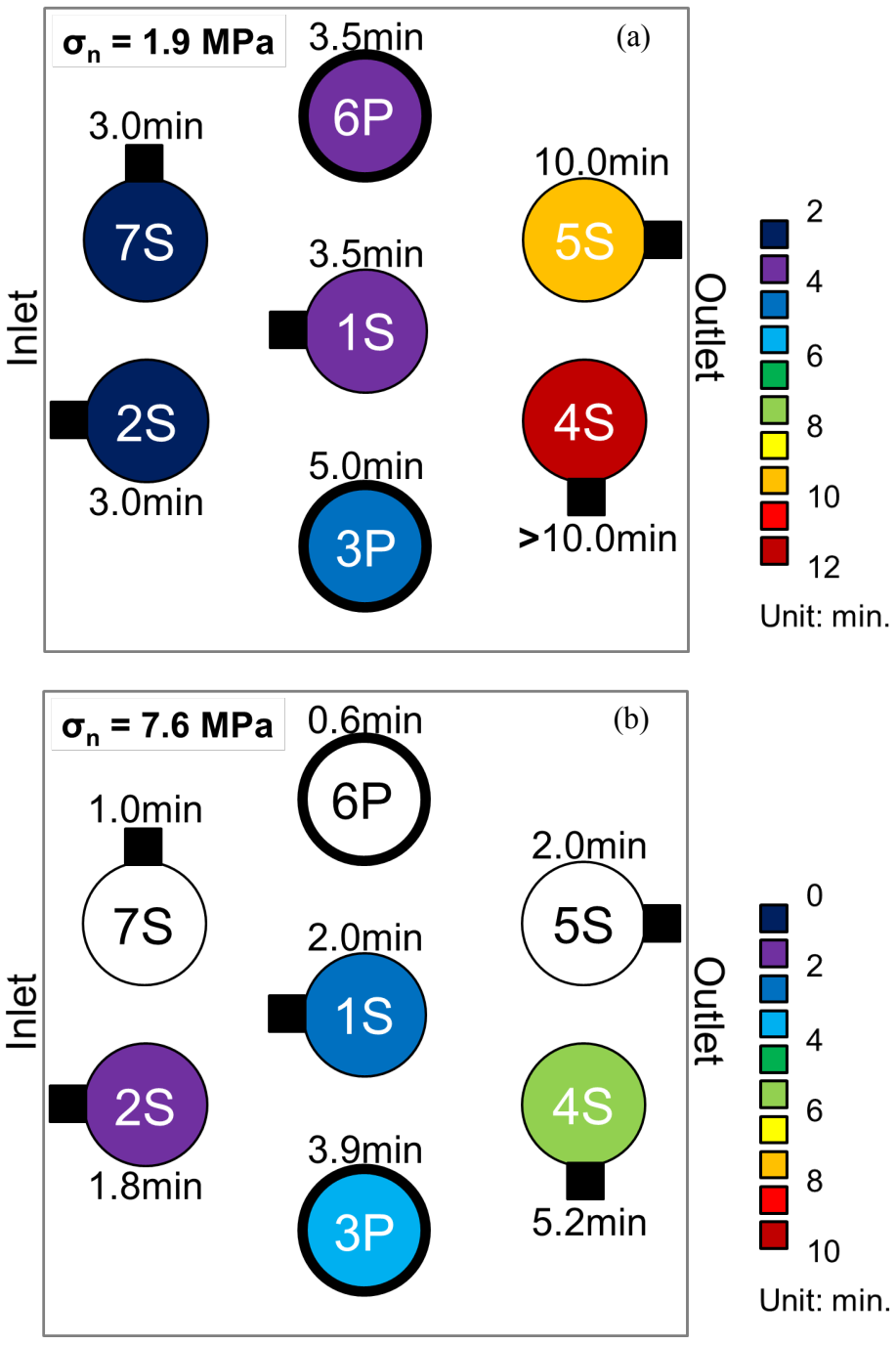

Figure 5.3.3-2. Detected arrival times of fluid front for GS01 in: (a) Test-I; and (b) Test-II.

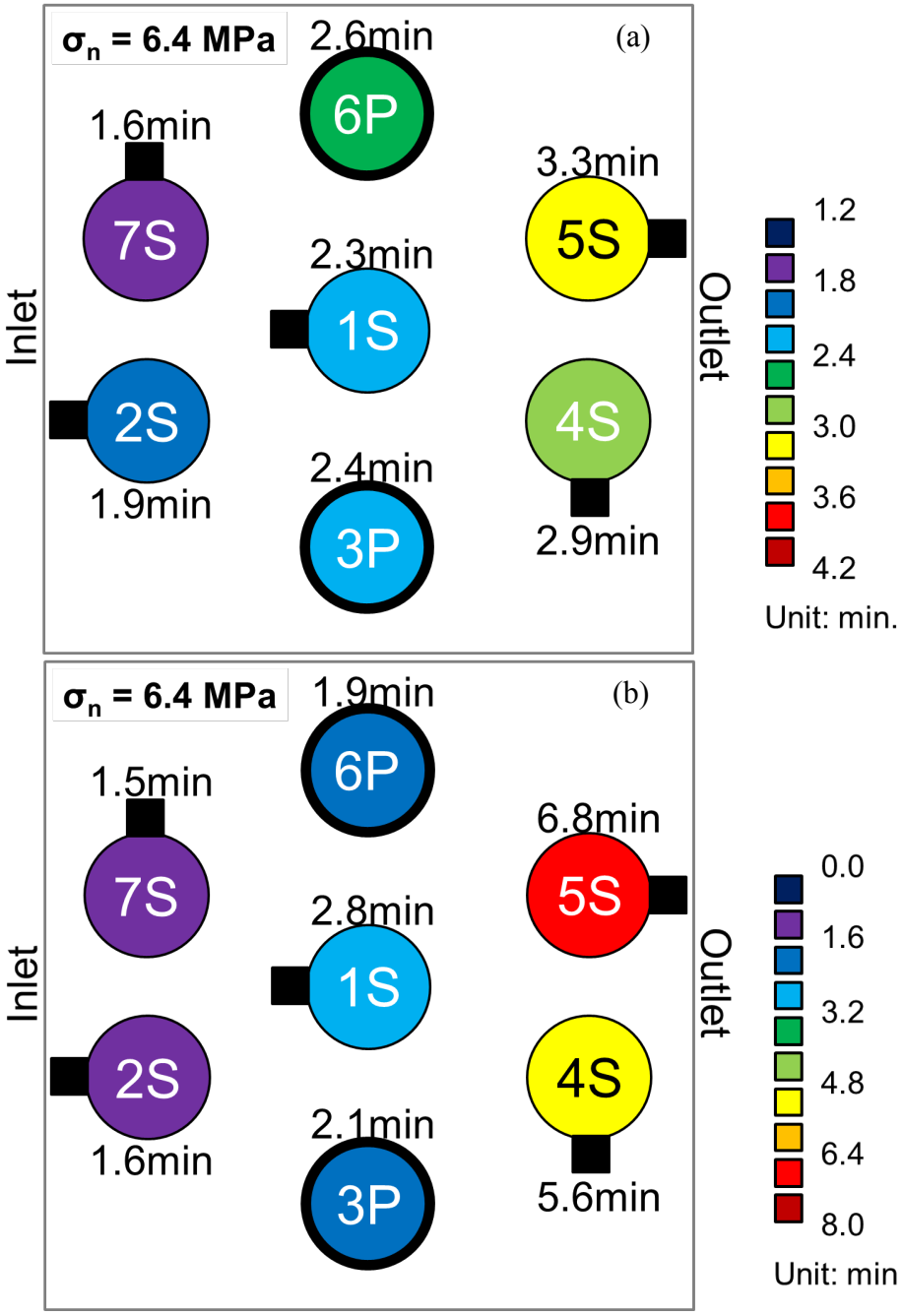

Figure 5.3.3-3. Detected arrival times of fluid front for: (a) GS03, Test-III; and (b) for GS06, Test-IV.

5.4 Relationship between Fluid Flow and Fracture Specific Stiffness

5.4.1 Fluid Front and Spatial Distribution of Fracture Specific Stiffness

During fluid invasion, the amplitude of both the compressional and shear waves decreased as fluid filled the fracture, while the velocity of the waves increased. By tracking the arrival time of the waves, the fluid path was identified. Detection of the fluid front, as discussed in section 5.3.3, is interpreted here in relation to the spatial distribution of fracture specific stiffness.

For Test-I, as shown in Figure 5.4.1-1 (a), three minutes after fluid invasion started, the fluid front was sensed by transducers 2S and 7S, which were closest to the inlet. Transducer pairs 1S and 6P sensed the front half a minute later. The fluid front arrived at the area under transducer pair 3P 5 minutes after the experiment began and spread to transducer 5S at time 10 minutes. During the first 10 minutes of fluid invasion, the fluid travelled through the fracture plane from 2S and 7S to 5S. The transmitted S- wave from transducer 4S did not change during the first 10 minutes, indicating that the fluid front did not reach 4S.

The spatial distribution of specific stiffness in Figure 5.4.1-1 (b) can be interpreted in relation to the fluid front detection time in Figure 5.4.1-1 (a). For example, after the fluid passed transducers 2S and 7S, the fluid front was detected simultaneously by 1S and 6P, and then by 3P. The specific stiffnesses under 1S and 6P were relatively lower than under 3P, as seen in Figures 5.4.1-1 (b). It is plausible that the fluid advanced first to the area where the fracture specific stiffness was relatively low and then spread to areas of higher stiffness, as it invaded the fracture. Low values of fracture specific stiffness along a

fracture plane indicate less contact area and larger apertures than regions with high stiffness.

The results of Test-II on GS01 confirmed the relation between fracture specific stiffness and fluid front detection time. The spatial pattern of detection time obtained in Test-II was similar to Test-I, as seen in Figure 5.4.1-1 (c). The arrival of fluid was sensed first at 2S and then at 1S, 3P, and 4S, in that order. The detection times at 7S, 6P, and 5S are excluded from the discussion because they were affected by an operational error during the experiment; at the beginning of Test-II, the other inlet reservoir, located close to 6P, was filled with water during the first couple of minutes. This error explains the early detection time at 6P, 7S and 5S in Figure 5.4.1-1 (c). The fluid front detection time in Test-II can be interpreted in relation with the spatial distribution of fracture specific stiffness, in a similar manner as Test-I. After the fluid front was detected at 2S at time 1.8 minutes, the fluid reached 1S and then arrived at 3P, as seen in Figure 5.4.1-1 (c). As expected, the fracture area under transducer 1S had relatively lower specific stiffness than at 3P, as can be seen in Figure 5.4.1-1 (d).

The arrival times of fluid front detected from each transducer during Test-III (Figure 5.4.1-2 (a)) are compared with the spatial distribution of the fracture specific stiffness in Figure 5.4.1-2 (b). Similarly to Test-I and Test-II, the fluid front was detected earlier in areas with low fracture specific stiffness and then advanced to portions of the fracture with relatively higher specific stiffness. The fluid front was first sensed by transducer 7S at time 1.6 minutes and then the fluid propagated into the regions under the transducers 2S, 1S, 3P, and 6P in that order. Thus, the fluid invaded first areas with low fracture

specific stiffness; the stiffness at transducer 7S is lower than 2S, and 1S shows the lowest stiffness among 1S, 3P, and 6P.

Figure 5.4.1-3 presents the detected arrival times of the fluid front for GS06 during Test-IV, together with the spatial distribution of fracture specific stiffness. The data correspond to a normal stress of 6.4 MPa. Again, the experimental results of Test-IV confirm that non-uniform fluid invasion into a fracture is related to the spatial variability of fracture specific stiffness. Since the highest stiffness was measured at the center of the fracture (transducer 1S), the fluid flow split in two directions during the early stages of fluid invasion. That is: first, from 7S to 6P, and then from 2S to 3P. Finally the fluid reached 5S and 4S after 6.8 minutes and 5.6 minutes, respectively.

The experiments show that the propagation of fluid through a fracture changed the velocity and amplitude of the transmitted waves. Hence, the fluid path can be identified by tracking changes of the waveforms. They also show that the fluid flow path can be correlated with the spatial distribution of the fracture specific stiffness. The fluid first invades the portions of the fracture that have a relatively low stiffness and then spreads to regions with higher stiffness. Clearly, fluid flow across a fracture is not uniform.

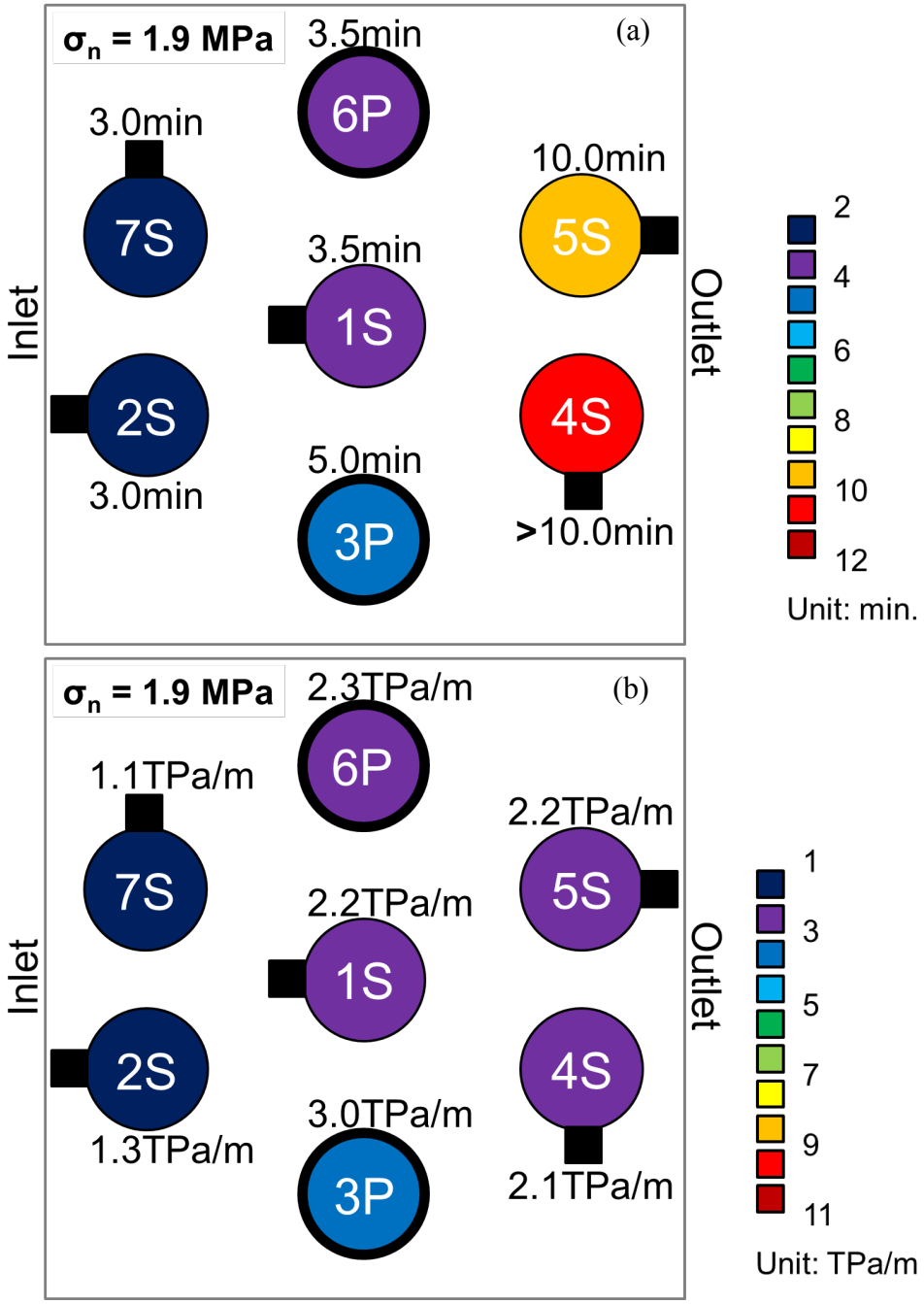

Figure 5.4.1-1. Specimen GS01. Detected arrival times of fluid front in: (a) Test-I; and (c) Test-II and spatial distribution of specific fracture stiffness for: (b) Test-I at 1.9 MPa; and (d) Test-II at 7.6 MPa (continued).

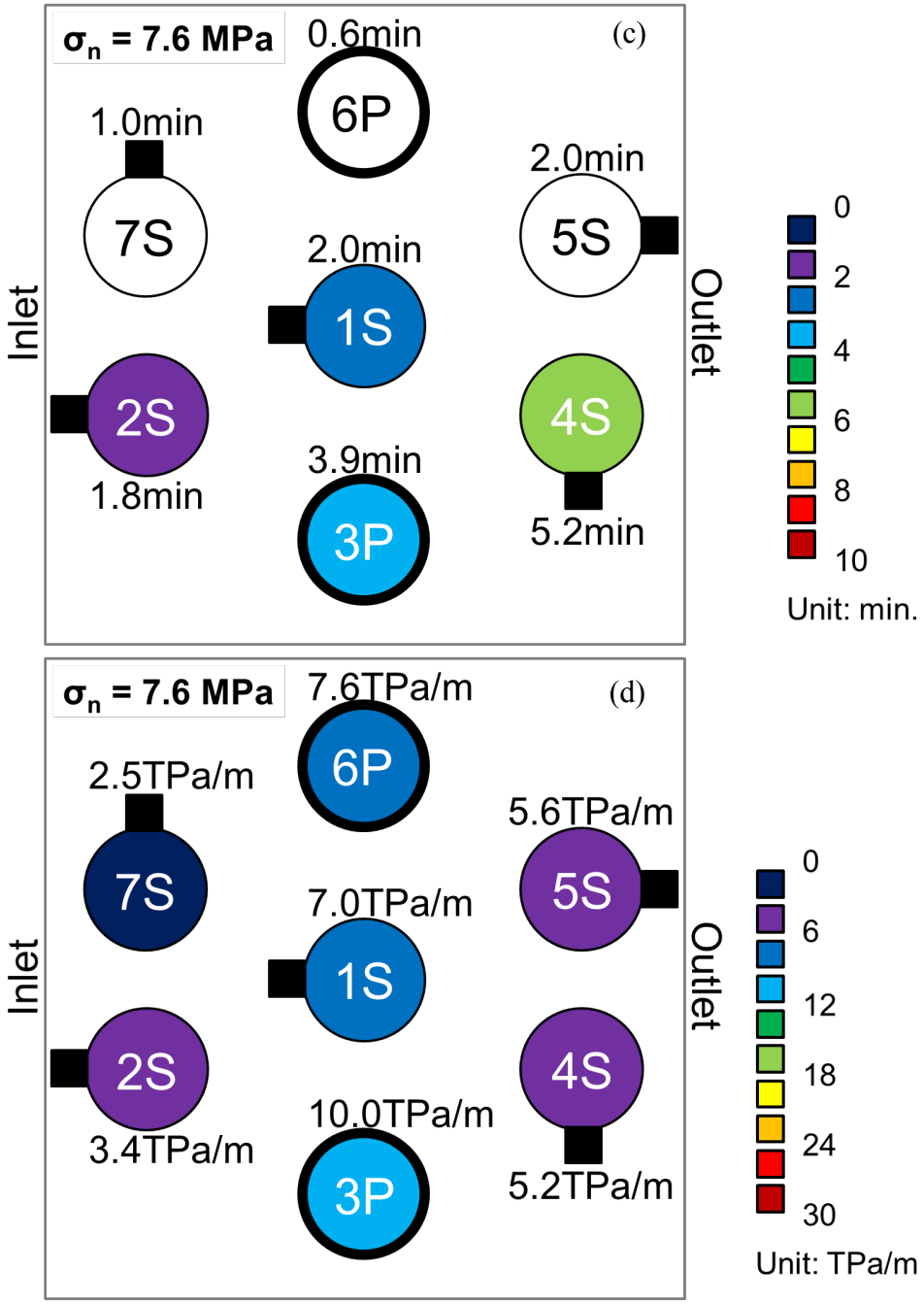

Figure. 5.4.1-1. Specimen GS01. Detected arrival times of fluid front in: (a) Test-I; and (c) Test-II and spatial distribution of specific fracture stiffness for: (b) Test-I at 1.9 MPa; and (d) Test-II at 7.6 MPa.

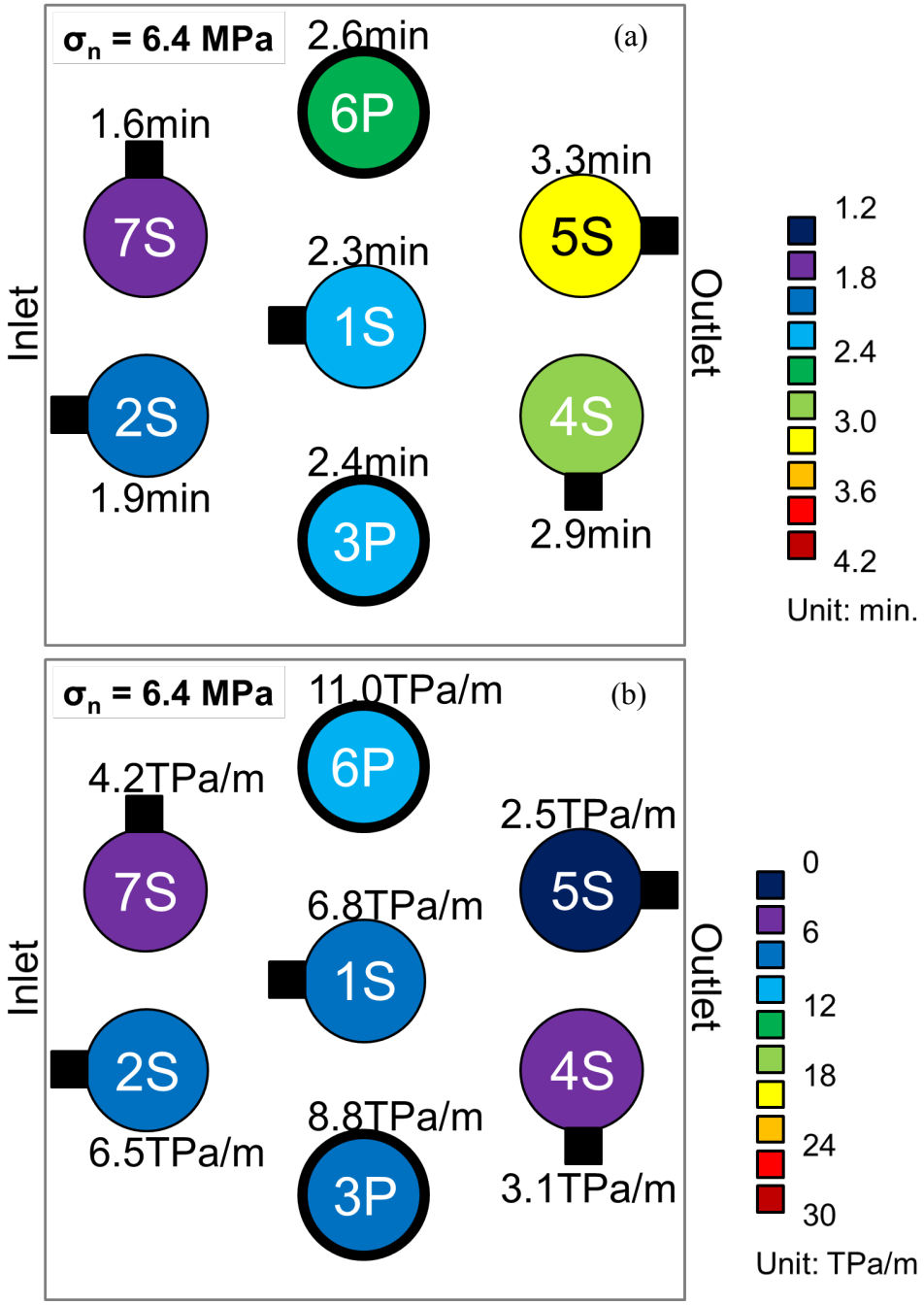

Figure 5.4.1-2. Specimen GS03, Test-III. (a) Detected arrival times of fluid front; and (b) spatial distribution of specific fracture stiffness at 6.4 MPa normal stress.

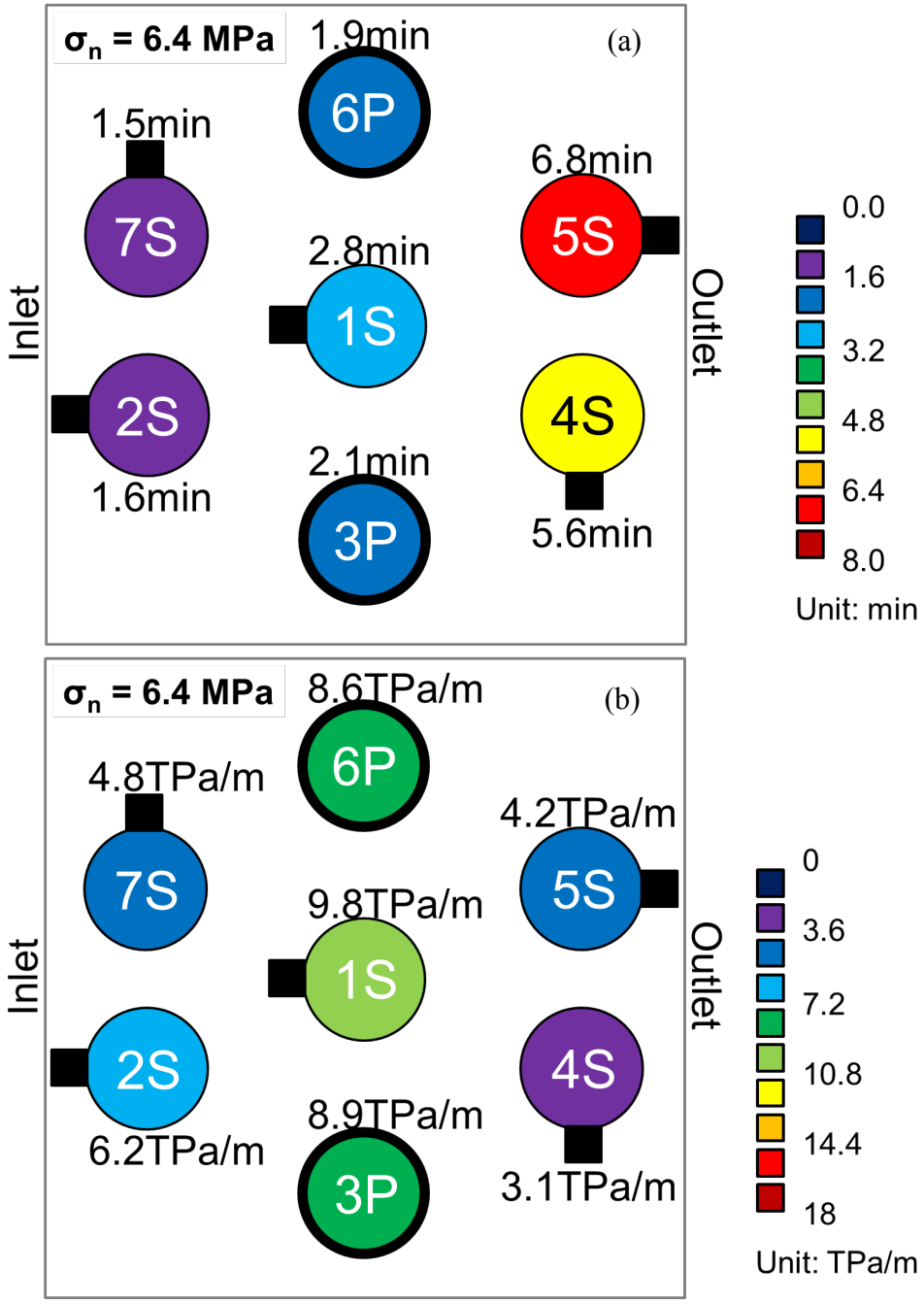

Figure 5.4.1-3. Specimen GS06, Test-IV. (a) Detected arrival times of fluid front; and (b) spatial distribution of specific fracture stiffness at 6.4 MPa normal stress.

5.4.2 Fluid Flow and Fracture Specific Stiffness

Fluid flow in two orthogonal directions was measured for specimens GS01 and GS06. Water was injected into the specimens with a constant pressure 100 kPa while the outlet was closed to obtain saturation/wetting of the granite matrix. Upon wetting of the granite matrix, the amplitudes of both shear and compressional waves decreased and reached a constant value after 20 hours. Then fluid flow measurements in two orthogonal directions (*x*- and *y*- directions in Figure 5.2.1-2) were made under a constant given load. The fluid pressure used to inject water into the inlet reservoir was held constant at 100 kPa during the tests and outflow rates were measured as a function of normal stress. Fluid outflow in the *x*- direction was measured first by opening only the inlet and the outlet tubing in the *x*- direction of flow, i.e., the tubing in the *y*- direction was initially closed. The fluid outflow was collected in an external reservoir and its weight was measured with a scale at given time intervals. Once the outflow rate in *x*- direction reached steady-state, fluid outflow in the *y*- direction was measured in a similar manner, i.e. by opening the inlet and outlet in the *y*- direction and closing the inlet and outlet in the *x*- direction. After the fluid flow measurements in the *x*- and *y*- directions were completed, the load was increased and flow measurements in the *x*- and *y*- directions were repeated. The specimen was loaded from 22.2 kN up to 222 kN with six loading steps: 22.2 kN, 44.4 kN, 88.8 kN, 133.2 kN, 177.6 kN, and 222 kN.

Figure 5.4.2-1 shows the flow per unit head, i.e. specific flow rate, in the *x*- and *y*- directions as a function of normal stress for specimens GS01 and GS06. Because the fracture in GS06 was oriented at 15° with respect to the horizontal, the fracture was subjected to normal and shear stress. The magnitude of the shear stress acting on the

fracture in GS06 is included on the second *x*- axis, at the bottom of the Figure. The amount of specific flow in GS01 and GS06 specimens decreased from 10^{-9} to 10^{-11} m^2/sec with increasing stress. There was no significant difference in the flow rates between the *x*- and *y*- directions, suggesting that the fluid flow through the fractures in GS01 and GS06 was isotropic. It is interesting to note that GS06, subjected to both shear and normal stress, had isotropic flow. Though many researchers (Yeo et al. (1998), Watanabe et al. (2008), Koyama et al. (2006), Nemoto et al. (2009), and Matsuki et al. (2010)) observed shear-induced anisotropic flow in a fracture numerically and experimentally, this was not the case for GS06. This was because the fracture in GS06 did not have slippage during the experiments and the shear stress applied was not large enough for shear-induced anisotropic flow. Shear-induced anisotropic flow requires a shear displacement large enough to increase the spatial correlation length of the apertures in a direction perpendicular to the shear displacement. Nemoto et al. (2009), also experimentally, observed that the permeability of a fracture becomes close to isotropic when the induced shear displacement is smaller than 2 mm.

As indicated by Pyrak-Nolte and Morris (2000), the fluid flow through the fracture is implicitly related to the fracture specific stiffness because both fluid flow and fracture specific stiffness depend on fracture geometry, i.e. on the size and spatial distribution of the aperture and contact area. Representative normal and shear fracture specific stiffness for GS01 and GS06 were calculated. Figure 5.4.2-2 contains: (a) the normal and (b) shear fracture specific stiffness as a function of normal stress, along with the fracture specific stiffness measured from each transducer pair. For both specimens, the averaged normal and shear fracture specific stiffness ranged from 10^3 to 10^4 MPa/mm.

Figure 5.4.2-3 shows the fluid flow - fracture specific stiffness relationship obtained from GS01 and GS06. The specific flow is related to normal fracture specific stiffness in Figure 5.4.2-3 (a) and to shear fracture specific stiffness in Figure 5.4.2-3 (b). It is observed that the specific flow decreases as the fracture specific stiffness increases. The slopes of the specific flow in the *x*- and y- directions with respect to the normal fracture specific stiffness are -1.49 and -1.34 for GS01, respectively, and -1.56 and -1.31 for GS06. For the shear fracture specific stiffness, the slopes are -2.35 and -2.22 for GS01, respectively, and -1.92 and -1.60 for GS06. The negative sign in the slopes indicates that fluid flow decreases with increasing fracture specific stiffness. The slopes of flow with shear specific stiffness are steeper than with normal stiffness, so specific flow seems to be more sensitive to changes in shear specific stiffness than in normal specific stiffness.

Compared to the specific flow rate of GS06, GS01 showed a larger decrease in the specific flow rate with increase of fracture specific stiffness (Figure 5.4.2-3). The ratio of specific flow between GS01 and GS06 was around 2 at the start of the test and increased up to approximately 10 as the fracture specific stiffness increased. As seen in Table 5.3.1-2, the most probable apertures for GS01 and GS06 were 0.60 mm and 0.75 mm, respectively. These apertures can be regarded as initial apertures at zero or low stress. Based on the cubic law, the ratio of specific flow rates between GS01 and GS06 should be approximately $(0.75/0.60)^3 \approx 2$, which is comparable to the ratio of 2 measured at their smallest fracture specific stiffness. As the fractures were compressed, the aperture decreased and the contact area increased, which lead to a decrease of fluid flow and an increase of fracture specific stiffness. It would be reasonable to expect that the aperture closures should be similar when the same normal stress is applied to the fractures,

because the fracture specific stiffness for GS01 and GS01 are similar to each other. Assuming that the aperture closures for GS01 and GS06 were around 0.40-0.50mm, the ratio of specific flow rates between GS01 and GS06 would increase up to 5.4-15.6, which is of the same order of the observation of a ratio of 10, as mentioned before; that is, for a closure of 0.4 mm, the ratio would be $[(0.75\text{-}0.40)/(0.60\text{-}0.40)]^3 \approx 5.4$; and for a closure of 0.5 mm, $[(0.75\text{-}0.50)/(0.60\text{-}0.50)]^3 \approx 15.6$. This approximation shows that the same magnitude of aperture closures for GS01 and GS06 might induce a larger decrease of fluid flow in GS01 than GS06 because the initial aperture of GS01 was smaller than that of GS06.

Pyrak-Nolte and Morris (2000) associated fracture stiffness-fluid flow behavior with a spatial correlation length of the aperture distribution of the fracture. They presented experimental and numerical evidence to support that fluid flow through a fracture decreased steeply with an increase of normal fracture specific stiffness when the spatial correlation length was comparable to the size of the fracture. In contrast, flow through a fracture was less dependent on the change of stiffness if the fracture was spatially uncorrelated. Figure 5.4.2-4 compares the fluid flow - fracture specific stiffness behavior in GS01 (red) and GS06 (blue) with experimental data from thirteen fracture samples (black) collected from the study of Pyrak-Nolte and Morris (modified after Pyrak-Nolte and Morris (2000)). Those thirteen fracture samples ranged in size from 0.052 m to 0.295 m. As mentioned in section 2.4.2, the fluid flow - fracture specific stiffness behavior for the thirteen fracture samples was divided in two groups: i) STR2, S9, S10, S33, Sample 1-3, E30, E32, and E35 (represented by black open symbols) and ii) H1, Sample 5, and Granite (black solid symbols). The first group showed a stiff decrease in flow rate with an

increase in fracture specific stiffness: a nine order of magnitude decrease of flow for only a three order of magnitude increase in fracture specific stiffness. The second group had flow less sensitive to the change of specific stiffness. As observed in Figure 5.4.2-4, the fluid flow - fracture specific stiffness behavior for GS01 and GS06 fall within the data from the literature. GS01 and GS06 had smaller slopes of specific flow and fracture specific stiffness than the first group of samples. GS01 and GS06 had a three order of magnitude decrease in specific flow for a two orders of magnitude increase of normal specific stiffness. This seems to indicate that the fractures in GS01 and GS06 were weakly correlated, though the exact aperture distribution and its spatial correlation length for GS01 and GS06 are not known.

Petrovitch et al. (2013) showed that a universal scaling function exists that encompassed fluid flow - fracture specific stiffness behavior. The scaling function had two distinct regions: effective medium regime and percolation regime. In the effective medium regime, the flow velocity across the fracture was homogenous (e.g. uniform). However, in the percolation regime, a few narrow channels remained open and the tortuosity of the flow paths increased, which resulted in non-uniform fluid flow across the fracture. Thus, the non-uniform flow patterns observed in GS01 and GS06 suggests that the observed fluid flow - fracture specific stiffness regime is in the percolation regime. In the study of Petrovitch et al., all fractures smaller than 0.25 m were in the percolation regime, while fractures between 0.5 m and 1.0 m in size fell in the effective medium regime. Given that the fracture size in GS01 and GS06 were 0.15 m, it seems reasonable that the flow-stiffness regime was in the percolation regime.

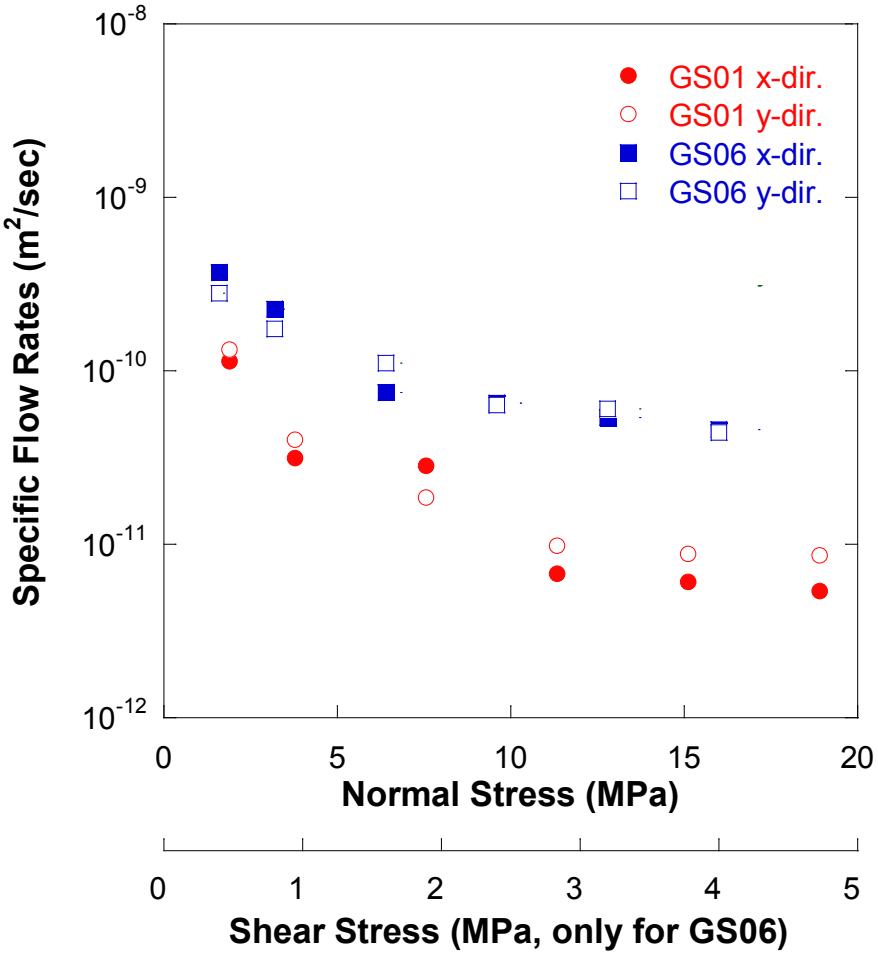

Figure 5.4.2-1. Flow per unit head (specific flow rates) in *x*- and *y*- directions as a function of normal stress from specimens GS01 and GS06. The magnitude of shear stress in GS06 is indicated by the second x- axis, at the bottom.

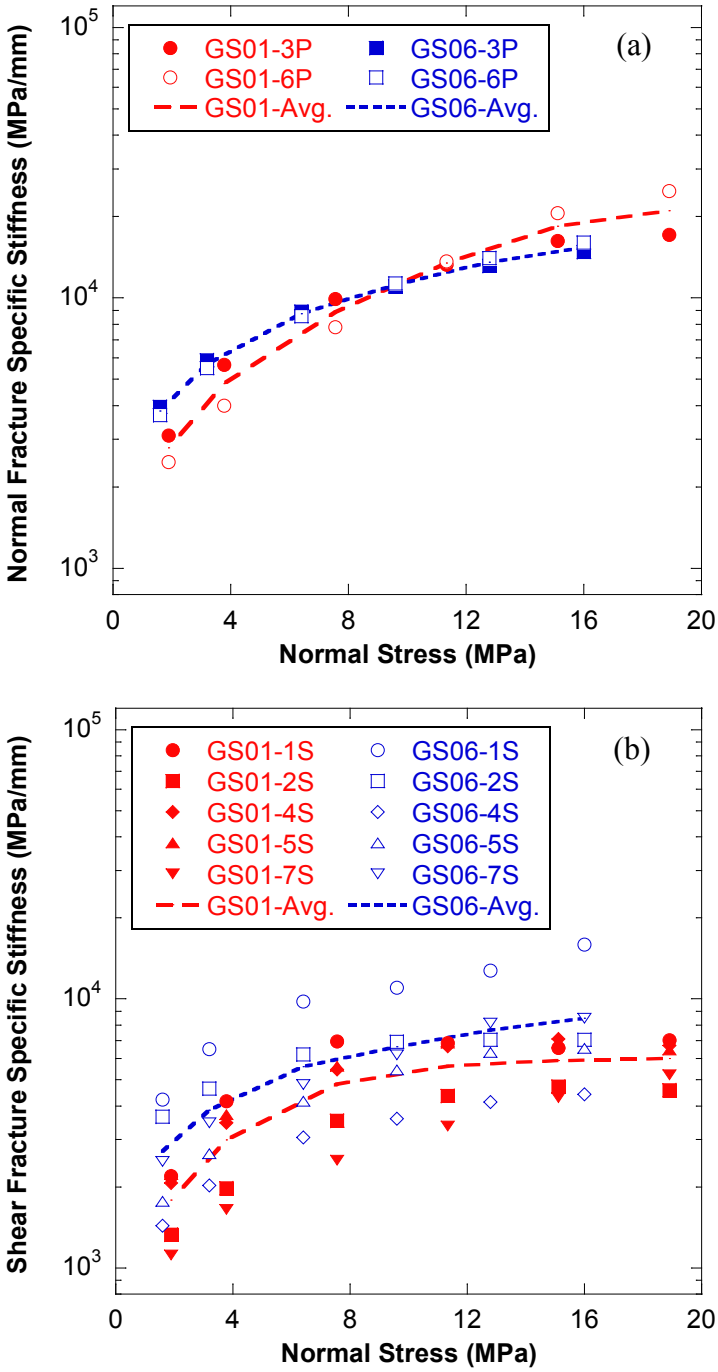

Figure 5.4.2-2. Specimens GS01 and GS06. (a) Normal fracture specific stiffness measured from transducer pairs 3P and 6P and averaged normal fracture specific stiffness; and (b) shear fracture specific stiffness measured from transducer pairs 1S, 2S, 4S, 5S, and 7S and averaged shear fracture specific stiffness.

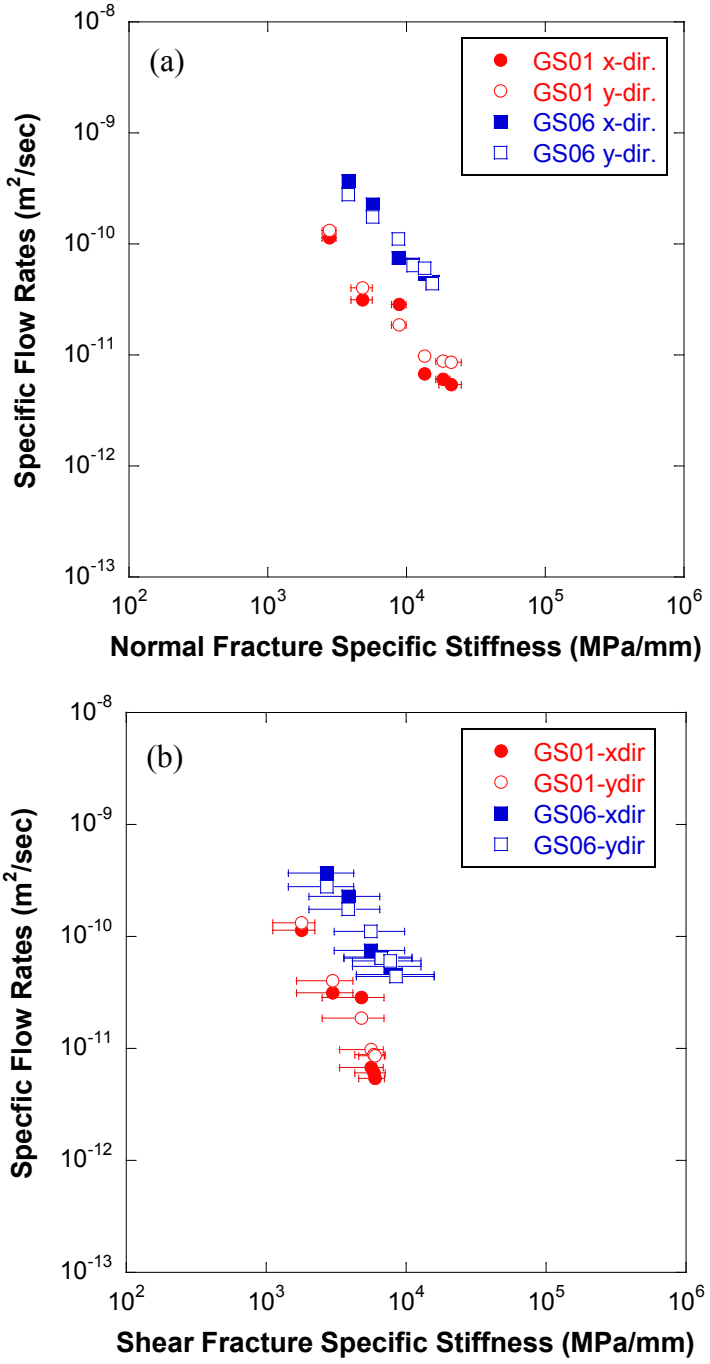

Figure 5.4.2-3. Specific fluid flow from specimens GS01 and GS06 with: (a) normal fracture specific stiffness; and (b) shear fracture specific stiffness. Error bars show the level of variation in fracture specific stiffness.

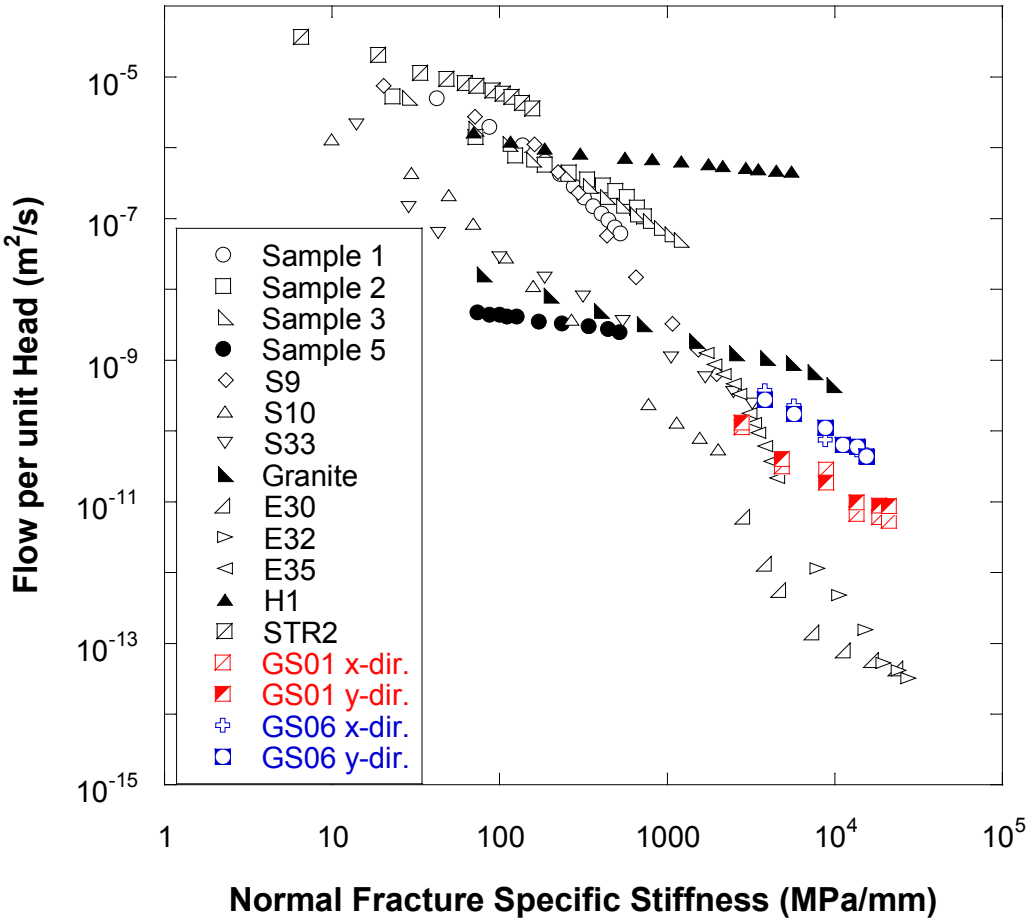

Figure 5.4.2-4. Fluid flow - fracture specific stiffness. Comparison between data from GS01 (red) and GS06 (blue) and from thirteen fracture samples (black) from Pyrak-Nolte and Morris (2000).

5.5 Summary

A series of laboratory experiments was performed to investigate the relationship between fluid flow in a fracture and fracture specific stiffness. Seismic measurements were used to investigate the invasion of water into the matrix and along a fracture. The decrease in the arrival time and the change in peak-to-peak amplitude of transmitted waves were indicators used to identify the arrival of the fluid-air front. Fluid flow measurements through fractures were made and interpreted in relation with fracture specific stiffness. Based on the experimental results, the following conclusions are drawn:

- A decrease in amplitude and an increase in velocity of the transmitted signal indicate the time of arrival of the fluid-air front.
- Spatial variability of fracture specific stiffness results in a non-uniform invasion front.
- The most conductive flow paths through a fracture can be determined given the spatial distribution of fracture specific stiffness.
- Fluid flow through a fracture is stress-dependent and is related to the variation of fracture stiffness. The fluid flow decreased from 10^{-9} to 10^{-11} m^2/sec as the fracture stiffness increased from 10^3 to 10^4 MPa/mm.
- Anisotropic flow in a fracture induced by shear displacement was not observed and seems to require significant slippage on the fracture.
- Specific flow is more sensitive to the change in shear specific stiffness than on normal specific stiffness

- Fluid flow - fracture specific stiffness observations indicate that the fractures in specimens GS01 and GS06 were weakly spatially correlated and were in the percolation regime.

CHAPTER 6. CONCLUSIONS AND RECOMMENDATIONS FOR FURTHER STUDY

6.1 Summary and Conclusions

The objective of the thesis is the characterization of the specific stiffness of fractures and the investigation of relations between spatial distribution of fracture specific stiffness and fluid flow.

A series of experiments was performed on synthetic fractures in gypsum and lucite specimens to investigate the ratio of shear to normal fracture specific stiffness. The specimens were made by placing two blocks in contact with each other to form a fracture. The fracture surfaces were prepared such that they were well-mated or non-mated and had different fracture surface roughness. To prepare a well-mated fracture surface, a block of gypsum was cast first against sandpaper and then a second block was cast against the first block such that the contact surface (i.e. the fracture) was well-mated. The fracture surface roughness was controlled by using sandpaper with different average grit size. The non-mated fractures were made by placing two lucite blocks in contact with each other. The contact surfaces were polished or sand-blasted.

There were two types of experiments: no slip and slip. For the no slip experiments, the applied shear stress was set to be less than the shear strength of the fracture, so shear failure would not occur. Each well-mated and non-mated fracture specimen was

subjected to normal and shear loading. This was done using a horizontal loading frame to apply the normal stress and a conventional loading machine to apply the shear, which was accomplished by applying compression to one of the blocks in a direction parallel to the fracture. The magnitude of the shear stress was calculated from the applied normal stress multiplied by tan θ where θ ranged from 0˚ to 40˚. In the second type of experiments, where slip was induced, the shear stress was applied to the fracture with a constant displacement rate until final slip/failure occurred. The normal stress was applied first and then held constant during the application of the shear load. The experiments that induced slip were performed only on well-mated fracture specimens. During all tests, the fracture was probed with transmitted and reflected compressional and shear waves. The stiffness ratio, defined as a ratio of shear to normal fracture specific stiffness, was calculated using the displacement discontinuity theory. The stiffness ratio found from the experiments was compared to a theoretical ratio that was determined by assuming that the transmissions of compressional and shear waves were equal.

The stiffness ratio of non-mated fractures with no slip showed that the stiffness ratio ultimately converged to the theoretical ratio as the applied normal stress increased. For the polished non-mated fracture, the stiffness ratio decreased with increasing normal stress, from 1.3 to the theoretical value of 0.46. However, the stiffness ratio for the sand-blasted non-mated fracture increased with increasing normal stress, from a value of 0.3 to the theoretical 0.46. The stiffness ratio of non-mated fractures showed no sensitivity to shear stress.

For well-mated fractures with no slip, the stiffness ratio was stress-dependent but close to the theoretical value when only normal loading (0˚ loading) was applied. For combined

normal and shear loading (15˚-40˚ loading), the stiffness ratio was stress-independent when the normal stress was greater than 1.5 MPa. Compared to the 0˚ loading (only normal loading), the stiffness ratio increased with increasing shear stress (from 15˚-40˚ loading). This dependency of shear stiffness on shear stress was observed in all well-mated fractures. Also, the stiffness ratio increased with increasing fracture surface roughness. As the mean asperity size of the fracture increased from 62-70 μm to 2,680-2,870 μm, the stiffness ratio for the 0˚-30˚ loading increased from 0.55-0.67 to 0.7-1.23. Results from the experiments suggest that the conventional assumption that the shear and normal fracture specific stiffnesses are equal may be incorrect. Also, the experiments show that the stiffness ratio increases with fracture roughness and that it changes with the stress path imposed on the fracture.

For well-mated fractures undergoing slip (shearing under constant normal load until failure), it was observed that both the normal and the shear fracture specific stiffness increased with shear. However, the specific shear fracture stiffness increased faster than the normal, and so the specific fracture stiffness ratio increased with shear. Stiffness ratios increased with increasing surface roughness. In all the experiments, it was observed that the ratio reached a maximum, after which it decreased with further loading/shear displacement. For fractures with mean asperity smaller than 70 μm, the maximum stiffness ratio was obtained at or after failure of the fracture. For surfaces with larger asperities, the maximum stiffness ration was always found prior to failure. This can be taken as an event precursory to failure. Further, the larger the roughness of the fracture, the earlier the precursor was observed. The difference between the displacements at maximum stiffness ratio and at failure of the fracture decreased from +0.50 to -0.23 mm

as the mean asperity increased from 59 to 537 μm. The positive sign means that the maximum stiffness ratio was found after the failure of the fracture, and a negative sign before the failure. The experiments indicate that the displacement required to induce irrecoverable damage to a frictional surface decreases with the increase of surface roughness. However, the decrease in stiffness ratio before failure needs to be investigated further to determine if it is related to the properties of the background material, the size of the fracture asperities, or the loading condition applied to the fracture.

The spatial variability of fracture specific stiffness was investigated seismically on granite specimens with a single fracture. Nine cylindrical specimens were cored from the same granite slab. A fracture was produced in six specimens by cutting two diametrically opposed notches and then loading the specimen in compression. Once the fracture was created, two parallel flat surfaces were cut on opposite sides of the specimens in such a manner to have the desired fracture orientation relative to the horizontal, i.e. 0˚, 15˚, or 30˚. Three intact specimens without a fracture were also prepared to have the same external dimensions as the fractured specimens. The intact specimens were used as standard reference.

Steel platens that housed compressional (P) and shear (S) wave transducers were placed in contact with the flat surfaces of the specimen (top and bottom) prior to loading. Two pairs of P-wave transducers and five pairs of S-wave transducers were employed to measure the spatial distribution of fracture specific stiffness. Transmitted compressional and shear waves were measured on intact and fractured granite specimens under different normal stresses up to 18.9 MPa. The load was applied in ten increments of 1.89MPa each.

At the end of each step, P- and S- waves from each transducer pair were recorded to determine the variation of fracture stiffness with the increase of normal and shear stress.

The granite matrix, from data from intact specimens, showed a stress-dependent seismic behavior due to the existence of micro-cracks. The amplitude and velocity of seismic waves increased with increasing stress. For fractured granite specimens, the amplitude and velocity of seismic waves transmitted across the fracture were smaller than those of intact specimens, but significantly increased as the fracture compressed. The increase of amplitude and wave velocity was interpreted as the increase of fracture specific stiffness. Spectral analysis on the transmitted waves showed that the transmission of high frequency components of the signals and the dominant frequency approached the values of the intact material.

Fracture specific stiffness along a fracture was calculated using the displacement discontinuity theory. The variation in fracture specific stiffness caused by the heterogeneity of the granite material was ±8~12%, depending on the selection of the intact standard. The fracture stiffness estimated from each transducer pair showed spatially different values, indicating that the local fracture specific stiffness varied along the fracture plane. The fracture specific stiffness increased locally as the fracture compressed. The spatial variability of specific stiffness along the fracture exceeded the variation of stiffness caused by the heterogeneity of the granite matrix. Local fracture specific stiffness was correlated with the local fracture geometry, e.g. local surface roughness distribution and local micro-slope angles. Fracture specific stiffness increased as the asperity heights of the fracture became uniform and the micro-slope angles increased.

The relationship between fluid flow and fracture specific stiffness was studied using the seismic response of the granite matrix and fracture with and without flow. Transmitted compressional and shear waves were recorded during fluid flow invasion. Wetting the rock matrix and fracture with fluid increased the wave velocity and decreased the wave amplitude. Water invasion into the fracture was much faster than the invasion into the voids of the rock matrix. The faster invasion into the fracture enabled us to detect seismically the propagation of the fluid in the fracture during the early stages of fluid invasion. A decrease in arrival time and amplitude of the transmitted waves were indicative of the fluid-air front reaching the center of the transducers. The fluid-air front detection time was tracked along the fracture and compared with the spatial distribution of the fracture specific stiffness determined prior to the fluid invasion. The invasion of the fluid was not uniform throughout the fracture, but the sequence of fluid invasion within the fracture correlated well with the spatial distribution of the fracture specific stiffness. The fluid first invaded portions of the fracture that had relatively low fracture specific stiffness and then spread to regions with higher specific stiffness. These experimental results seem to support the notion that fluid invasion can be seismically detected and that the fluid flow path through a fracture can be correlated with the spatial distribution of the fracture specific stiffness.

Fluid flow through a fracture was measured in two orthogonal directions, i.e., parallel and perpendicular to the shear loading, and as a function of stress. The fluid flow in the two orthogonal directions was stress-dependent and approximately isotropic. With stress, the specific fluid flow, defined as flow rate per unit head, decreased from 10^{-9} to 10^{-11} m^2/sec as the normal stress stress increased up to 18.9 MPa. Shear-induced anisotropic flow,

which is preferential flow perpendicular to the direction of shear, was not observed in this experiment. The shear-induced flow seems to require that substantial slip has taken place on the fracture; however no significant slip occurred in the experiments. Finally specific fluid flow in the fracture was correlated with fracture specific stiffness determined prior to fluid flow. Specific fluid flow decreased from 10^{-9} to 10^{-11} m^2/sec while the fracture specific stiffness increased from 10^3 to 10^4 MPa/mm. Flow through the fractures was more sensitive to the changes in shear fracture specific stiffness than to normal fracture specific stiffness.

In conclusion, the experiments performed in this thesis showed that fracture surface roughness is an important factor to determine the ratio of shear to normal fracture specific stiffness. For non-mated surfaces, the stiffness ratio converged to the value predicted by theory at large normal stress. However, at small normal stresses, polished fractures had a larger than theoretical ratio, that then decreased with increasing normal stress; for sand-blasted fractures the ratio was smaller than the theoretical and then it increased with normal stress. For well-mated fractures, the stiffness ratio increased with the increase of surface roughness and shear stress. The data gathered from the experiments on fracture specific stiffness and fluid flow shows that seismic wave propagation can be used to detect the fluid invasion front in the fracture and that the most conductive fluid path can be predicted from the spatial distribution of the fracture specific stiffness.

6.2 Recommendations for Future Work

The experiments carried out in this research have contributed to a better understanding of fracture specific stiffness. Specifically to understand better how specific stiffness depends

on loading (type and magnitude), how to evaluate and determine spatial variability, how fluid invades a fracture, and how the fluid front can be detected using seismic methods. However, due to limitations of the experimental program, there are a number of issues that require attention. They include:

- Scale effects. There is the issue of using lab-scale stiffnesses to field-scale since, as discussed in this research, the stiffness ratio is sensitive to the magnitude and type of loading. Hence, it seems appropriate to test larger fractures under stresses that represent field conditions.
- Theory shows that the stiffness ratio is a function of wave frequency, seismic impedance of rock material and wave transmission across the fracture. If the transmission of seismic wave is strongly frequency-dependent, the stiffness ratio will be also frequency-dependent. Thus, it seems necessary to study how the frequency dependent fracture changes the stiffness ratio changes.
- The fluid flow-fracture stiffness behavior should be the result of the complex interaction between the geometry of asperities in contact and the apertures in the fracture. The deformation of asperities and fracture voids (apertures) with increasing stress results in increasing the number of asperities in contact and decreasing the volume of voids. These geometrical changes with stress induced non-linear changes in fracture stiffness and in apertures which fluid flows through. Hence, estimation on aperture distribution and its deformation under stress will give a better understanding of the hydro-mechanical behavior of fractures.

- Significant decrease in amplitude of transmitted waves was observed as the fluid invaded the rock matrix or the voids in the fractures. Since the fluid was injected with relatively low pressure, i.e. 10 to 100 kPa, air bubbles could have been entrapped in the rock matrix and/or voids in the fractures and might have caused the amplitude decay, observed in the tests, by scattering the seismic waves. To remove the entrapped air, it may be necessary to inject fluid with high pressure and/or to use vacuum saturation for full saturation of the rock.

REFERENCES

REFERENCES

Angus, D. A., J. P. Verdon, Q. J. Fisher, and J.-M. Kendall, 2009, Exploring trends in microcrack properties of sedimentary rocks: An audit of dry core velocity-stress measurements: Geophysics, 74, E193-E203.

Acosta-Colon, A., Pyrak-Nolte, L. J. and Nolte, D. D., 2009. Laboratory-scale study of field of view and the seismic interpretation of fracture specific stiffness, Geophysical Prospecting, 57, 209-224.

Baik, J.M. and R.B. Thompson, 1984, Ultrasonic scattering from imperfect interfaces. Journal of Nondestructive Evaluation, 4, 177-197.

Bandis, S.C., A.C. Luden, and N.R. Barton, 1983, Fundamentals of rock joint deformation, International Journal of Rock Mechanics and Mining Science and Geomechanics Abstract, 20, 249-268.

Beck, J. V. and K. J. Arnold, 1977, Parameter Estimation in Engineering and Science, John Wiley & Sons, New York.

Bobet, A. and H.H. Einstein, 1998, Fracture Coalescence in Rock-type Materials under Uniaxial and Biaxial Compression, International Journal of Rock mechanics and Mining Science, 35, 863-888.

Brown, S.R., 1987, Fluid flow through rock joints, The effect of surface roughness, Journal of Geophysics Research, 92, 1337-1347.

Cook,N.G.W., 1992, Natural joints in rock: mechanical, hydraulic and seismic behavior and properties under normal stress, International Journal of Rock Mechanics and Mining Science and Geomechnic Abstract, 29, 198-223.

Engelder, T. and C.H. Scholz, 1988, Fluid flow along very smooth joints at effective pressures up to 200 megapascals, Mechanical Behavior of Crustal Rocks, The Handin Volume, AGU Monograph 25, 147-152.

Eshelby, J.D., 1961, Elastic inclusions and inhomogeneities, In:Progress in Solid Mechanics, Vol. II, 89-140.

Far, M., 2011, Seismic characterization of naturally fractured reservoirs, Ph.D. thesis, University of Houston.

Fischer, T., S. Hainzl, L. Eisner, S.A. Shapiro, and J. Le Calvez, 2008, Microseismic signatures of hydraulic fracture growth in tight-sandstone-shale formation: Observation and modeling, Journal of Geophysical Research, 113, B02307.

Gale, J.E., 1975, A numerical field and laboratory study of flow in rocks with deformable fractures, Ph.D dissertation, University of California, Berkeley.

Gangi, A.F., 1978, Variation of whole and fractured porous rock permeability with confining pressure, International Journal of Rock Mechanics and Mining Science, 15, 249-257.

Hill, R. 1963, Elastic properties of reinforced solids: Some theoretical principles, Journal of the Mechanics and Physics of Solids, 11, 357-372.

Hedayat, A., L.J. Pyrak-Nolte, and A. Bobet, 2012, Monitoring slip initiation and propagation along frictional interfaces with seismic wave transmission, 46th U.S. Rock Mechanics Geomechanics Symposium, PaperNo. ARMA 12-227, 9 pp.

Hobday, C., and M. H.Worthington, 2012, Field measurements of normal and shear fracture compliance, Geophysical Prospecting, 60, 488-499.

Hopkins, D.L, N.G.W. Cook, and L.R. Myer, 1987, Fracture stiffness and aperture as a function of applied stress and contact geometry, 28th U.S. Symposium on Rock Mechanics, Tucson.

Hsu, C.-J., and M. Schoenberg, 1993, Elastic waves through a simulated fractured medium, Geophysics, 58, 964-977.

Hudson, J.A., 1981, Wave speeds and attenuation of elastic waves in material containing cracks, Geophysical Journal of the Royal Astronomical Society, 64, 133-150.

Hudson, J.A., and L. Knopoff, 1989, Predicting the overall properties of composite materials with small-scale inclusions or cracks, Pure Applied Geophysics, 131, 551-576.

Hudson, J.A., E. Liu, and S. Crampin, 1997, The mean transmission properties of a fault imperfect facial contact, Geophysics Journal International, 129, 720-726

Jaeger, J.C., N.G.W Cook, and R.W. Zimmerman, 2007, Fundamentals of rock mechanics, 4th ed. London: Wiley-Blackwell.

Johnson, K. L., 1985, Contact Mechanics: Cambridge University Press.

Kachanov M., 1980, Continuum model of medium with cracks, Journal of the Engineering Mechanics Division of the American Society of Civil Engineers 106, 1039-1051.

Kachanov, M., R. Prioul, and J. Jocker, 2010, Incremental linear-elastic response of rocks containing multiple rough fractures: Similarities and differences with traction-free cracks: Geophysics, 75, D1-D11.

Klimczak C., R.A. Schultz, R. Parashar, and D.M. Reeves, 2010, Cubic law with aperture-length correlation: implications for network scale fluid flow, Hydrology Journal, 18, 851-861.

Kitsunezaki, C., 1983, Behavior of plane elastic waves across a plane crack, Journal of Mining College of Akita University, 6, 173-187.

Ko, T. Y., H.H. Einstein, and J. Kemeny, 2006, Crack Coalescence in Brittle Material under Cyclic Loading, 41st U.S. Symposium on Rock Mechanics, ARMA/USRMS 06-930.

Koyama, T., N. Fardin, L. Jing, and O. Stephansson, 2006, Numerical simulation of shear-induced flow anisotropy and scale-dependent aperture and transmissivity evolution of rock fracture replicas, International Journal of Rock Mechanics and Mining Science, 43, 89-106.

Kraz, R.L., A.D. Frankel, T. Engelder, and C.H. Scholz, 1979, The permeability of whole and jointed Barre granite, International Journal of Rock Mechanics and Mining Science, 16, 225-234.

Lanaro, F., 2000, A random field model for surface roughness and aperture of rock fratures, International Journal of Rock Mechanics and Mining Science, 37, 1195-1210.

Lanaro, F. and O. Stephansson, 2003, A unified model for characterization and mechanical behavior of rock fractures, Pure and Applied Geophysics, 160, 989-998.

Li, Weiwei, 2012, Seismic wave propagation in fractured anisotropic corbonate rock: experiment and theory, Ph.D. dissertation, Purdue University, West Lafayette.

Li, Yingping, Chuen H. Cheng, and M. Nafim Toksoz, 1998, Seismic monitoring of the growth of a hydraulic fracture zone at Fenton Hill, New Mexico, Goephysics, 63, 120-131.

Liu, E., J.A. Hudson, and T. Pointer, 2000, Equivalent medium representation of fractured rock, Journal of Geophysical Research, 105, B2, 2981-3000.

Liu, E. 2005, Effects of fracture aperture and roughness on hydraulic and mechanical properties of rocks: implication of seismic characterization of fractured reservoiors, Journal of Geophysics and Engineering, 2, 38-47.

Lubbe, R., J. Sothcott, M.H. Worthington, and C. McCann, 2008, Laboratory estimates of normal and shear fracture compliance, Geophysical Prospecting, 56, 239-247.

MacBeth, C., and H. Schuett, 2007, The stress dependent elastic properties of thermally induced microfractures in aeolian Rotliegend Sandstone, Geophysical Prospecting, 55, 323-332.

Masuki, K., Y. Kimura, K. Sakaguchi, A. Kizaki, and A.A. Giwelli, 2010, Effect ofshear displacement on the hydraulic conductivity of a fracture, International Journal of Rock Mechanics and Mining Science, 47, 436-449.

Myer, L.R., 2000, Fractures as collections of cracks, International Journal of Rock Mechanics and Mining Sciences, 37, 231-243.

Myer, L.R., D. Hopkins, and N.G.W. Cook, 1985, Effect of contact area of an interface on acoustic wave transmission characteristics, Proceedings of the 26th U.S.Rock Mechanics Symposium, Vol.1, 565-572, A.A. Balkema, Boston, Mass.

Mollhoff, M., and Bean, C.J., 2009, Validation of elastic wave measurements of rock fracture compliance using numerical discrete particle simulations, Geophysical Prospecting, 57, 883-895.

Nagy, P.B., 1992, Ultrasonic classification of imperfect interfaces, Journal of Nondestructive Evaluation, 11, 127-139.

Nakagawa, S., K.T. Nihei, and L.R. Myer, 2000, Stop-pass behavior of acoustic waves in a 1D fractured system, Journal of the Acoustical Society of America, 107, 40-50.

Nemoto, K., N. Watanabe, N. Hirrano, and N. Tsuchiya, 2009, Direct measurement of contact area and stress dependence of anisotropic flow through rock fracture with heterogeneous aperture distribtution, Earth adn Planeetary Science Letters, 291, 81-87.

Nihei, K.T., 1992, Micromechanics of Seismic Wave Propagation in Granular Rocks, Ph.D. thesis, University of California, Berkeley.

Nolte, D.D. and L.J. Pyrak-Nolte, 1991, Stratified continuum percolation: scaling geometry of hierarchical cascades, Physical Review A 44, 632G-6333.

Park, Jung-Wook and Jae-Joon Song, 2013, Numerical method for the determination of contact areas of a rock joint under normal and shear loads, International Journal of Rock Mechanics and Mining Science, 58, 8-22.

Pervukhina, M., B. Gurevich, P. Golodoniuc, and D.N. Dewhurst, 2011, Parameterization of elastic stress sensitivity in shales, Geophysics, 76, WA147-WA155.

Petrovitch, C.L., D.D Nolte, and L.J. Pyrak-Nolte, 2013, Scaling of fluid flow versus fracture stiffness, Geophysical Research Letters, 40, 2076-2080.

Power, W.L. and W.B. Durham, 1997 Topography of natural and artificial fractures in granitic rocks: Implications for studies of rock friction and fluid migraion, International Journal of Rock Mechanics and Mining Science, 34, 979-989.

Pyrak-Nolte, L.J., L.R. Myer, N.G.W. Cook, and P.A. Witherspoon, 1987, Hydraulic and mechanical properties of natural fractures i low permeability rock, In Proceedings of Sixth International Congress on Rock Mechanics, Montreal, Canada, Balkema, Rotterdam.

Pyrak-Nolte, L.J., 1988, Seismic visibility of fractures, Ph.D. dissertation, Department of Material Science and Mineral Engineering, University of California, Berkeley.

Pyrak-Nolte, L.J., N.G.W. Cook and D.D. Nolte, 1988, Fluid percolation through single fractures. Geophysical Research Letters, 15, 1247-1250.

Pyrak-Nolte, L.J., L.R. Myer, and N.G.W. Cook, 1990, Transmission of seismic waves across single natural fractures, Journal of Geophysical Research, 95, 8617-8638.

Pyrak-Nolte, L.J., and C.D. Montemagno, 1994, The effect of the critical path on fluid flow through a fracture, Proceedings of the 1st North American Rock Mechanics Symposium, Austin, Texas, Balkema, Rotterdam.

Pyrak-Nolte, L.J., D.D. Nolte, and N.G.W. Cook, 1995, Hierarchical cascades and the single fracture, In Fractals in the Earth Sciences, Edited by C. Barton and P. LaPointe, Plenum Scientific.

Pyrak-Nolte, L.J., 1996, The seismic response of fractures and the interrelationships among fracture properties, International Journal of Rock Mechanics and Mining Science & Geomechanics Abstracts, 33, 782-802.

Pyrak-Nolte, L.J., S. Roy, B.L. Mullenbach, 1996, Interface waves propagated along a fracture, Journal of Applied Geophysics, 35, 79-87.

Pyrak-Nolte, L.J., Montemagno, C. D., and Nolte, D. D., 1997, Volumetric imaging of aperture distributions in connected fracture networks, Geophysical Research Letters, 24, 2343-2346.

Pyrak-Nolte, L.J. and J.P. Morris, 2000, Single fracture under normal stress: the relation between fracture specific stiffness and fluid flow, International Journal of Rock Mechanics and Mining Sciences, 37, 245-262.

Pyrak-Nolte, L.J, D.D. Nolte, C.J. de Pater, and J. Jocker, 2006, Monitoring propagating fracture fronts: exploiting fresnel seismic precursors, Golden Rocks 2006, The 41st U.S. Symposium on Rock Mechanics (USRMS): 50 Years of Rock Mechanics - Landmarks and Future Challenges, Golden, Colorado.

Queen, J.H. and W.D. Rize, 1990, An integrated study of seismic anisotropy and the natural fracture systems at the Conoco Borehole Test Facility, Journal of Geophysical Research, 95, 11255-11273.

Rathore, J.S., E. Fjaer, R.M. Holt, and L. Renlie, 1995, P- and S-wave anisotropy of a synthetic sandstone with controlled crack geometry, Geophysical Prospecting, 43, 711-728.

Renshaw, C.E., 1995, On the relationship between mechanical and hydraulic apertures in rough-walled fractures, Journal of Geophysical Research, 100, B12, 24629-24636.

Reyes, O. and H.H. Einstein, 1991, Failure Mechanism of Fractured Rock- A Fracture Coalescence Model, Proceedings 7th International Congress of Rock Mechanics, 1, 333-340.

Rice, J.R., 1979, Theory of precursory processes in the inception of earthquake rupture, Gerlands Beitrage Geophysik, 88, 91-121.

Santamarina, J.C. and D. Fratta, 2005, Discrete signals and inverse problems: An introduction for engineers and scientists, John Wiley & Sons, Ltd.

Sayers, C.M., and M. Kachanov, 1991, A simple technique for finding effective elastic constants of cracked solids for arbitrary crack orientation statistics, International Journal of Solids and Structures, 12, 81-97.

Sayers, C.M., and M. Kachonov, 1995, Microcrack-induced elastic wave anisotropy of brittle rock, Journal of Geophysical Research, 100:B3, 4149-4156.

Sayers, C.M., 1999, Stress-dependent seismic anisotropy of shales, Geophysics, 64, 93-98.

Sayers, C.M., and D.-H. Han, 2002, The effect of pore fluid on the stress-dependent elastic wave velocities in sandstones, SEG Expanded Abstracts, 21, 1842-1845.

Sayers, C.M., A.D. Taleghani, and J. Adachi, 2009, The effect of mineralization on the ratio of normal to tangential compliance of fractures, Geophysical Prospecting, 57, 439-446.

Schoenberg, M., 1980, Elastic wave behavior across linear slip inter-faces, Journal of the Acoustical Society of America, 68, 1516-1521.

Schoenberg, M. and C.M. Sayers, 1995, Seismic anisotropy of fractured rock, Geophysics, 60, 204-211.

Sharifzadeh, M., Y. Mitani, and T. Esaki, 2008, Rock joint surfaces measurement and analysis of aperture distribution under different normal and shear loading using GIS, Rock Mechanics and Rock Engineering, 41, 299-323.

Sharp, J.C., 1970, Fluid flow through fissured media, Ph.D. dissertation, University of London, Imperial College, London.

Shen, B., O. Stephansson, H.H. Einstein, and B. Ghahreman, 1995, Coalescence of fractures under shear stress experiments, Journal of Geophysical Research, 100, 5975-5990.

Sisavath , S., A. Al-yaarubi, C.C. Pain, and R.W. Zimmerman, 2003, A simple model for deviations from the cubic law for a fracture undergoing dilation or closure, Pure and Applied Geophysics, 160, 1009-1022.

Suraez-Rivera, R., 1992, The influence of thin clay layers containing liquids on the propagation of shear waves, Ph. D. thesis, University of California, Berkeley.

Takeuchi, K., 1991, Mixed-Mode Fracture Initiation in Granular Brittle Materials, M.S. Thesis, Massachusetts Institute of Technology, Cambridge.

Tsang, Y.W. and P.A. Witherspoon, 1983, The dependence of fracture mechanical and fluid flow properties on fracture roughness and sample size, Journal of Geophysical Research, 88, B3, 2359-2366.

Tsang, Y.W. and P.A. Witherspoon, 1981, Hydromechanical Behavior of a deformable rock fracture subject to normal stress, Journal of Geophysical Research, 86, B10, 9287-9298.

Verdon, J.P., D.A. Angus, J.-M. Kendall, and S.A. Hall, 2008, The effects of microstructure and nonlinear stress on anisotropic seismic velocities, Geophysics, 73, D41-D51.

Verdon, J.P. and A. Wustefeld, 2013, Measurement of the normal/tangential compliance ratio (ZN/ZT) during hydraulic fracture stimulation using shear wave splitting data, Geophysical Prospecting, doi: 10.1111/j.1365-2478.2012.01132.x.

Watanabe, N., N. Hirano, N. Tsuchiya, 2008, Determination of aperture distribution and fluid flow in a rock fracture by high-resolution numerical modeling on the basis of a flow-through experiment under confining pressure, Water Resource Research, 44, W06412. doi:10.1029/2006WR005411.

Witherspoon, P.A., J.S.Y. Wang, K. Iwai, and J.E. Gale, 1980, Validity of cubic law for fluid flow in a deformable rock fracture, Water Resource Research, 16, 1016-1024.

Wong, L.N.Y. and Einstein, H.H, 2006, Fracturing Behavior of Prismatic Specimens Containing Single Flaws, Golden Rocks 2006, 41st U.S. Symposium on Rock Mechanics (USRMS), ARMA/USRMS 06-899.

Worthington, M. H. and J.A. Hudson, 2000, Fault properties from seismic Q, Geophysical Journal International, 143, 937-944.

Yeo, I.W., M.H. De Freitas, and R.W. Zimmerman, 1998, Effect of shear displacement on the aperture and permeability of a rock fracture, International Journal of Rock Mechanics and Mining Science, 35, 1051-1070.

APPENDICES

Appendix A Matlab Code for Stiffness Calculation

```
% The program is developed to calculate specific fracture stiffness of off-angle fractures.
% Applicable to  P-wave, SV-wave, SH-wave incident
% Kelvin model - Spring & Dashpot are connected in series

% SV-wave : channel 1,2,5
% SH-wave : channel 4,7
% P-wave : channel 3,6

K_max = 10^17 ;
Ratio = 1.0 ; % Ratio of Kx to Kz
Tolerance = 0.5 ;  % Unit: %

% # of channel
NofS = 7 ;

% # of loading step
NofL =40 ;

% Load experimental data of Intact and Fractured sample
Int_sp_data =  'GS08_1029_L1_' ;
Frac_sp_data = 'GS04_0825_L1_' ;
```

```
prefix = 'GS08+04_L1_' ;

% Frequency
% Angular frequency : w = 2*pi*f
Freq = xlsread('Freq.xls', 'sheet1', 'A2:A166') ;
w = 2*pi()*Freq *10^6;  % Unit : Hz

% Find the size of Angular frequency matrix
s_w = size(w) ;

% Define Fracture orientation & Incident angle
FO = 0 ;   % Fracture Orientation
IA = FO ;   % Incident Angle

% Density : Rho1 & Rho2
% P-wave velocity : VP1 & VP2
% S-wave velocity : VS1 & VS2
% Subscipt 1 and 2 means upper and lower half space respectively.

Rho1 = 2.7 * 10^3 ; % Units : kg/m3
Rho2 = 2.7 * 10^3 ;
```

```
% Specific viscosity : Eta_z & Eta_x & Eta_y
Eta_z = 0;
Eta_x = 0;
Eta_y = 0;

for ch=1:1:NofS

   % Load the amplitude of FFT results
   s1 = strcat('Int_sp_Abs_WF', num2str(abs(ch)),'to', num2str(abs(ch)) ) ;
   file = strcat (Int_sp_data,'Abs_WF_Taper',num2str(abs(ch)),'to', num2str(abs(ch)) );
   temp1 = xlsread(file, file, 'B2:AT166') ;
   eval( [s1 '=temp1'] );

   s2 = strcat('Frac_sp_Abs_WF', num2str(abs(ch)),'to', num2str(abs(ch)) ) ;
   file = strcat (Frac_sp_data,'Abs_WF_Taper',num2str(abs(ch)),'to', num2str(abs(ch)) );
   temp2 = xlsread(file, file, 'B2:AT166') ;
   eval( [s2 '=temp2'] );

   % Calcuate Transmission coefficient
   s3 = strcat('Tr_Co_Exprmt_', num2str(abs(ch)),'to', num2str(abs(ch)) ) ;
   eval( [s3 '=temp2./temp1'] );

   xlswrite(strcat(prefix,s3,'.xls'),Freq, strcat(prefix,s3), 'A2')
```

```
    xlswrite(strcat(prefix,s3,'.xls'),eval(s3), strcat(prefix,s3), 'B2')

    % Load the wave velocity
    s11 = strcat('Int_sp_Vel_', num2str(abs(ch)),'to', num2str(abs(ch)) ) ;

    if ch==1 || ch==2 || ch==5
       disp(strcat (num2str(ch),'SV-', num2str(ch), 'SV')) ;
       file = strcat (Int_sp_data,'Nor_Vel_S_', num2str(abs(ch)),'to', num2str(abs(ch)) ) ;
       temp11 = xlsread(file, file, 'B2:B41') ;
    elseif ch==4 || ch==7
       disp(strcat (num2str(ch),'SH-', num2str(ch), 'SH')) ;
       file = strcat (Int_sp_data,'Nor_Vel_S_', num2str(abs(ch)),'to', num2str(abs(ch)) ) ;
       temp11 = xlsread(file, file, 'B2:B41') ;
    elseif ch==3 || ch==6
       disp(strcat (num2str(ch),'P-', num2str(ch), 'P')) ;
       file = strcat (Int_sp_data,'Nor_Vel_P_', num2str(abs(ch)),'to', num2str(abs(ch)) ) ;
       temp11 = xlsread(file, file, 'B2:B41') ;
    end;

    eval( [s11 '=temp11'] );
    temp11 = zeros ;

end;
```

```
[mm,nn] = size(Tr_Co_Exprmt_1to1) ;

% Make the matrix form for Angular Frequency and wave velocity
for n = 1:1:nn
   Ang_Freq_mat(:,n:n)= w ;
   Freq_mat(:,n:n)= Freq ;
end ;

for n = 1:1:NofS
   s12 = strcat('Int_sp_Vel_', num2str(abs(n)),'to', num2str(abs(n)) ) ;
   temp12 = eval(s12);

   for k = 1:1:mm
      temp13(k:k,:) = temp12';
   end;

   s14 = strcat('Int_sp_Mat_Vel_', num2str(abs(n)),'to', num2str(abs(n)) ) ;
   eval ( [s14 '= temp13']);

end;

% Calcuate average SV, SH, and P wave velocity (matrix form)
```

```
Int_sp_Mat_Avg_SV_Vel                                                    =
(Int_sp_Mat_Vel_1to1+Int_sp_Mat_Vel_2to2+Int_sp_Mat_Vel_5to5) / 3 ;
Int_sp_Mat_Avg_SH_Vel = (Int_sp_Mat_Vel_4to4+Int_sp_Mat_Vel_7to7) / 2 ;
Int_sp_Mat_Avg_P_Vel  = (Int_sp_Mat_Vel_3to3+Int_sp_Mat_Vel_6to6) / 2 ;

% Find Reflected and Transmitted angle based on Snell's Law
% Find frequnecy-dependent Stiffness to satisfy the Transmission Coefficient from
experiment
for ch=1:1:NofS ;

   s14 = strcat('Int_sp_Mat_Vel_', num2str(abs(ch)),'to', num2str(abs(ch)) ) ;
   temp_int_vel = eval(s14) ;

   if ch==1 || ch==2 || ch==5 || ch==4 || ch==7 ;
      VS1 = temp_int_vel ;
      VS2 = temp_int_vel ;
      VP1 = Int_sp_Mat_Avg_P_Vel ;
      VP2 = Int_sp_Mat_Avg_P_Vel ;
   elseif ch==3 || ch==6 ;
      VS1 = Int_sp_Mat_Avg_SV_Vel ;
      VS2 = Int_sp_Mat_Avg_SV_Vel ;
      VP1 = temp_int_vel ;
      VP2 = temp_int_vel ;
```

```
    end ;

    % P-wave Impedence : ZP1 & ZP2
    % S-wave Impedence : ZS1 & ZS2
    ZP1 = Rho1 * VP1 ;
    ZP2 = Rho2 * VP2 ;
    ZS1 = Rho1 * VS1 ;
    ZS2 = Rho2 * VS2 ;

    if ch==1 || ch==2 || ch==5 ;
        % Reflected and Transmitted angle
        RA_P  = asin( (VP1.* sin(IA*pi()/180))./ VS1 ) ;  % Reflected Angle of P-wave ->
upper space (Unit : Radians)
        RA_SV = asin( (VS1.* sin(RA_P))./ VP1 )  ;        % Reflected Angle of SV-wave ->
upper space (Unit : Radians)
        TA_P  = asin( (VP2.* sin(RA_P))./ VP1 )  ;        % Transmitted Angle of P-wave ->
lower space (Unit : Radians)
        TA_SV = asin( (VS2.* sin(RA_P))./ VP1 )  ;        % Transmitted Angle of SV-wave
-> lower space (Unit : Radians)

    elseif ch==4 || ch==7 ;
        % Reflected and Transmitted angle
```

```
    RA_SH = asin( (VS1.* sin(IA*pi()/180))./VS1 ) ;   % Reflected Angle of SV-wave -
> upper space (Unit : Radians)
    TA_SH = asin( (VS2.* sin(RA_SH))./ VS1 )  ;       % Transmitted Angle of SV-
wave -> lower space (Unit : Radians)

  elseif ch==3 || ch==6 ;
    % Reflected and Transmitted angle
    RA_P  = asin( (VP1.* sin(IA*pi()/180))./VP1 ) ;   % Reflected Angle of P-wave ->
upper space (Unit : Radians)
    RA_SV = asin( (VS1.* sin(RA_P))./ VP1 )  ;        % Reflected Angle of SV-wave ->
upper space (Unit : Radians)
    TA_P  = asin( (VP2.* sin(RA_P))./ VP1 )  ;        % Transmitted Angle of P-wave ->
lower space (Unit : Radians)
    TA_SV = asin( (VS2.* sin(RA_P))./ VP1 )  ;        % Transmitted Angle of SV-wave
-> lower space (Unit : Radians)

  end ;

  % Load Transmission Coefficient
  s33 = strcat('Tr_Co_Exprmt_', num2str(abs(ch)),'to', num2str(abs(ch)) ) ;
  temp33 = eval(s33);

  % Channel SV-Incident
```

```
    if ch==1 || ch==2 || ch==5 ;
        disp(strcat (num2str(ch),'SV-', num2str(ch), 'SV')) ;
        for ls=1:1:NofL ;
%           disp(strcat('Loading Step: ',num2str(ls))) ;
          for k=1:1:s_w(1) ;

            if k==1
               % Initial Stiffness for iteration
               K_x(k:k,ls:ls)  = 10^12 ;
            else
               % Initial Stiffness for iteration
               K_x(k:k,ls:ls)  = K_x(k-1:k-1,ls:ls) ;
               if K_x(k:k,ls:ls) >= K_max
                  K_x(k:k,ls:ls)  = 0.9*K_max ;
               else
                  % Initial Stiffness for iteration
                  K_x(k:k,ls:ls)  = K_x(k-1:k-1,ls:ls) ;
               end ;

            end ;

            K_z(k:k,ls:ls) = 1 / Ratio * K_x(k:k,ls:ls) ;
```

```
Solution_Matrix_SV

% Check Transmission Coefficient
Abs_Tsv(k:k,ls:ls) = abs(Tsv(k:k,ls:ls)) ;

iteration = 1;
while abs( (Abs_Tsv(k:k,ls:ls)-temp33(k:k,ls:ls))/temp33(k:k,ls:ls) ) >=
Tolerance/100
   if K_x(k:k,ls:ls) > K_max ;
      disp('K > Kmax' ) ;
      break ;
   end ;
   iteration = iteration +1 ;

   if Abs_Tsv(k:k,ls:ls) > temp33(k:k,ls:ls) ;
      K_x(k:k,ls:ls) = 0.96 * K_x(k:k,ls:ls) ;
   elseif Abs_Tsv(k:k,ls:ls) < temp33(k:k,ls:ls) ;
      K_x(k:k,ls:ls) = 1.04 * K_x(k:k,ls:ls) ;
   end ;

   K_z(k:k,ls:ls) = 1 / Ratio * K_x(k:k,ls:ls) ;

   % Call Solution matrix for SV-incident
```

```
            Solution_Matrix_SV


            % Check Transmission Coefficient
            Abs_Tsv(k:k,ls:ls) = abs(Tsv(k:k,ls:ls)) ;


        end ;
        disp(strcat('Loading Step: ', num2str(ls),'{ }', 'Iteration: ', num2str(iteration))) ;


    end ;


end ;


% Transmission Coefficient
Abs_Rp = abs(Rp) ;
Abs_Rsv = abs(Rsv) ;
Abs_Tp = abs(Tp) ;
Abs_Tsv = abs(Tsv) ;


E_Check_SV_I =(((ZP1./ZS1).*cos(RA_P))./cos(RA_SV)).*Abs_Rp.^2 +
Abs_Rsv.^2 + (((ZP2./ZS1).*cos(TA_P))./cos(RA_SV)).*Abs_Tp.^2 +
((ZS2./ZS1).*(cos(TA_SV))./cos(RA_SV)).*Abs_Tsv.^2 ;
```

```
        xlswrite(strcat(prefix,'Tr_Co_Prdt_',num2str(abs(ch)),'to',
num2str(abs(ch))  ),Abs_Tsv,  strcat(prefix,'Tr_Co_Prdt_',num2str(abs(ch)),'to',
num2str(abs(ch)) ), 'B2');
        xlswrite(strcat(prefix,'Tr_Co_Prdt_',num2str(abs(ch)),'to',  num2str(abs(ch))  ),Freq,
strcat(prefix,'Tr_Co_Prdt_',num2str(abs(ch)),'to', num2str(abs(ch)) ), 'A2');
        xlswrite(strcat(prefix,'Stiff_',num2str(abs(ch)),'to',  num2str(abs(ch))  ),K_z,
strcat(prefix,'Stiff_',num2str(abs(ch)),'to', num2str(abs(ch)) ), 'B2');
        xlswrite(strcat(prefix,'Stiff_',num2str(abs(ch)),'to',  num2str(abs(ch))  ),Freq,
strcat(prefix,'Stiff_',num2str(abs(ch)),'to', num2str(abs(ch)) ), 'A2');

    % Channel SH-Incident
    elseif ch==4 || ch==7 ;
        disp(strcat (num2str(ch),'SH-', num2str(ch), 'SH')) ;
        for ls=1:1:NofL ;
%           disp(strcat('Loading Step: ',num2str(ls))) ;
            for k=1:1:s_w(1) ;

                if k==1
                    % Initial Stiffness for iteration
                    K_y(k:k,ls:ls)  = 10^12 ;
                else
                    % Initial Stiffness for iteration
                    K_y(k:k,ls:ls)  = K_y(k-1:k-1,ls:ls) ;
```

```
    if K_y(k:k,ls:ls) >= K_max
       K_y(k:k,ls:ls)  = 0.9*K_max ;
    else
       % Initial Stiffness for iteration
       K_y(k:k,ls:ls)  = K_y(k-1:k-1,ls:ls) ;
    end ;

end ;

% Call Solution matrix for SV-incident
Solution_Matrix_SH

% Check Transmission Coefficient
Abs_Tsh(k:k,ls:ls) = abs(Tsh(k:k,ls:ls)) ;

iteration = 1;
while abs( (Abs_Tsh(k:k,ls:ls)-temp33(k:k,ls:ls))/temp33(k:k,ls:ls) ) >=
Tolerance/100

    if K_y(k:k,ls:ls) > K_max ;
       disp('K > Kmax' ) ;
       break ;
    end ;
```

```
        iteration = iteration +1 ;

        if Abs_Tsh(k:k,ls:ls) > temp33(k:k,ls:ls) ;
           K_y(k:k,ls:ls) = 0.96 * K_y(k:k,ls:ls) ;
        elseif Abs_Tsh(k:k,ls:ls) < temp33(k:k,ls:ls) ;
           K_y(k:k,ls:ls) = 1.04 * K_y(k:k,ls:ls) ;
        end ;

        % Call Solution matrix for SV-incident
        Solution_Matrix_SH

        % Check Transmission Coefficient
        Abs_Tsh(k:k,ls:ls) = abs(Tsh(k:k,ls:ls)) ;

      end ;
      disp(strcat('Loading Step: ', num2str(ls),'{ }', 'Iteration: ', num2str(iteration))) ;

   end ;

end ;

% Transmission Coefficient
Abs_Rsh = abs(Rsh) ;
```

```
        Abs_Tsh = abs(Tsh) ;

        E_Check_SH_I = Abs_Rsh.^2 +
(((ZS2./ZS1).*cos(TA_SH))./cos(RA_SH)).*Abs_Tsh.^2 ;

        xlswrite(strcat(prefix,'Tr_Co_Prdt_',num2str(abs(ch)),'to',
num2str(abs(ch)) ),Abs_Tsh, strcat(prefix,'Tr_Co_Prdt_',num2str(abs(ch)),'to',
num2str(abs(ch)) ), 'B2');
        xlswrite(strcat(prefix,'Tr_Co_Prdt_',num2str(abs(ch)),'to',  num2str(abs(ch))  ),Freq,
strcat(prefix,'Tr_Co_Prdt_',num2str(abs(ch)),'to', num2str(abs(ch)) ), 'A2');
        xlswrite(strcat(prefix,'Stiff_',num2str(abs(ch)),'to', num2str(abs(ch)) ),K_y,
strcat(prefix,'Stiff_',num2str(abs(ch)),'to', num2str(abs(ch)) ), 'B2');
        xlswrite(strcat(prefix,'Stiff_',num2str(abs(ch)),'to', num2str(abs(ch)) ),Freq,
strcat(prefix,'Stiff_',num2str(abs(ch)),'to', num2str(abs(ch)) ), 'A2');

    % Channel P-Incident
    elseif ch==3 || ch==6 ;
        disp(strcat (num2str(ch),'P-', num2str(ch), 'P')) ;
        for ls=1:1:NofL ;
%           disp(strcat('Loading Step: ',num2str(ls))) ;
            for k=1:1:s_w(1) ;

                if k==1
```

```
    % Initial Stiffness for iteration
    K_z(k:k,ls:ls)  = 10^12 ;
else
    % Initial Stiffness for iteration
    K_z(k:k,ls:ls)  = K_z(k-1:k-1,ls:ls) ;
    if K_z(k:k,ls:ls) >= K_max
        K_z(k:k,ls:ls)  = 0.9*K_max ;
    else
        % Initial Stiffness for iteration
        K_z(k:k,ls:ls)  = K_z(k-1:k-1,ls:ls) ;
    end ;

end ;

K_x(k:k,ls:ls) = Ratio * K_z(k:k,ls:ls) ;
% Call Solution matrix for SV-incident
Solution_Matrix_P

% Check Transmission Coefficient
Abs_Tp(k:k,ls:ls) = abs(Tp(k:k,ls:ls)) ;

iteration = 1;
```

```
        while abs( (Abs_Tp(k:k,ls:ls)-temp33(k:k,ls:ls))/temp33(k:k,ls:ls) ) >=
Tolerance/100
            if K_z(k:k,ls:ls) > K_max ;
               disp('K > Kmax' ) ;
               break ;
            end ;
            iteration = iteration +1 ;

            if Abs_Tp(k:k,ls:ls) > temp33(k:k,ls:ls) ;
               K_z(k:k,ls:ls) = 0.96 * K_z(k:k,ls:ls) ;
            elseif Abs_Tp(k:k,ls:ls) < temp33(k:k,ls:ls) ;
               K_z(k:k,ls:ls) = 1.04 * K_z(k:k,ls:ls) ;
            end ;

            K_x(k:k,ls:ls) = Ratio * K_z(k:k,ls:ls) ;

            % Call Solution matrix for SV-incident
            Solution_Matrix_P

            % Check Transmission Coefficient
            Abs_Tp(k:k,ls:ls) = abs(Tp(k:k,ls:ls)) ;

        end ;
```

```
        disp(strcat('Loading Step: ', num2str(ls),'{ }', 'Iteration: ', num2str(iteration))) ;

    end ;

end ;

% Transmission Coefficient
Abs_Rp = abs(Rp) ;
Abs_Rsv = abs(Rsv) ;
Abs_Tp = abs(Tp) ;
Abs_Tsv = abs(Tsv) ;

E_Check_P_I = Abs_Rp.^2 + ((ZS1./ZP1).*(cos(RA_SV)./cos(RA_P))).*Abs_Rsv.^2 + (((ZP2./ZP1).*cos(TA_P))./cos(RA_P)).*Abs_Tp.^2 + (ZS2./ZP1).*((cos(TA_SV)./cos(RA_P))).*Abs_Tsv.^2 ;

xlswrite(strcat(prefix,'Tr_Co_Prdt_',num2str(abs(ch)),'to', num2str(abs(ch)) ),Abs_Tp, strcat(prefix,'Tr_Co_Prdt_',num2str(abs(ch)),'to', num2str(abs(ch)) ), 'B2');
xlswrite(strcat(prefix,'Tr_Co_Prdt_',num2str(abs(ch)),'to', num2str(abs(ch)) ),Freq, strcat(prefix,'Tr_Co_Prdt_',num2str(abs(ch)),'to', num2str(abs(ch)) ), 'A2');
```

```
    xlswrite(strcat(prefix,'Stiff_',num2str(abs(ch)),'to',  num2str(abs(ch))  ),K_z,
strcat(prefix,'Stiff_',num2str(abs(ch)),'to', num2str(abs(ch)) ), 'B2');
    xlswrite(strcat(prefix,'Stiff_',num2str(abs(ch)),'to',  num2str(abs(ch))  ),Freq,
strcat(prefix,'Stiff_',num2str(abs(ch)),'to', num2str(abs(ch)) ), 'A2');

  end ;

  k=1 ;
  for i =1:1:NofL/4

    Normal_Str = (i) * 1.89; %Unit MPa)
    header = cellstr(strcat(num2str(Normal_Str,3))) ;

    Header(1:1,k:k+3) = header ;
    k=k+4 ;

  end ;

  if ch==3 || ch==6 || ch==1 || ch==2 || ch==5 ;
    K_N = K_z ;
    K_S = K_x ;
    Ext_Freq = [51, 83] ;
    Top_str = [ cellstr('Normal Stress (MPa)'), cellstr('0.3MHz'), cellstr('0.5MHz') ] ;
```

```
        xlswrite(strcat(prefix,'Ex_Kx_',num2str(abs(ch)),'to',
num2str(abs(ch))),K_S(Ext_Freq(1):Ext_Freq(1),:)',
strcat(prefix,'Ex_Kx_',num2str(abs(ch)),'to', num2str(abs(ch))), 'B2') ;
        xlswrite(strcat(prefix,'Ex_Kx_',num2str(abs(ch)),'to',
num2str(abs(ch))),K_S(Ext_Freq(2):Ext_Freq(2),:)',
strcat(prefix,'Ex_Kx_',num2str(abs(ch)),'to', num2str(abs(ch))), 'C2') ;
        xlswrite(strcat(prefix,'Ex_Kz_',num2str(abs(ch)),'to',
num2str(abs(ch))),K_N(Ext_Freq(1):Ext_Freq(1),:)',
strcat(prefix,'Ex_Kz_',num2str(abs(ch)),'to', num2str(abs(ch))), 'B2') ;
        xlswrite(strcat(prefix,'Ex_Kz_',num2str(abs(ch)),'to',
num2str(abs(ch))),K_N(Ext_Freq(2):Ext_Freq(2),:)',
strcat(prefix,'Ex_Kz_',num2str(abs(ch)),'to', num2str(abs(ch))), 'C2') ;
        xlswrite(strcat(prefix,'Ex_Kx_',num2str(abs(ch)),'to',      num2str(abs(ch))),Top_str,
strcat(prefix,'Ex_Kx_',num2str(abs(ch)),'to', num2str(abs(ch))), 'A1') ;
        xlswrite(strcat(prefix,'Ex_Kx_',num2str(abs(ch)),'to',      num2str(abs(ch))),Header',
strcat(prefix,'Ex_Kx_',num2str(abs(ch)),'to', num2str(abs(ch))), 'A2') ;
        xlswrite(strcat(prefix,'Ex_Kz_',num2str(abs(ch)),'to',      num2str(abs(ch))),Top_str,
strcat(prefix,'Ex_Kz_',num2str(abs(ch)),'to', num2str(abs(ch))), 'A1') ;
        xlswrite(strcat(prefix,'Ex_Kz_',num2str(abs(ch)),'to',      num2str(abs(ch))),Header',
strcat(prefix,'Ex_Kz_',num2str(abs(ch)),'to', num2str(abs(ch))), 'A2') ;

    elseif ch==4 || ch==7 ;
        K = K_y ;
```

```
        Ext_Freq = [51] ;
        Top_str = [ cellstr('Normal Stress (MPa)'), cellstr('0.3MHz')] ;
        xlswrite(strcat(prefix,'Ex_Ky_',num2str(abs(ch)),'to',
num2str(abs(ch))),K(Ext_Freq(1):Ext_Freq(1),:)',
strcat(prefix,'Ex_Ky_',num2str(abs(ch)),'to', num2str(abs(ch))), 'B2') ;
        xlswrite(strcat(prefix,'Ex_Ky_',num2str(abs(ch)),'to',       num2str(abs(ch))),Top_str,
strcat(prefix,'Ex_Ky_',num2str(abs(ch)),'to', num2str(abs(ch))), 'A1') ;
        xlswrite(strcat(prefix,'Ex_Ky_',num2str(abs(ch)),'to',       num2str(abs(ch))),Header',
strcat(prefix,'Ex_Ky_',num2str(abs(ch)),'to', num2str(abs(ch))), 'A2') ;

    end ;

    % Empty variables
    temp_int_vel = [];
    VS1 = [];
    VS2 = [];
    VP1 = [];
    VP2 = [];
    K_N = [];
    K_S = [];
    K = [];

end ;
```

Appendix B Matalb Code for Aperture Distribution

```
%Load the scanning data
load AL_GS01os.txt ; %GS02 sample without slits
load AL_GS01s.txt ; %GS02 sample with slits

Sample_name = 'AL_GS01' ;

%Hand over the measurement data to Raw_os and Raw_s matrix
Raw_os = AL_GS01os ;
Raw_s = AL_GS01s ;

% Calibration factor to transform voltage to height
VtoH = 0.9969 ;

%Step size (units : mm) for surface scanning
Inc_S = 0.25 ;

% Number of data in X- & Y- direction
Col = 400 ; % X- direction
Row = 458 ; % Y- direaction
T_num = Col * Row ;
```

```
% Transpose the input matrix
Raw_osT = Raw_os' ;
Raw_sT = Raw_s' ;

% Divide into x-, y-, z- coordination
X_Raw_osT = Raw_osT(1:1 , 1:T_num)'  ;% X- coordinate
Y_Raw_osT = Raw_osT(2:2 , 1:T_num)'  ;% Y- coordinate
Z_Raw_osT = VtoH * Raw_osT(3:3 , 1:T_num)'  ;% Z- coordinate (Voltage -> Height)

X_Raw_sT = Raw_sT(1:1 , 1:T_num)'  ;% X- coordinate
Y_Raw_sT = Raw_sT(2:2 , 1:T_num)'  ;% Y- coordinate
Z_Raw_sT = VtoH * Raw_sT(3:3 , 1:T_num)'  ;% Z- coordinate (Voltage -> Height)

% Find "NaN" & change to 'average value' of two points adjacent to it or to min.
i = find (isnan(Z_Raw_osT));
[a1, a2] = size(i) ;
% if i(a1) == T_num ;
%     Z_Raw_osT(T_num) = 0 ;
% end ;
Z_Raw_osT_int = Z_Raw_osT ;
i = find (isnan(Z_Raw_osT));
Z_Raw_osT_int (i) = (Z_Raw_osT (i-1) + Z_Raw_osT (i+1))/2 ; % interpolation
j = find (isnan(Z_Raw_osT_int));
```

```
Z_Raw_osT_int (j) = min(min(Z_Raw_osT)) ; % change NaN with Zero
% Z_Raw_osT_int (j) = min(Z_Raw_osT_int) ;

ii = find (isnan(Z_Raw_sT));
[b1, b2] = size(ii) ;
% if ii(b1) == T_num ;
%     Z_Raw_sT(T_num) = 0 ;
% end ;
Z_Raw_sT_int = Z_Raw_sT ;
ii = find (isnan(Z_Raw_sT));
Z_Raw_sT_int (ii) = (Z_Raw_sT (ii-1) + Z_Raw_sT (ii+1))/2 ; % interpolation
jj = find (isnan(Z_Raw_sT_int));
Z_Raw_sT_int (jj) = min(min(Z_Raw_sT)) ;  % change NaN with Zero
% Z_Raw_sT_int (j) = min(Z_Raw_sT_int) ;

% Transform into 2-d matrix form
Re_Z_Raw_osT_int = reshape (Z_Raw_osT_int, Row, Col) ;
Re_Z_Raw_sT_int = reshape (Z_Raw_sT_int, Row, Col) ;

Diff_osT = zeros(Row, Col) ;
Diff_sT = zeros(Row, Col) ;

%Calculated the difference from the adjacent data.
```

```
iCol = 1 ;

while iCol <= Col;

   iRow = 1 ;

   while iRow <= Row-1;
      Diff_osT(iRow+1, iCol) = (Re_Z_Raw_osT_int (iRow, iCol) - Re_Z_Raw_osT_int
(iRow+1, iCol)) ;
      Diff_sT(iRow+1, iCol) = (Re_Z_Raw_sT_int (iRow, iCol) - Re_Z_Raw_sT_int
(iRow+1, iCol)) ;

      iRow = iRow + 1 ;
   end;

  iCol = iCol + 1 ;

end ;

% Stard deviation and average of the difference from the adjacent data
std_osT = std( reshape (Diff_osT, T_num, 1) );
std_sT = std ( reshape (Diff_sT, T_num, 1) );
avg_osT = mean ( reshape (Diff_osT, T_num, 1) ) ;
```

```
avg_sT = mean ( reshape (Diff_sT, T_num, 1) ) ;

% Find abnormally large or small data and interpolate it with the adjacent
% data.

iCol = 1 ;

while iCol <= Col;

   iRow = 1 ;

   while iRow <= Row-1;
      if ( (Diff_osT(iRow, iCol) >= ( avg_osT + 1 * std_osT)) || (Diff_osT(iRow, iCol) <=
( avg_osT - 1 * std_osT)) );
        Re_Z_Raw_osT_int (iRow, iCol) = (Re_Z_Raw_osT_int(iRow-1, iCol) +
Re_Z_Raw_osT_int(iRow+1, iCol))/2 ;
      end ;
      if ( (Diff_sT(iRow, iCol) >= (avg_osT + 1 * std_osT)) || (Diff_sT(iRow, iCol) <=
(avg_osT - 1 * std_osT)) );
        Re_Z_Raw_sT_int (iRow, iCol) = (Re_Z_Raw_sT_int(iRow-1, iCol) +
Re_Z_Raw_sT_int(iRow+1, iCol))/2 ;
      end;
```

```
        iRow = iRow + 1 ;
    end;
    iCol = iCol + 1 ;
end ;

Z_Raw_osT_int = reshape (Re_Z_Raw_osT_int, T_num, 1) ;
Z_Raw_sT_int = reshape (Re_Z_Raw_sT_int, T_num, 1) ;

% Export to txt file.
osT = [ X_Raw_osT Y_Raw_osT Z_Raw_osT_int ] ;
sT = [ X_Raw_sT Y_Raw_sT Z_Raw_sT_int ] ;

% Set the minimum value and change the origing point for plotting
Re_Z_Raw_osT_int = Re_Z_Raw_osT_int - min(min(Re_Z_Raw_osT_int));
Re_Z_Raw_sT_int = Re_Z_Raw_sT_int - min(min(Re_Z_Raw_sT_int));

s = strcat(Sample_name,'os_NaN', '.txt') ;
fid = fopen (s, 'w') ;
fprintf(fid, '%f  %f  %f\r\n',osT');
status = fclose(fid);

% Plot the roughness by using "imagesc" function.
hFig = figure(1);
```

```
set(hFig, 'Position', [100 100 Col+100 Row])


imagesc(X_Raw_osT, Y_Raw_osT, Re_Z_Raw_osT_int) ;
colorbar ;
set(gca,'YDir','normal') ;
title(strcat(Sample_name, {' '},'without slits'  )) ;
xlabel('X-Axis (mm)') ;
ylabel('Y-Axis (mm)') ;
% axis([0 Inc_S*Col 0 Inc_S*Row])
fn = strcat(Sample_name,'os_NaN', '.fig') ;
saveas(gcf, fn);
fn = strcat(Sample_name,'os_NaN', '.jpg') ;
saveas(gcf, fn);

% Export to txt file.
s = strcat(Sample_name,'s_NaN', '.txt') ;
fid = fopen (s, 'w') ;
fprintf(fid, '%f  %f  %f\r\n',sT');
status = fclose(fid);

% Plot the roughness by using "imagesc" function.
hFig = figure(2);
set(hFig, 'Position', [100 100 Col+100 Row])
```

```
imagesc(X_Raw_sT, Y_Raw_sT, Re_Z_Raw_sT_int) ;
colorbar ;
set(gca,'YDir','normal') ;
title(strcat(Sample_name, {' '},'with slits'  )) ;
xlabel('X-Axis (mm)') ;
ylabel('Y-Axis (mm)') ;
% axis([0 Inc_S*Col 0 Inc_S*Row])
fn = strcat(Sample_name,'s_NaN', '.fig') ;
saveas(gcf, fn);
fn = strcat(Sample_name,'s_NaN', '.jpg') ;
saveas(gcf, fn);

%Load the scanning data
load AL_GS01s_NaN.txt ; %GS02 sample without slits

SampNm = 'AL_GS01' ;
Raw_s = AL_GS01s_NaN ;
Raw_sT = Raw_s' ;

% Number of data in X- & Y- direction
Col = 400 ; % X- direction
Row = 458 ; % Y- direaction
```

```
T_num = Col * Row ;

Stepsize = 0.25 ;


% area surrounded by slits --> surface with slits

j_b = 64 ; % the first column

j_e = 337 ; % the last column

i_b = 38 ; % the first row

i_e = 400 ; % the last row


%Set the origin of coordinates system

X_Sht = Raw_sT(1:1 , :)' - Col*Stepsize/2;

Y_Sht = Raw_sT(2:2 , :)' - Row*Stepsize/2;

Z_Sht = Raw_sT(3:3 , :)';


Sht_s = [ X_Sht Y_Sht Z_Sht ];

Sht_sT = Sht_s' ;


%Prepare the interpolation with scanned step size

X = Sht_sT(1:1 , :)' ;

Y = Sht_sT(2:2 , :)' ;

Z = Sht_sT(3:3 , :)' ;


X_re = reshape(X, Row, Col);
```

```
Y_re = reshape(Y, Row, Col);

Z_re = reshape(Z, Row, Col);


% Find every rotation in X direction from every column

kk = 1;

for i = ( j_b : 1 : j_e);


   p_x = polyfit( Y_re( i_b:i_e , i:i),Z_re( i_b:i_e , i:i ) , 1 );

   Output_x = polyval(p_x,Y_re( i_b:i_e , i:i));

   %Correlation_x = corrcoef(Z_re( : , i:i ), Output_x);

   m_x = 180/pi* atan (p_x(1,1)) ; % radians to degres

   slope_X_s(:, kk:kk ) = m_x ;

   kk = kk+1;


end;


% Find every rotation in Y direction from every row

kk = 1;

for j = ( i_b : 1 : i_e);


   p_y = polyfit( X_re( j:j , j_b:j_e),Z_re( j:j , j_b:j_e ) , 1 );

   Output_y = polyval(p_y,X_re( j:j , j_b:j_e));

   %Correlation_y = corrcoef(Z_re( : , i:i ), Output_y);
```

```
   m_y = 180/pi* atan (p_y(1,1)) ;
   slope_Y_s(kk:kk, : ) = m_y ;
   kk = kk+1 ;
end;

% Find average slope in x- & y- dir.

   temp_slp_X = 180/pi* atan( (mean(Z_re(i_e:i_e,j_b:j_e)) -
mean(Z_re(i_b:i_b,j_b:j_e)) )/((i_e-i_b)*Stepsize)) ;
   temp_slp_Y = 180/pi* atan( (mean(Z_re(i_b:i_e,j_e:j_e)) -
mean(Z_re(i_b:i_e,j_b:j_b)) )/((j_e-j_b)*Stepsize)) ;

   Avg_slope_X_s = temp_slp_X ;
   Avg_slope_Y_s = temp_slp_Y ;

% Defind rotation angle
i = -Avg_slope_X_s ; % x-dir. rotation angle
j = Avg_slope_Y_s ; % y-dir. rotation angle
k = 0; % z-dir. rotation angle

% X- & Y- dir. rotation

   CosPhi = cos(i*pi/180);
```

```
CosTheta = cos(j*pi/180);

CosPsi = cos(k*pi/180);

SinPhi = sin(i*pi/180);

SinTheta = sin(j*pi/180);

SinPsi = sin(k*pi/180);


Rm = zeros(3, 3);

Rm(1, 1) = CosTheta*CosPsi;

Rm(1, 2) = SinPhi*SinTheta*CosPsi - CosPhi*SinPsi;

Rm(1, 3) = CosPhi*SinTheta*CosPsi + SinPhi*SinPsi;

Rm(2, 1) = CosTheta*SinPsi;

Rm(2, 2) = SinPhi*SinTheta*SinPsi + CosPhi*CosPsi;

Rm(2, 3) = CosPhi*SinTheta*SinPsi - SinPhi*CosPsi;

Rm(3, 1) = -SinTheta;

Rm(3, 2) = SinPhi*CosTheta;

Rm(3, 3) = CosPhi*CosTheta;


% Rotate the scanned data

Rot_sT = Rm * Sht_sT ;


Rot_s = Rot_sT' ;


%Prepare the interpolation with scanned step size
```

```
X = Rot_sT(1:1 , :)' ;

Y = Rot_sT(2:2 , :)' ;

Z = Rot_sT(3:3 , :)' ;


X_re = reshape(X, Row, Col);

Y_re = reshape(Y, Row, Col);

Z_re = reshape(Z, Row, Col);


% Interpolation function

F = TriScatteredInterp(X,Y,Z);


xi = (Stepsize - Col*Stepsize/2)  : Stepsize : (Col*Stepsize/2) ;

yi = (Stepsize - Row*Stepsize/2)  : Stepsize : (Row*Stepsize/2) ;

[qx,qy] = meshgrid(xi,yi);


Z_int = F(qx,qy);


% Find "NaN" & set it zero

nan = find (isnan(Z_int));

Z_int (nan) = min(min(Z_int)) ; % change NaN with Zero


sT = [ reshape(qx, T_num, 1), reshape(qy, T_num, 1), reshape(Z_int, T_num, 1)];
```

```
% Export to txt file
s = strcat( SampNm, 's_NaN_rot.txt') ;

fid = fopen (s, 'w');
fprintf(fid, '%f  %f  %f\r\n',sT');

% Plot the roughness by using "imagesc" function.

Z_int = Z_int - min(min(Z_int));

X_Raw_sT = Raw_sT(1:1 , 1:T_num)'  ;% X- coordinate
Y_Raw_sT = Raw_sT(2:2 , 1:T_num)'  ;% Y- coordinate

hFig = figure(1);
set(hFig, 'Position', [100 100 Col+100 Row])

imagesc( X_Raw_sT, Y_Raw_sT, Z_int ) ;
colorbar ;
set(gca,'YDir','normal') ;
title(strcat('Rotated', {' '}, SampNm, {' '},'with slits') );
xlabel('X-Axis (mm)') ;
ylabel('Y-Axis (mm)') ;
% axis([0 Inc_S*Col 0 Inc_S*Row])
```

```
    fn = strcat(s, '.fig') ;
    saveas(gcf, fn);
    fn = strcat(s, '.jpg') ;
    saveas(gcf, fn);

% Clipped area

    Clipped_Z_int = Z_int(i_b:i_e, j_b:j_e) ;
    Clipped_Z_int = Clipped_Z_int - min(min(Clipped_Z_int));

    x_coordi = (j_b*Stepsize : Stepsize : j_e*Stepsize);
    y_coordi = (i_b*Stepsize : Stepsize : i_e*Stepsize);

    imagesc( x_coordi, y_coordi, Clipped_Z_int ) ;
    colorbar ;
    set(gca,'YDir','normal') ;
    title(strcat('Clipped & Rotated', {' '}, SampNm, {' '},'with slits') );
    xlabel('X-Axis (mm)') ;
    ylabel('Y-Axis (mm)') ;
    % axis([0 Inc_S*Col 0 Inc_S*Row])
    Clip_s = strcat( 'Clipped_', SampNm, 's_NaN_rot') ;
    fn = strcat(Clip_s, '.fig') ;
    saveas(gcf, fn);
```

```
    fn = strcat(Clip_s, '.jpg') ;
    saveas(gcf, fn);

    Real_Avg_slope_Y_s = -Avg_slope_Y_s ;
    save ( 'S_Avg_Rot_X.mat', 'Avg_slope_X_s');
    save ( 'S_Avg_Rot_Y.mat', 'Real_Avg_slope_Y_s');

%Load the scanning data
load AL_GS01os_NaN.txt ; %GS04 sample without slits

SampNm = 'AL_GS01' ;

Raw_os = AL_GS01os_NaN ;

Raw_osT = Raw_os' ;

% Number of data in X- & Y- direction
Col = 400 ; % X- direction
Row = 458 ; % Y- direaction
T_num = Col * Row ;

Stepsize = 0.25 ;
```

```
By_rng = 15 ;

Bx_rng = 15 ;


% area surrounded by slits --> surface with slits

j_b = 64 ; % the first column

j_e = 337 ; % the last column

i_b = 38 ; % the first row

i_e = 400 ; % the last row


%Set the origin of coordinates system

X_Sht = Raw_osT(1:1 , :)' - Col*Stepsize/2;

Y_Sht = Raw_osT(2:2 , :)' - Row*Stepsize/2;

Z_Sht = Raw_osT(3:3 , :)';


Sht_os = [ X_Sht Y_Sht Z_Sht ];

Sht_osT = Sht_os' ;


%Prepare the interpolation with scanned step size

X = Sht_osT(1:1 , :)' ;

Y = Sht_osT(2:2 , :)' ;

Z = Sht_osT(3:3 , :)' ;


X_re = reshape(X, Row, Col);
```

```
Y_re = reshape(Y, Row, Col);

Z_re = reshape(Z, Row, Col);


% Find every rotation in X direction from every column

kk=1;

for i = ( Col-j_e-Bx_rng : 1 : Col-j_b+Bx_rng);


   p_x = polyfit( Y_re( i_b-By_rng:i_e+By_rng , i:i),Z_re( i_b-By_rng:i_e+By_rng , i:i ) ,
1 );

   Output_x = polyval(p_x,Y_re( i_b-By_rng:i_e+By_rng , i:i));

   %Correlation_x = corrcoef(Z_re( : , i:i ), Output_x);

   m_x = 180/pi* atan (p_x(1,1)) ; % radians to degres

   slope_X_os(:, kk:kk ) = m_x ;

   kk = kk+1;


end;


% Find every rotation in Y direction from every row

kk=1;

for j = ( i_b-By_rng : 1 : i_e+By_rng);


   p_y = polyfit( X_re( j:j , Col-j_e-Bx_rng:Col-j_b+Bx_rng),Z_re( j:j , Col-j_e-
Bx_rng:Col-j_b+Bx_rng ) , 1 );
```

```
    Output_y = polyval(p_y,X_re( j:j , Col-j_e-Bx_rng:Col-j_b-Bx_rng));
    %Correlation_y = corrcoef(Z_re( : , i:i ), Output_y);
    m_y = 180/pi* atan (p_y(1,1)) ;
    slope_Y_os(kk:kk, : ) = m_y ;
    kk=kk+1 ;

end;

% Find average slope in x- & y- dir.

    temp_slp_X = 180/pi* atan( (mean(Z_re(i_e:i_e,j_b:j_e)) -
mean(Z_re(i_b:i_b,j_b:j_e)) )/((i_e-i_b)*Stepsize)) ;
    temp_slp_Y = 180/pi* atan( (mean(Z_re(i_b:i_e,j_e:j_e)) -
mean(Z_re(i_b:i_e,j_b:j_b)) )/((j_e-j_b)*Stepsize)) ;

    Avg_slope_X_os = temp_slp_X ;
    Avg_slope_Y_os = temp_slp_Y ;

% Defind rotation angle
i = -Avg_slope_X_os ; % x-dir. rotation angle
j = Avg_slope_Y_os ; % y-dir. rotation angle
k = 0; % z-dir. rotation angle
```

```
% X- & Y- dir. rotation

    CosPhi = cos(i*pi/180);
    CosTheta = cos(j*pi/180);
    CosPsi = cos(k*pi/180);
    SinPhi = sin(i*pi/180);
    SinTheta = sin(j*pi/180);
    SinPsi = sin(k*pi/180);

    Rm = zeros(3, 3);
    Rm(1, 1) = CosTheta*CosPsi;
    Rm(1, 2) = SinPhi*SinTheta*CosPsi - CosPhi*SinPsi;
    Rm(1, 3) = CosPhi*SinTheta*CosPsi + SinPhi*SinPsi;
    Rm(2, 1) = CosTheta*SinPsi;
    Rm(2, 2) = SinPhi*SinTheta*SinPsi + CosPhi*CosPsi;
    Rm(2, 3) = CosPhi*SinTheta*SinPsi - SinPhi*CosPsi;
    Rm(3, 1) = -SinTheta;
    Rm(3, 2) = SinPhi*CosTheta;
    Rm(3, 3) = CosPhi*CosTheta;

    % Rotate the scanned data
    Rot_osT = Rm * Sht_osT ;
```

```
Rot_os = Rot_osT' ;

%Prepare the interpolation with scanned step size
X = Rot_osT(1:1 , :)' ;
Y = Rot_osT(2:2 , :)' ;
Z = Rot_osT(3:3 , :)' ;

X_re = reshape(X, Row, Col);
Y_re = reshape(Y, Row, Col);
Z_re = reshape(Z, Row, Col);

% Interpolation function
F = TriScatteredInterp(X,Y,Z);

xi = (Stepsize - Col*Stepsize/2)  : Stepsize : (Col*Stepsize/2) ;
yi = (Stepsize - Row*Stepsize/2)  : Stepsize : (Row*Stepsize/2) ;
[qx,qy] = meshgrid(xi,yi);

Z_int = F(qx,qy);

% Find "NaN" & set it zero
nan = find (isnan(Z_int));
Z_int (nan) = min(min(Z_int)) ; % change NaN with Zero
```

```
osT = [ reshape(qx, T_num, 1), reshape(qy, T_num, 1), reshape(Z_int, T_num, 1)];

% Export to txt file
s = strcat( SampNm, 'os_NaN_rot.txt') ;

fid = fopen (s, 'w');
fprintf(fid, '%f  %f  %f\r\n',osT');

% Plot the roughness by using "imagesc" function.

Z_int = Z_int - min(min(Z_int));

X_Raw_osT = Raw_osT(1:1 , 1:T_num)'  ;% X- coordinate
Y_Raw_osT = Raw_osT(2:2 , 1:T_num)'  ;% Y- coordinate

hFig = figure(1);
set(hFig, 'Position', [100 100 Col+100 Row])

imagesc( X_Raw_osT, Y_Raw_osT, Z_int ) ;
colorbar ;
set(gca,'YDir','normal') ;
title(strcat('Rotated', {' '}, SampNm, {' '},'without slits')) ;
```

```
    xlabel('X-Axis (mm)') ;
    ylabel('Y-Axis (mm)') ;
    % axis([0 Inc_S*Col 0 Inc_S*Row])
    fn = strcat(s, '.fig') ;
    saveas(gcf, fn);
    fn = strcat(s, '.jpg') ;
    saveas(gcf, fn);

    Real_Avg_slope_Y_os = -Avg_slope_Y_os ;
    save ( 'OS_Avg_Rot_X.mat', 'Avg_slope_X_os');
    save ( 'OS_Avg_Rot_Y.mat', 'Real_Avg_slope_Y_os');

SampNm2 = 'AL_GS01' ; % sample data with slits

% area surrounded by slits --> surface with slits
j_b = 64 ; % the first column
j_e = 337 ; % the last column
i_b = 38 ; % the first row
i_e = 400 ; % the last row

% Number of data in X- & Y- direction
Col = 400 ; % X- direction
Row = 458 ; % Y- direaction
```

```
T_num = Col * Row ;


Stepsize = 0.25 ;

By_rng = 15 ; %25

Bx_rng = 15 ; %20


%Define Z-dir. Maximum & Minimum rotation angles and its rotation increment

Min_Z_rot = -2.50 ;

Max_Z_rot = +2.50 ;

d_inc = 0.25 ;


%Import the data file rotated in x- & y- dir.

s2 = strcat(SampNm2, 's_NaN_rot.txt') ; % sample with slits


% Prepare matrix A & B for cross-correlation

% A : sample with slits

% B : sample without slits


fid2 = fopen (s2);

A = fscanf( fid2, '%f', [ 3, T_num ] ) ; % Z-coordinate values of the sample with slits

A = A' ;

AT = A' ;
```

```
% Z- coordinate

A_Z = AT(3:3 , :)' ;


% Transform to 2-D matrix form

A_re_Z = reshape (A_Z, Row, Col) ;


% Extract the area surrounded by slits

A_sub = A_re_Z (i_b:i_e, j_b:j_e) ;


% Inverse the column order from right to left & multiply (-1)

A_fl = -1 * fliplr (A_sub) ;


%Find the minimum & maximum values of matrix

A_mn = min(A_fl) ;

A_min = min(A_mn) ;


%Re-Set reference level of A_fl : make all the values to be positive

AA = A_fl - A_min ;


% Load the surface scanning data of the sample without slits


   s = strcat(SampNm2, 'os_NaN_rot.txt') ; % sample without slits
```

```
fid = fopen (s);
B = fscanf( fid, '%f', [ 3, T_num ] ) ; % Z-coordinate values of the sample without slits

%Prepare matrix B for cross-correlation

% Transform to 2-D matrix form
B_X = B(1:1 , 1:T_num)' ; % X- coordinate
B_Y = B(2:2 , 1:T_num)' ; % Y- coordinate
B_Z = B(3:3 , 1:T_num)' ; % Z- coordinate

B_re_X = reshape (B_X, Row, Col);
B_re_Y = reshape (B_Y, Row, Col);
B_re_Z = reshape (B_Z, Row, Col);

% Reset the area of B
%    B_sub = B_re_Z ((i_b-B_rng):(i_e+B_rng), (Col-j_e-B_rng):(Col-j_b+B_rng)) ;
%                B_sub = B_re_Z ((i_b-1*By_rng):(i_e+1*By_rng), (j_b-1*Bx_rng):(j_e+1*Bx_rng)) ;
   B_sub = B_re_Z ((i_b-1*By_rng):(i_e+1*By_rng), (Col-j_e-1*Bx_rng):(Col-j_b+1*Bx_rng)) ;
%    B_sub = B_re_Z  ;

%Find the minimum & maximum values of matrix
```

```
B_mn = min(B_sub) ;

B_min = min(B_mn) ;


%Re-Set reference level of B_re_Z : make all the values to be positive

BB = B_sub - B_min ;


%Cross-Correlation function

CC0 = xcorr2(AA,BB) ;


%Find the maximum value of CC

CC_mx = max(CC0) ;

CC_mxm = max(CC_mx) ;


CC_Zrot0 = CC_mxm ;


B_mx = max(BB) ;

B_mxm = max(B_mx) ;


% Extract sub-matrix of BB

   % r = row when CC is maximum

   % c = column when CC is maximum

   [ r,c,v ] = find(CC0 == max(max(CC0))) ;
```

```
CC_r = r; % Shift in row to maximize the cross correlation
CC_c = c; % Shift in column to maximize the cross correlation

 if (((i_e-i_b+1+2*By_rng)-r+1)>=1 && ((j_e-j_b+1+2*Bx_rng)-c+1) >=1) ;
%    if ((Row-r+1)>=1 && (Col-c+1) >=1) ;
    sub_BB = BB (((i_e-i_b+1+2*By_rng)-r+1):((i_e-i_b+1+2*By_rng)-r+1+(i_e-i_b)),
((j_e-j_b+1+2*Bx_rng)-c+1):(((j_e-j_b+1+2*Bx_rng)-c+1)+(j_e-j_b))) ;
%            sub_BB = BB ((Row-r+1):(Row-r+1+(i_e-i_b)), (Col-c+1):((Col-c+1)+(j_e-
j_b))) ;
%              sub_BB_X = B_re_X ((Row-r+1):(Row-r+1+(i_e-i_b)), (Col-c+1):((Col-
c+1)+(j_e-j_b))) ;
%              sub_BB_Y = B_re_Y ((Row-r+1):(Row-r+1+(i_e-i_b)), (Col-c+1):((Col-
c+1)+(j_e-j_b))) ;
%
%       sub_BB_X_re = sub_BB_X (:) ;
%       sub_BB_Y_re = sub_BB_Y (:) ;
%       sub_BB_Z_re = sub_BB (:) ;
%
%       sub_BB_XYZ = [ sub_BB_X_re, sub_BB_Y_re, sub_BB_Z_re ];

    %Calculate the counterpart of Matrix Sub_B
    BBB = B_mxm - sub_BB ;
```

```
    %Summation of A_fl & BB (ideally, all the compoments of sum_AB should have
    %same values.
    sum_AB = AA + BBB ;
    AB_mx = max(sum_AB) ;
    AB_mxm = max(AB_mx) ;

    %Calculate the Aperture
    Apert0 = AB_mxm - sum_AB ;
    Hist_Apert_Z0 = Apert0(:) ;

  else
    Hist_Apert_Z0 = 0 ;

  end;

  s1 = strcat('Hist_Apert_Z_no_rot','.txt') ;
  fid = fopen (s1, 'w');
  fprintf(fid, '%f\r\n', Hist_Apert_Z0);

% Generate the cases of z-dir. rotation.
% Important !!!
% Only apply to the sample without slits!!!!
```

```
for k = ( Min_Z_rot : d_inc : Max_Z_rot );
    i=0;
    j=0;

    CosPhi = cos(i*pi/180);
    CosTheta = cos(j*pi/180);
    CosPsi = cos(k*pi/180);
    SinPhi = sin(i*pi/180);
    SinTheta = sin(j*pi/180);
    SinPsi = sin(k*pi/180);

    Rm = zeros(3, 3);
    Rm(1, 1) = CosTheta*CosPsi;
    Rm(1, 2) = SinPhi*SinTheta*CosPsi - CosPhi*SinPsi;
    Rm(1, 3) = CosPhi*SinTheta*CosPsi + SinPhi*SinPsi;
    Rm(2, 1) = CosTheta*SinPsi;
    Rm(2, 2) = SinPhi*SinTheta*SinPsi + CosPhi*CosPsi;
    Rm(2, 3) = CosPhi*SinTheta*SinPsi - SinPhi*CosPsi;
    Rm(3, 1) = -SinTheta;
    Rm(3, 2) = SinPhi*CosTheta;
    Rm(3, 3) = CosPhi*CosTheta;
```

```
% Rotate the scanned data
Rot_Z_osT = Rm * B ;
% Rot_Z_osT = Rm * sub_BB_XYZ' ;

Rot_Z_os = Rot_Z_osT' ;

%Prepare the interpolation with scanned step size
X_Z = Rot_Z_osT(1:1 , :)' ;
Y_Z = Rot_Z_osT(2:2 , :)' ;
Z_Z = Rot_Z_osT(3:3 , :)' ;

X_Z_re = reshape(X_Z, Row, Col);
Y_Z_re = reshape(Y_Z, Row, Col);
Z_Z_re = reshape(Z_Z, Row, Col);

%    X_Z_re = reshape(X_Z, (i_e-i_b+1), (j_e-j_b+1));
%    Y_Z_re = reshape(Y_Z, (i_e-i_b+1), (j_e-j_b+1));
%    Z_Z_re = reshape(Z_Z, (i_e-i_b+1), (j_e-j_b+1));

% Interpolation function
F = TriScatteredInterp(X_Z,Y_Z,Z_Z);

xi_Z = ( min(B_X) : .25 : max(B_X) ) ;
```

```
   yi_Z = ( min(B_Y) : .25 : max(B_Y) ) ;
%     xi_Z = ( 0.25-Col*Stepsize/2 : .25 : Col*Stepsize/2 ) ;
%     yi_Z = ( 0.25-Row*Stepsize/2 : .25 : Row*Stepsize/2 ) ;
%     xi_Z = ( min(sub_BB_X_re)   : .25 : max(sub_BB_X_re) ) ;
%     yi_Z = ( min(sub_BB_Y_re)   : .25 : max(sub_BB_Y_re) ) ;

   [qx_Z,qy_Z] = meshgrid(xi_Z,yi_Z);

   Z_Z_int = F(qx_Z,qy_Z);

   % Find "NaN" & set it zero
   nan = find (isnan(Z_Z_int));
   Z_Z_int (nan) = min(min(Z_Z_int)) ; % change NaN with Zero

   osT_Z = [ reshape(qx_Z, T_num, 1), reshape(qy_Z, T_num, 1), reshape(Z_Z_int,
T_num, 1)];
%          osT_Z = [ reshape(qx_Z, (i_e-i_b+1)*(j_e-j_b+1), 1), reshape(qy_Z, (i_e-
i_b+1)*(j_e-j_b+1), 1), reshape(Z_Z_int, (i_e-i_b+1)*(j_e-j_b+1), 1)];

   % Export to txt file
   if k < 0 ;
   s = strcat(num2str((k/d_inc)+ - Min_Z_rot/d_inc+1),'_Ros_zdir_n', num2str(abs(k)),
'.txt') ;
```

```
   else
   s = strcat(num2str((k/d_inc)+ - Min_Z_rot/d_inc+1),'_Ros_zdir_p', num2str(abs(k)),
'.txt') ;
   end ;

   fid = fopen (s, 'w');
   fprintf(fid, '%f  %f  %f\r\n',osT_Z');

end;

% Increase the rotation angle in z-dir.
k = Min_Z_rot ;
ma = 1;  % counter

while k <= Max_Z_rot ;

   if k < 0 ;
   s = strcat(num2str((k/d_inc)+ - Min_Z_rot/d_inc+1),'_Ros_zdir_n', num2str(abs(k)),
'.txt') ;
   else
   s = strcat(num2str((k/d_inc)+ - Min_Z_rot/d_inc+1),'_Ros_zdir_p', num2str(abs(k)),
'.txt') ;
   end ;
```

```
   fid = fopen (s);
%      B = fscanf( fid, '%f', [ 3, (i_e-i_b+1)*(j_e-j_b+1) ] ) ; % Z-coordinate values of the
sample without slits
   B = fscanf( fid, '%f', [ 3, T_num ] ) ; % Z-coordinate values of the sample without slits

   %Prepare matrix B for cross-correlation

   % Transform to 2-D matrix form
   B_Z = B(3:3 , 1:T_num)' ; % Z- coordinate
   B_re_Z = reshape (B_Z, Row, Col);

%     B_Z = B(3:3 , 1:(i_e-i_b+1)*(j_e-j_b+1))' ; % Z- coordinate
%     B_re_Z = reshape (B_Z, (i_e-i_b+1), (j_e-j_b+1));

   % Reset the area of B
%     B_sub = B_re_Z ((i_b-B_rng):(i_e+B_rng), (Col-j_e-B_rng):(Col-j_b+B_rng)) ;
%                    B_sub     =     B_re_Z     ((i_b-1*By_rng):(i_e+1*By_rng),     (j_b-
1*Bx_rng):(j_e+1*Bx_rng)) ;
   B_sub     =     B_re_Z     ((i_b-1*By_rng):(i_e+1*By_rng),     (Col-j_e-1*Bx_rng):(Col-
j_b+1*Bx_rng)) ;
%     B_sub = B_re_Z ;
```

```
%Find the minimum & maximum values of matrix

B_mn = min(B_sub) ;

B_min = min(B_mn) ;

%Re-Set reference level of B_re_Z : make all the values to be positive

BB = B_sub - B_min ;

%Cross-Correlation function

CC = xcorr2(AA,BB) ;

%Find the maximum value of CC

CC_mx = max(CC) ;

CC_mxm = max(CC_mx) ;

CC_Zrot((k/d_inc)+ - Min_Z_rot/d_inc+1) = CC_mxm ;

% Extract sub-matrix of BB

   % r = row when CC is maximum

   % c = column when CC is maximum

   [ r,c,v ] = find(CC == max(max(CC))) ;

if (((i_e-i_b+1+2*By_rng)-r+1)>=1 && ((j_e-j_b+1+2*Bx_rng)-c+1) >=1) ;
```

```
%     if ((Row-r+1)>=1 && (Col-c+1) >=1) ;

      sub_BB = BB (((i_e-i_b+1+2*By_rng)-r+1):((i_e-i_b+1+2*By_rng)-r+1+(i_e-i_b)),
((j_e-j_b+1+2*Bx_rng)-c+1):(((j_e-j_b+1+2*Bx_rng)-c+1)+(j_e-j_b))) ;
%             sub_BB = BB ((Row-r+1):(Row-r+1+(i_e-i_b)), (Col-c+1):((Col-c+1)+(j_e-
j_b))) ;

      B_mx = max(sub_BB) ;
      B_mxm = max(B_mx) ;

      %Calculate the counterpart of Matrix Sub_B
      BBB = B_mxm - sub_BB ;

      %Summation of A_fl & BB (ideally, all the compoments of sum_AB should have
      %same values.
      sum_AB = AA + BBB ;
      AB_mx = max(sum_AB) ;
      AB_mxm = max(AB_mx) ;

      %Calculate the Aperture
      Apert = AB_mxm - sum_AB ;
      Hist_Apert_Z(:, (k/d_inc) - Min_Z_rot/d_inc+1) = Apert(:) ;
```

```
   else
      Hist_Apert_Z(:, (k/d_inc) - Min_Z_rot/d_inc+1) = 0 ;

   end;

%     s1 = strcat('Hist_Apert_Z_rot(', num2str(k), ').txt') ;
%     fid = fopen (s1, 'w');
%       fprintf(fid, '%f\r\n', Hist_Apert_Z(:, ((k/d_inc) - Min_Z_rot/d_inc+1):((k/d_inc) -
Min_Z_rot/d_inc+1)));
%
   if k < 0;
      s2 = strcat('Hist_Apert_Z_rot_n', num2str(abs(k/d_inc)) ) ;
      s3 = strcat('Sht_Hist_Apert_Z_rot_n', num2str(abs(k/d_inc)) ) ;
   else
      s2 = strcat('Hist_Apert_Z_rot_p', num2str(abs(k/d_inc)) ) ;
      s3 = strcat('Sht_Hist_Apert_Z_rot_p', num2str(abs(k/d_inc)) ) ;
   end;

   % Calculate the number of data to be shifted for Histogram : 0.5%
   % => Aperture distribution
      Sort_Hist_Apert_Z = sort(Hist_Apert_Z); % Sorting by ascending order to find the
reference aperture
```

```
Num_sht = floor((j_e-j_b+1)*(i_e-i_b+1) * 0.5 / 100 ); % Number of data to be shifted : 0.5%

Sht_Ref = Sort_Hist_Apert_Z(Num_sht:Num_sht,:); % Find the reference aperture


Temp_Hist_Apert_Z = Hist_Apert_Z;


for sht_counter = ( 1:1:(j_e-j_b+1)*(i_e-i_b+1) );
Sht_Hist_Apert_Z(sht_counter:sht_counter, ((k/d_inc)-Min_Z_rot/d_inc+1):((k/d_inc)-Min_Z_rot/d_inc+1)) = Temp_Hist_Apert_Z(sht_counter:sht_counter,((k/d_inc)-Min_Z_rot/d_inc+1):((k/d_inc)-Min_Z_rot/d_inc+1))-Sht_Ref((k/d_inc)-Min_Z_rot/d_inc+1);
end;


Temp0 = reshape( Hist_Apert_Z(:, ((k/d_inc) - Min_Z_rot/d_inc+1):((k/d_inc) - Min_Z_rot/d_inc+1)), (i_e-i_b+1), (j_e-j_b+1)) ;
eval( [s2 '= Temp0'] ) ;
Temp1 = reshape( Sht_Hist_Apert_Z(:, ((k/d_inc) - Min_Z_rot/d_inc+1):((k/d_inc) - Min_Z_rot/d_inc+1)), (i_e-i_b+1), (j_e-j_b+1)) ;
eval( [s3 '= Temp1'] ) ;


% Find the maximum aperture value
Max_Aper(ma) = max(max(Temp0));
ma = ma + 1 ;
```

```
    k = k + d_inc ;

end ;

% export Cross-Correlation values
xlswrite ('CrossCor.xls', CC_Zrot');
xlswrite ('Max_Aper.xls', Max_Aper');
dlmwrite('Hist_Apert_all.txt', Hist_Apert_Z, 'delimiter', '\t', 'newline', 'pc');
dlmwrite('Sht_Hist_Apert_all.txt', Sht_Hist_Apert_Z, 'delimiter', '\t', 'newline', 'pc');


% Find the optimum aperture distribution by looking for the minimum
% standard deviation of each Z-rotation cases
    Std_Hist_Apert = std(Hist_Apert_Z);
    xlswrite ('Std_Hist_Apert.xls', Std_Hist_Apert');

    [ rm,cm,vm ] = find(Std_Hist_Apert == min(Std_Hist_Apert)) ;

    Opti_Hist_APert_Z = Sht_Hist_Apert_Z(:, cm:cm) ;
    dlmwrite('Opti_Hist_Apert.txt', Opti_Hist_APert_Z, 'delimiter', '\t', 'newline', 'pc');

    Opti_Z_rot = (cm-1)*d_inc + Min_Z_rot ;
```

```
    save ( 'Opti_Z_rot.mat', 'Opti_Z_rot');



% Plot all the 2-D aperture distribution
% Plot the aperture distribution by using "imagesc" function.

% Prepare the coordinate for figures
for xcoordi = (1:1:j_e-j_b+1);
    X_Coord(xcoordi:xcoordi,:) = (xcoordi + j_b - 1)* 0.25;
end;

for ycoordi = (1:1:i_e-i_b+1);
    Y_Coord(ycoordi:ycoordi,:) = (ycoordi + i_b - 1)* 0.25;
end;

% Prepare the coordinate to export txt file.
    for xcoordi = (1:1:j_e-j_b+1);
        for ycoordi = (1:1:i_e-i_b+1);
            temp_X_Coord = (xcoordi + j_b - 1)* 0.25;
            temp_Y_Coord = (ycoordi + i_b - 1)* 0.25;
            if ycoordi == 1 && xcoordi == 1 ;
                Temp_X = [ temp_X_Coord ];
```

```
            Temp_Y = [ temp_Y_Coord ];
        else
            Temp_X = [ Temp_X temp_X_Coord ];
            Temp_Y = [ Temp_Y temp_Y_Coord ];
        end;
    end;
end;


k = Min_Z_rot ;

while k <= Max_Z_rot ;

    % Set negative aperture to be zero
    for p_counter = (1:1:((i_e-i_b+1)*(j_e-j_b+1)));
        if Sht_Hist_Apert_Z(p_counter:p_counter, ((k/d_inc)-
Min_Z_rot/d_inc+1):((k/d_inc)-Min_Z_rot/d_inc+1)) <= 0 ;
            Sht_Hist_Apert_Z(p_counter:p_counter, ((k/d_inc)-
Min_Z_rot/d_inc+1):((k/d_inc)-Min_Z_rot/d_inc+1)) =0;
        else
            Sht_Hist_Apert_Z(sht_counter:sht_counter, ((k/d_inc)-
Min_Z_rot/d_inc+1):((k/d_inc)-Min_Z_rot/d_inc+1))
```

```
=Sht_Hist_Apert_Z(sht_counter:sht_counter,  ((k/d_inc)-Min_Z_rot/d_inc+1):((k/d_inc)-
Min_Z_rot/d_inc+1)) ;
      end;
   end;

   % Reshape to 2-D matrix
   Temp1 = reshape( Sht_Hist_Apert_Z(:, ((k/d_inc) - Min_Z_rot/d_inc+1):((k/d_inc) -
Min_Z_rot/d_inc+1)), (i_e-i_b+1), (j_e-j_b+1)) ;

   % Plot & Save figures
   hFig = figure(((k/d_inc) - Min_Z_rot/d_inc+1));
   set(hFig, 'Position', [100 100 Col+100 Row])

   imagesc(X_Coord, Y_Coord, Temp1) ;
   colorbar ;
   ttl = strcat('Apert Dist of ', SampNm2, '(', num2str(k) ,')');
   set(gca,'YDir','normal') ;
   title(ttl) ;
   xlabel('X-Axis (mm)') ;
   ylabel('Y-Axis (mm)') ;
   fn = strcat(num2str((k/d_inc) - Min_Z_rot/d_inc+1),'_',ttl, '.fig') ;
   saveas(gcf, fn);
```

```
    ttl1 = strcat(SampNm2,'_',num2str((k/d_inc) - Min_Z_rot/d_inc+1),'_', '(', num2str(k) ,')');
    fn = strcat(ttl1, '.jpg') ;
    saveas(gcf, fn);

    % Export to txt file.
    Two_Dim_Apert = [ Temp_X', Temp_Y', Sht_Hist_Apert_Z(:, ((k/d_inc) - Min_Z_rot/d_inc+1):((k/d_inc) - Min_Z_rot/d_inc+1)) ] ;

    stt = strcat('Apert Dist of ', SampNm2, '_', num2str((k/d_inc) - Min_Z_rot/d_inc+1),'_(', num2str(k) ,')','.txt') ;
    fid = fopen (stt, 'w');
    fprintf(fid, '%f  %f  %f\r\n', Two_Dim_Apert' );

    if k == Opti_Z_rot;

       ttl2 = strcat('Opti_Apert_',SampNm2, '(', num2str(k) ,')');
       fn = strcat(ttl2, '.jpg') ;
       saveas(gcf, fn);

       stt1 = strcat(ttl2, '.txt') ;
       fid = fopen (stt1, 'w');
       fprintf(fid, '%f  %f  %f\r\n', Two_Dim_Apert' );
```

```
    end;

    k = k + d_inc ;

end;

for i=1:1:i_e-i_b+1  ;
    for j = 1:1:j_e-j_b+1 ;
        if Sht_Hist_Apert_Z_rot_n1(i:i,j:j)<=0
            Sht_Hist_Apert_Z_rot_n1(i:i,j:j)=0 ;
        end;
    end;
end;
```

VITA

VITA

Min-Kwang Choi
Graduate School, Purdue University

Education
B.S., Civil Engineering, 2002, Korea University, Seoul, Korea
M.S., Civil Engineering, 2004, Korea University, Seoul, Korea
Ph.D., Civil Engineering, 2013, Purdue University, West Lafayette, Indiana

He received his B.S degree in Civil Engineering from Korea University and earned his Master of Science in Geotechnical Engineering from Korea University. After working as a tunnel and geotechnical engineer in Yongma Engineering in Korea for five years, he joined the Geotechnical Engineering in School of Civil Engineering at Purdue University in August 2009. In 2013, He received Doctor of Philosophy in Civil Engineering.

Research Interests
Seismic wave propagation in fractured media, fracture geometry and stiffness, rock mechanics and engineering